Rate Effects for Monopile Foundations

Kuen-Wei Wu
Harris Manchester College
University of Oxford

A thesis submitted for the degree of
Doctor of Philosophy
Trinity Term 2022

Abstract

Rate effects for monopile foundations

Kuen-Wei Wu

Harris Manchester College, University of Oxford

A thesis submitted for the degree of *Doctor of Philosophy*

Monopile pile foundations are the most commonly used support system for offshore wind turbines in Europe. These foundations are subject to lateral loading, which is cyclic in nature, with the loading rate and load eccentricity varying with time. Under extreme conditions, such as the emergency stop of the turbine, yawing or ship impact, transient loading is applied to the monopile, and a high loading rate is induced in the surrounding soil. With the increase in the soil loading rate, soil strength can be enhanced, leading to a higher pile capacity. These beneficial phenomena, known as rate effects, have been principally reported in element testing research and observed in laterally-loaded monopile testing in glacial till and dense marine sand in the Pile Soil Analysis (PISA) project. However, current design methods have yet to include rate effects, and more data are required to quantify rate effects to inform optimised monopile design.

This thesis systematically explores rate effects on the response of monopiles to lateral loading through laboratory-floor model testing in artificial dry sand and naturally-formed saturated stiff clay. First, a new loading apparatus for model pile testing was developed. It features a high-speed loading system which can apply rapid loading to the pile, and the height of the loading point is variable to investigate load eccentricity effects. Next, monotonic and uni-directional one-way cyclic lateral loading tests were conducted at different loading rates. In addition to rate effects, model piles were tested for various vertical loading and load eccentricities to study combined load effects. Finally, rate effects were quantified based on test data. It was found that rate effects are evident in monotonic and cyclic lateral loading in stiff clay (approximately 10% increase in capacity per log-10 cycle of the pile rotation rate). In contrast, rate dependency in dry sand appears to be negligible.

Together with the experimental work, a new practical monopile design model is developed under the hyperplasticity framework in this thesis. The model captures the coupled moment-horizontal load response using a yield surface approach. In addition to lateral soil resistance, base resistance can be implemented in the model. Furthermore, rate effects for monopiles can be modelled by incorporating rate-dependent functions. To simulate pile response to cyclic loading, the Hyperplastic Accelerated Ratcheting Model (HARM) can also be integrated into the design model. Theoretical modelling results are presented in this thesis to demonstrate the performance of the model.

Acknowledgement

I would like to give my warmest thanks to my supervisors, Prof Byron Byrne and Prof Guy Houlsby, who made this work possible. Their guidance and support carried me through all the stages of my research, especially during the coronavirus pandemic when my experimental work was severely impacted.

My research was funded by Ørsted through the EPSRC Centre for Doctoral Training in Renewable Energy Marine Structures (REMS-CDT) (EP/L016303/1), the Oxford-Ørsted collaboration framework and the scholarship by the Ministry of Education, Taiwan. The experimental work at Cowden was assisted by SOCOTEC. Their support is acknowledged.

Working in the Civil Engineering Group with many wonderful people was a great pleasure. I want to thank Dr. Thomas Andolfsson and Dr Iona Richards for advising on the rig design. Prof Byron Byrne, Dr. Róisín Buckley and Sarah Martin, who assisted me in the field testing at Cowden, are acknowledged. I am grateful to Prof Guy Houlsby, who came up with the original idea of theoretical modelling and allowed me to use his codes. I also thank Dr Toby Balaam, Sarah Martin and Rachel Keane for proofreading my work. Luc Simonon for reviewing my theoretical work and Zhenghui (Mark) Qiu for soil characterisation of the Cowden stiff clay are also appreciated. I thank Clive Baker and Alison May, who provided administrative and technical support for my research activities.

Outside my research group, I want to thank Prof. Ali Mehmanparast for his support and my REMS colleagues for making me feel at home during my visits to Cranfield and Strathclyde Universities. I also thank my friends and colleagues in the Civil Engineering group for sharing fun and gossip with me. I am grateful to my friends, especially Yun-Kai (Albert) Lee, Dr Gu-Lung Lin, Dr Chee Kin Then and Tzu-Hao (David) Wang, for having fun, travelling and exploring delicious food together.

Finally, I want to give my sincere thanks to my parents, sisters and late grandfather for supporting me in achieving my doctorate. I want to give special thanks to my girlfriend, Mi Jun, for accompanying me during my time in Oxford.

Kuen-Wei (Wayne) Wu
2022.10 in Oxford, UK

Nomenclature

Greek alphabet variables

α_{en}	Internal variable (hyperplasticity)
α_{s_u}	Cohesion factor between the pile and clay
$\dot{\alpha}_{ref}$	Quasi-static reference rate (RPT in hyperplasticity)
β	Increasing rate of θ under cyclic loading
	Shaft friction factor
	Hardening parameter (HARM)
β^*	Reference hardening parameter (HARM)
$\chi,\ \bar{\chi}$	Generalised stress (force) (hyperplasticity)
$\Delta\varepsilon_N$	Accumulated strain after N cycles
ΔF	Activation energy (RPT)
Δu	Accumulated pore pressure
δ	Ratio between the depth of the pivot point and pile embedment length
δt	Timestep for numerical implementation
ε	Strain
ε_t	Normalised load eccentricity ($= e/L$)
η_N	Energy loss factor per cycle
$\eta_{0.1Hz}$	Energy loss factor measured at $f = 0.1$ Hz
η_{10}	Rate parameter (element scale)
$\eta_{10\dot{\theta}}$	Rate parameter (model testing)
γ	Bulk unit weight of soil
γ'	Effective unit weight of soil
λ	Distance between successive equilibrium positions of a flow unit (RPT)
	Dimensionless scaler for the internal variable rate (hyperplasticity)

λ'	Displacement of an activated flow unit
ϕ'	Drained friction angle
ϕ'_a	Effective pile-soil friction angle
ϕ'_{cr}	Critical state friction angle
ρ	Rate of increasing undrained shear strength of clay with depth
$\rho_{0.1}$	Rate parameter (Graham *et al.*, 1983)
σ	Stress
	Winkler-type expression of lateral earth pressure
σ_{AV}	Average stress per cycle
σ_c	Cyclic load magnitude
σ_e	Maximum reversal stress in a cycle
σ_R	Reference stress
σ_r	Minimum reversal stress in a cycle
σ'_v	Effective vertical stress
τ	Shear stress in triaxial conditions
θ	Ground-level pile rotation
θ_i	Initial ground-level pile rotation
θ_R	Reference ground-level pile rotation ($\theta = 2°$)
$\dot{\theta}_o$	Slow rotation rate
$\dot{\theta}_r$	Reference rotation rate
$\tilde{\theta}$	Non-dimensional form of ground-level rotation
ϑ	Ground-level pile rotation times pile embedment length ($= \theta L$)
μ	Viscous component of the rate-dependent kinematic hardening model (hyperplasticity)
ν	Poisson’s ratio of soil
ζ_b	Cyclic load parameter

Latin alphabet variables

1-D	One-dimensional (modelling)
3-D	Three-dimensional (modelling)
A	Parameter to control the initial increment of $\Delta\theta_N$
A_b	Pile steel annulus area
a_{N^*}	Normalised elastic term in the linear viscosity model (hyperplasticity)
B	Parameter to determine the rate of k evolution
C	Perimeter of pile
C_{N^*}	Integration constant for the linear viscosity model (hyperplasticity)
c_1	Dimensionless constant for the shear stiffness of sand
c_3	Dimensionless parameter for vertical loading in sand (between 0 and 1)
c_4	Dimensionless parameter for base shear in clay (between 0 and 1)
c_v	Coefficient of consolidation
D	Pile diameter
D_{10}, D_{30}, D_{50}, D_{60}	Particle size indexes for soil classification
D_r	Relative density
d	Depth of the pile pivot point
	Dissipation function (hyperplasticity)
E	Experimental activation energy (RPT)
	Tangent stiffness of the calibration curve (hyperplasticity)
E_E	Energy stored in the cycle
E_H	Energy dissipated during the cycle
E_P	Young’s modulus of the pile
E_S	Secant soil modulus under small strains

e	Load eccentricity
	Void ratio
e_{in}	Input error (PID)
e_N	Maximum reversal load point during the $N^{\text{-th}}$ cycle
$\dot{F}$	Loading rate
F_1, F_2, F_3	Equations for solving pile pose
$\boldsymbol{F}$	Matrix of equations F_1, F_2, F_3
f	Force applied to a single flow unit (RPT)
	Frequency of cyclic loading
	Helmholtz free energy (hyperplasticity)
f_0	Fundamental frequency of the offshore wind turbine structure
f_0, f_1, f_2	Dimensionless factors for elastic pile stiffness
f_{1_p}	Rotational frequency during the turbine operation
f_{3_p}	Blade-passing frequency during the turbine operation
f_3, f_4	Dimensionless parameters for the elliptical equation of the failure surface
f_b	Base shear factor
f_{c_s}	Ultimate base shear factor for clay
f_{s_s}	Ultimate base shear factor for sand
f_{s_v}	Ultimate base moment factor for sand induced by vertical loading
f_θ	Base moment factor
G	Shear stiffness of soil
G_L	Shear stiffness of soil at the pile base
G_{max}	Shear modulus measured from the CPT
G_s	Secant shear modulus under small strains in element testing
	Specific gravity

g	Gravity acceleration
	Gibbs free energy (hyperplasticity)
H	Horizontal loading on the pile at the ground level
H_1, H_2	Applied horizontal loading by the two actuators
$\widetilde{H}$	Non-dimensional form of horizontal loading
H_0	Intercept on the H-axis of the failure surface
H_e	Horizontal loading on the pile at the loading point
H_R	Ultimate (reference) horizontal load capacity
h	Planck’s constant
	Height of the loading point in the PISA testing
	Elastic spring of the kinematic hardening model (hyperplasticity)
I_P	Moment of inertia
I_R	Dilatancy index (Bolton, 1986)
I_r	Rigidity index
$\boldsymbol{J}$	Jacobian matrix of equations F_1, F_2, F_3
K	Ultimate lateral earth pressure factor for sand ($= 3K_p$)
K_C	Controller gain
K_p	Coefficient of passive lateral earth pressure
K_R	Pile-flexibility factor
K_S	Coefficient of pile shaft resistance in sand

k	Boltzmann’s constant
	Dimensionless factor for lateral earth pressure
	Permeability of soil
	Pile stiffness
	Plastic slider of the kinematic hardening model (hyperplasticity)
k_1, k_2, k_3	Constants for the pile stiffness matrix for sand
k_4, k_5, k_6	Constants for the pile stiffness matrix for clay
k_b	Base shear stiffness
k_{max}	Initial secant pile stiffness
k_N	Pile secant stiffness per cycle
k_θ	Rotational stiffness
$\widetilde{k_H}$	Non-dimensional stiffness of horizontal loading
$\widetilde{k_M}$	Non-dimensional stiffness of moment
L	Pile embedment length
l	Travelling length of the LDT
M	Moment loading on the pile at the ground level
M'	Moment divided by pile embedment length ($= M/L$)
$\widetilde{M}$	Non-dimensional form of moment
M_e	Target moment for cyclic loading
M_R	Ultimate (reference) moment capacity
m_r	Factor controlling the rate of ratcheting (HARM)
m_v	Coefficient of compressibility

N	Avogadro’s number
	Number of cycles
	Number of elements/ yield surfaces (hyperplasticity)
N_h	Ultimate lateral earth pressure factor for clay ($=$ 9 ~ 12)
	(Randolph and Houlsby, 1984)
N_q	End bearing factor
N^*	Number of elements/ yield surfaces calculated (hyperplasticity)
n	Number of iterations for solving pile pose
	Pressure exponent
	Index for the yield surfaces ($1 \leq n \leq N$)
O	Theoretical reference point for solving pile pose
O'	Actual reference point for solving pile pose
p	Lateral resistance in $p - y$ curves
p'	Effective stress
p_a	Probability of flow units being activated (RPT)
	Atmospheric pressure
p_f'	Mean effective stress at failure
q^{ampl}	Cyclic load magnitude in element testing
R	Universal gas constant
R_{e0}	Pre-defined ratcheting parameter (HARM) ($=$ 1)
R_e	Ratcheting parameter (HARM)
R_e^*	Reference ratcheting parameter (HARM)
r	Normalised rate of increasing undrained shear strength of clay with depth
r_N	Minimum reversal load point in the $N^{\text{-th}}$ cycle

S	Number of flow units (RPT)
	Length of the LDT linkage rod
s_u	Undrained shear strength of clay
s_{u0}	Undrained shear strength of clay at the soil surface
s_{uL}	Undrained shear strength of clay at the pile base
T	Absolute temperature
T_{10}, T_{50}, T_{90}	Time for 10%, 50% and 90% consolidation
T_A, T_B	Functions of temperature (RPT in hyperplasticity)
T_d	Derivative time (PID)
T_i	Integral time (PID)
t	Pile wall thickness
	Time
U	Degree of consolidation
u	Ground-level horizontal pile displacement
$\tilde{u}$	Non-dimensional form of ground-level horizontal pile displacement
u_e	Horizontal displacement at the loading point
u_i	Initial ground-level horizontal displacement
u_{out}	Output (PID)
u_R	Reference horizontal displacement ($u = 0.1D$)
u_r	Ratcheting of u (HARM)
u_z	Horizontal displacement at the depth z below the ground level
V	Vertical loading on the pile at the ground level
$\tilde{V}$	Non-dimensional form of ground-level vertical loading

V_u	Ultimate vertical pile capacity
v	Vertical pile displacement
	Actuation rate
v_a	Frequency of activation (RPT)
v_G	Horizontal displacement at the ground level in the PISA testing
v_i	Initial ground-level vertical displacement
v_{net}	Net frequency of activation (RPT)
v_o	Slow actuation rate
w	Flow potential (hyperplasticity)
X	Proportion of successful barrier crossings (RPT)
x	Theoretical location of the LDT connection along the x-axis
x'	Actual location of the LDT connection along the x-axis
x^*	Location of the LDT along the x-axis
u_R	Allowable horizontal displacement $(= 0.1D)$
y	Lateral deflection in $p - y$ curves
	Theoretical location of the LDT connection along the y-axis
	Yield function (hyperplasticity)
y'	Actual location of the LDT connection along the y-axis
y^*	Location of the LDT along the y-axis
z	Depth below the ground level
	Force potential (hyperplasticity)

Common subscripts, prefixes and diacritics

X_{en}	Function/variable for $n = 1 \ldots N$ at the loading point (hyperplasticity)
X_{fast}	Fast rate of X
X_n	Function/variable for $n = 1 \ldots N$ (hyperplasticity)
X_N	Value of X for the $N^{\text{-th}}$ cycle

X_{max}	Maximum value of X
X_{min}	Minimum value of X
X_r	Variable for ratcheting (HARM)
X_{slow}	Slow rate of X
X_{un}	Function/variable for $n = 1\ldots N$ for u (hyperplasticity)
X_{ur}	Variable for ratcheting in u (HARM)
$X_{\vartheta n}$	Function/variable for $n = 1\ldots N$ for ϑ (hyperplasticity)
$X_{\vartheta r}$	Variable for ratcheting in ϑ (HARM)
$\dot{X}$	Rate of X
ΔX	Accumulated value of X Change in X

Other abbreviations

ALS	Accidental Limit State
CSV	Comma Separated Value
CPT	Cone Penetration Test
FLS	Fatigue Limit State
FPGA	Field Programmable Gate Array
HARM	Hyperplasticity Accelerated Ratcheting Model
LDT	Linear Displacement Transducer
LL	Liquid Limit
OWT	Offshore Wind Turbine
PI	Plasticity Index
PICASO	Pile Cyclic Analysis: Oxford and Ørsted
PID	Proportional Integral Derivative
PISA	Pile Soil Analysis

PL	Plastic Limit
RPT	Rate Process Theory
SLS	Serviceability Limit State
ULS	Ultimate Limit State
VST	Vane Shear Test
YLB	Yellow Leighton Buzzard

1 Introduction

1.1 Application

1.1.1 Offshore wind energy

Offshore wind energy is an essential element of the energy transition to reduce reliance on fossil fuels. Over recent years, offshore wind has grown rapidly in Europe and worldwide. The Global Wind Energy Council (2020) estimated that the global offshore wind market will continue to grow at an average annual rate of 18.6% until 2024, as shown in Figure 1-1. Offshore wind is expected to account for more than 20% of total wind installations by 2025.

There are many ambitious targets for offshore wind around the world. For instance, the UK aims to reach 40 GW of installed offshore wind capacity by 2030 (Great.gov.uk, 2022). The European Commission has also announced the intention to boost its offshore wind capacity to 60 GW by 2030 and 300 GW by 2050, achieving net-zero emissions (European Commission, 2022).

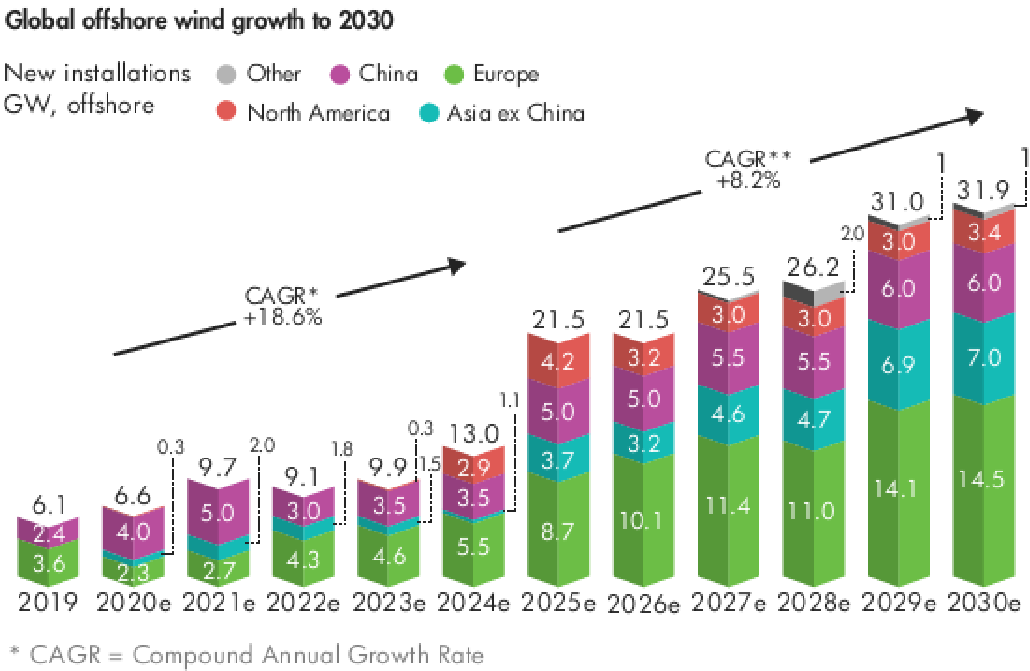

* CAGR = Compound Annual Growth Rate
Source: GWEC Market Intelligence, June 2020

Figure 1-1 Estimate of the global offshore wind market growth to 2030 (Global Wind Energy Council, 2020).

Driving down the cost of offshore wind turbine (OWT) foundations is a key element for developing offshore wind. An OWT structure comprises a tower, a nacelle, a rotor and a foundation system; the foundation accounts for 25% ~ 34% of the total cost (Bhattacharya, 2019). With the development of offshore wind technology, the turbine capacity has increased from 3 MW to 14 MW over the last decade and continues to grow (Wind Europe, 2021). As the turbine size becomes larger to capture more energy, the foundation size increases significantly, stimulating the need to achieve more economical foundation designs.

1.1.2 Offshore wind turbines monopiles

Monopiles are the most commonly used foundation system for OWTs among various fixed-bottom foundations (see Figure 1-2), accounting for more than 81% of existing OWTs in Europe (Wind Europe, 2021). The monopile is a large-diameter steel tube impact driven into the seabed (see Figure 1-3). The structural design is straightforward, and there is a well-sourced supply chain for monopile fabrication (Kallehave *et al*., 2015). Monopiles are often installed in shallow waters or up to 60 m depth. Current monopile dimensions are up to 8 m ~ 10 m in diameter (D) and 30 m ~ 40 m long (L), but the dimensions are continuing to increase for next-generation OWTs and for deeper waters (Byrne, 2020).

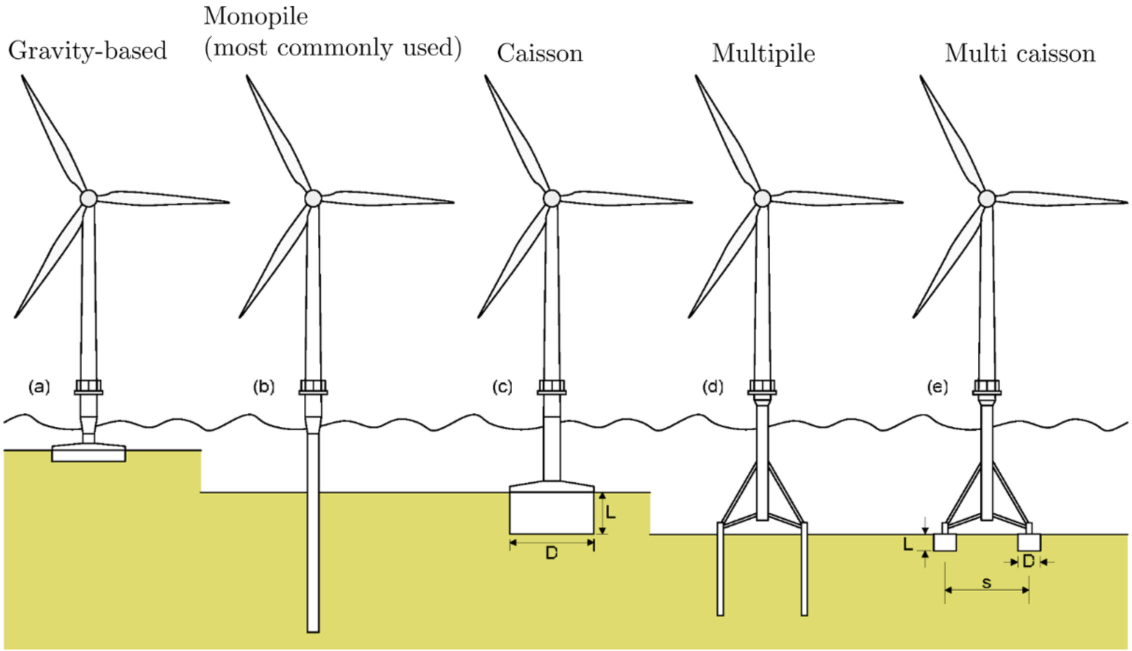

Figure 1-2 Various types of fixed-bottom foundations for supporting OWTs (Byrne and Houlsby, 2006).

Figure 1-3 Monopile foundation (D = 7.5 m) for the Veja Mate offshore wind farm (EEW, 2022).

1.1.3 Loading on OWT monopiles

The design standard *DNV-OS-J101 Design of Offshore Wind Turbine Structures* (DNV, 2014) summarises the design loads for OWT structural design, as set out in Table 1-1. Typical loads, such as environmental loads, OWT self-weight and turbine excitations, are routinely applied to the monopile (see Figure 1-4). At the foundation level, these load components are presented in terms of combined vertical (V), horizontal (H) and moment (M) loading.

Table 1-1 Summary of various loads on the OWT structure (DNV, 2014).

Load type	Example(s)
Permanent loads	Mass of the OWT structure (self-weight)
Variable functional loads	Ship impacts Loads caused by installation operations Wind turbine control and operation (actuation loads)
Environmental loads	Wind loads Wind-generated loads on the blades Braking forces due to breaking of the turbine Hydrodynamic loads (*e.g.* waves) Ice loads Other transient load cases (*e.g.* start-up, emergency shut down, fault events and yawing)
Accidental loads	Loads from extreme breaking waves Impacts from vessels
Deformation loads	Temperature loads Foundation settlement

Dynamic interactions for OWT structures are assessed for OWT monopile design. Typical dynamic loads arise from wind, waves and rotor excitations, as shown in Figure 1-5. The dynamic response depends on the fundamental frequency (f_0) of the structure (*i.e.* the first bending frequency), which is usually placed between the rotational frequency (f_{1p}) and the blade-passing frequency (f_{3p}). The peak frequency of wave loads may overlap with f_{1p} and is often between 0.1 Hz and 0.3 Hz, depending on the site conditions and wind speed. For a 6 – 8 MW OWT, for example, f_0 is designed to be approximately 0.2 Hz to 0.23 Hz to avoid resonances (Kallehave *et al*., 2015).

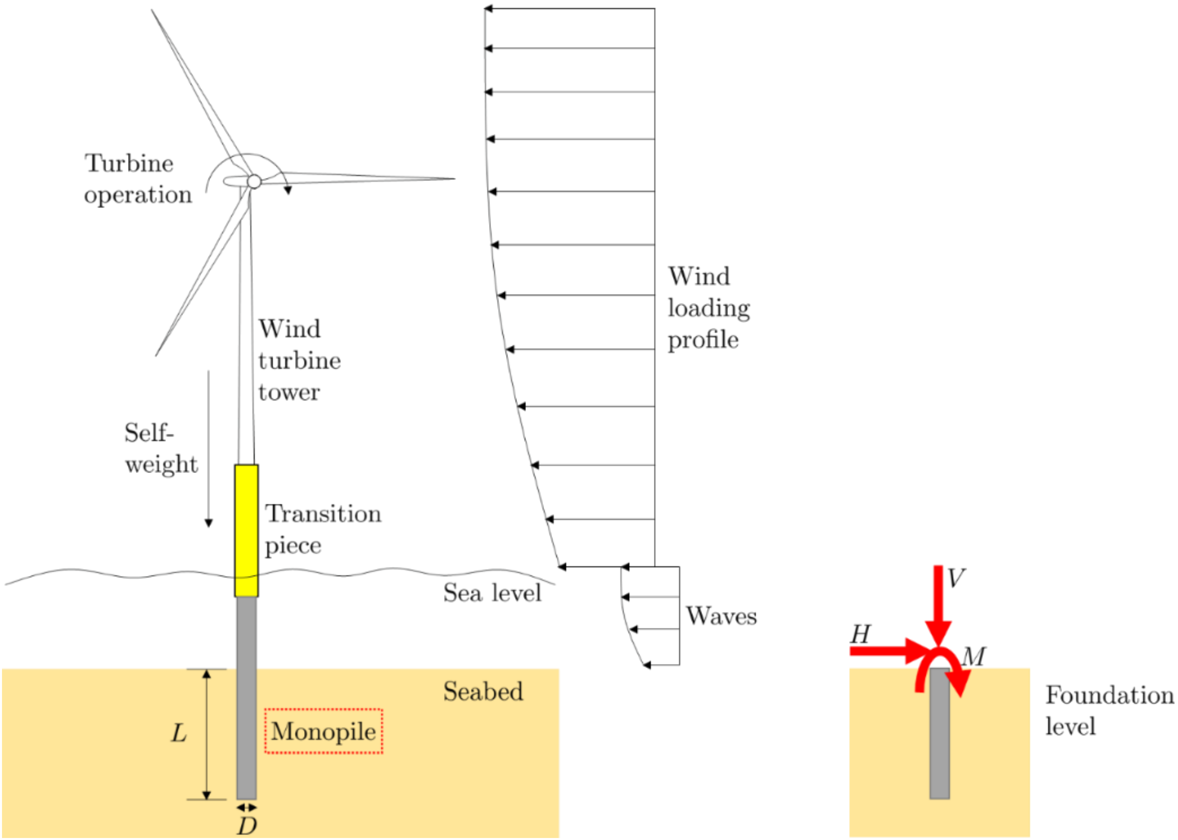

Figure 1-4 Illustration of typical loads on OWT monopiles (after Richards, 2019).

On some occasions, extreme transient loads are applied to the monopile. These include accidental loading from vessels, emergency stop, start or yawing of the turbine and harsh environmental conditions (*e.g.* storm loading). For instance, during an accidental ship impact event, the vessel speed can be approximately 2 m/s (DNV, 2014), reflecting a high loading rate being applied to the OWT structure and monopile. In these conditions, the loading applied to the surrounding soil typically occurs at a higher rate, leading to a stiffer pile response and a higher pile capacity.

Byrne *et al*. (2020b) and McAdam *et al*. (2020) found that monopile response is enhanced with the increase in loading rate (see further discussions in Section 1.2.4). Such beneficial effects may become more significant for future designs as the next-generation turbine will become larger. The magnitude of transient loading may also increase with the turbine size. If rate effects are incorporated into monopile design, less steel may be used for monopile fabrication, and savings may be made.

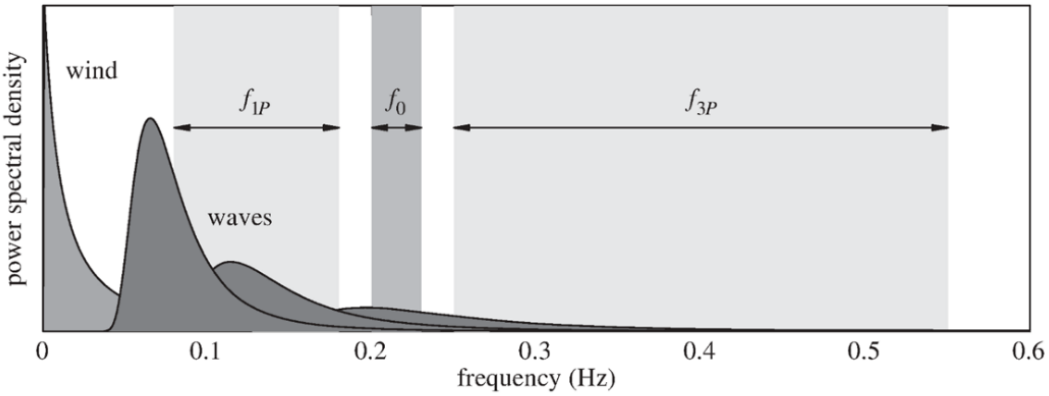

Figure 1-5 Typical excitation ranges for modern OWTs
(wave spectra represent various wind speeds) (Kallehave *et al.*, 2015).

1.1.4 Design requirements for loads and deformation

The design standards *DNVGL-ST-0126: Support Structures for Wind Turbines* (DNV GL, 2016a) and *DNVGL-ST-0437: Loads and Site Conditions for Wind Turbines* (DNV GL, 2016b) specify four load limit states for OWT support structures, as listed in Table 1-2. The ULS condition considers ultimate resistance and deformation, while the SLS condition is the criterion for normal operation. For OWT foundation design, these limit states need to be assessed to ensure that the structure can maintain integrity and performance under various integrated load conditions. The ULS and SLS conditions, typically considered in geotechnical design practice, are a focus of this thesis to evaluate pile movement. Under the ULS condition, the monopile is required to provide sufficient resistance to the maximum combined $H - M$ loading. The SLS design load magnitude is approximately 50% of the ULS load (see, *e.g.* LeBlanc *et al.*, 2010). Load cases for assessing these load limits, including the load duration distribution, are found in Section 5.1 in *DNV-OS-J101* and Section 4 in *DNVGL-ST-0437*.

Table 1-2 Load limit states for OWT support structures (DNV GL, 2016a).

Load limit type	Corresponding to
Ultimate limit state (ULS)	The maximum load-carrying resistance
Serviceability limit state (SLS)	Tolerance under normal use or durability
Accidental limit state (ALS)	The maximum load-carrying resistance to accidental loads and post-accidental integrity
Fatigue limit state (FLS)	Failure due to (long-term) repeated dynamic loading (*e.g.* cyclic loading)

Ground-level pile rotation (θ) and horizontal displacement (u) limits are often specified for the ULS and SLS conditions (see definitions in Figure 1-6). Under the ULS condition, the allowable pile deformation is often considered as $u = 0.1D$ or $\theta = 2°$ (*e.g.* Byrne *et al.*, 2017). However, there are no clear definitions in the design manuals or standards, and these values may be site-specific. Under regular use (*i.e.* the SLS condition), $\theta = 0.5°$ is often considered the limit of tilt rotation angle, and the installation tolerance is taken as $\theta = 0.25°$ (DNV GL, 2016a).

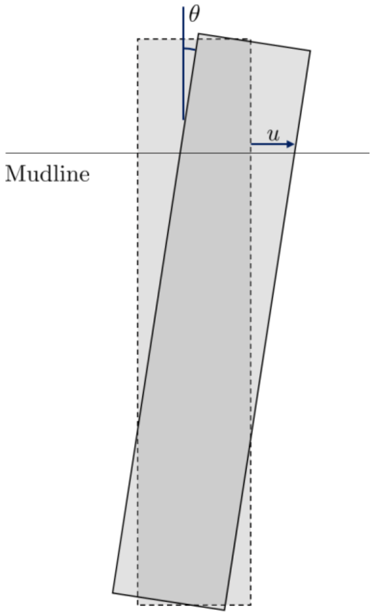

Figure 1-6 Illustration of pile deformation at the ground level.

1.1.5 Current design methods for monopiles under lateral loading

1.1.5.1 The '*p-y*' method

Design guidance and manuals, such as API (2007) and DNV GL (2016a), recommend the *p-y* method for pile design under lateral loading. The *p-y* method was developed for lateral loading applied to long and slender piles for oil and gas structures (*e.g.* $D \approx 610$ mm, $L/D = 100$). It has also been adopted in the offshore wind industry for laterally-loaded OWT monopiles. The *p-y* method was formulated based on field testing on long and slender piles (*e.g.* Matlock, 1970; Cox *et al.*, 1974; Reese *et al.*, 1975). These piles have a small diameter D of 24 inches ($\approx$ 0.61 m) with an aspect ratio L/D of 34, while monopiles have a large diameter and a small L/D ratio between 3 and 6. Therefore, deploying *p-y* curves for monopiles is questionable.

In the *p-y* method, the pile is assumed to act as a beam, and the lateral pile resistance is composed of a series of non-linear independent springs at different depths, given the Winkler assumption (see Figure 1-7). The springs are described by p (lateral resistance)-y (lateral deflection) curves.

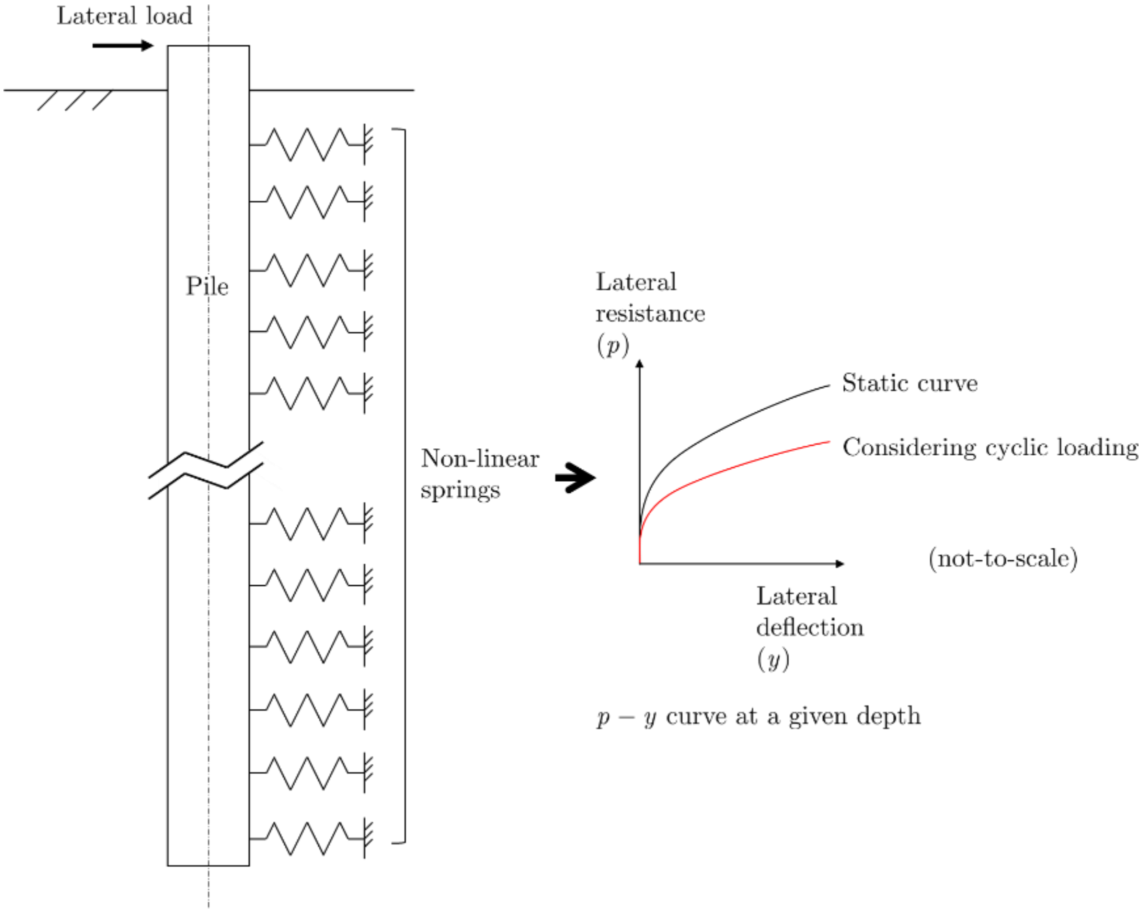

Figure 1-7 Illustration of the *p-y* method.

Strength reduction due to cyclic loading is typically considered for clay and sand in the *p*-*y* method. Under cyclic loading, accumulated pore water pressures may not have sufficient time to dissipate, leading to strength reduction depending on the pile size and depth (see details in API, 2007). Strength reduction factors for sand and soft clay are suggested by empirical correlations developed from field test data. Engineering judgement is required in the case of stiff clay.

For large-diameter piles, such as monopiles, DNV GL (2016a) suggests that the design needs to be validated through other comprehensive approaches (*e.g.* finite element analysis). Work is ongoing to assess and update the *p*-*y* method for large-diameter monopiles (*e.g.* Jeanjean *et al*., 2022).

1.1.5.2 The PISA method

The industry-led PISA (Pile Soil Analysis) project developed a new design method for monopiles. Field testing and comprehensive finite element modelling were undertaken in the PISA project to develop a new one-dimensional (1-D) beam model building on the conventional *p*-*y* model (*e.g.* Byrne *et al*., 2015a). The field testing was conducted in dense marine sand at Dunkirk, France (McAdam *et al*., 2020) and stiff clay till at Cowden, northeast England (Byrne *et al*., 2020b). These soil conditions were selected to be broadly representative of multiple North Sea wind farm sites. Piles of different diameters ($D = 0.273$ m to 2 m) with aspect ratios $L/D = 3$ ~ 10 were tested under monotonic loading. The field test data were used to validate 3-D finite element models to inform the parameterisation of a 1-D beam model. The conceptual monopile model and the 1-D beam model are shown in Figure 1-8. The pile is illustrated using a line of finite elements based on Timoshenko beam theory. The model is extended from the *p*-*y* model by incorporating additional components representing the base reactions and distributed moments resulting from vertical shaft resistance.

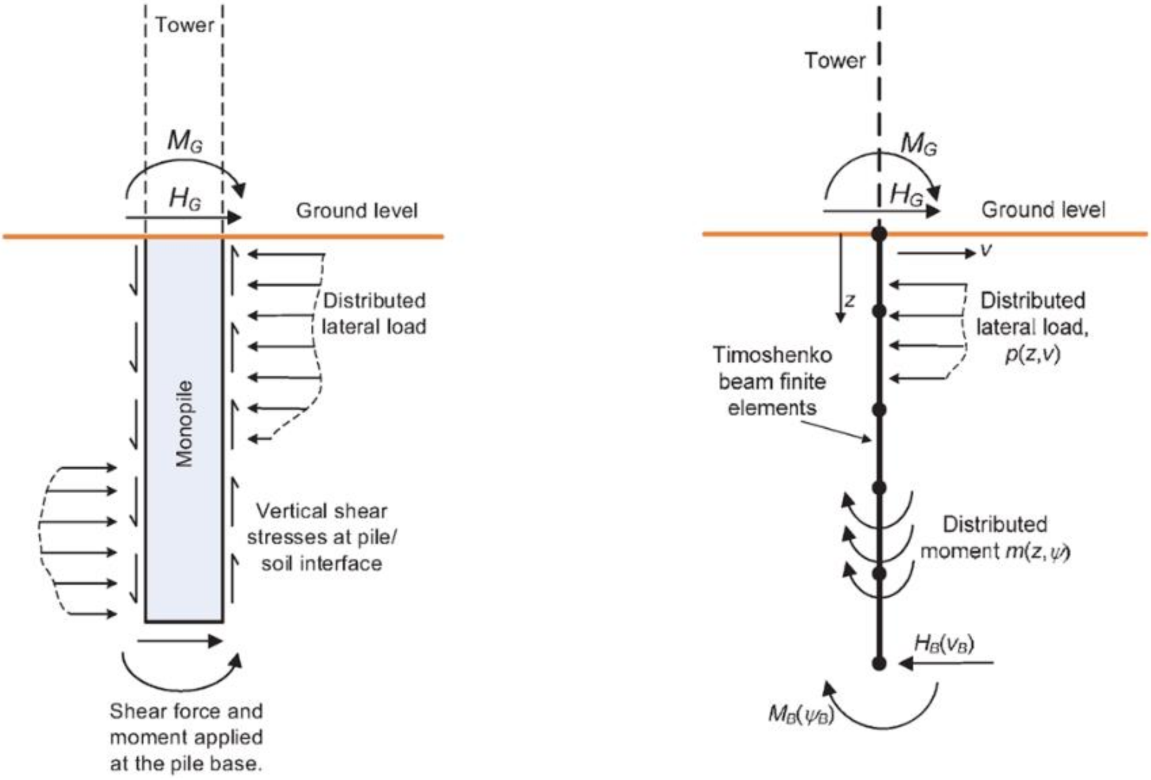

Figure 1-8 Illustration of the PISA design model (Byrne *et al*., 2017).

The *p*-*y* method was found to be over-conservative compared to the PISA design method (Byrne *et al*., 2017). An example design case in Figure 1-9 compares 3-D finite element modelling, the 1-D PISA model, and the *p*-*y* method. In this case, L/D = 4, D = 8.75 m and the load eccentricity (e) is equal to $10D$, and the *p*-*y* analysis shows a much softer response and a lower capacity than the others. To achieve the same ultimate capacity of 25 MN, in the *p*-*y* analysis, the pile length has to be extended by 55% (from $L/D = 4$ to $L/D = 6.2$). The PISA model considers the reactions from pile shaft, base shear and base moment, which can significantly contribute to pile resistance against lateral loading. As a result, if these additional components are incorporated into monopile design, shorter piles can be used, and the foundation cost can be reduced.

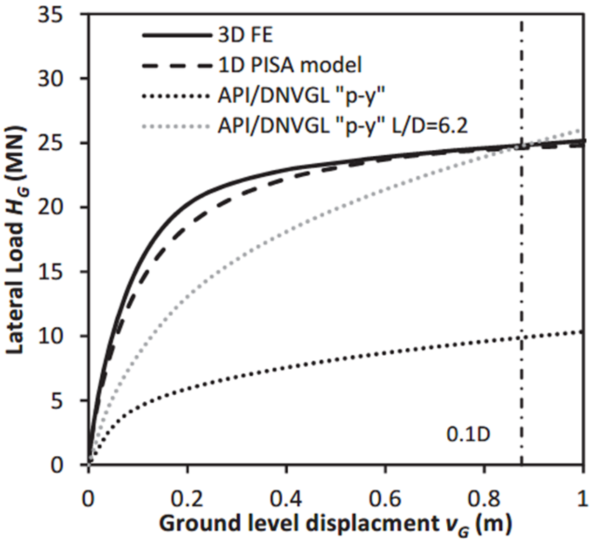

Figure 1-9 Example design case to compare 3-D finite element modelling, the PISA model and the *p-y* method (Byrne *et al.*, 2017).

1.1.5.3 Assessing cyclic lateral loading of monopiles

Lateral pile capacity is assumed to reduce due to cyclic loading using the conventional $p - y$ analysis (see Section 1.1.5.1). However, experimental evidence (*e.g.* Richards, 2019) shows that lateral pile capacity in drained sand does not decrease due to cyclic loading. In addition, only limited pile test data in the literature is available on cyclic responses of monopiles. Therefore, questions arise as to whether the empirical correlations adopted in the *p-y* analysis are appropriate for monopile design under cyclic lateral loading. In addition, OWT monopiles are subject to cyclic loads at different frequencies, such as wind and waves (see Figure 1-5). If rate effects are considered in cyclic loading analysis, soil strength may be enhanced (Lefebvre and LeBoeuf, 1987), leading to a stiffer pile response.

The PISA project focused specifically on monotonic pile behaviour, with further research needed to address cyclic loading problems. For instance, an ongoing research project, PICASO (Pile Cyclic Analysis: Oxford and Ørsted), explores cyclic lateral loading responses of monopiles through field testing and theoretical development based on the existing PISA method (Byrne *et al.*, 2020a). Along with other research in the literature, work is underway to inform design methods for a more detailed analysis of pile response to cyclic lateral loading.

1.1.5.4 Importance of rate effects for monopiles

Rate effects were observed in the PISA field testing in both ground conditions (Byrne *et al*., 2020b; McAdam *et al*., 2020) (see discussions in Section 1.2.4). Previous research, principally through element testing, showed that soil strength properties can be enhanced with the increase in loading rate (see Section 1.2.2). This phenomenon can derive that pile capacity increases with loading rate at a macro scale. However, monopiles are usually designed for slow loading rates without considering rate effects. Pile resistance may be underestimated when rapid loading (*e.g.* emergency stop, yawing and other extreme transient load cases) is applied to the OWT monopile. The tests in the PISA project are insufficient to quantify rate dependency for monopiles rigorously, and therefore, more data are required for investigating rate effects further.

1.1.6 Summary

Most OWTs are found on monopiles in Europe, and there is a well-established supply chain to support the monopile industry. The monopile is a short, rigid steel tube installed into the seabed. The monopile size continues growing to support the next-generation turbine and deeper waters.

Optimising monopile design is key to developing offshore wind because the foundation accounts for more than 20% of the total cost. Therefore, the total offshore wind cost can be driven down if improved monopile design methods are available, and less steel will be used to fabricate monopiles.

Various load conditions are analysed for monopile design. Environmental loads, such as wind and waves, are cyclic in nature. In some extreme cases, rapid transient loads are applied to the OWT monopile, and the loading rate can suddenly increase. In such conditions, the soil loading rate becomes faster, which may increase soil strength and pile capacity.

Current design methods for OWT monopiles are reviewed. In addition to lateral resistance, vertical shaft resistance, base shear and base moment need to be considered in monopile design, as reported in the PISA project. For cyclic loading design, the $p-y$ method outlines empirical strength reduction factors for post-cyclic pile capacity. However, these factors were based on pile testing dated back to the 1960s for oil and gas offshore structures, which may not accurately reflect realistic monopile response. Although the PISA project reported that pile capacity increases with the loading rate, the results are insufficient to incorporate this beneficial phenomenon into design confidently. In addition, rate effects for monopiles under cyclic lateral loading are unclear. Therefore, further investigations are required to explore rate effects for monopiles to improve design methods.

1.2 Review of soil rate effects

As discussed in Section 1.1.6, new research is needed to investigate soil rate effects to inform improved monopile design. This section reviews previous work on rate effects through theoretical and experimental approaches in the literature.

Most soils are rate-dependent due to their viscous properties. Typically, soil strength increases with the loading rate. Common rate-dependent phenomena include creep, stress relaxation and the effects of shearing at different rates. Clay usually exhibits a more significant rate response than sand because it has a greater specific surface area (Mitchell and Soga, 2005).

It is noted that soil rate effects are associated with soil skeleton behaviour (Wroth and Houlsby, 1985). This thesis does not discuss other “time-dependent” phenomena, such as primary consolidation and excess pore pressure dissipation response.

1.2.1 Rate process theory for soil deformation (Mitchell and Soga, 2005)

Rate process theory (RPT) was developed in physical chemistry through statistical mechanics approaches and provides insights into soil rate effects at microscale. The following summarises the framework of RPT for soils developed by Mitchell and Soga (2005).

At a microscale, relative movements between atoms, molecules and other particles (known as "flow units") are constrained by an energy barrier. Activation energy (ΔF), often from thermal energy, is required to cross the barrier and allow flow units to move to new positions. Based on statistical mechanics, the energy is divided and allocated within the flow units, and only part of the units are activated following a Boltzmann distribution. The probability (p_a) of flow units being activated during an oscillation is expressed as

$$p_a(\Delta F) = \exp\left(\frac{-\Delta F}{NkT}\right) \qquad \text{Equation 1-1}$$

where N is Avogadro's number (6.02×10^{23}), k is Boltzmann's constant (1.38×10^{-23} J·K^{-1}), and T is the absolute temperature (unit: K). Nk (≈ 8.3145 J·K^{-1}·mol^{-1}) is equal to the universal gas constant, R. Then, the frequency of activation (ν_a) can be derived:

$$\nu_a = \frac{kT}{h}\exp\left(\frac{-\Delta F}{RT}\right) \qquad \text{Equation 1-2}$$

in which h is Planck's constant (6.624×10^{-34} J·s^{-1}).

The energy barrier is changed if a shear force is applied to the flow units. If f is the force applied to a single flow unit, and λ is the distance between successive equilibrium positions, the barrier height decreases in the direction of f and increases in the opposite direction by $f\lambda/2$. Therefore, the net frequency of activation (ν_{net}) in both directions becomes

$$\nu_{net} = \frac{kT}{h}\exp\left(\frac{-\Delta F}{RT} - \frac{f\lambda}{kT}\right) + \frac{kT}{h}\exp\left(\frac{-\Delta F}{RT} + \frac{f\lambda}{kT}\right)$$

Equation 1-3

$$= \frac{2kT}{h}\exp\left(\frac{-\Delta F}{RT}\right)\sinh\left(\frac{f\lambda}{2kT}\right).$$

It is expected that some of the flow units may be activated, while others may not cross the barrier. For each activated unit, there will be a displacement λ'. In a given direction, the component of λ' times the number of activated units per unit time equals the movement rate per unit time. On a per unit length basis, the movement rate per unit time then becomes the strain rate ($\dot{\varepsilon}$). By considering the proportion of successful barrier crossings (X), $\dot{\varepsilon}$ is expressed as

$$\dot{\varepsilon} = X\nu_{net} = 2X\frac{kT}{h}\exp\left(\frac{-\Delta F}{RT}\right)\sinh\left(\frac{f\lambda}{2kT}\right)$$

Equation 1-4

in which the magnitude of X may be time- and structure-dependent.

Mitchell *et al*. (1968) suggested that $(f\lambda/2kT)$ > 1 for most solid deformation problems, and thus $\sinh\left(\frac{f\lambda}{2kT}\right)$ is approximately equal to $\frac{1}{2}\exp\left(\frac{f\lambda}{2kT}\right)$. The above equation becomes

$$\dot{\varepsilon} \approx 2X\frac{kT}{h}\exp\left(\frac{-\Delta F}{RT}\right)\cdot\frac{1}{2}\exp\left(\frac{f\lambda}{2kT}\right) = X\frac{kT}{h}\exp\left(\frac{-\Delta F}{RT} + \frac{f\lambda}{2kT}\right).$$

Equation 1-5

Defining that the experimental activation energy (E) is equal to $\Delta F - \frac{f\lambda N}{2}$, $\dot{\varepsilon}$ can be expressed as

$$\dot{\varepsilon} = X\frac{kT}{h}\exp\left(-\frac{E}{RT}\right).$$

Equation 1-6

As X, k, h and R are constant, the resistance of flow units is dependent on $\dot{\varepsilon}$ and T, which explains the underlying mechanism of soil rate effects at microscale. E is often obtained from creep test data.

In triaxial compression conditions, the shear stress (τ) is assumed to be uniformly distributed among S flow units, and therefore $f = \tau/S$. Equation 1-5 can be re-written as

$$\dot{\varepsilon} = X\frac{kT}{h}\exp\left(\frac{-\Delta F}{RT} + \frac{\tau\lambda}{2SkT}\right).$$ Equation 1-7

By taking the logarithm of 10 on both sides, the above equation can be expressed as

$$\log_{10}\dot{\varepsilon} = \log_{10}\left(X\frac{kT}{h}\right)\cdot\log_{10}e\cdot\left(\frac{-\Delta F}{RT} + \frac{\tau\lambda}{2SkT}\right).$$ Equation 1-8

If the temperature remains unchanged, the term $\log_{10}\left(X\frac{kT}{h}\right)\cdot\log_{10}e$ is assumed to be fixed. Therefore, the difference in resistance at different strain rates $\dot{\varepsilon}$ may be described using a semi-logarithmic relationship, as discussed later in Figure 1-20. Similarly, Equation 1-4 can be re-written as $\dot{\varepsilon} = 2X\frac{kT}{h}\exp\left(\frac{-\Delta F}{RT}\right)\sinh\left(\frac{f\lambda}{2kT}\right) = T_A\cdot\sinh\left(\frac{f}{T_B}\right)$, in which T_A and T_B are functions of temperature. This format has been derived for modelling under the hyperplasticity framework (Houlsby and Puzrin, 2006) and is adopted for the theoretical modelling in this thesis (see Section 6.2.2.3 and Appendix A.4).

1.2.2 Rate effects in element testing

1.2.2.1 Monotonic loading

The strain-stress-strain rate response of sand is more complex and less consistent than clay. For instance, Kiyota and Tatsuoka (2006) and Tatsuoka *et al*. (2008) found that τ transiently changes when $\dot{\varepsilon}$ increases/decreases in Toyoura sand and Monterey No.0 sand, but the overall stress-strain response is consistent (see Figure 1-10). This phenomenon is recognised as acceleration-sensitivity by Tatsuoka *et al*. (2008), although the mechanism is still unclear. Watanabe and Kusakabe (2013) carried out a series of “drained” triaxial compression tests on dry Toyoura sand at constant $\dot{\varepsilon}$. In Figure 1-11, their results show that rate dependency is not apparent when the axial strain is less than 3%, but the post-peak response appears to be rate-sensitive. When $\dot{\varepsilon}$ becomes larger, the volumetric deformation tends to decrease so that the soil may become partially drained or undrained. For saturated sand, this phenomenon may become significant, and time-dependent pore pressure response needs to be analysed. For example, Figure 1-12 shows that the drainage condition may become “partially drained” with the increase in $\dot{\varepsilon}$ during a saturated, undrained triaxial test. However, this thesis focuses on time effects due to soil skeleton behaviour; pore pressure dissipation is not addressed.

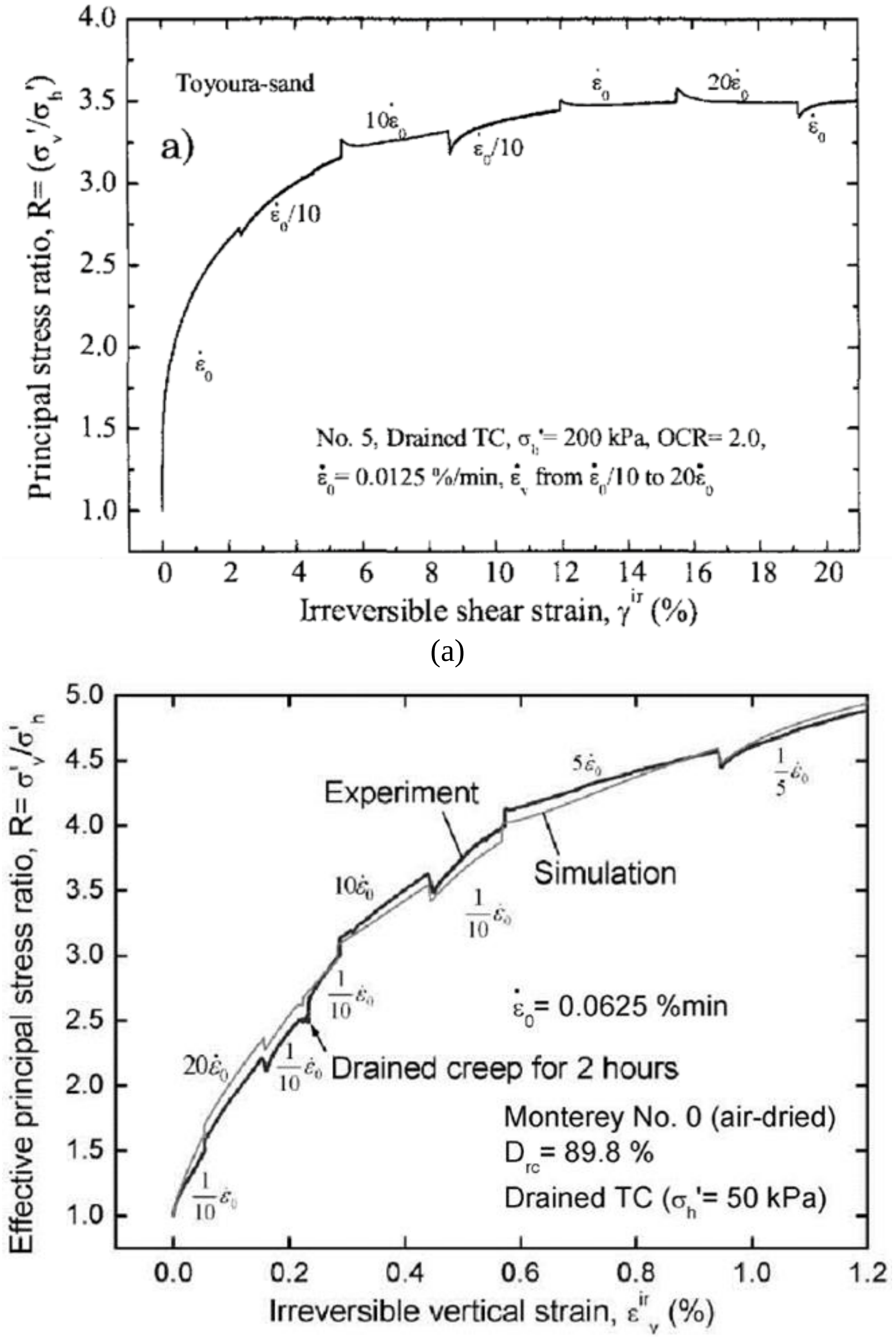

(a)

(b)

Figure 1-10 Transient behaviour is observed during $\dot{\varepsilon}$ changes in (a) Toyoura sand; (b) Monterey No.0 sand (Kiyota and Tatsuoka, 2006; Tatsuoka *et al*., 2008).

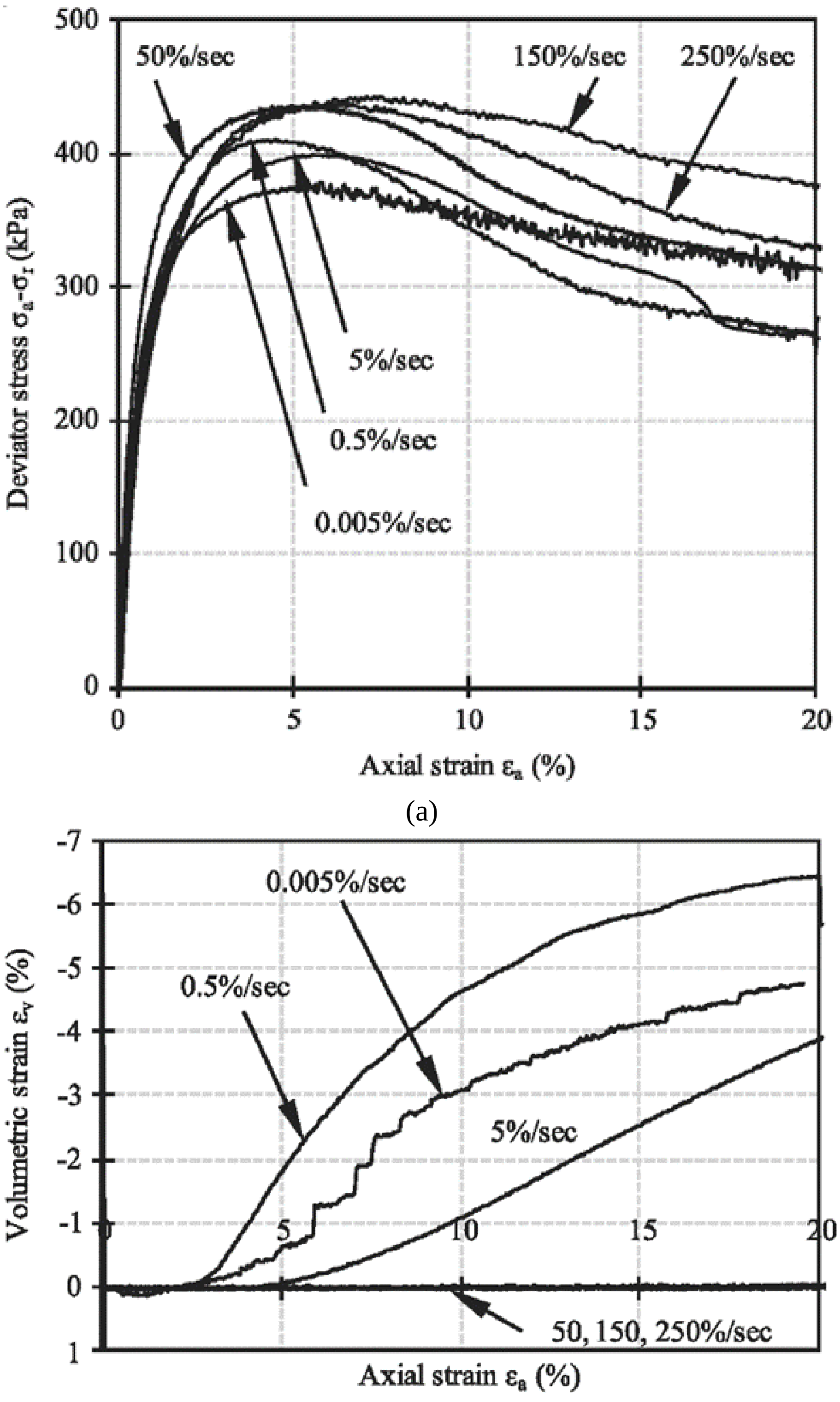

(a)

(b)

Figure 1-11 Drained triaxial compression tests on dry Toyoura sand

(confining stress = 100 kPa, relative density = 80%):

(a) stress-strain response; (b) volumetric strain response (Watanabe and Kusakabe, 2013).

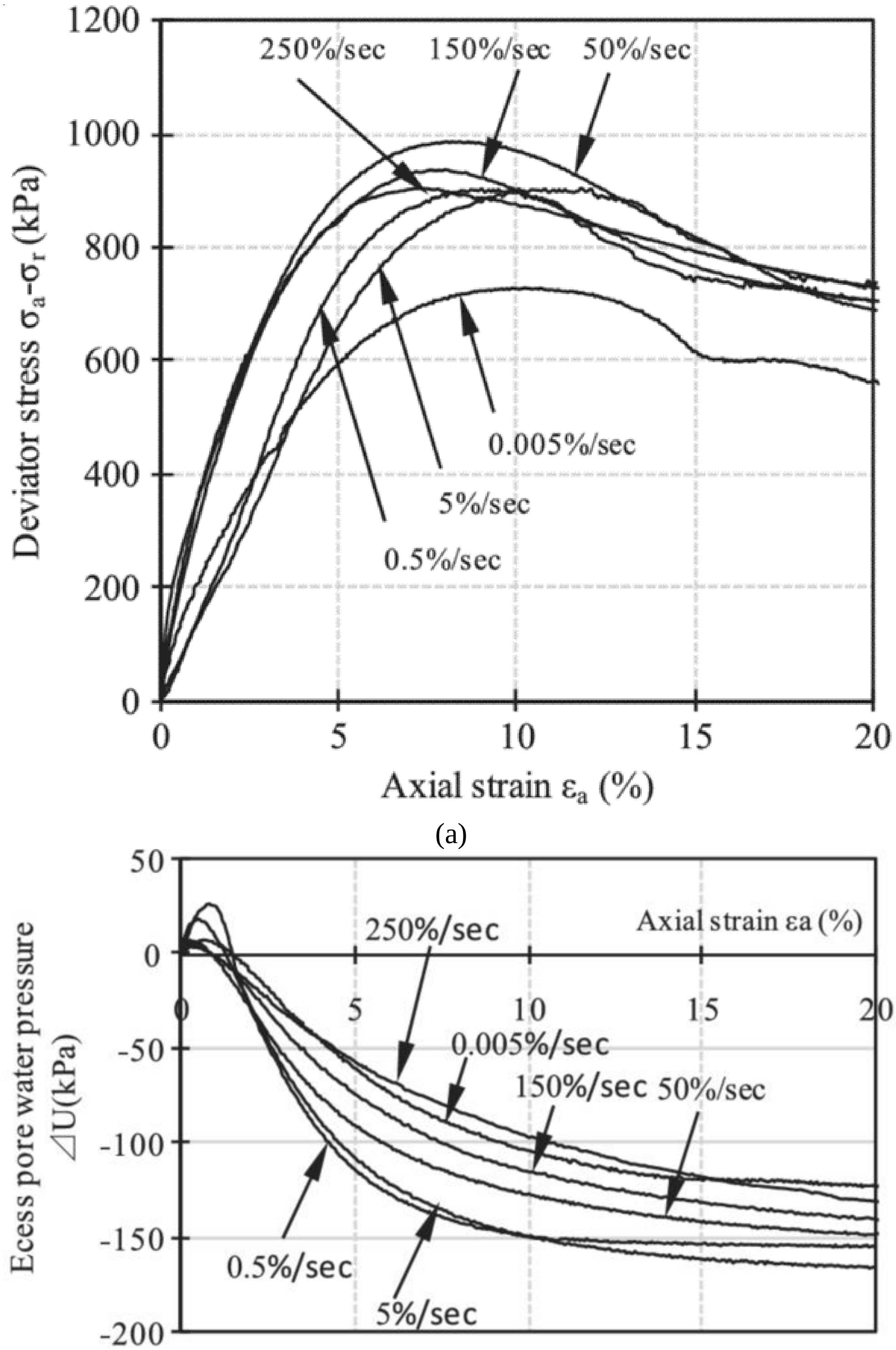

(a)

(b)

Figure 1-12 Undrained triaxial compression tests on saturated Toyoura sand (confining stress = 100 kPa, relative density = 80%): (a) stress-strain response; (b) volumetric strain response (Watanabe and Kusakabe, 2013).

Most clays demonstrate a unique strain-strength-strain rate response (Šuklje, 1969). This viscous behaviour is described in terms of "isotach" by Oka *et al*. (2003), Augustesen *et al*. (2004) and Tatsuoka *et al*. (2008). The undrained shear strength (s_u) is irrespective of the strain history but is dependent on the strain rate $\dot{\varepsilon}$. For isotach type soils, the current viscous stress component can be obtained as a function of ε and $\dot{\varepsilon}$ (Tatsuoka *et al*., 2008). Similarly, Vaid and Campanella (1977) and Leroueil *et al*. (1985) suggest that s_u is a function of ε and $\dot{\varepsilon}$ (see isotach example in Figure 1-13). When $\dot{\varepsilon}$ increases stepwise to approximately 4.4×10^{-2}%/min, the stress suddenly increases and reaches the monotonic curve at the new rate. Oka *et al*. (2003) reported that a unique stress-strain curve is found for each $\dot{\varepsilon}$ in both normally-consolidated and over-consolidated clay. This phenomenon is also found in stiff sedimentary clay (*e.g.* London clay) (see Figure 1-14), and pore pressure response is not significantly sensitive to $\dot{\varepsilon}$ under monotonic loading (Sorensen *et al*., 2007).

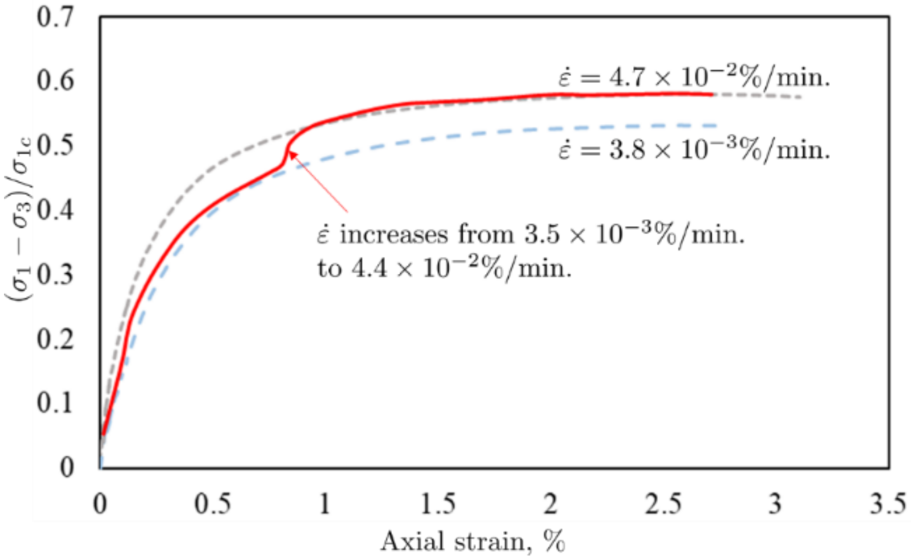

Figure 1-13 Influence of step-change in $\dot{\varepsilon}$ on the undrained stress-strain response of Haney clay (isotach type response) (Vaid and Campanella, 1977).

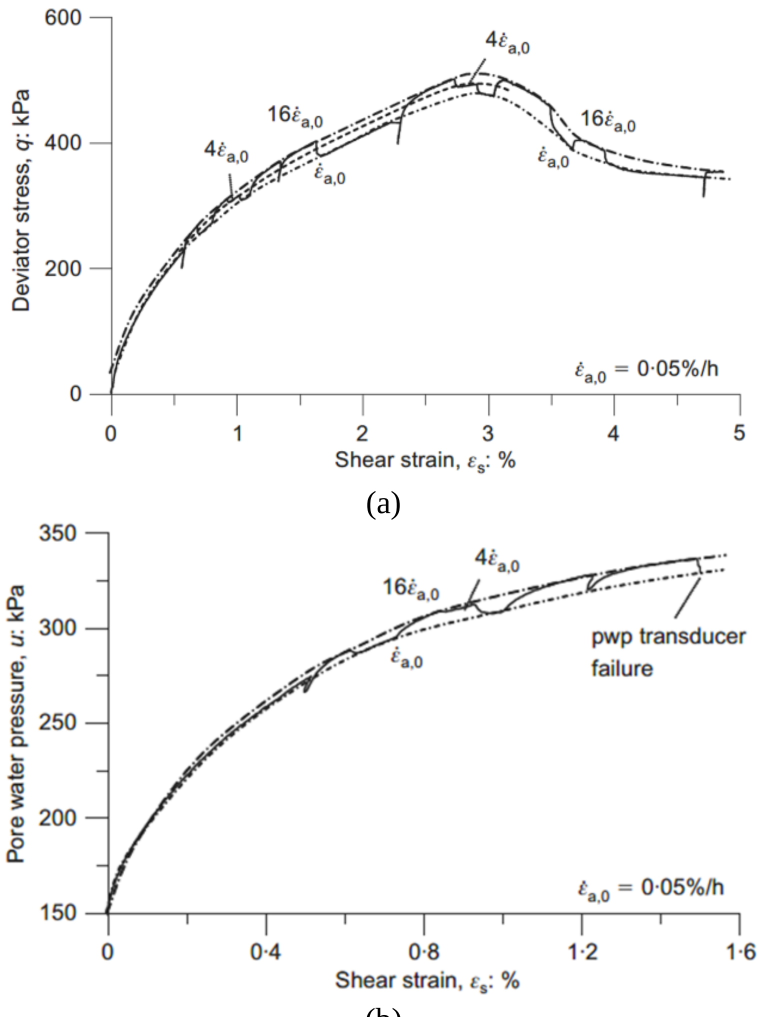

(a)

(b)

Figure 1-14 Undrained triaxial compression tests by applying stepwise variable $\dot{\varepsilon}$ on London clay (over-consolidated ratio = 7, in-situ pre-consolidation stress ≈ 2000 kPa): (a) deviator stress vs. shear strain; (b) pore pressure response (Sorensen *et al*., 2007).

1.2.2.2 Cyclic loading

OWT monopiles are subject to irregular cyclic lateral loads, with the load magnitude and frequency varying with time. However, current design methods for monopiles do not typically include rate effects under cyclic loading. Previous findings on soil rate dependency under cyclic loading are discussed below.

Rate effects under cyclic loading are observed in element testing. In general, the secant stiffness increases with the cyclic frequency. Vucetic and Tabata (2003) examined the secant shear modulus (G_s) under small strains using an NGI-type direct simple shear device. Figure 1-15 shows that G_s increases with the cyclic shear strain rate in sand and clay, which can also be expressed in a semi-logarithmic format shown in Figure 1-20. This approach was also used by Abdellaziz *et al.* (2021) for simple shear testing on various Canadian fine-grained soils. Kim (1991) conducted resonant column and torsional shear tests on dry sand and clay to determine their rate-dependent responses under cyclic loading at different loading frequencies. Similar to Vucetic and Tabata (2003), the magnitude of rate effects in sand was observed to be negligible, while clay was found to be rate-sensitive. Ushev and Jardine (2022a) examined the cyclic response of Cowden stiff clay, which is representative of ground conditions of multiple North Sea wind farms. They reported that the number of cycles to failure increases with the frequency under load-controlled cyclic loading.

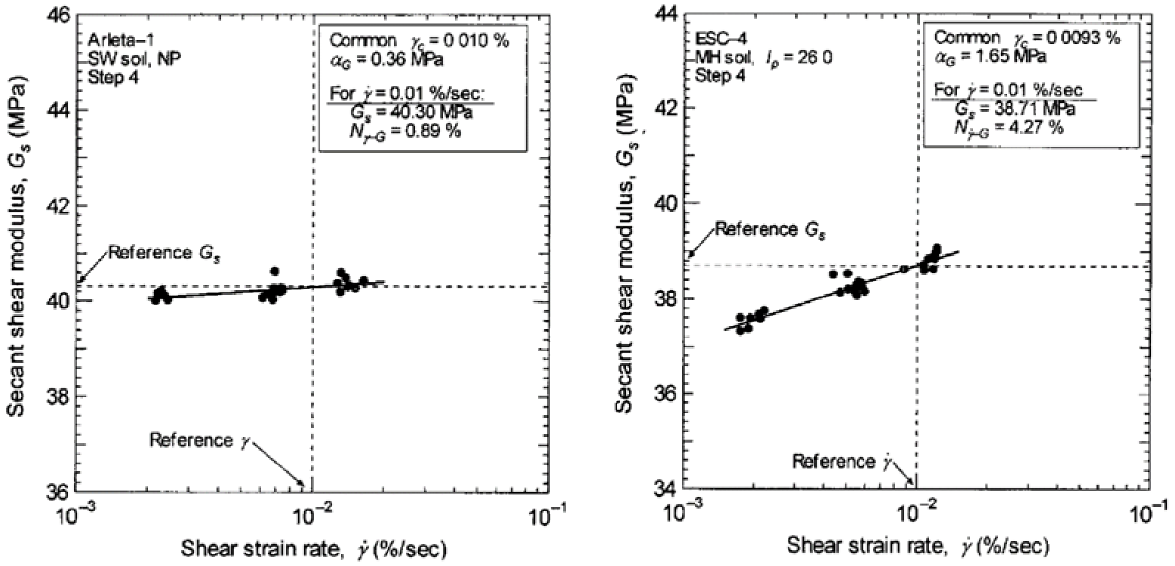

(a) (b)

Figure 1-15 Direct simple shear testing to explore rate effects under cyclic loading: (a) sandy soil; (b) clayey soil (Vucetic and Tabata, 2003).

Figure 1-16 shows that the damping ratio of clay under small strains becomes rate-sensitive when the loading frequency is larger than 2 Hz (Kim, 1991). Based on the above experimental observations, cyclic properties of monopiles, such as ratcheting and secant stiffness per cycle, may also be rate-dependent.

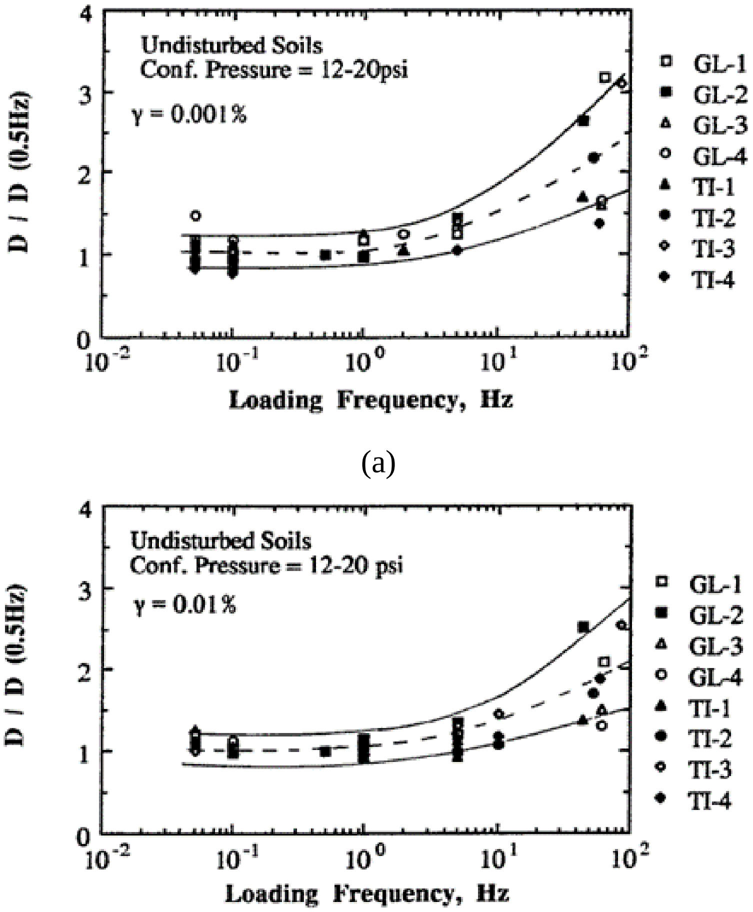

(a)

(b)

Figure 1-16 Normalised damping ratios under different cyclic loading frequencies in clay: (a) shear strain magnitude = 0.001%; (b) shear strain magnitude = 0.01% (Kim, 1991).

Wu *et al*. (2022b) conducted load-controlled cyclic triaxial compression tests on reconstituted clay at different frequencies from 0.001 Hz to 0.1 Hz (see Figure 1-17). The results show that the accumulated pore pressure (Δu) is time-dependent. For slow frequency tests, Δu may increase significantly with cyclic loading. Therefore, for long-term cyclic loading, in addition to rate effects, pore pressure response may be assessed for cyclic loading of clay.

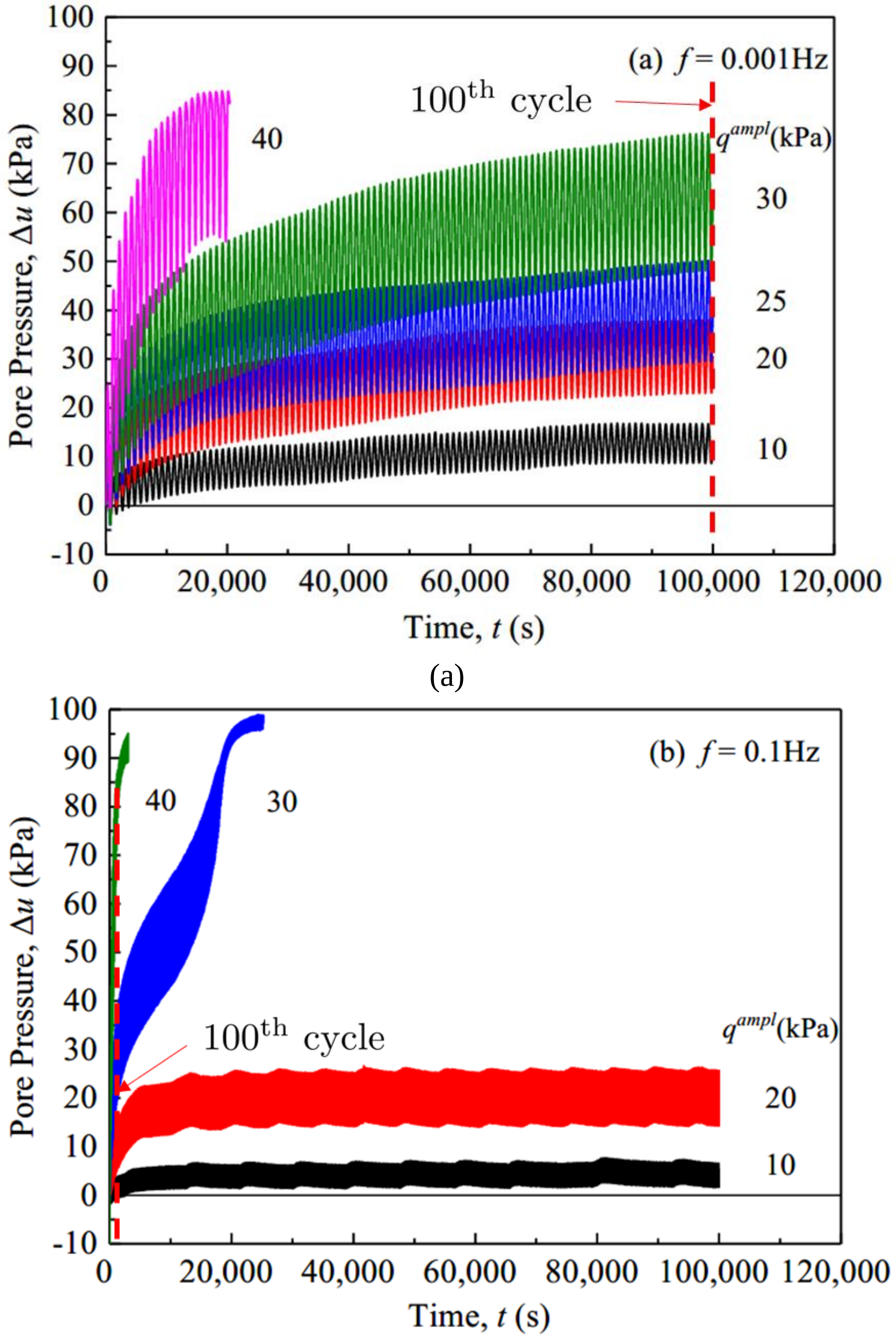

(a)

(b)

Figure 1-17 Pore pressure accumulation during cyclic loading at different frequencies (q^{ampl}: cyclic load magnitude): (a) 0.001 Hz; (b) 0.1 Hz (edited from Wu *et al*., 2022b).

1.2.2.3 Strain dependency

Matešić and Vucetic (2003) found that the magnitude of rate effects under small strain cyclic loading is strain-dependent. Graham *et al.* (1983) reported that the rate magnitude (*i.e.* the rate parameter) decreases with the strain in Belfast clay under large strains, as shown in Figure 1-18. However, this strain-dependent phenomenon has rarely been observed in the literature and is only found in certain clays.

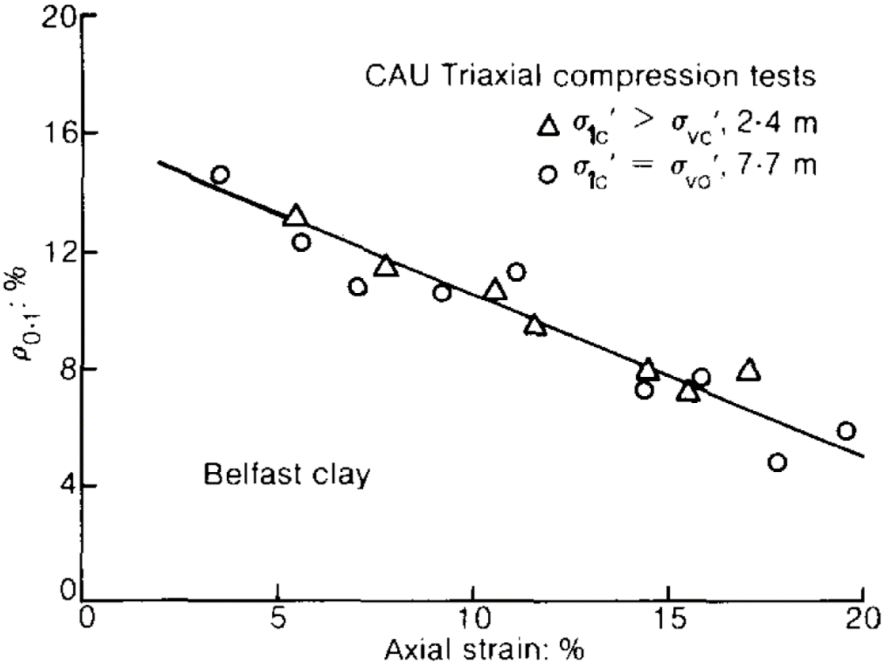

Figure 1-18 Strain-dependent rate effects in Belfast clay ($\rho_{0.1}$ = rate parameter) (Graham *et al.*, 1983).

1.2.2.4 Negative viscous response

Some soils demonstrate "negative" viscous behaviour (*i.e.* the shear strength decreases with increasing rate). For example, Tatsuoka *et al.* (2008) reported that the soil strength of dry Albany sand decreases with $\dot{\varepsilon}$ (see Figure 1-19 (a)). The soft clay from Le Flument dam in France also demonstrates a similar response (see Figure 1-19 (b)) (Fodil *et al.*, 1997). Whilst this phenomenon is rare and might involve other factors (*e.g.* sample variations and post-peak behaviour), it should be carefully assessed during the design stage.

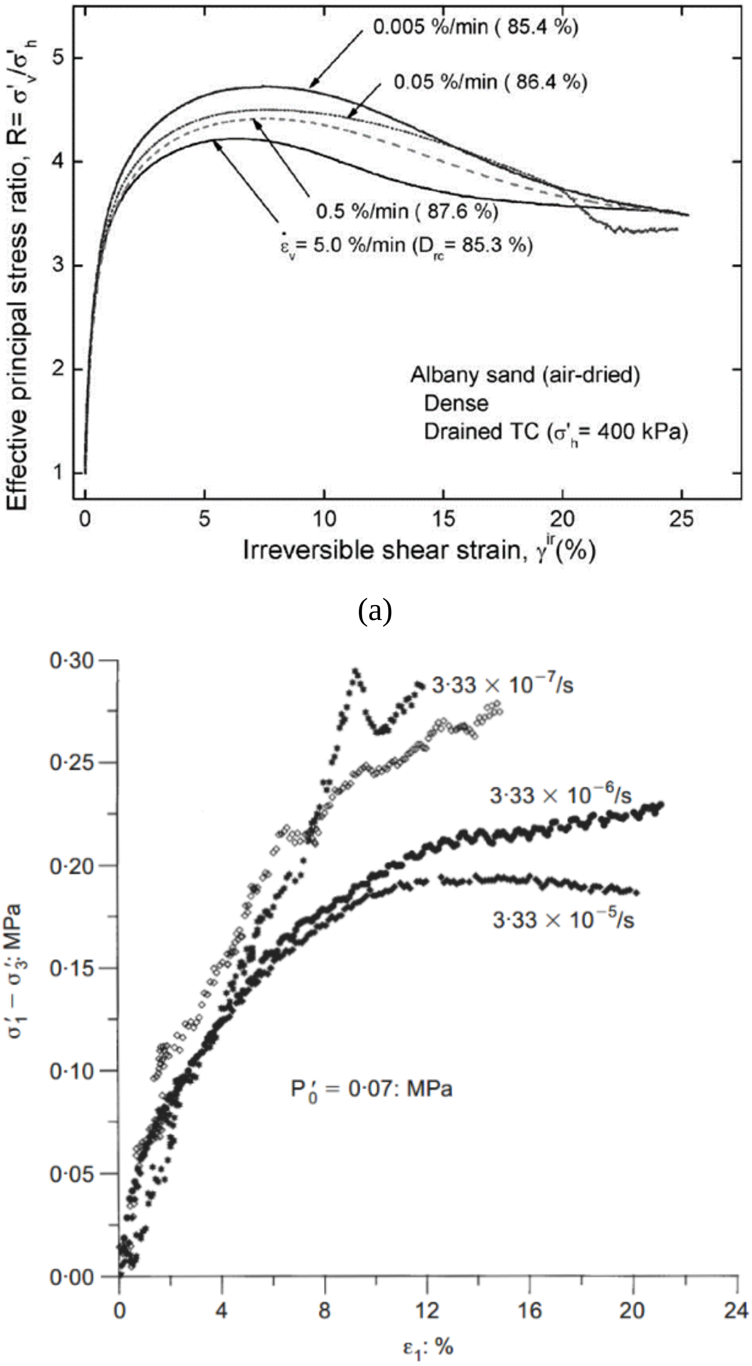

(a)

(b)

Figure 1-19 Soils exhibit negative viscous response under triaxial compression:

(a) air-dried Albany sand (Tatsuoka *et al*., 2008);

(b) soft clay from Le Flument dam (Fodil *et al*., 1997).

1.2.3 Quantification of rate effects

As shown in Figure 1-20, in element testing, the relationship between the shear stress τ and the strain rate $\dot{\varepsilon}$ is often expressed using a semi-logarithmic equation to quantify soil rate effects:

$$\eta_{10} = \frac{(\tau_{fast} - \tau_{slow})/\tau_{slow}}{\log_{10}\dot{\varepsilon}_{fast} - \log_{10}\dot{\varepsilon}_{slow}} \qquad \text{Equation 1-9}$$

where η_{10} is the rate parameter (non-dimensional). The concept of η_{10} is similar to the rate parameters proposed by several researchers (*e.g.* Yong and Japp, 1969; Vaid and Campanella, 1977; Graham *et al.*, 1983; Lefebvre and LeBoeuf, 1987; Kulhawy and Mayne, 1990; Mitchell and Soga, 2005) and can capture isotach behaviour.

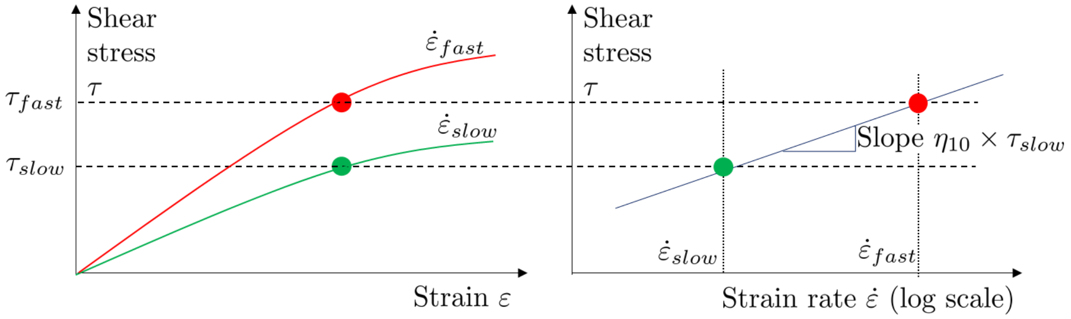

Figure 1-20 Illustration of soil rate effects.

Rate effects for sand are negligible in most cases. For example, Watanabe and Kusakabe (2013) summarised element test data from various papers, indicating that η_{10} for sand is often less than 5% per log-10 cycle of $\dot{\varepsilon}$ ($\eta_{10} = 0.05$). Also, the magnitude does not appear to change under different confining stresses. For saturated sand under a high loading rate, the influence of partial drainage appears to be more significant. Although this phenomenon is recognised as important, it is fundamentally unrelated to the viscous properties of soils and not included in the research scope.

Rate effects in clay are more evident than in sand. For instance, Graham *et al.* (1983) conducted element tests on various clays. Their results show that the s_u increases by 9.4% to 19.4% with a tenfold increase in $\dot{\varepsilon}$. Similarly, Kulhawy and Mayne (1990) examined 26 clays in triaxial compression tests, and a 10% increase in s_u per log-10 cycle of $\dot{\varepsilon}$ was found ($\eta_{10} = 0.10$) (see Figure 1-21). The magnitude of rate effects for clays is also influenced by the plasticity index, activity and water content (Mitchell and Soga, 2005). The smaller the soil particle size, the greater the specific surface, and more water is absorbed.

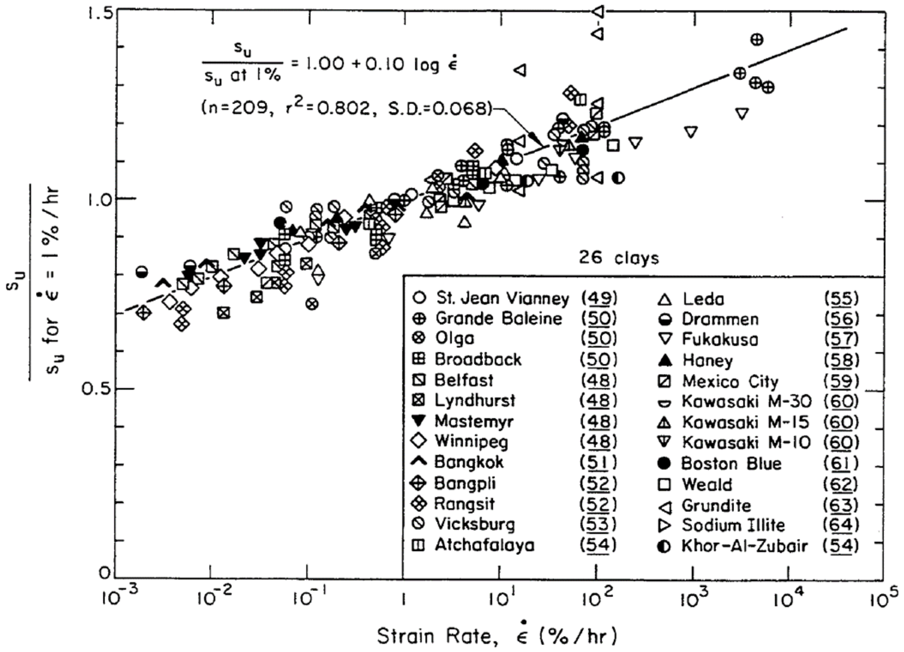

Figure 1-21 Triaxial compression tests on 26 clays to explore rate effects (Kulhawy and Mayne, 1990).

A linear correlation between the logarithmic strain rate and shear strength is found in the region of fast rates, while under a lower limit of strain rate, a further reduction in strength is not seen (Vaid and Campanella, 1977). This limit is often called the upper yield, and an example for Haney clay is shown in Figure 1-22. When $\dot{\varepsilon}$ is near the upper yield, soil strength approximately linearly increases with $\dot{\varepsilon}$. If $\dot{\varepsilon}$ becomes larger, the semi-logarithmic expression in Equation 1-9 can get a better fit. To quantify rate effects using Equation 1-9, $\dot{\varepsilon}_{slow}$ needs to be larger than the upper yield. Later, in Section 6.2.4.3 and Appendix A.3 and A.4, the upper yield is considered when modelling rate effects using theoretical approaches.

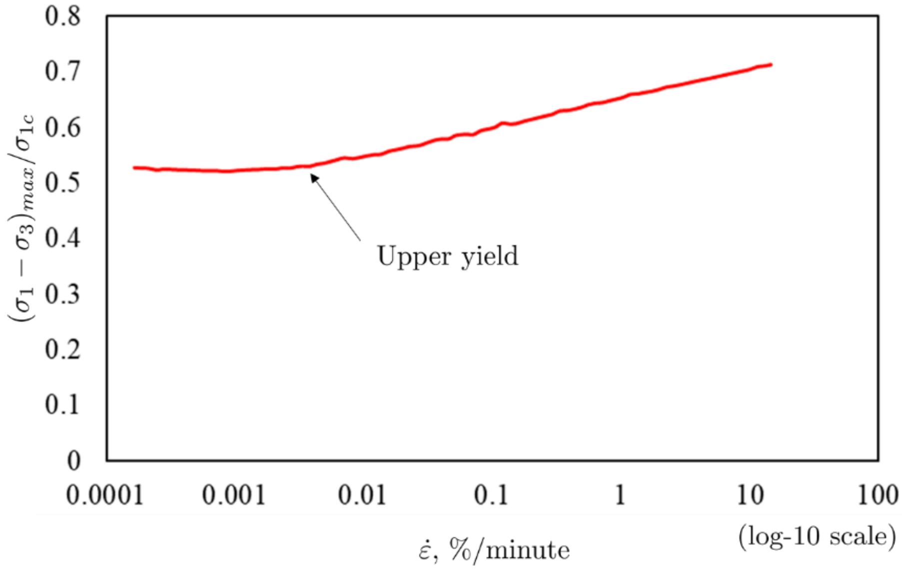

Figure 1-22 Strain rate dependency of Haney clay (after Vaid and Campanella, 1977).

1.2.4 Rate effects for piles under loading

Similar to element testing research, rate effects have been found in pile testing. For example, Brown and Hyde (2008) used an instrumented pile to carry out vertical pile load tests at different loading rates in stiff glacial till in Grimsby, UK. They reported that the pile head load significantly increases with the loading rate (Figure 1-23).

As reported in the PISA project, pile response to lateral loading is rate-dependent (Byrne *et al*., 2020b; McAdam *et al*., 2020). The configuration of the PISA pile testing is shown in Figure 1-24. The horizontal load H was applied at a fixed height (h) above the ground level. H was measured from the pile head and is equivalent to the horizontal load at the ground level. The horizontal displacement at the ground level (v_G) was monitored. In these tests, variable displacement rates were applied to explore rate effects. The pile diameter (D) was 0.762 m, and the pile embedded length (L) was 5.25D. As shown in Figure 1-25, isotach type viscous behaviour is found in the Dunkirk dense marine sand and Cowden stiff clay. It can be seen that a 7.5% increase in capacity per log10-cycle of the displacement rate is found in dense sand, and an 8% increase is evident in the clay till. Ushev and Jardine (2022b) also demonstrated rate effects in the Cowden till through element testing (approximately 6% increase in s_u per log10-cycle of shear strain rate). It is noted that the sand composition at Dunkirk is classified as uniform and fine to medium (Zdravkovic *et al*., 2020b). Fines content may influence the magnitude of soil rate dependency. In addition, the water table was 5.4 m in depth at Dunkirk, which suggests that the top few metres of soil may be unsaturated. Thus, in addition to rate effects, suctions may influence pile response at Dunkirk.

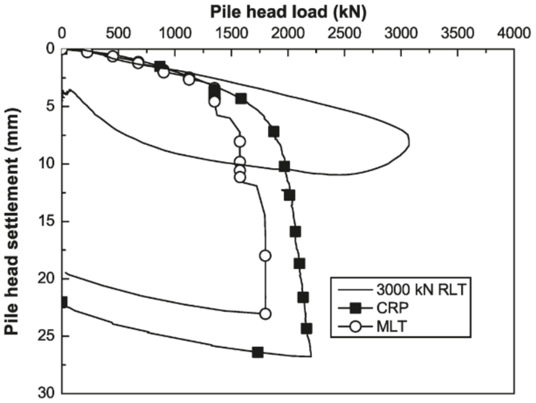

Figure 1-23 Vertical load tests at different rates in glacial till (RLT: rapid load test; CRP: constant rate of penetration at 0.01 mm/s; MLT: maintained load test) (Brown and Hyde, 2008).

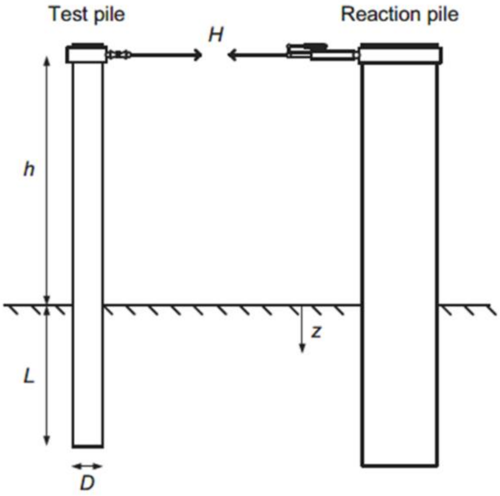

Figure 1-24 Configuration of the pile testing (Byrne *et al*., 2020b).

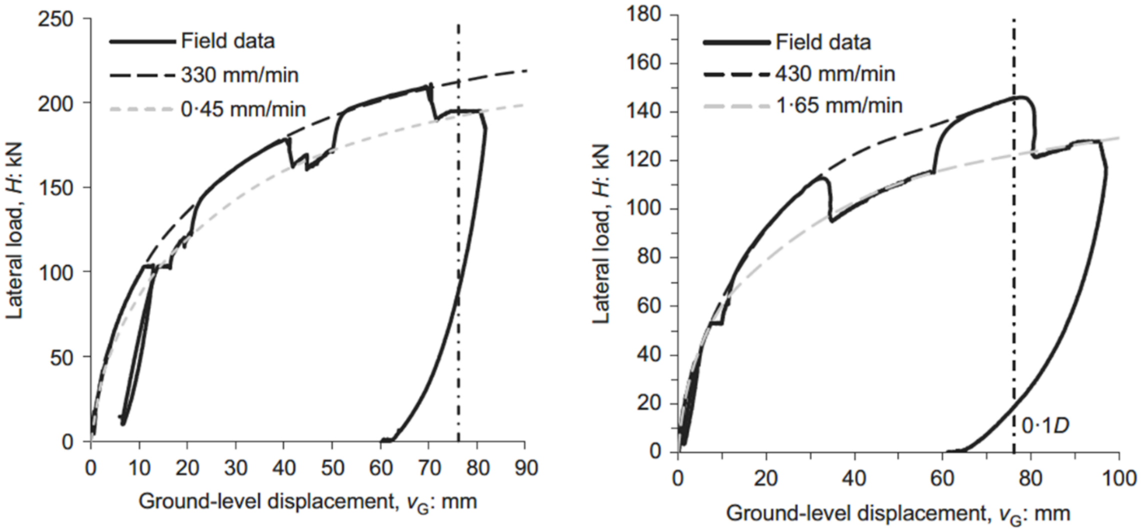

(a) (b)

Figure 1-25 Variable rate testing on laterally-loaded piles: (a) DM6 test at Dunkirk; (b) CM1 test at Cowden (Byrne *et al*., 2020b; McAdam *et al*., 2020).

Other time effects in saturated sand, such as the dissipation of excess pore water pressures, are not essentially related to soil rate effects. For further reference, pile response in saturated sand can be found in recent studies, such as centrifuge testing using a viscous fluid (Takahashi *et al.*, 2022) and numerical modelling (Staubach *et al.*, 2022).

1.2.5 Modelling rate effects for monopiles

There is significant literature on constitutive modelling of soil rate effects, principally based on element testing (*e.g.* Yin and Graham, 1989; Kutter and Sathialingam, 1992; Oka *et al.*, 2002; Grimstad *et al.*, 2010; Balaam, 2020; Shi *et al.*, 2021; Dadras-Ajirloo *et al.*, 2022). Different modelling techniques have been adopted in the literature, including empirical methods using curve fitting, extensions of RPT, rheological models and advanced theories of viscoelasticity and viscoplasticity (Mitchell and Soga, 2005). Based on RPT, soil deformation is essentially dependent on $\dot{\varepsilon}$. Some soil models use time functions to describe rate effects, which may not be fundamentally correct (Tatsuoka *et al.*, 2008). Most models only describe a specific phenomenon, such as creep or stress relaxation, and reliable theoretical explanations are needed to aid model development.

Among various modelling techniques, the hyperplasticity framework is adopted to develop a practical engineering model describing rate-dependent pile behaviour in this thesis. Hyperplasticity-based models obey thermodynamic principles, and strain rate effects are implemented using linear viscosity or RPT (Houlsby and Puzrin, 2006). Instead of deploying time functions, strain rate functions are derived following hyperplasticity principles.

Previous work shows that hyperplasticity models capture rate-dependent pile response quite well. For instance, Balaam (2020) used a PISA-type model and a macro-element model in hyperplasticity, considering soil rate effects to capture pile CM1 (Figure 1-25 (b)) response in the PISA testing. The model was calibrated against element and monotonic pile test data to determine the necessary parameters. The rate-dependent parameter η_{10} at element scale is assumed to be the same as at pile scale. As shown in Figure 1-26, the model performs well compared to the test data and provides insights into monopile modelling, considering strain rate effects. In addition, previous work demonstrates that pile response to cyclic lateral loading is captured using an advanced hyperplasticity macro-element model (*e.g.* Abadie *et al*., 2019). Details about the model development, including the hyperplasticity framework, are discussed in Chapter 6.

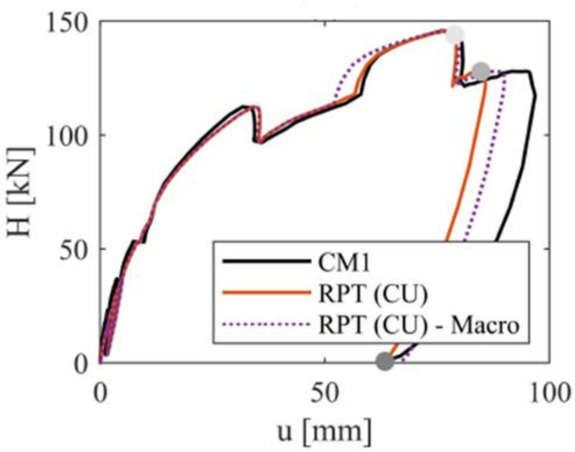

Figure 1-26 Comparing the data and modelling results for the PISA CM1 test in stiff clay (Balaam, 2020).

1.3 Review of a framework for characterisation of cyclic loading properties for monopiles

A framework of cyclic definitions by Richards (2019) and Balaam (2020) is reviewed to characterise cyclic response. The framework defines the cyclic load, permanent strain (ratcheting), stiffness and energy loss. The cyclic response is presented in terms of stress (σ) and strain (ε), which can be extended for physical modelling. For example, the macro pile responses of moment-rotation ($M-\theta$) or horizontal load-displacement ($H-u$) can replace σ and ε. In this thesis, one-way cyclic loading is of concern. Definitions for multi-directional and two-way cyclic loads can be found in Richards (2019).

1.3.1 Cycle definition

A loading cycle is a loading-unloading loop between the maximum and minimum reversal stresses, denoted as σ_e and σ_r. σ_r is equal to zero for the uni-directional one-way cyclic load testing presented in this thesis. In the $N^{\text{-th}}$ cycle, the stress increases from the point r_N to the point e_N, followed by unloading to the point r_{N+1}, as illustrated in Figure 1-27. The initial loading-unloading loop is defined as the 0th cycle (dashed). During the initial loading, relatively large permanent strain is often seen.

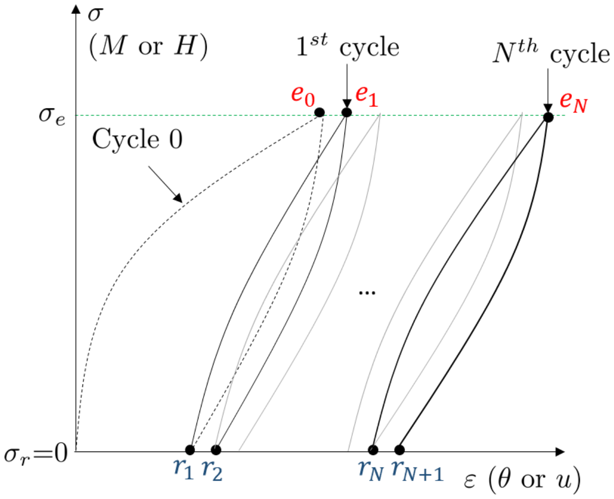

Figure 1-27 Characterisation of loading cycles.

1.3.2 Cyclic load characterisation

The magnitude of cyclic loading for pile tests (σ_e) is characterised by LeBlanc *et al.* (2010):

$$\zeta_b = \sigma_e/\sigma_R \qquad \text{Equation 1-10}$$

where ζ_b is the cyclic load parameter and σ_R is the reference stress. Balaam (2020) indicated that there is no consistent method in the literature for determining σ_R. In this thesis, σ_R is defined as the ultimate horizontal load capacity (H_R) obtained at the allowable ground-level horizontal displacement $u = u_R = 0.1D$. Since H_R can vary due to rate effects, in defining a reference load, a displacement rate or a loading rate may be specified. Considering the ultimate capacity as reference load σ_R, ζ_b often falls in a range of 30% ~ 50% for the SLS design.

1.3.3 Accumulated permanent strain

The accumulated permanent strain, also known as ratcheting, is measured per cycle. Previous physical modelling research (LeBlanc *et al*., 2010; Klinkvort and Hededal, 2013; Abadie, 2015; Arshad and O'Kelly, 2017) adopted the strain at point e_N or point r_{N+1} to quantify ratcheting in the N-th cycle (see Figure 1-27). In element testing, for example, Andersen (2015) used the mean strain value between points r_N and e_N to present the accumulated permanent strain.

A new definition for measuring the ratcheting response, developed by Richards (2019) and Balaam (2020), is implemented in this thesis. As shown in Figure 1-28, the mean strain value at the average stress per cycle (σ_{AV}) represents the permanent strain ε_N:

$$\varepsilon_N = \frac{1}{2}(\varepsilon_{aN} + \varepsilon_{bN}) \qquad \text{Equation 1-11}$$

The above definition is also similar to Andersen's description of element testing. For pile testing, it is useful to present ratcheting as an accumulated strain after N cycles ($\Delta\varepsilon_N$):

$$\Delta\varepsilon_N = \frac{1}{2}\big((\varepsilon_{aN} + \varepsilon_{bN}) - (\varepsilon_{a0} + \varepsilon_{b0})\big) \qquad \text{Equation 1-12}$$

In this way, the initial monotonic and cyclic loading behaviours can be differentiated.

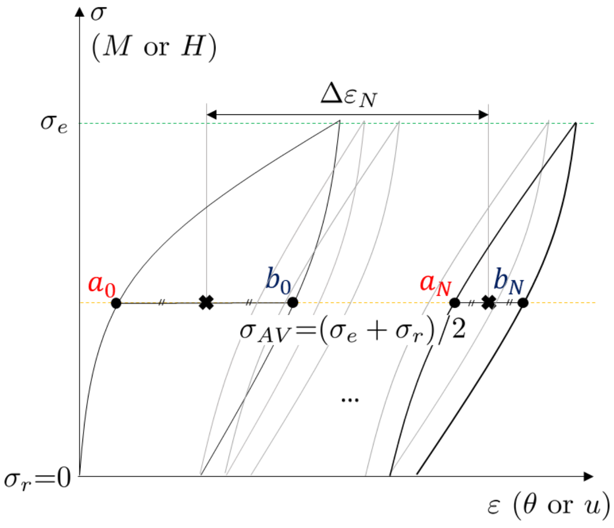

Figure 1-28 Characterisation of ratcheting.

1.3.4 Stiffness and energy loss per cycle

Previous physical modelling research adopted a loading stiffness (measured from r_N to e_N) or an unloading stiffness (measured from e_N to r_{N+1}) to determine the secant stiffness per cycle (k_N) (*e.g.* LeBlanc *et al*., 2010; Klinkvort and Hededal, 2013; Abadie, 2015). Instead, a new definition of k_N proposed by Richards (2019) and Balaam (2020) is adopted in this thesis. The central stiffness (see Figure 1-29) is used to minimise conflation of stiffness change with ratcheting:

$$k_N = \frac{\sigma(e_N) - \sigma(r_N)}{\varepsilon(e_N) - \frac{1}{2}(\varepsilon(r_{N+1}) + \varepsilon(r_N))}. \qquad \text{Equation 1-13}$$

An energy loss factor, η_N, is used to quantify cyclic energy dissipation in a closed hysteresis loop:

$$\eta_N = \frac{E_H}{2\pi E_E} = \frac{4k_N}{\pi(\sigma_e - \sigma_r)^2}\left(\int_{r_N}^{e_N} \sigma d\varepsilon + \int_{e_N}^{r_{N+1}} \sigma d\varepsilon\right) \qquad \text{Equation 1-14}$$

where E_H is the hysteresis loop area, representing the energy dissipated during the cycle, and E_E corresponds to the energy stored for σ_{AV}. This format is the same as that used by Tatsuoka *et al*. (1978) and is similar to Abadie (2015) and Taborda *et al*. (2016), who used a factor equivalent to half of η to describe energy loss in a cycle ($E_H/4\pi E_E$).

Due to ratcheting, E_E and E_H are adapted to quantify energy loss in a non-closed loop, as illustrated in Figure 1-29. Under uni-directional cyclic loading, for example, for the N-th cycle, the area E_E is equal to $(\sigma_e^2)/(2k_N)$, and E_H is the area of the hysteresis loop.

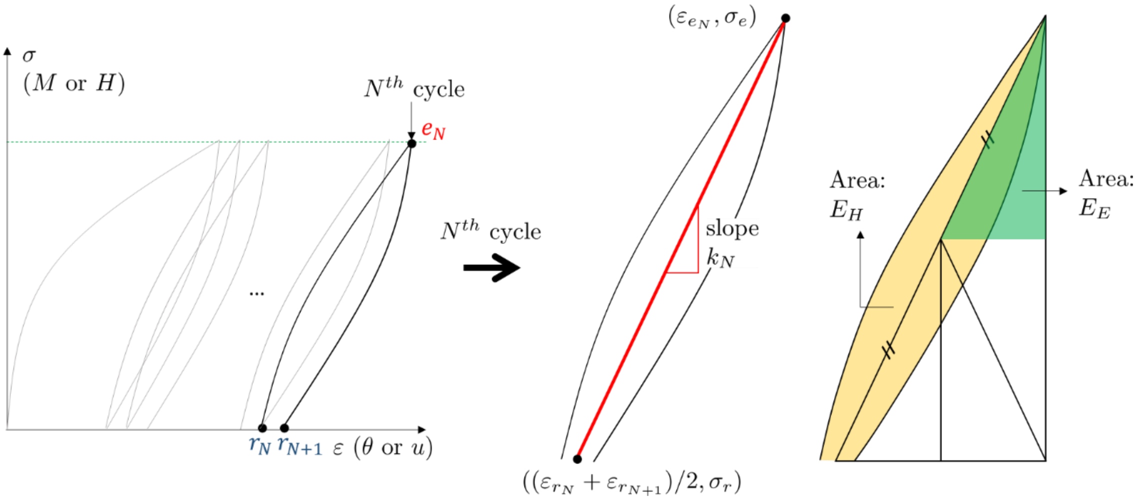

Figure 1-29 Illustration of secant stiffness and energy dissipation per cycle.

1.4 Research contributions

1.4.1 Research questions

Monopile foundation design can be improved if soil rate effects are incorporated into design calculations. Monopiles can be subject to transient loads from the emergency stop of the turbine, vessel impacts (accidental loading), storms (extreme environmental loading), etc. The pile loading rate increases rapidly in these conditions, with the potential for the soil resistance to increase, leading to a stiffer pile response and a higher pile capacity. Although there is significant literature on soil rate effects (see Section 1.2), principally through element testing, the interaction between the monopile and surrounding soil considering rate effects is rarely explored. The PISA project reported preliminary results of rate-dependent pile behaviour. With more pile testing data available, rate effects can be quantified and implemented into design methods.

This thesis investigated rate effects for monopiles through experimental and theoretical approaches. Laboratory-floor model testing on scaled piles was conducted, and a practical engineering model was developed to capture rate-dependent pile response. The model was validated using experimental data. With appropriate scaling techniques, full-scale pile response can be assessed using model test data. The key research questions are summarised as follows:

1.4.1.1 Investigate the pile response to monotonic loading at different rates

Isotach type viscous behaviour is seen in element testing on most clays (*e.g.* Vaid and Campanella, 1977). A similar response is observed in laterally-loaded pile testing in stiff clay and dense marine sand (*e.g.* Byrne *et al*., 2020b; McAdam *et al*., 2020). The magnitude of soil rate effects in element testing may be quantified using a semi-logarithmic format or RPT (Mitchell and Soga, 2005). This concept is extended in this thesis to quantify rate effects for monopiles. Data from model pile tests at different rates were analysed to determine the magnitude of rate effects (see examples in Section 4.3.3).

1.4.1.2 Investigate the pile response to cyclic lateral loading at different frequencies

Monopiles are subject to cyclic lateral loads at different rates, such as wind and waves with different frequencies (see Figure 1-5). Several researchers examined pile response to cyclic lateral loading in drained and saturated sand (*e.g.* Abadie, 2015; LeBlanc *et al*., 2010; Richards, 2019; Takahashi *et al*., 2022) and soft clay (*e.g.* Lau, 2015). However, little work has been done to assess cyclic response in stiff clay through physical modelling. Furthermore, cyclic load properties, such as permanent strain and stiffness, may change with the loading rate, as discussed in Section 1.2.2.2. For example, the SLS design can be optimised if less permanent strain occurs due to soil rate effects. Thus, new research on the rate-dependent cyclic response is required. This thesis conducted a series of model pile tests under uni-directional cyclic lateral loading at different frequencies, as presented in Sections 3.6 and 4.4.

1.4.1.3 Theoretical development considering soil rate effects to inform design methods

Soil rate effects are described in various constitutive models. However, these models are often calibrated against element test data and can only describe specific phenomena. In addition, some models use time-dependent variables, which may be fundamentally wrong. Therefore, a practical engineering model with sound theoretical background is required to capture rate-dependent pile response. A new practical pile design model with a sound theoretical basis was developed in this thesis to simulate rate-dependent pile response. Further details are found in Chapter 6.

1.4.2 Research overview

The research overview is shown in Figure 1-30. It broadly comprises a literature review, preparations for experimental research, experimental work and theoretical development. The literature review is discussed in Sections 1.1 to 1.3, and the importance of rate effects for monopiles is highlighted in this thesis.

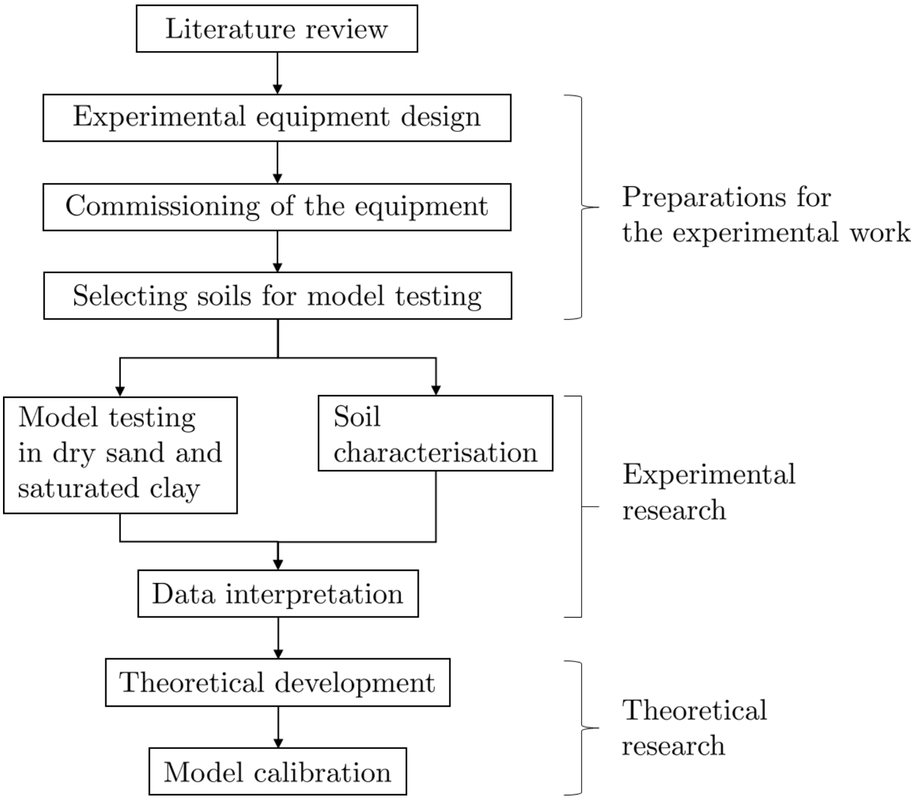

Figure 1-30 Research overview of the DPhil project.

A novel loading rig was designed for conducting model pile testing. The rig has a high-speed dual actuation system to change the height of the loading point and the loading rate. As a result, complex combined load problems, such as wind and waves acting simultaneously and high-speed loading, can be simulated.

Dry sand and saturated stiff clay were chosen for model pile testing as these ground conditions are related to previous research (Richards, 2019) and the ongoing PICASO project (Byrne *et al.*, 2020a). The dry sand testing follows Richards' work on the pile response to multi-directional cyclic lateral loading at Oxford University. Different soil densities were adopted to study pile behaviour in sand under fully drained conditions. A stiff glacial till at Cowden, northeast England, was chosen for the clay testing. The clay is similar to the glacial formations for multiple North Sea offshore wind farms. The test site was shared with the PICASO test site (Byrne *et al.*, 2020a), so soil characterisation and pile test data from both projects can be compared to investigate pile response in glacial till more rigorously.

The experimental work provides a unique dataset to aid theoretical development. Monotonic and cyclic loading tests at different rates were performed to investigate rate effects systematically. Additionally, combined load effects were investigated by changing the pile self-weight and loading point. Combined load effects on the lateral pile response, principally through centrifuge modelling, were investigated in the literature (*e.g.* Klinkvort and Hededal, 2014; Lu and Zhang, 2018; Lu *et al.*, 2021; Li *et al.*, 2022). Following this, data from the experimental research in this thesis help to investigate combined load problems further.

Data processing was carried out to interpret raw data and compare test results. Monotonic test results are illustrated in terms of the coupled moment-horizontal load response. For cyclic loading tests, data are presented following the framework in Section 1.3.

Theoretical development under the hyperplasticity framework was carried out to capture monopile response. The new design model considers the coupled moment-horizontal load response of a pile, and rate effects are simulated using linear viscosity or RPT. In addition, base resistance against horizontal loading and moment is incorporated into the design model, as suggested by the PISA design method. Also, the features from the Hyperplasticity Accelerated

Ratcheting Model (HARM) (Houlsby *et al.*, 2017) are adopted to capture ratcheting. The model was calibrated and validated using test data in this thesis, providing new insights into rate-dependent monopile design.

1.4.3 Thesis structure

This thesis forms part of broader research on cyclic lateral loading of monopiles currently being undertaken at Oxford University. Ongoing research includes:

(1) medium-scale laterally-loaded pile testing in sand and clay,

(2) laboratory-scale model testing in saturated sand,

(3) advanced element testing (*e.g.* the resonant column test and multi-directional direct simple shear test),

(4) theoretical development of an effective stress model for sand,

(5) numerical methods with machine learning techniques to improve design methods.

Table 1-3 summarises the thesis structure. The main content comprises three parts: (1) preparations for the experimental work, (2) experimental research and (3) theoretical research. Each chapter is summarised below:

Chapter 1 introduces the research background, reviews relevant work in the literature, such as current pile design methods, rate effects and characterisation of cyclic loading of monopiles, and outlines the research contributions.

Chapter 2 describes the experimental equipment for model testing, including the rig design, model piles, pile kinematics and the software. First, the actuation and measurement systems are introduced, and model piles with slightly different geometries are compared. Next, pile kinematics is derived to obtain pile pose using displacement measurements. Finally, the software design for control and data logging is introduced.

Chapter 3 focuses on the testing in dry sand. The sample preparation process follows Richards (2019) to compare data from both sources for further research. Pile responses to monotonic and cyclic lateral loading at different rates are studied. In addition, combined load problems, such as the impact of vertical loading and load eccentricity effects, are discussed with illustrative examples. Other experimental observations, such as pile uplift and the pivot position, are reported in this chapter.

Chapter 4 presents the clay testing at Cowden. The test site and its ground condition are introduced. The test programme comprises a series of monotonic and cyclic lateral loading tests at different rates to explore rate effects and load eccentricity effects. In addition, pseudo-random cyclic loading tests are presented to simulate realistic loads on OWT monopiles. Pile gapping and the rotational point are also reported in this chapter.

Chapter 5 discusses analytical equations and scaling issues for laboratory-scale model piles in dry sand and clay. Relevant work on physical modelling of monopile behaviour is reviewed to derive elastic pile stiffness and the ultimate pile response for normalisation and theoretical development in Chapter 6. Factors influencing scaling effects, such as the in-situ stress and soil shear strength profile, are listed. Pore pressure dissipation responses in clay at different scales are discussed in this chapter.

Chapter 6 introduces the theoretical work in hyperplasticity considering rate effects. In this chapter, hyperplasticity principles and model development are discussed. Results from theoretical modelling and model testing are compared to demonstrate the performance of the model.

At the end of this thesis, Chapter 7 concludes with the up-to-date experimental observations, research outcomes and suggestions for future research.

Table 1-3 Thesis structure.

Chapter 1: Introduction - Research background - Review of relevant literature (current pile design practice, rate effects and the cyclic loading framework) - Research contributions	
Chapter 2: Development of a loading rig - Rig design - Model piles and pile kinematics - Design of the control and data logging system	Experimental work preparation
Chapters 3 and 4: Model testing in dry sand and saturated stiff clay - Soil characterisation - Sample preparation methods - Monotonic responses at different rates - Cyclic lateral loading responses at different frequencies - Combined load effects - Other observations (*e.g.* the pile pivot point)	Experimental research
Chapter 5: Analytical equations and scaling issues for monopiles - Reviewing scaling techniques for dry sand and clay - Deriving elastic and ultimate pile responses for normalisation - Illustrations of pore pressure dissipation responses at different scales	Theoretical research
Chapter 6: Theoretical development - Review of the hyperplasticity framework - Development of a practical engineering model - Model calibration	
Chapter 7: Conclusions and future work	

2 Development of a loading rig

2.1 Introduction

A laboratory-floor model pile testing campaign was conducted in this research. Although small-scale modelling of geotechnical problems under 1*g* may not perfectly simulate representative ground conditions (*e.g.* achieving high confining stress), it allows flexibility in terms of test setups and provides useful observations. Compared to large-scale testing and centrifuge modelling under enhanced gravity, fewer resources are required for small-scale testing under 1*g*, and high-quality data can be obtained to calibrate engineering models. In addition to these advantages, a large number of tests can be conducted to provide sufficient experimental observations to calibrate soil models. By adopting appropriate scaling laws, experimental data can inform more detailed modelling to simulate full-scale monopile response.

This chapter describes the design of a novel loading rig to explore rate-dependent monopile response to monotonic and cyclic lateral loading. Firstly, previous designs of monopile loading rigs are reviewed, and details of the rig design are illustrated. Hardware and software for the rig are also introduced. Secondly, selected 1:100 scale model piles and their mechanical properties are presented. These piles are treated as rigid in the test soils, and their geometries are approximately representative of OWT monopiles. Finally, kinetic equations for solving pile movement are derived. These equations are solved by the Newton-Raphson iteration method and coded in the software to obtain pile pose in real time.

2.2 Rig design

2.2.1 Review of existing rig designs

Figure 2-1 shows previous rig designs for model monopile testing. Lee *et al*. (2011) fitted a hydraulic jack on a rigid chamber to apply lateral loads at a fixed loading point, as illustrated in Figure 2-1 (a). A similar design has previously been adopted by Mayne *et al*. (1995) and

Rao *et al*. (1996) for laterally-loaded pile testing. The hydraulic jack can be replaced with an electric actuator to achieve more precise control.

To apply long-term cyclic lateral loading, LeBlanc *et al*. (2010) and Abadie (2015) utilised a motor-driven device with pulleys and wires (see Figure 2-1 (b)). The pulley and wire system is also found in Peng *et al*. (2006) and Arshad and O'Kelly (2017) for performing long-term cyclic lateral loading. The motor is equipped with loading weight, and repeated loading is applied to the pile when it rotates. The rotary rate may be adjustable to produce cyclic loading at different rates, but the cyclic load magnitude cannot be changed during the motor operation.

Richards (2019) developed an advanced computer-controlled loading rig with a dual actuation system with six degrees of freedom to apply multi-directional loading, as shown in Figure 2-1 (c). The actuation system is composed of a pair of electric actuators controlled through real-time measurements from displacement transducers and load cells. The electric actuation system can run continuously over a long period (*i.e.* more than 24 hours) with an appropriate power protection system. Complex loading conditions, such as long-term and pseudo-random cyclic loading, can be precisely simulated. The pile is monitored through horizontal and vertical displacement transducers. Bi-directional, vertical and rotation pile motions are measured.

Richards (2019) reported that vertical pile movement might become evident when a pile is subject to lateral loading in dry sand. However, the designs in Figure 2-1 (a) and (b) only utilise horizontal displacement transducers to measure horizontal pile movement, while vertical pile movement is assumed to be minimal. Therefore, care is required to investigate the mechanism of vertical pile movement, and additional monitoring is needed.

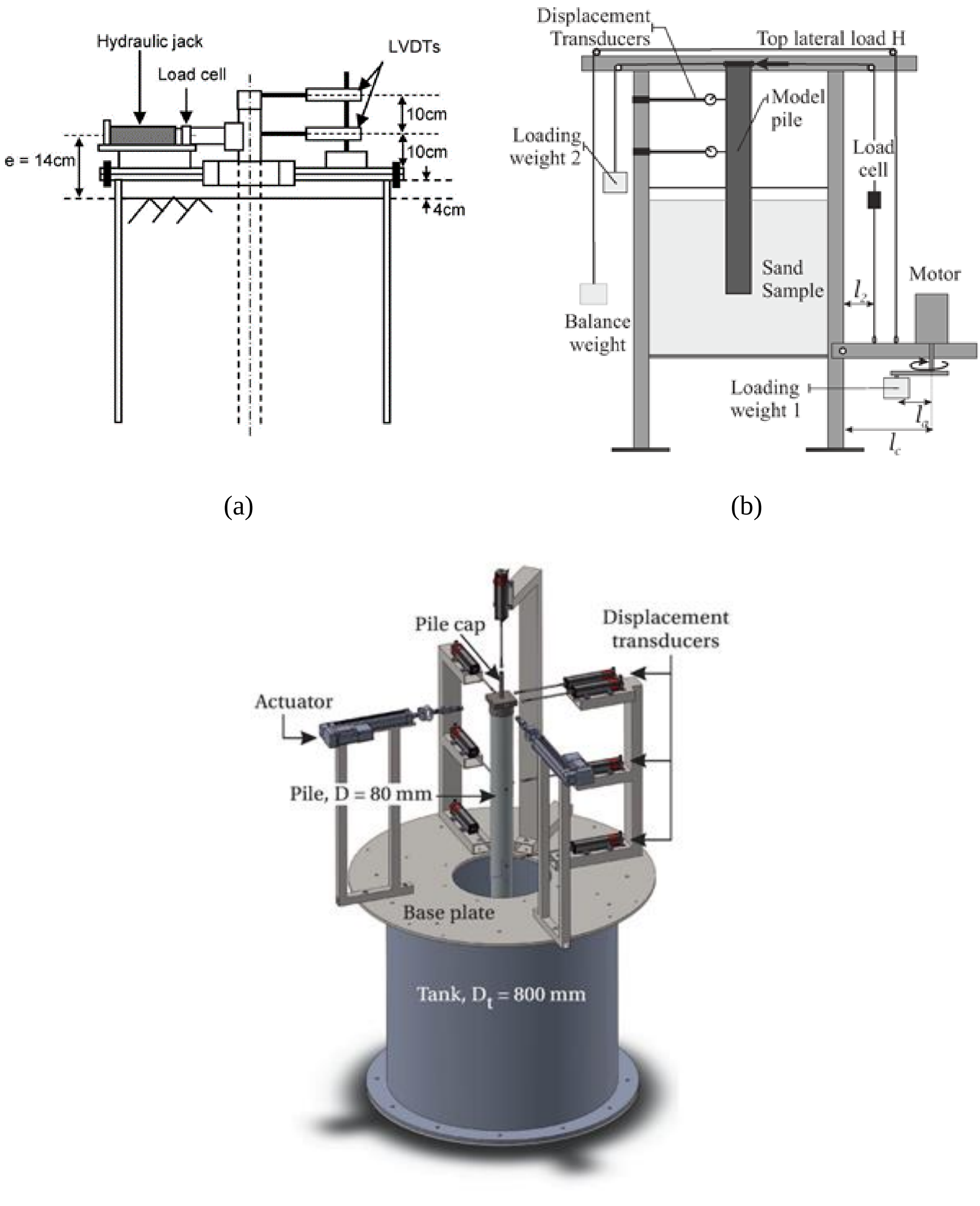

(a) (b)

(c)

Figure 2-1 Schematics of rig designs in the literature:

(a) single actuation system (Lee *et al*., 2011); (b) motor-driven system (Abadie, 2015); (c) dual actuation system for multi-directional loading (Richards, 2019).

2.2.2 Proposed design

Following Richards' work, a bespoke loading rig with an advanced electric actuation system to apply uni-directional lateral loading was proposed in this research. The rig design is illustrated in Figure 2-2, and photographs are shown in Figure 2-3.

The rig comprises a dual high-speed actuation system, a measurement system, a rigid model pile and pile clamps. Realistic loading conditions, such as wind and waves acting at different heights, can be simulated by applying loads at two different loading points. In addition, extra weight can be added to the pile using weighted clamps to study the influence of vertical loading on lateral pile response.

A purpose-built control and data logging system has been developed for the rig, and its detailed design is introduced in Section 2.3. Real-time planar pile movement is monitored, with load and displacement data being processed to control the actuation system simultaneously. The hardware and the actuation system are connected to a heavy-duty uninterruptible power supply. Long-term testing, such as high-cycle loading over 24 hours, is achievable.

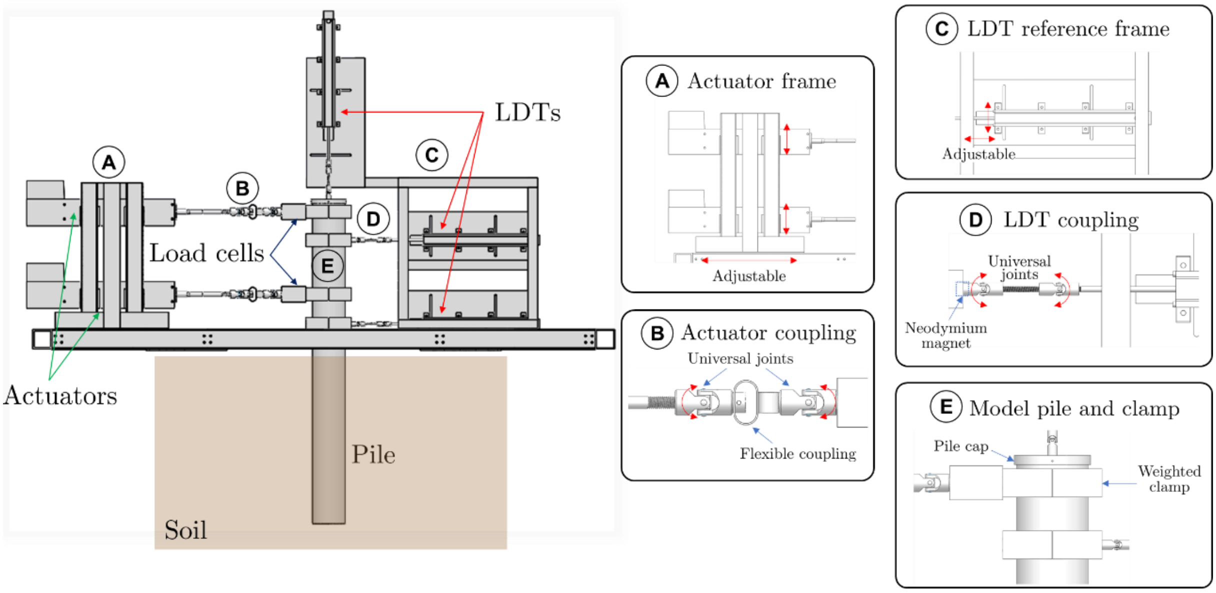

Figure 2-2 Schematic of the proposed rig design.

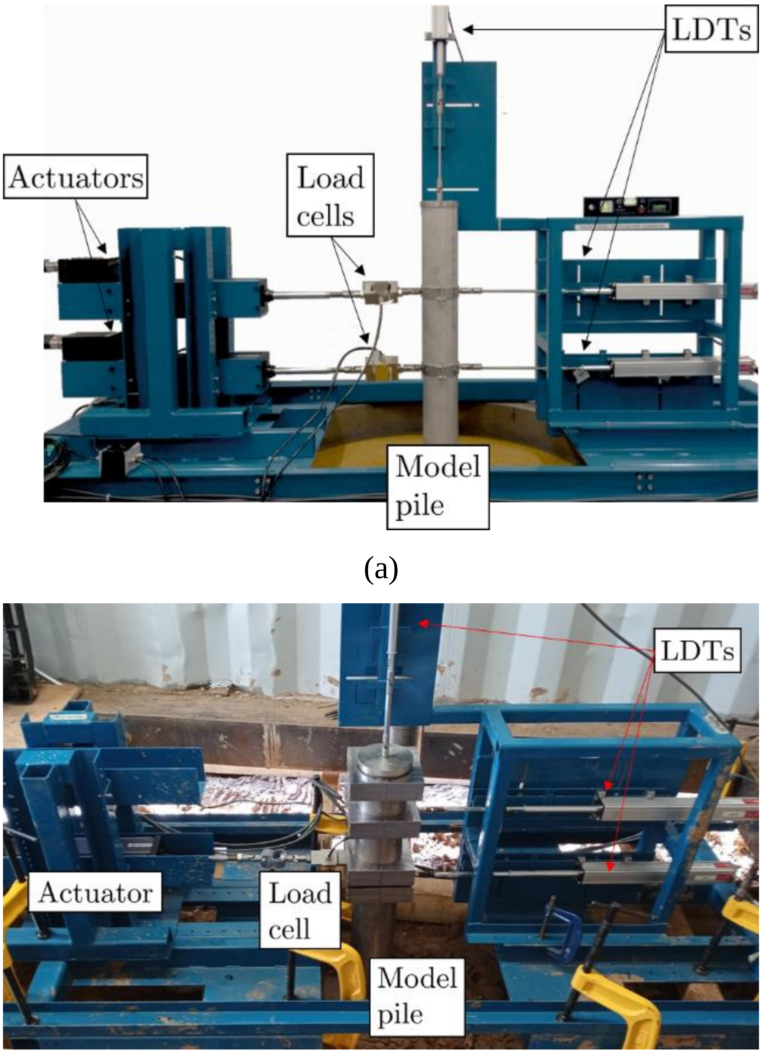

(a)

(b)

Figure 2-3 Photographs of the rig:

(a) testing in dry sand; (b) testing in saturated stiff clay.

2.2.2.1 Actuation system

The actuation system has a pair of electric linear actuators secured on a rigid frame and connected to two pile loading points (part A). To allow more flexibility, the vertical and horizontal locations of the actuators are adjustable.

A double-loop elastomer coupler with two universal joints on both sides connects the actuator and load cell (part B) (see the picture in Figure 2-4). Richards (2019) adopted a similar coupling design to achieve precise load control due to the flexibility of the coupling. The coupler is fastened using set screws to avoid additional loading being applied to the pile during installation.

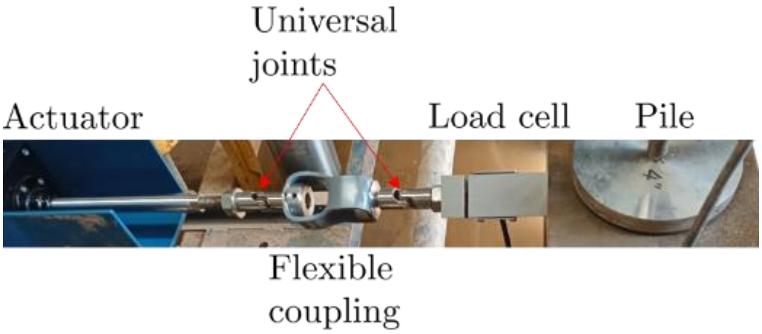

Figure 2-4 Actuator coupling.

Tritex II® TDX-075 DC linear actuators are adopted in this design. Their maximum continuous force is approximately 2 kN, and the top speed is 127 mm/s (5 inches/s). These limits were coded in an embedded controller by the factory and are amendable via the Tritex software tool. The maximum stroke length is 254 mm (10 inches). The actuators are controlled via analogue voltage signals in the range of ± 10V with flying wires connected to an external controller. The input signal is programmable as position, velocity or torque command. Other connection options (*e.g.* Ethernet) are also available.

The actuation system was fully commissioned by undertaking trial tests in dry sand, and its performance is reported in Wu *et al*. (2020). Figure 2-5 (a) shows that the actuator tracks the command signal well in a trial cyclic loading test with variable frequencies. Irregular cyclic loading (*i.e.* time-varying cyclic frequency and magnitude) is also achievable. Figure 2-5 (b) demonstrates the use of both actuators to apply loads simultaneously. Simplified wind and wave load spectra by Nikitas *et al*. (2017) are simulated in this case. It can be seen that the two actuators can successfully perform sinusoidal cyclic loads at 0.1 Hz and 0.01 Hz to represent waves and wind being applied on the monopile, respectively.

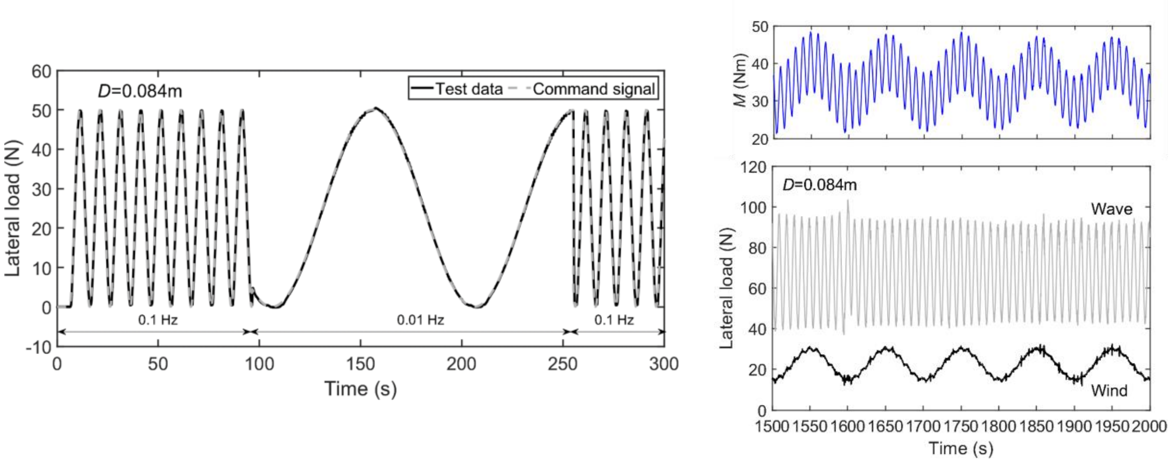

(a) (b)

Figure 2-5 Commissioning of the actuation system:
(a) variable cyclic loading; (b) simulating wind and waves (Wu *et al.*, 2020).

The actuators are feedback-controlled by processing real-time load measurements with programmable controllers. Once the stiffness of the whole system changes, these controllers need to be tuned by performing trials. Factors influencing the system stiffness include the connection between the pile and actuator(s), soil condition and pile size. Also, using two actuators simultaneously is more complex than using only one. The controller design is discussed in Section 2.3.

2.2.2.2 Measurement system

The measurement system contains strain-gauged S-beam load cells, linear displacement transducers (LDTs) and a temperature probe (see descriptions of the sensors in Table 2-1). The LDTs and load cells share an industrial 24VDC power supply for excitation, and each load cell is equipped with a factory-calibrated miniature amplifier. The temperature probe is embedded into the soil to identify whether any changes in soil or rig behaviour may be due to temperature effects.

Table 2-1 List of the sensors.

Item	Brand/model	Descriptions
LDT	Temposonic® E-Series Model ER	Stroke length: approximately 200 mm Outputs: 0 to 10 VDC (linear to the active stroke length) Resolution: infinite (subject to output ripple)
Load cell	Applied Measurements® S-beam Load Cell	Capacity: 500 kg Operation mode: both tension and compression Outputs: 0.1 V (5 kN tension) to 10 V (5 kN compression)
Temperature sensor	RS PRO KM07 Immersion Probe	Measurement range: -50 °C to 250 °C Thermocouple: K type PTFE fine wire Response time: 0.1 seconds

The LDTs are secured on a reference frame (part C) (Figure 2-6), and their locations are adjustable to fit different sizes of piles. Two horizontal LDTs are connected to the pile using neodymium magnets to prevent running out of stroke (part D). A vertical LDT is fastened to the pile head using a threaded universal joint. Each LDT has a specialised linkage with a pair of universal joints. The linkage dimensions and LDT locations are known, so pile movement is obtained through LDT measurements, as detailed in Section 2.4.3.

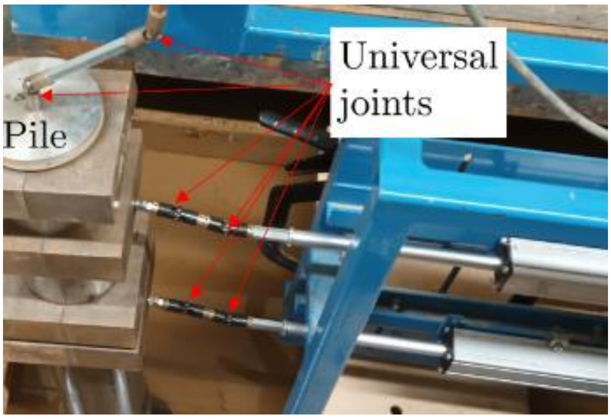

Figure 2-6 LDT linkage.

2.3 Control and data logging system

2.3.1 Hardware

The hardware includes an industrial controller and input/output modules for signal transmission, as listed in Table 2-2. The CompactRIO controller features a field-programmable gate array (FPGA) unit, allowing software and hardware to start simultaneously and operate at the maximum rate of 1 MHz. Data are stored in the controller and can be transferred to the computer via universal serial bus 3.0. Control commands are sent from the computer to the controller. Other communication options between the controller and computer, such as Ethernet and RS232, are also available.

Table 2-2 List of the hardware components.

Name	Type	Main Function(s)
CompactRIO	NI-cRIO-9045	Data storage and exchange Controller
Analogue input module (± 10V)	NI 9220	Input signals from the measurement system
	NI 9210	Temperature monitoring
Analogue output module (± 10V)	NI 9263	Output signals for the actuators and relay module

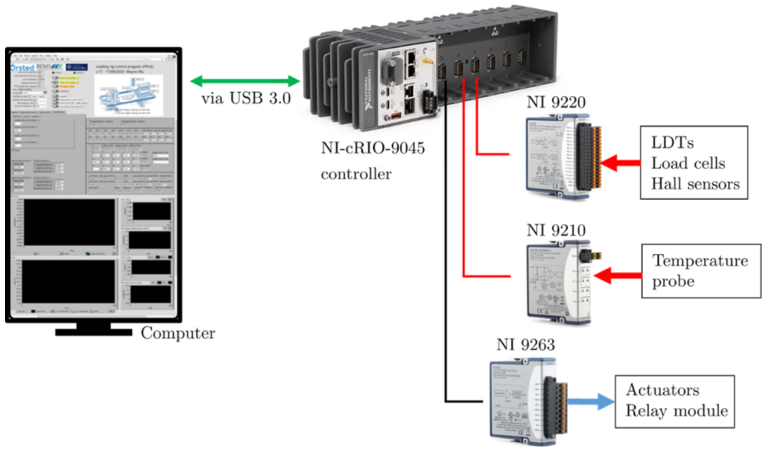

Hardware configuration

The input modules NI 9220 and NI 9210 are used for data logging. The NI 9220 module is connected to the LDTs and load cells to acquire analogue signals, and the NI 9210 module is linked to the temperature probe. The NI 9210 module features a factory-calibrated filter and a cold junction for thermocouple measurements, but its maximum sampling rate (= 2.3 scans/s) is much lower than the NI 9220 module (= 100k scans/s).

The output module NI 9263 sends high-accuracy signals to the actuators and relay module. The sampling rate is up to 100k scans/s to achieve real-time control. The relay module is linked to the power. In an emergency case (*e.g.* overloading), the relay switch is turned off to cut out the power to the actuator.

2.3.2 Software design

A specialised control and data logging program under the LabVIEW FPGA framework was developed for the loading rig (see Figure 2-7). The maximum loop rate is set to 10 ~ 100 kHz, allowing pile pose to be solved in real-time. Essential functions, such as monotonic and sinusoidal cyclic loading, are embedded in the program, and customised loading paths coded into comma-separated value (.csv) files are executable. Data are continuously acquired at the maximum rate of 1 kHz and are backed up separately for every hour.

Embedded proportional-integral-derivative (PID) controllers in LabVIEW (NI, 2022) are implemented to process command signals and measurements for feedback control. The mathematical form for the controller is expressed as

$$u_{out}(t) = K_C \left[e_{in} + \frac{1}{T_i} \int_0^t e_{in} dt + T_d \frac{de_{in}}{dt} \right] \qquad \text{Equation 2-1}$$

where u_{out} is the output for the actuation system (analogue signal), e_{in} is the input error from the setpoint and process variable, K_C is the controller gain, T_i is the integral time, and T_d is the derivative time (t). Following the discussion in Section 2.2.2.1, these PID parameters are tuned when the stiffness of the system changes. Trials are needed to obtain suitable values manually because these parameters cannot be derived from theoretical relationships.

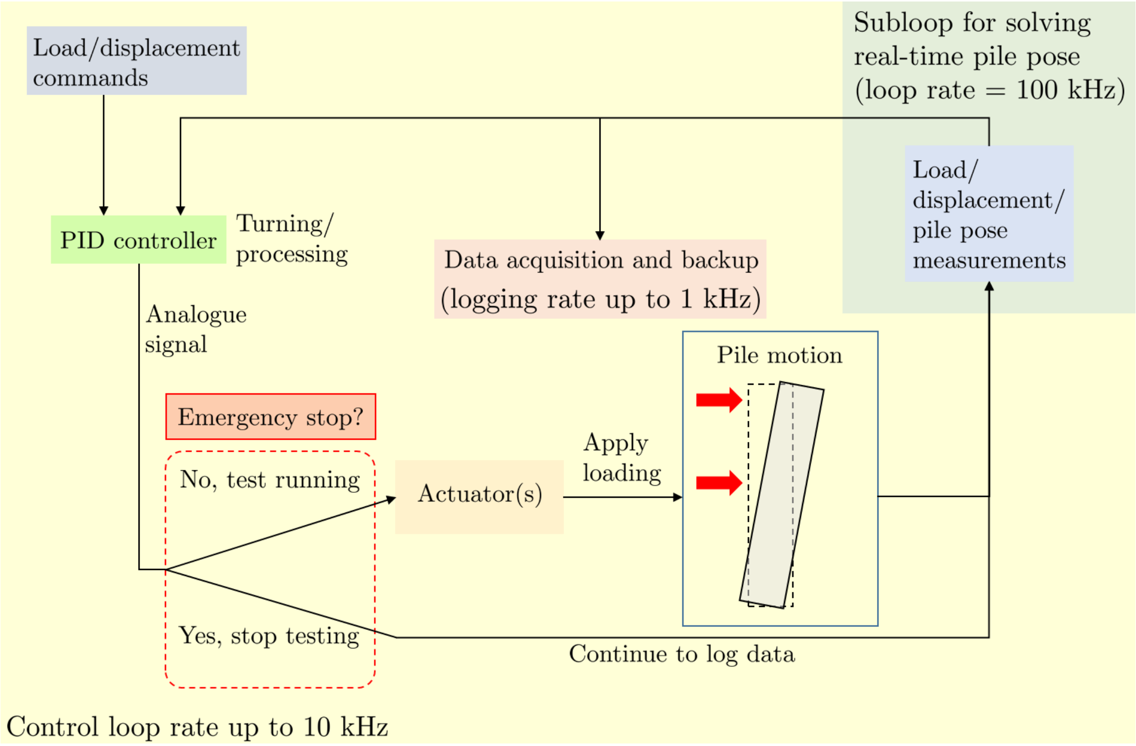

Figure 2-7 Design of the control and data logging system.

Load and displacement measurements are recorded and processed for feedback load and displacement control in the program. Load measurements are converted into horizontal loading at the loading point (H_e) and moment M at the ground level. Real-time pile pose is calculated as horizontal, vertical and rotational movements at the ground level (u, v, θ) by assuming that the pile is rigid.

A purpose-built emergency stop system was designed to protect the equipment, as illustrated in Figure 2-8. The actuation system stops immediately when the pre-set load or displacement limit is reached. It is also triggered by pressing the external stop button or the embedded Boolean button in the LabVIEW program. If one of the above conditions is met, the relay switch is off, disconnecting the power to the actuator(s). At the same time, the data logging system keeps running to monitor the pile.

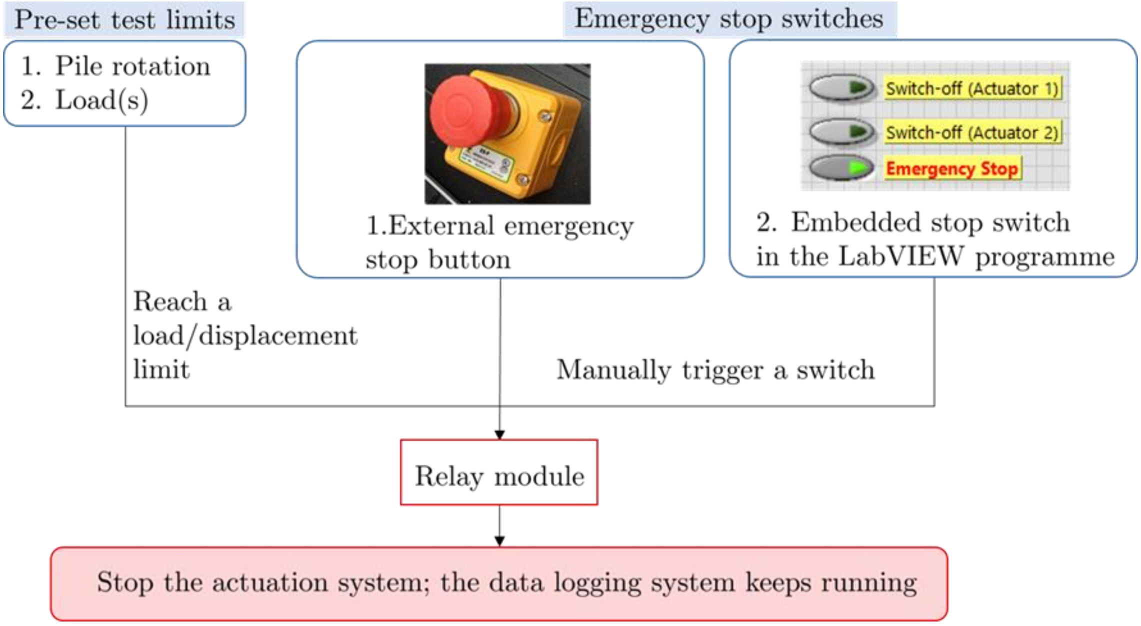

Figure 2-8 Design of the emergency stop system.

2.4 Model piles

2.4.1 Pile rigidity

Full-scale monopiles have a diameter D of 8 m to 10 m (*e.g.* Byrne, 2020), and 1:100 scale model piles were chosen for testing, as shown in Table 2-3. These piles were made of aluminium and stainless steel tubes with D between 80 mm and 101 mm and the wall thickness (t) between 2 mm and 5 mm. The Type I and II piles with slightly different pile geometries and stiffness were tested in dry sand. The pile embedment in dry sand aligns with Richards (2019) ($L/D = 4$) to compare test results and examine the performance of the new loading rig. The Type III pile was used for testing in clay, and the L/D ratio is the same for the medium-scale piles in the PICASO project (Byrne *et al.*, 2020a) to study scaling effects. Work is ongoing to examine pile behaviour with a broader range of L/D ratios at Oxford University by Keane (2022) using the rig developed in this thesis.

Table 2-3 Pile properties and rigidity analysis

		Type I	Type II	Type III
D	mm	80	84	101.6
t	mm	5	2	2
L	mm	320	336	304.8
D/t	-	16	42	50.5
L/D	-	4	4	3
Material		Aluminium	304 Stainless steel	316 Stainless steel
E_p	kPa	7×10^{7}	1.9×10^{8}	1.9×10^{8}
I_p	m^4	8.32×10^{-7}	4.33×10^{-7}	7.76×10^{-7}
E_pI_p	$kN\cdot m^2$	58.24	82.34	147.5
	Estimated E_s (kPa)	K_R		
Loose sand	27500 ~ 55000	0.101 ~ 0.202	0.117 ~ 0.235	-
Dense sand	70000 ~ 110000	-	0.059 ~ 0.092	-
Stiff clay	25000 ~ 40000	-	-	0.427 ~ 0.684

Pile rigidity is assessed using the pile-flexibility factor (K_R) proposed by Poulos and Davis (1980):

$$K_R = \frac{E_P I_P}{E_S L^4} \qquad \text{Equation 2-2}$$

where E_P is Young's modulus of the pile, I_P is the moment of inertia, and E_s may be derived from the secant soil modulus under small strains. Piles are considered relatively rigid compared to the soil if K_R > 0.01. In practice, E_s is difficult to estimate, and an ideal way to measure it is through laterally-loaded pile testing, as suggested by Poulos and Davis (1980). For the test design, a wide range of E_s values for each soil condition is estimated at the model-scale under low confining stress, as given in Table 2-3. For full-scale monopiles, E_s may be depth-varying. In general, the selected piles are considered rigid, and pile deflections are minimal.

For testing in dry sand, it can be seen that the Type II pile has a larger diameter-to-thickness (D/t) ratio and is stiffer than the Type I pile. For prototype monopiles, current design practice (*e.g.* API, 2007) suggests that the D/t ratio is approximately 100. Therefore, the Type II pile is more preferable.

The factor K_R only considers the pile geometry, material properties and elastic soil strength properties, while other factors can also influence the initial pile behaviour. For example, soil strength properties, such as the secant stiffness, may be enhanced when a pile is subject to rapid loading due to soil rate effects. Also, lateral pile response may become stiffer if additional vertical loading is applied. Therefore, although the selected piles are treated as rigid, care is required for data interpretation.

2.4.2 Pile clamp designs

Figure 2-9 shows two different pile clamp designs. The lightweight clamp (≈ 725 g) was used for testing in dry sand. It is secured onto the pile using set screws and fastened using screws and nuts. The clamp body was made of a 5-mm thick stainless steel sheet and is unsuitable for bearing heavy loads (*i.e.* > 100 N). The heavyweight clamp (≈ 2.5 kg) is preferable for testing in dense sand and stiff clay due to its high stiffness. It was made of steel blocks and fastened using screws. More clamps can be added to apply additional vertical loading onto the pile.

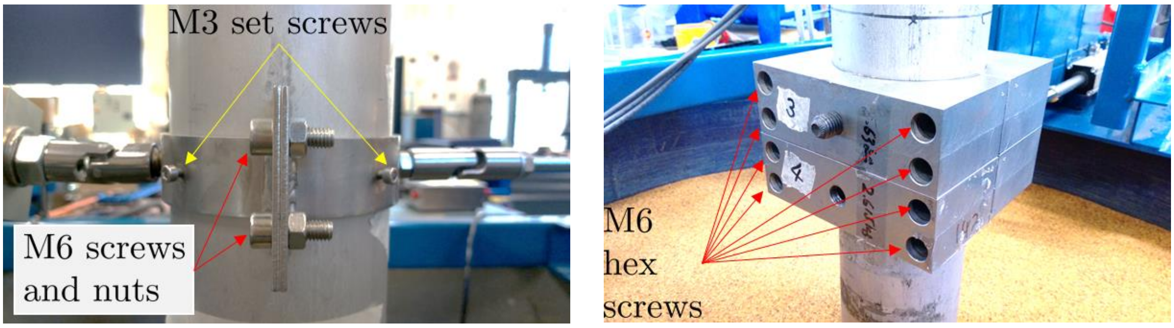

(a) (b)

Figure 2-9 Pile clamp designs: (a) lightweight clamp; (b) heavyweight clamp.

2.4.3 Pile kinematics

Pile movement is captured through LDT measurements. The pile is subject to uni-directional lateral loading and is considered rigid in the analysis of pile motion. Combined horizontal, vertical and rotational movements (u, v, θ) at the ground level are obtained using planar kinetic equations below.

Before a test starts, a pile is assumed to be perfectly installed in a target position. The coordinates of the three LDT connections on the pile are (x_1, y_1), (x_2, y_2) and (x_3, y_3), and the LDT 1, 2 and V are located at (x_1^*, y_1^*), (x_2^*, y_2^*) and (x_3^*, y_3^*), respectively (see Figure 2-10). The LDT locations (x_1^*, y_1^*), (x_2^*, y_2^*) and (x_3^*, y_3^*) were carefully measured during the installation of the rig. Before the LDTs and pile are connected, the LDT travelling lengths are zero (*i.e.* the initial measurements are zeroed).

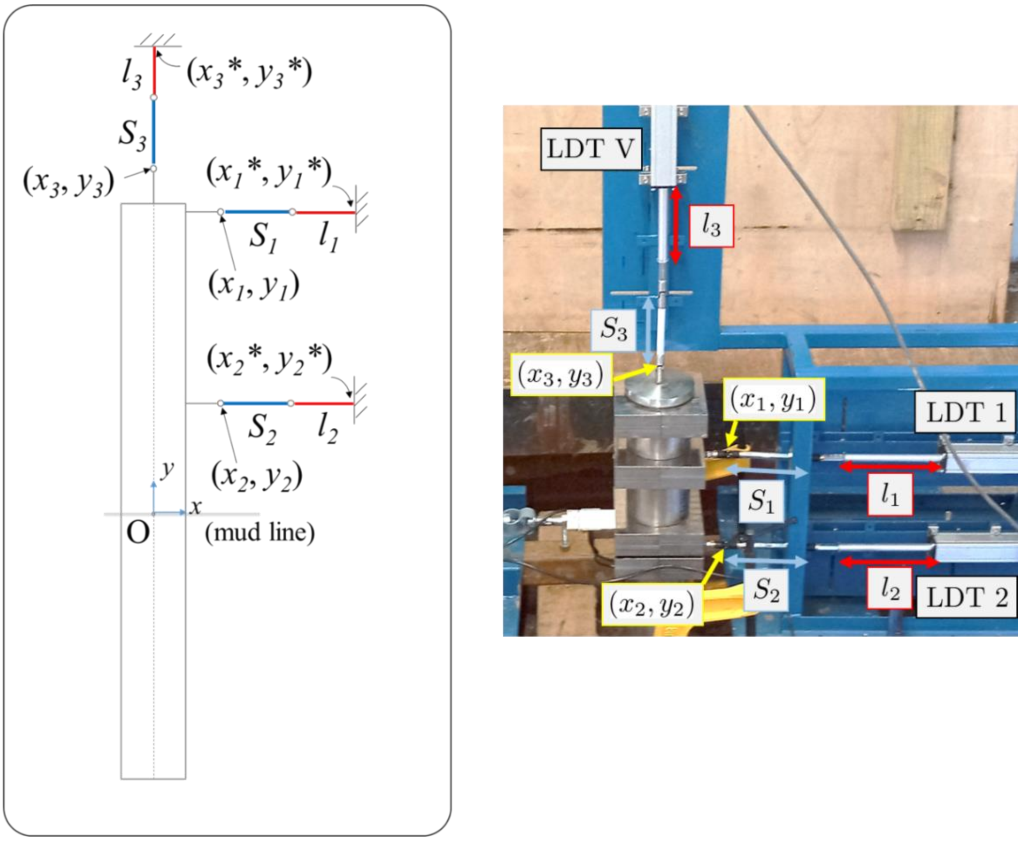

Figure 2-10 Initial coordinates of the LDTs and their connecting points on the pile.

In Figure 2-10, it can be seen that $x_3 = x_3^*$, $y_1 = y_1^*$ and $y_2 = y_2^*$, and the lengths of the linkage rods, denoted as S_1, S_2 and S_3, are known. The LDT travelling lengths (l_1, l_2 and l_3) are measured from data when the LDTs and pile are connected. The LDT positions (x_1^*, y_1^*), (x_2^*, y_2^*) and (x_3^*, y_3^*) can be expressed as

$x_1^* = x_1 + S_1 + l_1$ Equation 2-3 (a)

$x_2^* = x_2 + S_2 + l_2$ Equation 2-3 (b)

$x_3^* = x_3$ Equation 2-3 (c)

and

$y_1^* = y_1$ Equation 2-4 (a)

$y_2^* = y_2$ Equation 2-4 (b)

$y_3^* = y_3 + S_3 + l_3.$ Equation 2-4 (c)

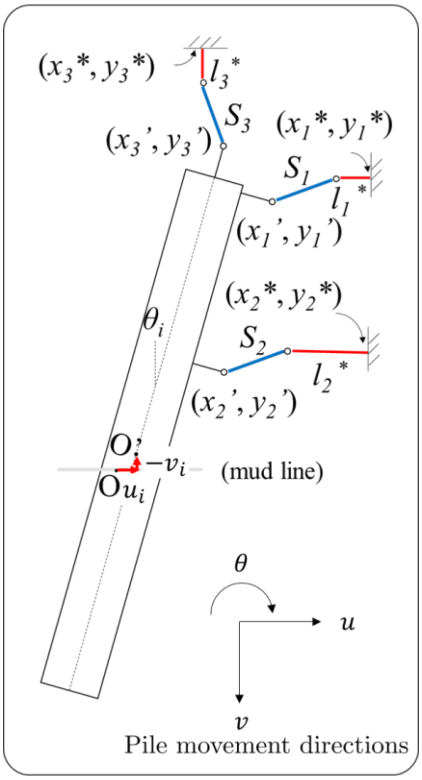

Figure 2-11 Illustration of pile pose after installation.

However, in practice, the target pile position and the actual pile position are slightly misaligned after pile installation. The reference point O moves (u_i,v_i) to the actual point (O') and with the rotation angle (θ_i), and the LDT connection points move from (x_1, y_1), (x_2, y_2) and (x_3, y_3) to (x'_1, y'_1), (x'_2, y'_2) and (x'_3, y'_3), respectively (see Figure 2-11). The directions of u, v and θ align with the directions of H, V and M, respectively. The coordinates of (x'_1, y'_1), (x'_2, y'_2) and (x'_3, y'_3) are expressed as

$$x'_1 = u_i + x_1 \, cos\, \theta_i + y_1 \, sin\, \theta_i \qquad \text{Equation 2-5 (a)}$$

$$x'_2 = u_i + x_2 \, cos\, \theta_i + y_2 \, sin\, \theta_i \qquad \text{Equation 2-5 (b)}$$

$$x'_3 = u_i + y_3 \, sin\, \theta_i \qquad \text{Equation 2-5 (c)}$$

and

$$y'_1 = -v_i - x_1 \, sin\, \theta_i + y_1 \, cos\, \theta_i \qquad \text{Equation 2-6 (a)}$$

$$y'_2 = -v_i - x_2 \, sin\, \theta_i + y_2 \, cos\, \theta_i \qquad \text{Equation 2-6 (b)}$$

$$y'_3 = -v_i + y_3 \, cos\, \theta_i. \qquad \text{Equation 2-6 (c)}$$

The extended lengths of the LDTs then become l_1^*, l_2^* and l_3^*. As the linkage lengths S_1, S_2 and S_3 can be expressed in terms of x', x^*, y', y^* and l^*, the following relationships can be derived:

$$S_1^2 = (x_1^* - x'_1 - l_1^*)^2 + (y_1^* - y'_1)^2 \qquad \text{Equation 2-7 (a)}$$

$$S_2^2 = (x_2^* - x'_2 - l_2^*)^2 + (y_2^* - y'_2)^2 \qquad \text{Equation 2-7 (b)}$$

$$S_3^2 = (x_3^* - x'_3)^2 + (y_3^* - y'_3 - l_3^*)^2. \qquad \text{Equation 2-7 (c)}$$

Next, x', x^*, y' and y^* can be substituted in Equations 2-7 (a)~(c):

$$\begin{aligned} F_1 &= (x_1 + S_1 + l_1 - u_i - x_1 \, cos\, \theta_i - y_1 \, sin\, \theta_i - l_1^*)^2 \\ &+ (y_1 + v_i + x_1 \, sin\, \theta_i - y_1 \, cos\, \theta_i)^2 - S_1^2 = 0 \end{aligned} \qquad \text{Equation 2-8 (a)}$$

$$\begin{aligned} F_2 &= (x_2 + S_2 + l_2 - u_i - x_2 \, cos\, \theta_i - y_2 \, sin\, \theta_i - l_2^*)^2 \\ &+ (y_2 + v_i + x_2 \, sin\, \theta_i - y_2 \, cos\, \theta_i)^2 - S_2^2 = 0 \end{aligned} \qquad \text{Equation 2-8 (b)}$$

$$\begin{aligned} F_3 &= (x_3 - u_i - y_3 \, sin\, \theta_i)^2 \\ &+ (y_3 + S_3 + l_3 + v_i - y_3 \, cos\, \theta_i - l_3^*)^2 - S_3^2 = 0 \end{aligned} \qquad \text{Equation 2-8 (c)}$$

where the expressions F_1, F_2 and F_3 are non-linear equations, and u_i,v_i and θ_i can be found by using the Newton-Raphson iteration method. The iteration process is expressed as

$$\begin{bmatrix} u_i^{(n+1)} \\ v_i^{(n+1)} \\ \theta_i^{(n+1)} \end{bmatrix} = \begin{bmatrix} u_i^{(n)} \\ v_i^{(n)} \\ \theta_i^{(n)} \end{bmatrix} - \left[\boldsymbol{J}\left(u_i^{(n)}, v_i^{(n)}, \theta_i^{(n)}\right)\right]^{-1} \left[\boldsymbol{F}\left(u_i^{(n)}, v_i^{(n)}, \theta_i^{(n)}\right)\right]$$

$$= \begin{bmatrix} u_i^{(n)} \\ v_i^{(n)} \\ \theta_i^{(n)} \end{bmatrix} - \begin{bmatrix} \frac{dF_1}{du_i} & \frac{dF_1}{dv_i} & \frac{dF_1}{d\theta_i} \\ \frac{dF_2}{du_i} & \frac{dF_2}{dv_i} & \frac{dF_2}{d\theta_i} \\ \frac{dF_3}{du_i} & \frac{dF_3}{dv_i} & \frac{dF_3}{d\theta_i} \end{bmatrix}^{-1} \begin{bmatrix} F_1 \\ F_2 \\ F_3 \end{bmatrix}$$

Equation 2-9

where n is the number of iterations, $\boldsymbol{J}$ is the Jacobian matrix of the equations F_1, F_2 and F_3. $u_i^{(0)}$, $v_i^{(0)}$ and $\theta_i^{(0)}$ are set to (0, 0, 0) as default. If $u_i^{(n+1)}$, $v_i^{(n+1)}$ and $\theta_i^{(n+1)}$ are almost equal to $u_i^{(n)}$, $v_i^{(n)}$ and $\theta_i^{(n)}$, respectively, the iteration process is complete. The iteration process in the control and data logging system is illustrated in Figure 2-12. If the difference in the values in the n-th and n+1-th iterations is less than 0.01%, the iteration loop will stop and send the updated values to the control loop.

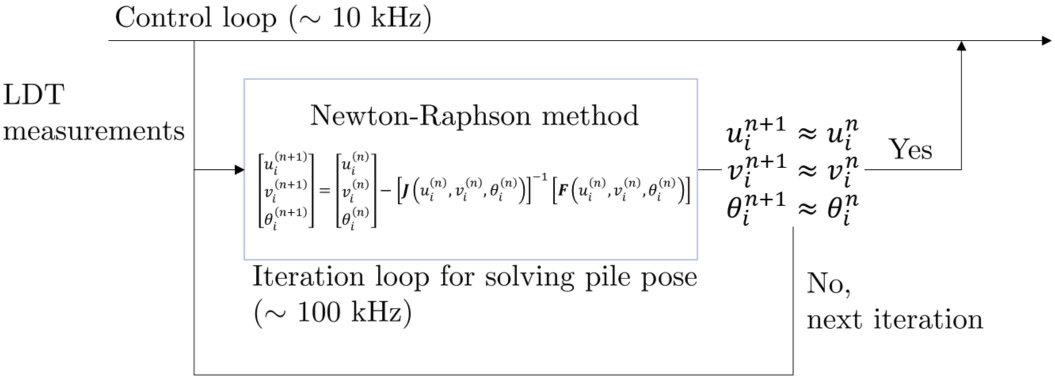

Figure 2-12 Illustration of the iteration process in the control and data logging system.

Following the above procedure, the initial pile pose (u_i, v_i, θ_i) is found. For pile installation, the maximum allowable θ_i is 0.25°, which aligns with current design practice for full-scale monopiles. After installation, the LDTs continue to monitor pile movement. As the initial pile pose is known, real-time pile pose (u, v, θ) during the test can be obtained by adopting the same procedure.

2.5 Summary

This chapter illustrates the development of a novel loading rig for the experimental work in this thesis. The performance of the rig is demonstrated, and the selected 1:100 model piles can be treated as rigid. During the test, load cell and LDT data are acquired and processed to control the actuator(s). LDT measurements are processed using the Newton-Raphson iteration process to obtain real-time pile movement. Later, Chapters 3 and 4 describe the experimental work and present test data to investigate monopile behaviour further.

3 Model testing in dry sand

3.1 Introduction

This chapter describes a series of model monopile tests in artificial clean sand with different soil densities. In these tests, piles were installed through impact driving to reflect the driving process for full-scale monopiles. Monotonic and uni-directional one-way cyclic lateral loading tests at different rates were performed to explore soil rate effects in sand. In addition, various combined load conditions are investigated by applying different vertical loads V and changing the load eccentricity e to explore pile behaviour more thoroughly. Additional experimental observations, such as the pile pivot position and pile uplift, are also presented.

3.2 Preparations for testing

3.2.1 Soil Characterisation

Yellow Leighton Buzzard (YLB) 14/25 sand was used for the model tests. The sand has been used in various projects in the Geotechnical Engineering Research Laboratory at Oxford University. Detailed soil characteristics are given in Table 3-1, and the particle size distribution is illustrated in Figure 3-1. The sand is uniformly graded, and two different soil relative densities (D_r) were achieved to simulate *very loose* and *dense* sand conditions at laboratory scale.

Table 3-1 Soil characteristics for YLB 14/25 sand
(data obtained from Richards (2019) and Schnaid (1991)).

Critical state friction angle	ϕ'_{cr}	34.3	°
Specific gravity	G_S	2.65	-
Particle sizes	D_{10}, D_{30}, D_{50}, D_{60}	0.56, 0.69, 0.81, 0.87	mm
Maximum dry unit weight	γ'_{max}	17.64*	kN/m^3
Minimum dry unit weight	γ'_{min}	14.43*	kN/m^3
Maximum void ratio	e_{max}	0.80	-
Minimum void ratio	e_{min}	0.47	-

* Data were acquired following the British Standard BS 1377: Part 4.

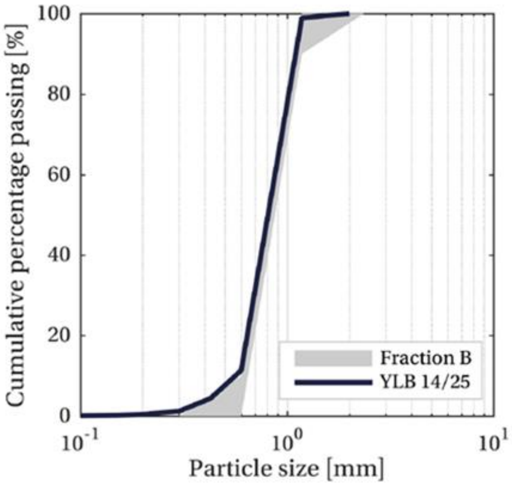

Figure 3-1 Particle size distribution of YLB 14/25 sand
(corresponding to the lower bound of Fraction B in BS 1377) (Richards, 2019).

Soil particle size effects may influence the drivability and performance of monopiles. Although pile installation effects are not addressed in the thesis, De Nicola and Randolph (1997) found that the pile wall thickness t and soil particle size influence the formation of the soil plug in an open-ended pile during impact driving. The ratios of D/D_{50} and t/D_{50} of the two model piles adopted in this research, and examples from the literature are given in Table 3-2. Comparing the two model piles used for the testing in this thesis, it can be seen that the Type I pile has a larger t/D_{50} ratio than the Type II pile. The responses of these two piles are presented in this chapter.

Table 3-2 D/D_{50} and t/D_{50} ratios of various open-ended model piles.

Pile type/ Source	Type I pile and Richards (2019)	Type II pile	Klinkvort and Hededal (2014)	Li *et al*. (2022)
D (mm)	80	84	40	18
D/D_{50}	99	104	222	164
t/D_{50}	6.2	2.5	11.1	9.1
D/t	16	42	20	18

3.2.2 Sample size

A circular sand tank with a diameter of 800 mm and a depth of 800 mm (see Figure 3-2) was used for dry sand samples. These dimensions were adopted to minimise boundary effects. The soil sample diameter is approximately ten times larger than the diameters of Type I and II model piles. De Nicola and Randolph (1997) suggested that the influence of the side boundary is negligible when the spacing between the tank wall and pile is $6D$. Bolton *et al.* (1999) reported that for the cone penetration test, side boundary effects are insignificant if the spacing between the wall and cone is more than five times the cone diameter. The sample height is close to $10D$, which gives a $6D$ clearance below the pile base.

3.2.3 Sample preparation

Very loose sand samples were prepared by manually pouring sand, layer-by-layer, using a shovel at a very low drop height (*i.e.* less than 50 mm) to reduce variation throughout the sample. The soil surface was carefully trimmed to minimise disturbance. Abadie (2015) and Richards (2019) also used this sample preparation method to obtain repeatable soil samples.

Figure 3-2 Photographs of the sand tank and sand rainer.

An air-dry pluviation method was employed to produce *dense* sand samples using a sand rainer designed by Richards (2019), as shown in Figure 3-2. This approach can produce a soil structure which simulates those found in natural soil deposits (Rad and Tumay, 1987). The rainer has a series of sieves, with different sizes of apertures at various heights beneath the hopper to control the flow rate of sand. Sand particles were dropped at a fixed height to achieve homogeneous soil layers. After pluviation, the soil surface was vacuumed to remove excess soil.

Table 3-3 gives the soil sample properties. The effective unit weight γ' is calculated using the sample weight and sample dimensions, and D_r is obtained using the characteristics provided in Table 3-1. In general, repeatable soil samples can be achieved using the two sample preparation methods.

Table 3-3 Soil sample properties.

	Number of samples prepared	γ' (kN/m^3)	Relatively density (D_r)
Very loose sand	35	14.53±0.06	4%
Dense sand	21	16.21±0.06	60%

3.2.4 Influence of stress level

The influence of stress level on the mechanical behaviour of sand is analysed in the following to address the scaling of soil strength properties. At the laboratory scale, the effective stress (p') is approximately 3 kPa. For a full-scale monopile, it is assumed that p' is approximately 200 kPa (at the pile pivot point), although the actual value would vary depending on the pile size. The maximum effective friction angle of sand (ϕ'_{max}) is related to the critical state friction angle ϕ'_{cr}, D_r and p'. Bolton (1986) proposed an empirical relationship based on triaxial test data:

$$\phi'_{max} - \phi'_{cr} = 3I_R \qquad \text{Equation 3-1}$$

where I_R is the dilatancy index, and $\phi'_{max} - \phi'_{cr}$ < 12°.

I_R becomes stress-dependent if p' is greater than 150 kPa, expressed as (Bolton, 1987)

$$I_R = \begin{cases} D_r\left[5 - \ln\left(\dfrac{p'}{150}\right)\right] - 1 & (\text{for } p' > 150\text{ kPa}) \\ 5D_r - 1 & (\text{for } p' < 150\text{ kPa}) \end{cases}. \qquad \text{Equation 3-2}$$

A recent study on sand behaviour under drained triaxial compression by White (2020) also agreed that a notable reduction in ϕ'_{max} in drained LB 14/25 sand is mobilised when p' > 150 kPa, as shown in Figure 3-3 (test series CIDc(+v')).

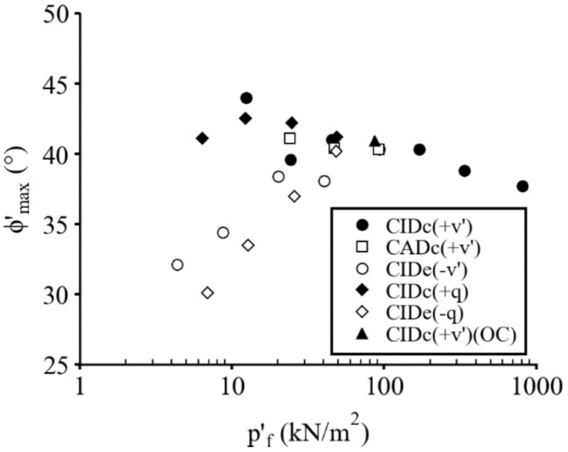

Figure 3-3 Strength reduction due to an increase in the stress level for drained LB 14/25 sand with D_r = 80 % (p'_f = mean effective stress at failure) (White, 2020).

Following Bolton's equations, the relationships between p' and ϕ'_{max} with different D_r are illustrated in Figure 3-4. At the laboratory scale, ϕ'_{max} when D_r = 4% and 60% are equivalent to D_r = 4% (*very loose*) and 64.9% (*dense*) at the full scale, respectively. However, from White's data (Figure 3-3), when D_r = 82 %, from p'_f = 12.4 kPa to p'_f = 170.5 kPa, ϕ'_{max} decreases from 44° to 40.3°. Thus, the *dense* condition in the laboratory may reflect a higher D_r at the full scale (see dashed arrow in Figure 3-4).

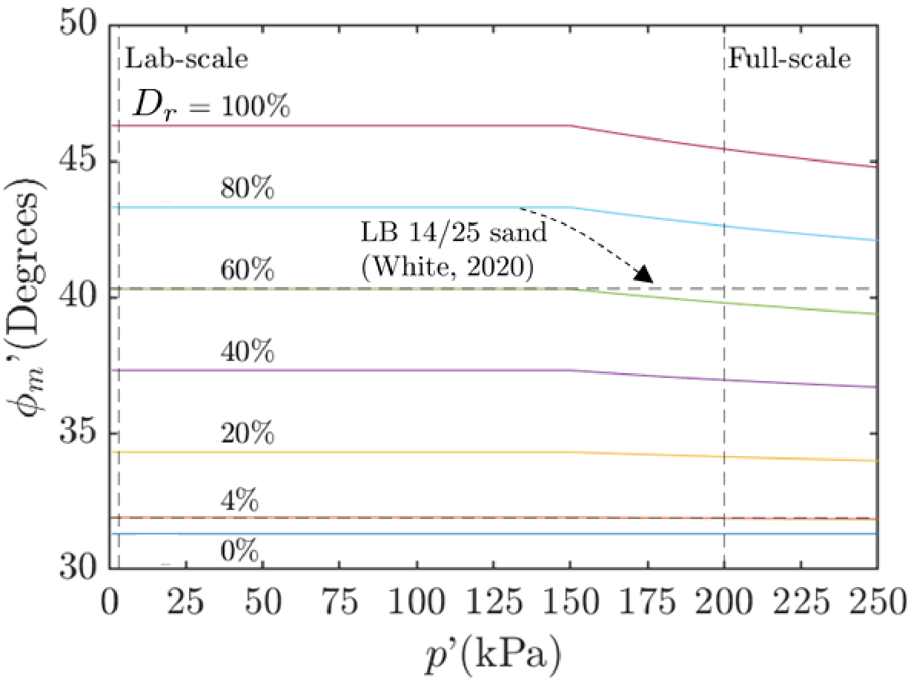

Figure 3-4 ϕ'_{max} versus stress level.

3.2.5 Pile installation process

The pile installation process is illustrated in Figure 3-5, and each step is described below:

(1) The pile is guided by a pile-driving device to maintain verticality.

(2) Repeated impact loading is applied by a 3 kg drop hammer. The falling height of the hammer is 300 mm, with 30 (*very loose* sand) ~ 150 (*dense* sand) blows required to penetrate the pile to the target depth.

(3) Once the target depth is reached, pile clamps are carefully fastened onto the pile. Meanwhile, the driving device holds the pile to prevent lateral movement.

(4) The pile and actuator(s) are connected, with the control and data logging system in operation to monitor the load being applied to the pile.

(5) The driving device is carefully removed. At the same time, the pile is monitored to detect disturbance.

(6) Linear displacement transducers, LDTs, are connected to the pile to measure the initial pile position at ground level (u_i, v_i, θ_i). θ_i is required to be less than 0.25° as this is often used as the tolerance limit for full-scale monopiles.

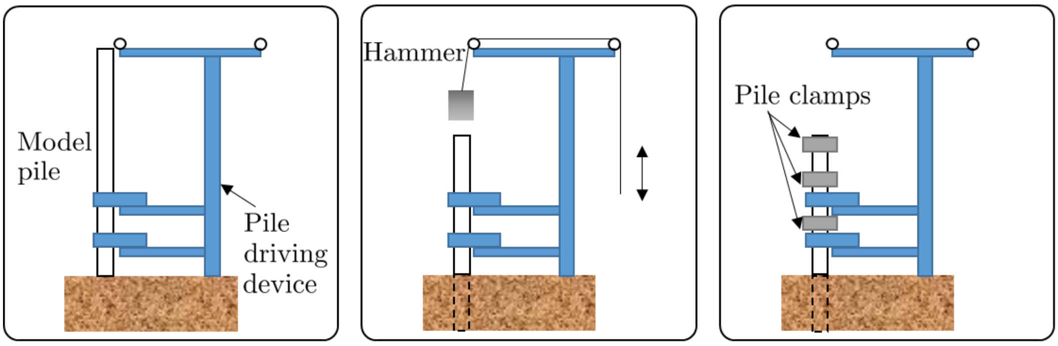

1. Locate the pile onto the pile driving device

2. Drive the pile to the target depth

3. Install pile clamps

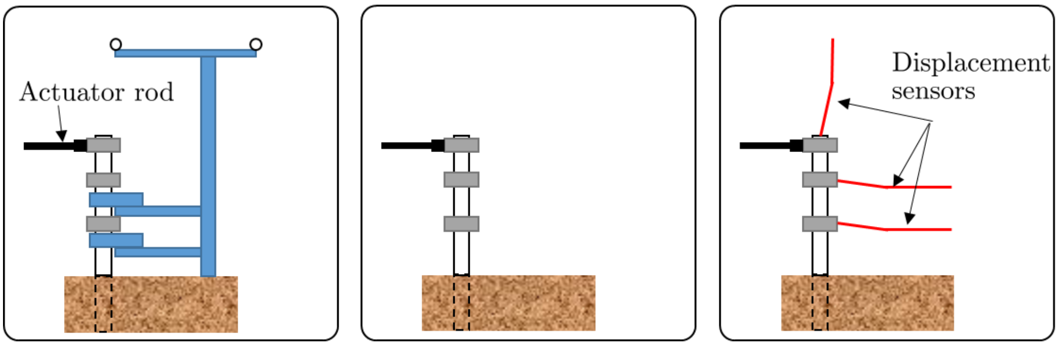

4. Connect the actuator, load cell and pile; measure loads

5. Remove the pile driving device; measure loads

6. Install displacement sensors; measure loads and calculate initial pile pose

Figure 3-5 Illustration of the pile installation process.

All piles were penetrated to the target level (see Figure 3-6). It was found that a cone-shaped subsidence was induced by local densification around the pile during installation, as illustrated in Figure 3-6. The depth of soil settlement is approximately 3% ~ 5% L, but the dimensions are difficult to quantify. As the stress condition in the laboratory differs from that in the field, this observation may not be seen for large-scale piles.

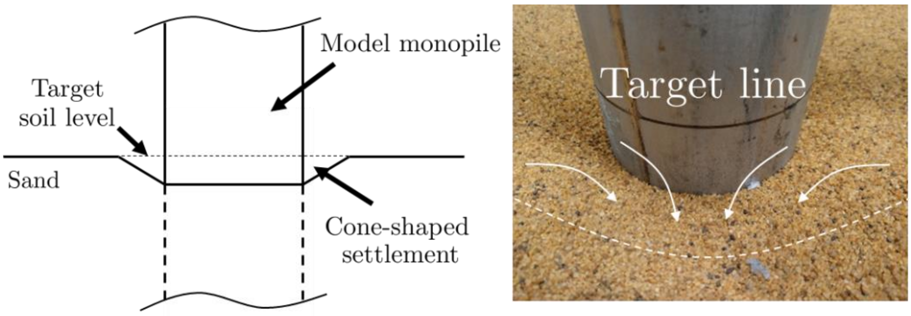

Figure 3-6 Cone-shaped settlement due to pile installation.

3.3 Test programme

The test programme extends the study on laboratory testing of monopiles in dry YLB 14/25 sand by Richards (2019). In Richards' work, tests were undertaken on the Type I pile by applying lateral loading at a fixed point (e = $10D$). The Type I pile was used in *very loose* sand in this research to compare with Richards' data, while the Type II pile was used in *very loose* and *dense* sand.

Figure 3-7 and Figure 3-8 show the design of the experimental work for dry sand and the detailed nomenclature. The test programme for dry sand is given in Table 3-4. Some of the tests were used for theoretical development in Chapter 6. The soil condition, loading pattern, pile type, loading rate, load eccentricity and vertical load are specified for each test. The work packages are described as follows:

(I) Constant actuation rate tests were conducted with a fixed load eccentricity (e = $7D$) and vertical load (V = 119 N or 139 N). These tests established reference pile reaction curves and identified potential rate effects. The ultimate capacities M_R and H_R were obtained from these tests for normalisation of data.

(II) Variable rate tests were performed to investigate rate dependency. In these tests, stepwise changes in the actuation rate (v) were applied to compare with the constant actuation rate tests and element test research (*e.g.* Kiyota and Tatsuoka, 2006; Tatsuoka *et al.*, 2008).

(III) Uni-directional one-way cyclic lateral loading tests at different frequencies f were undertaken. In these tests, sinusoidal cyclic loads were applied at a constant f and a fixed load magnitude, followed by monotonic loading until $\theta = \theta_R$. Cyclic characteristics, such as pile secant stiffness and permanent plastic deformation (*i.e.* ratcheting), were measured to evaluate rate dependency. Data were compared with the constant actuation rate tests (monotonic loading) to investigate post-cyclic monotonic behaviour.

(IV) Combined load effects were investigated by applying various load eccentricities e and vertical loads V. Coupled moment-horizontal load responses are illustrated to identify the failure surface for monopiles more rigorously. Previous research on combined load effects is reviewed and compared with the test data.

Some monotonic tests were also used to study combined load effects for comparison. In addition to rate and combined load effects, the responses of Type I and Type II piles and pile behaviours with different soil densities are compared. Together with the work of Richards (2019), this thesis provides a broader range of data for calibration of soil models for monopile design.

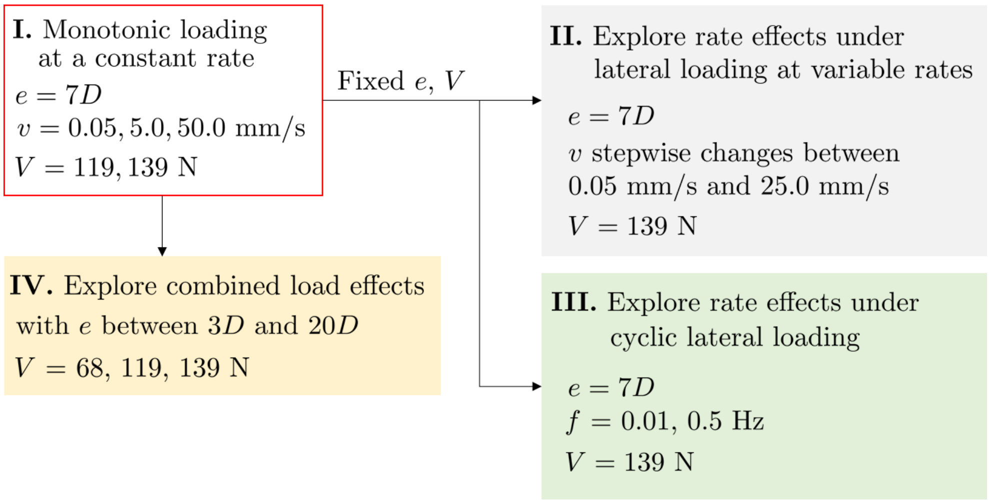

Figure 3-7 Design of testing in dry sand.

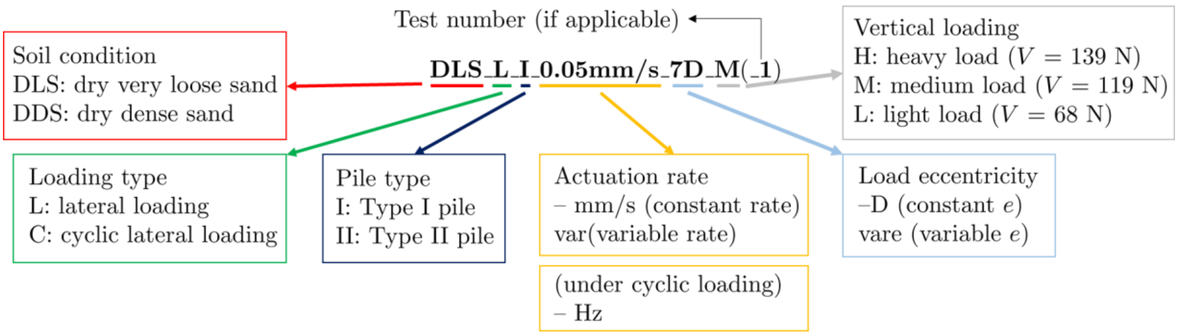

Figure 3-8 Nomenclature for dry sand.

Table 3-4 Test programme for dry sand.

I. Monotonic loading at a constant rate		Theoretical modelling
Very loose sand	DLS_L_II_0.05mm/s_7D_H	Section 6.3.1
	DLS_L_II_5mm/s_7D_H	
	DLS_L_II_50mm/s_7D_H	
	DLS_L_I_0.05mm/s_7D_H[‡]	
Dense sand	DDS_L_II_0.05mm/s_7D_H[#*]	
	DDS_L_II_50mm/s_7D_H	
II. Explore rate effects under lateral loading at variable rates		
Very loose sand	DLS_L_I_var_7D_M	
Dense sand	DDS_L_II_var_7D_H	
III. Explore rate effects under cyclic lateral loading		Section 6.3.4
Very loose sand	DLS_C_II_0.5Hz_7D_H	
	DLS_C_II_0.01Hz_7D_H	
Dense sand	DDS_C_II_0.5Hz_7D_H	
	DDS_C_II_0.01Hz_7D_H	
IV. Explore combined load effects		Sections 6.3.2 and 6.3.3
Very loose sand	DLS_L_I_0.05mm/s_7D_M[†‡]	
	DLS_L_I_0.05mm/s_7D_L[‡]	
	DLS_L_I_0.05mm/s_3D_M[†]	
	DLS_L_I_0.05mm/s_20D_M[†]	
Dense sand	DDS_L_II_0.05mm/s_7D_M[*]	
	DDS_L_II_0.05mm/s_3D_H[#]	
	DDS_L_II_0.05mm/s_20D_H[#]	
	DDS_L_II_var_vare_H_1[#]	
	DDS_L_II_var_vare_H_2[#]	

† : Exploring load eccentricity effects in dry *very loose* sand.

‡ : Investigating the impact of vertical loading in dry *very loose* sand.

: Exploring load eccentricity effects in dry *dense* sand.

* : Investigating the impact of vertical loading in dry *dense* sand.

3.4 Initial pile response and the initial secant pile stiffness

The initial secant pile stiffness ($k_{max} = \Delta M/\Delta\theta$) is obtained to evaluate the initial response of a pile. The initial response appears non-linear, even at very small strains. This observation is also found in Abadie (2015) and Richards (2019). In this thesis, k_{max} is the secant pile stiffness obtained from the moment-rotation response of the pile at $\Delta\theta$ = 0.003°, aligning with the definition by Richards (2019). The k_{max} value is used to analyse pile secant stiffness response to cyclic lateral loading as the initial response is often adopted as an input parameter for theoretical modelling.

Figure 3-9 (a) and (b) show the k_{max} values measured in different test conditions, combined with data from Richards (2019). The initial loading responses of all the model tests are analysed to obtain k_{max}. Richards (2019) estimated k_{max} using initial loading responses for monotonic tests and unloading responses for uni-directional cyclic loading tests.

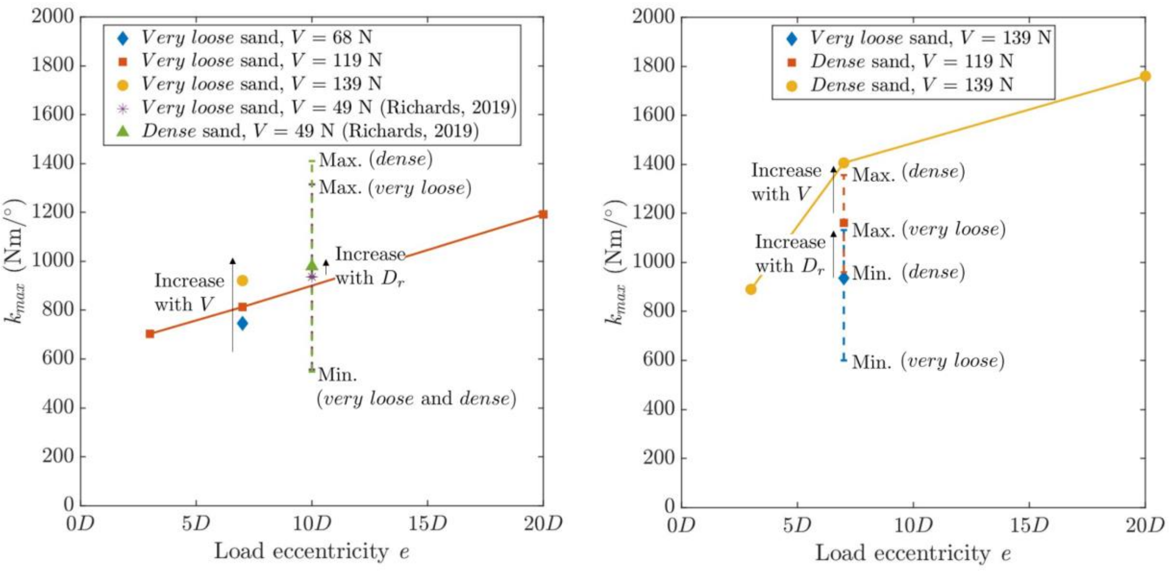

(a) (b)

Figure 3-9 k_{max} values under different test conditions: (a) Type I pile; (b) Type II pile.

Selected tests were repeated to evaluate the variation throughout the soil samples. Under the same test configuration, k_{max} falls in a wide range (see dashed lines in Figure 3-9 (a) and (b)), and potential rate-sensitive response at small strains may not be seen. In *very loose* sand, the variation from Richard's tests (Type I pile) is greater than tests on the Type II pile. Such a phenomenon is also seen in *dense* sand. From Table 3-2, the Type I pile has a larger t/D_{50} ratio than the Type II pile, which may cause more soil disturbance during installation.

With the increase in the load eccentricity e, the moment-rotation response of a pile becomes stiffer. In *very loose* sand, k_{max} increases from 703 Nm/° to 1192 Nm/°, with the loading point moving from $3D$ to $20D$ (Type I pile, V = 119 N). A similar trend is also observed in *dense* sand (Type II pile, V = 139 N).

Data from Figure 3-9 (a) and (b) indicate that the initial pile response may become stiffer with the increase in V. However, given that a wide range of variation is observed, the impact of vertical loading is impossible to quantify.

3.5 Monotonic lateral loading

3.5.1 Constant actuation rate tests

Figure 3-10 and Figure 3-11 show the responses from the constant actuation rate tests in *very loose* and *dense* sand. In these tests, constant actuation rates v fall in the range of 0.05 mm/s ~ 50 mm/s, and the vertical load V and load eccentricity e are fixed. From the data, it can be seen that both moment-rotational and horizontal load-displacement responses do not show any significant rate dependency. Sample variations are slight, and the pile responses at different rates are almost identical.

The rotation-horizontal displacement response is also rate-independent. Although slight differences between the $\theta - u$ slopes are observed in Figure 3-10 and Figure 3-11, data show satisfactory repeatability. These differences may be due to sample variations and installation effects. Typically, θ linearly increases with u when a rigid pile is subject to lateral loading, and the pile pivot position is approximately $0.78L$ (= $3.12D$) below the target ground level when $e = 7D$.

In the PISA testing in dense marine sand, gapping occurred on the active side of the pile, possibly due to slight cementation or suction effects (McAdam *et al.*, 2020), but this phenomenon is not found in the laboratory-scale testing in dry clean sand.

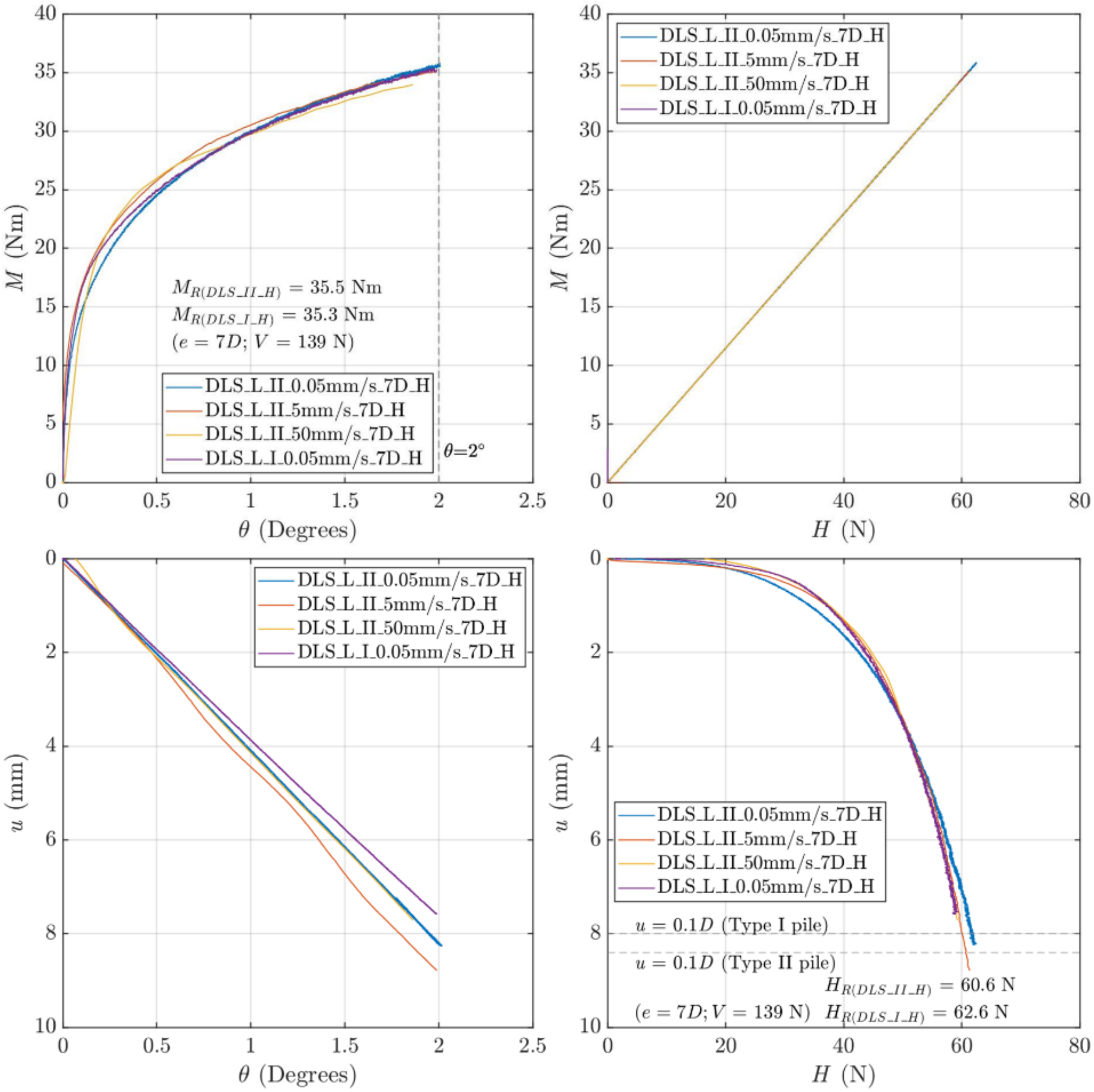

Figure 3-10 Constant actuation rate tests in *very loose* sand.

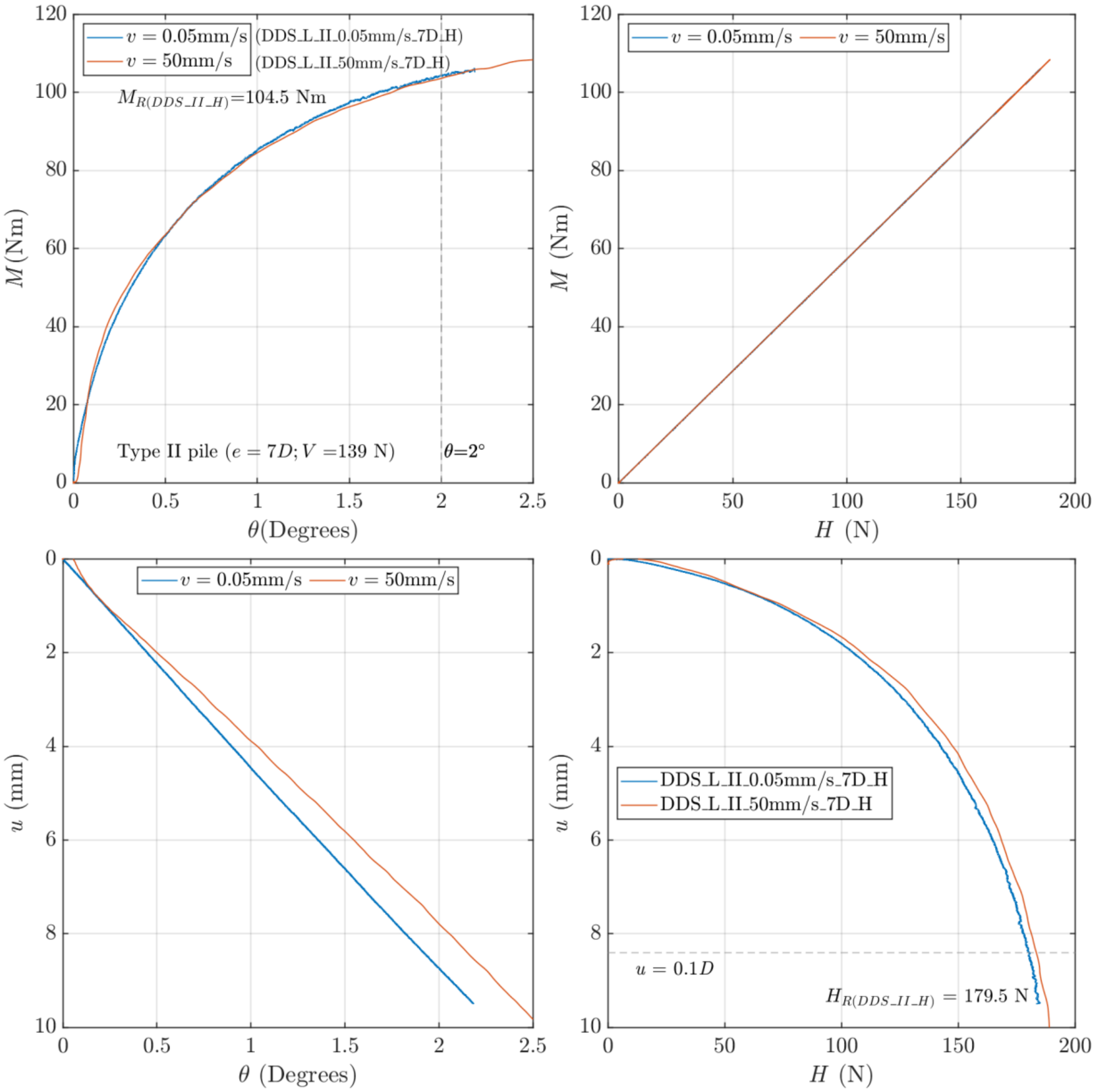

Figure 3-11 Constant actuation rate tests in *dense* sand.

3.5.2 Reference loads and normalisation

The results in Figure 3-10 and Figure 3-11 are used as reference responses for normalisation to help compare experimental data, as listed in Table 3-5. The reference loads of DLS_I_M (test DLS_L_I_0.05mms_7D_M) also are used for normalising test data. Since rate effects are not observed in the monotonic tests, the actuation rate v is not specified.

Table 3-5 Reference loads for the model tests in dry sand.

	Test name	M_R $(\theta = \theta_R = 2°)$ (Nm)	H_R $(u = u_R = 0.1D)$ (N)
Very loose sand	DLS_ I_H (Type I)	35.3	62.6
	DLS_ II_H (Type II)	35.5	60.6
	DLS_I_M (Type I)	33.2	59.0
Dense sand	DDS_ II_H	104.5	179.5

Figure 3-12 (a) shows the normalised responses $M/M_R - \theta/\theta_R$ of the piles in *very loose* and *dense* sand. Similar to Richards' tests (see Figure 3-12 (b)), the normalised tangent stiffness in *dense* sand changes slower than in *very loose* sand.

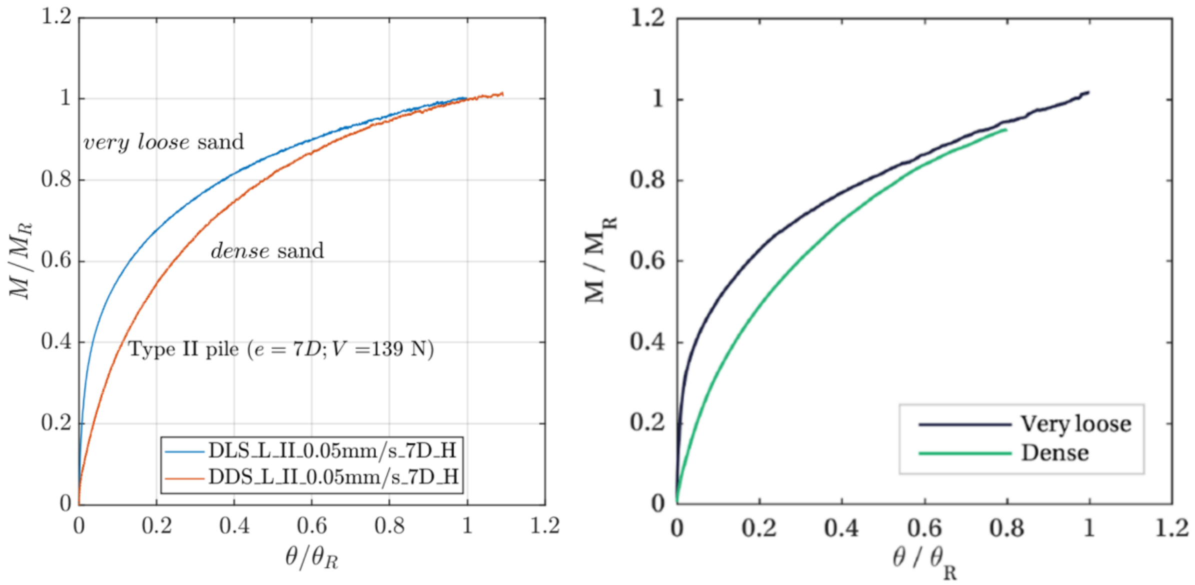

(a)

(b)

Figure 3-12 Normalisation for different soil conditions:
(a) this research; (b) data from Richards (2019).

3.5.3 Variable rate tests

Transient effects of strain rate and strain acceleration in certain types of sands are observed in triaxial compression tests (Kiyota and Tatsuoka, 2006; Tatsuoka *et al*., 2008). For example, as shown earlier in Figure 1-10, transient responses are seen when the strain rate $\dot{\varepsilon}$ changes. Although the experimental evidence indicates potential acceleration effects, theoretical explanations are required to support this hypothesis.

Variable rate tests were conducted to examine soil rate dependency further. The test in *very loose* sand is compared with the monotonic response at 0.05 mm/s ($V = 119$ N). The ultimate moment capacity ($M_{R(DLS\_I\_M)}$) is 33.2 Nm. During the variable rate test, an unloading-reloading loop was applied and did not appear to impact the overall pile response. The results of the constant and variable rate tests in *very loose* sand are approximately similar and rate-independent, as shown in Figure 3-13 (a). Similarly, in Figure 3-14 (a), rate dependency is not seen in *dense* sand.

As shown in Figure 3-13 (b) and Figure 3-14 (b), when the rate changes, an additional transient load of 1.5 N is observed in *very loose* sand, and a 2 N change is found in *dense* sand. These transient loads are induced by the actuation system and are thought to be inertial effects, which are commonly seen during dynamic testing. A recent study also suggested that inertial effects are found in triaxial compression tests, which is related to the mass of the soil specimen and cap (Suescun-Florez and Iskander, 2017). Further analysis is described below.

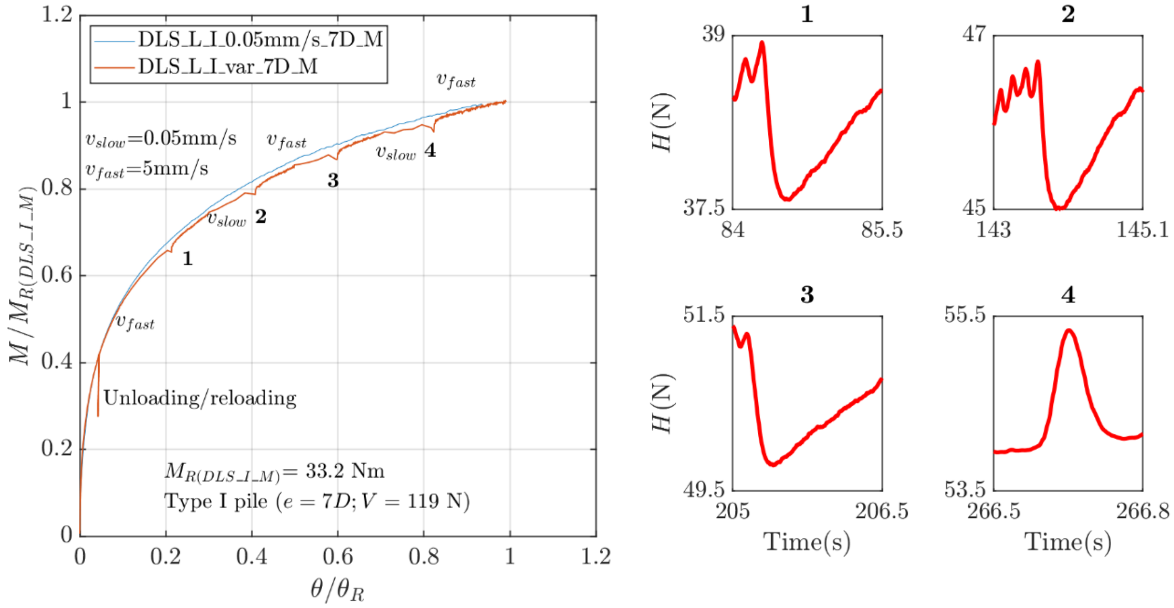

(a) (b)

Figure 3-13 Variable rate test in *very loose* sand:

(a) normalised response; (b) transient loads due to acceleration and deceleration.

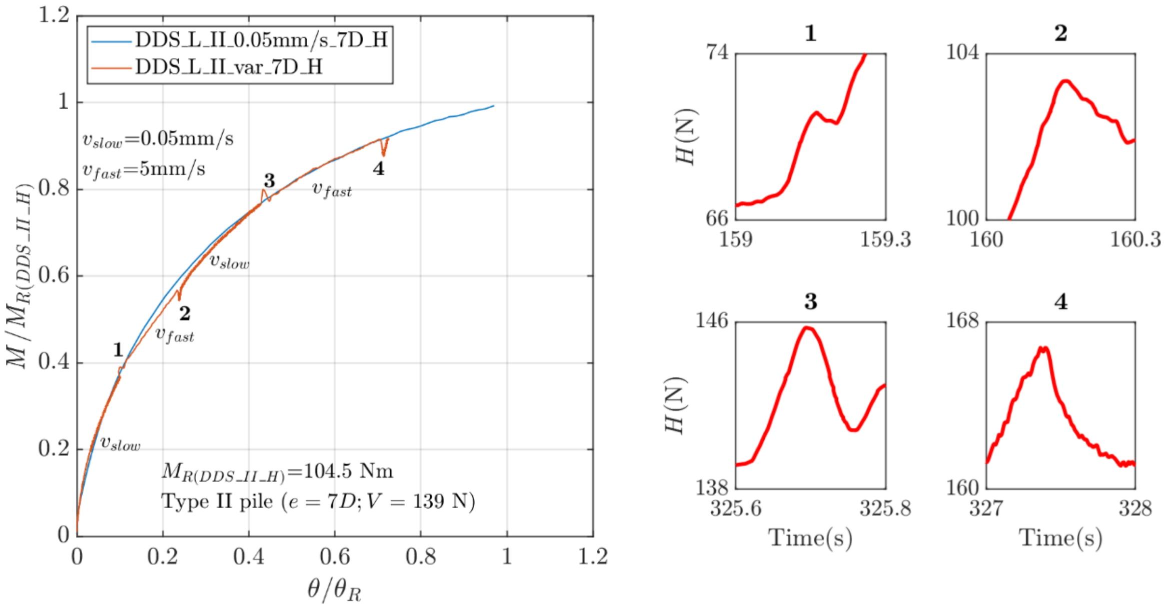

(a) (b)

Figure 3-14 Variable rate test in *dense* sand:

(a) normalised response; (b) transient loads due to acceleration and deceleration.

3.5.4 Inertial effects

The actuation system has been examined to quantify inertial effects (see Figure 3-15). In this configuration, a mass of 10 kg (similar to the pile weight) is added to the actuator. The maximum acceleration is 127 mm/s^2, and therefore, an additional inertial force (ΔV) of 1.27 N may occur during acceleration or deceleration. In this experiment, the actuation speed v started with 0.05 mm/s and then increased to 5 mm/s over a period of approximately 0.05 seconds, giving a transient increase in ΔV of 1.5 N. For the variable rate tests in dry sand, considering the pile weights V, an additional load of 0.9 N ~ 1.8 N is expected to occur during acceleration and deceleration, which agrees with the observations in Figure 3-13 (b) and Figure 3-14 (b). Thus, it can be concluded that the temporary load changes are due to inertial effects instead of rate or acceleration effects in the soil.

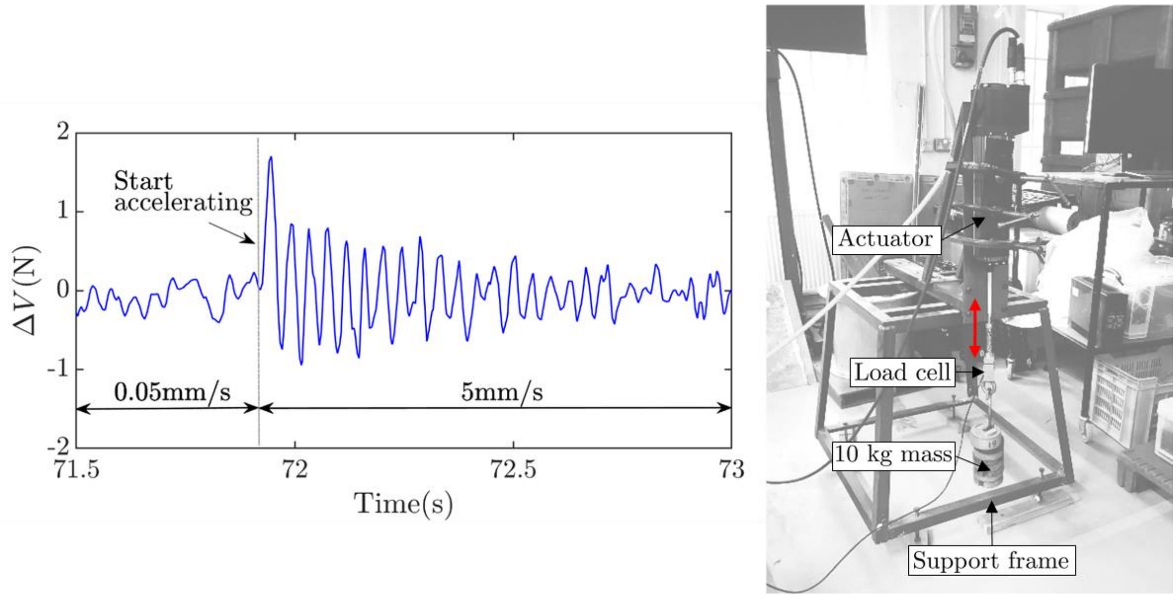

Figure 3-15 Evaluating inertial effects of the actuation system.

3.5.5 Summary of the pile response to monotonic lateral loading

In general, the responses of the model piles in dry sand to monotonic lateral loading are insensitive to the loading rate. With sudden changes in the actuation rate v, temporary loads are observed due to inertial effects induced by the actuation system instead of the soil skeleton response.

The PISA project reported rate effects on the piles embedded in the Dunkirk sand (McAdam *et al.*, 2020). Compared to the artificially made sand samples, the Dunkirk sand was formed in the marine environment, and fines content, cementation and potential suction effects can enhance the sensitivity to loading rate. However, it is not feasible to duplicate marine sand in the laboratory; further research is recommended to consider the influence of fines content on the mechanical behaviour of sand.

3.6 Pile response to one-way cyclic lateral loading at different frequencies

3.6.1 Load path

Figure 3-16 illustrates the load path for one-way cyclic lateral loading, which comprises three phases:

Phase I: Monotonic loading at a constant loading rate ($\dot{F}$) was applied until M reaches the target cyclic load magnitude, denoted as M_e, followed by unloading. $\dot{F}$ was 0.35 N/s during the initial loading and -0.35 N/s during the unloading.

Phase II: Sinusoidal cyclic loads at a frequency f of 0.01 Hz or 0.5 Hz were applied for 1000 cycles ($N = 1000$).

Phase III: Monotonic lateral loading ($\dot{F} = 0.35$ N/s) was applied until the pile rotation θ reaches θ_R to examine the post-cyclic response of a pile.

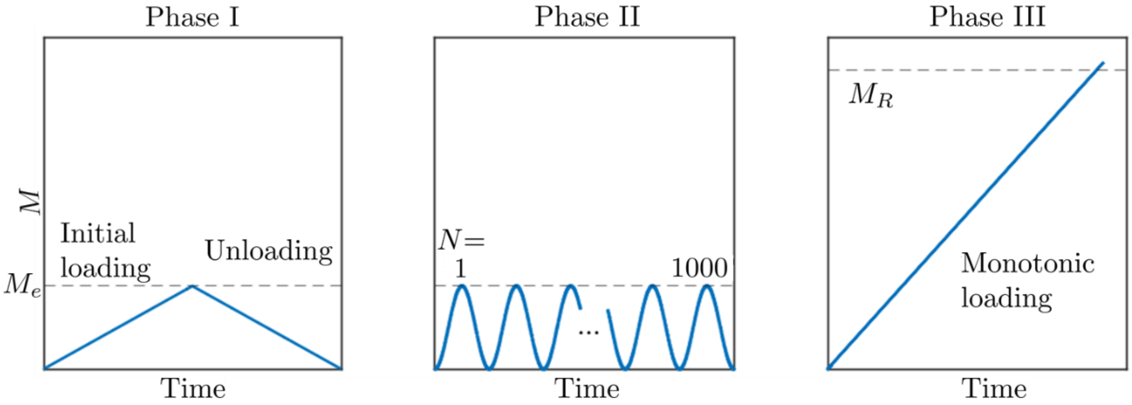

Figure 3-16 Load path for one-way cyclic lateral loading.

3.6.2 Key definitions for pile response to one-way cyclic lateral loading

The cyclic lateral loading response of the model piles is characterised using the procedure in Section 1.3, and the key definitions are given in Table 3-6. The $\sigma - \varepsilon$ domain extends to the moment-rotation ($M - \theta$) and horizontal load-displacement ($H - u$) domains for data interpretation. Pile secant stiffness k_N and energy loss per cycle η are described in the moment-rotation response. ζ_b is defined as the ratio of M_e over the reference moment capacity M_R.

Table 3-6 Cyclic definitions for pile testing.

Generic cyclic definitions	σ	ε	k_N and η	ε_N	ζ_b
Definitions for pile testing	M H	θ u	In the (M, θ) domain	θ_N u_N v_N	$\frac{M_e}{M_R}$

3.6.3 Very loose sand

In Figure 3-17, it can be seen that during the initial loading in Phase I, the two cyclic tests and the monotonic test show a similar pattern, and the impact of sample variations appears insignificant. During Phase II, permanent plastic pile movement occurs under cyclic loading, and soil rate dependency does not appear. Afterwards, during Phase III, data show that the ultimate capacity of the model pile does not reduce due to the cyclic loading. Instead, the pile response becomes slightly stiffer with a 5% higher capacity than the monotonic loading test. The possible reason is that the surrounding soil near the pile is densified under cyclic loading, slightly increasing soil resistance.

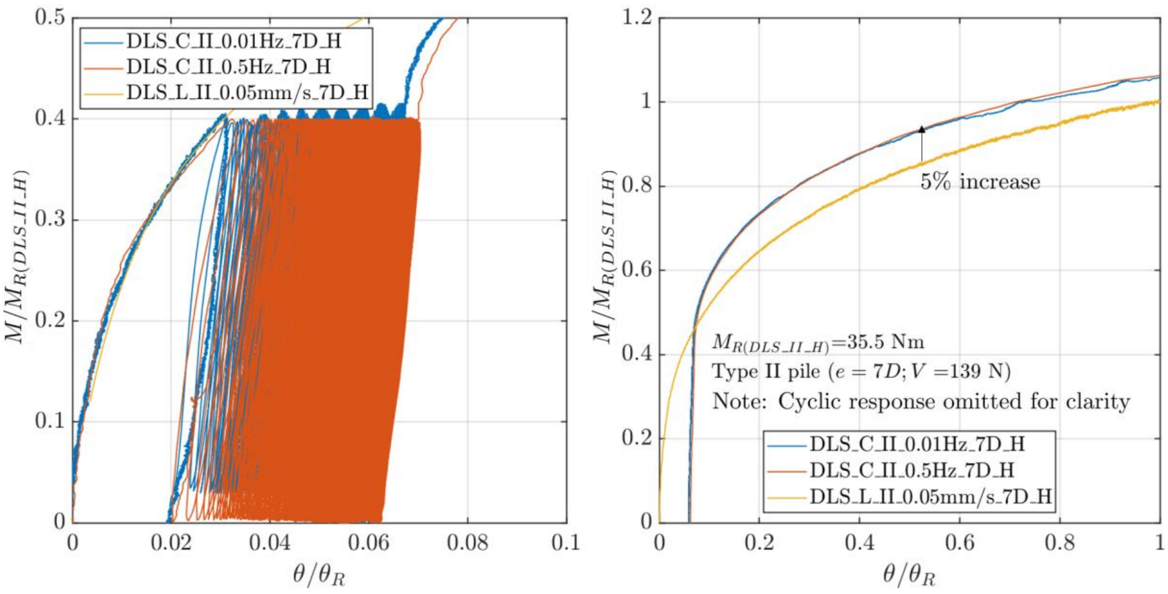

Figure 3-17 Normalised moment-rotation responses from the cyclic loading tests at different frequencies f in *very loose* sand.

The cyclic characteristics are shown in Figure 3-18. In general, both ratcheting and pile secant stiffness k are rate-insensitive. The rates of increasing θ and u with the cyclic loading do not vary with f. In addition, during cyclic loading, the pile tends to climb up (-v), but the amount of vertical movement is minimal relative to u. The hysteresis loops at different f are similar. k increases with the cyclic loading, along with η slightly decreasing. When N reaches 1000 cycles, k is nearly equal to k_{max}.

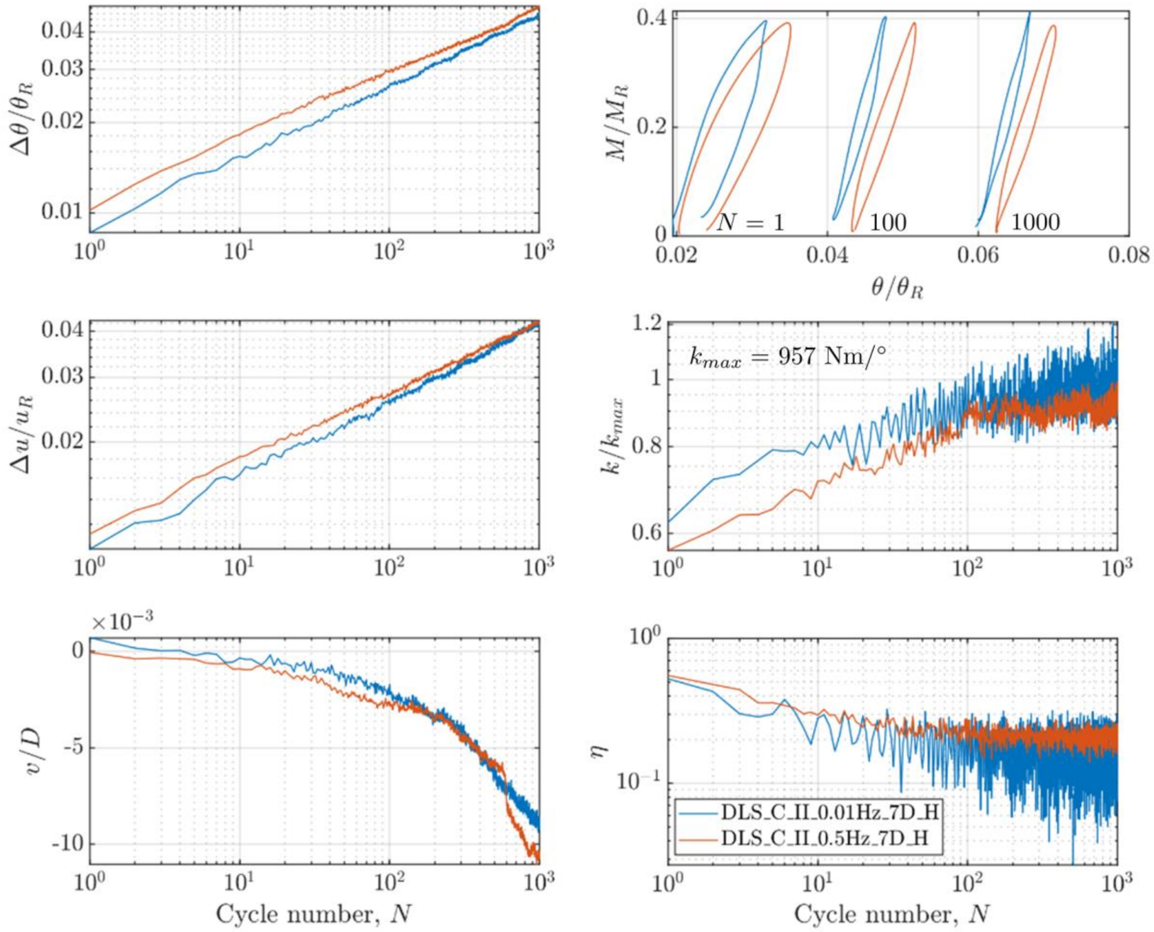

Figure 3-18 Cyclic characteristics of the cyclic loading tests at different frequencies f in *very loose* sand.

3.6.4 Dense sand

Figure 3-19 shows the normalised moment-rotation responses of the cyclic loading tests in *dense* sand ($\zeta_b = 0.25$; $f = 0.5$ Hz and 0.01 Hz). Similar to the *very loose* sand tests, rate effects are not observed during the cyclic loading (Phase II). During Phase III, the responses of the two cyclic loading tests and the monotonic test are almost identical, and M_R is not influenced by the cyclic loading.

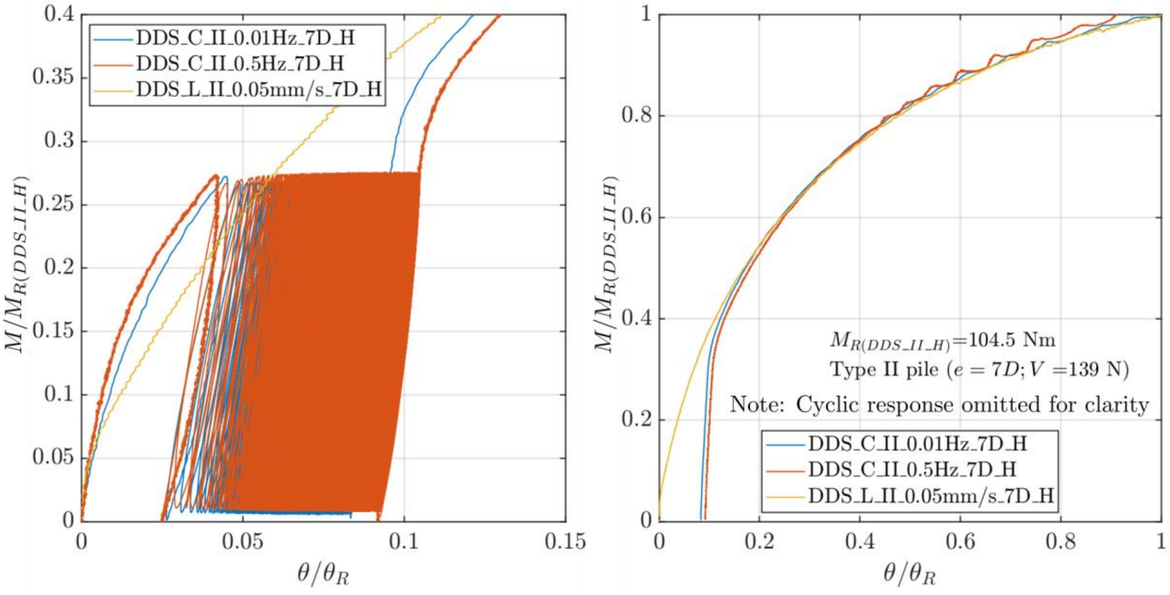

Figure 3-19 Normalised moment-rotation responses from the cyclic loading tests at different frequencies f in *dense* sand.

The cyclic characteristics are illustrated in Figure 3-20. Both tests have similar rates of increasing θ and u under the cyclic loading. At 0.01 Hz, the pile moves slightly downwards (-v), and there is no significant pile uplift at 0.5 Hz. k is also rate-independent and steadily increases with N; meanwhile, η decreases from 0.4 to 0.18 over 1000 cycles. The difference of k between the tests is due to sample variations and does not appear to influence pile capacity.

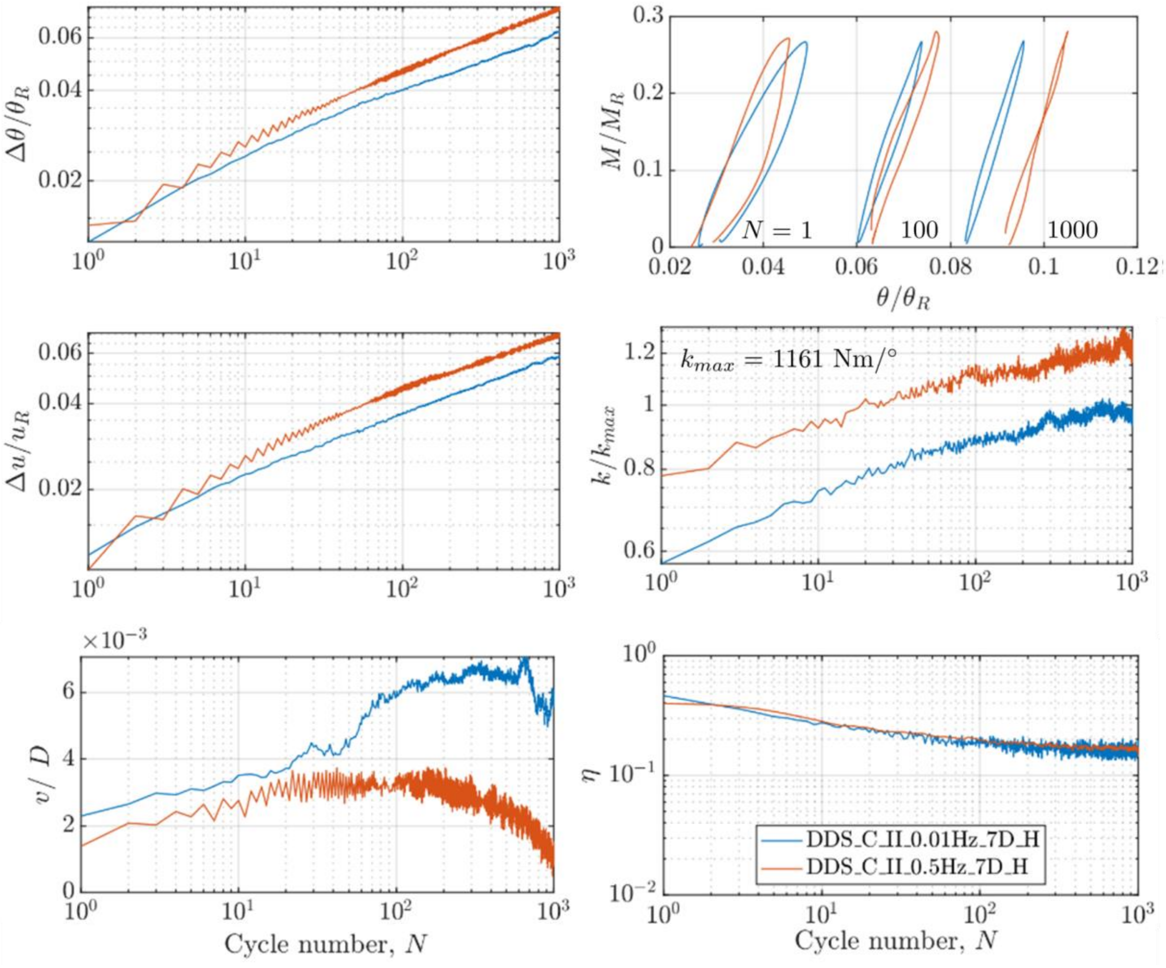

Figure 3-20 Cyclic characteristics of the cyclic loading tests
at different frequencies f in *dense* sand.

3.6.5 Quantifying ratcheting and pile secant stiffness

The rate of increasing pile rotation with the cycle number ($\Delta\theta_N$) can be fitted using a power law:

$$\frac{\Delta\theta_N}{\theta_R} = A \cdot N^{\beta} \qquad \text{Equation 3-3}$$

where A, β are constants. A controls the initial increment of $\Delta\theta_N$, and β represents the increasing rate of θ with N. This approach has been adopted in previous work, with good confidence in capturing the ratcheting rate of a monopile in sand (see, *e.g.* LeBlanc *et al.*, 2010; Abadie, 2015; Richards, 2019; Truong *et al.*, 2019).

LeBlanc *et al*. (2010) and Klinkvort and Hededal (2013) suggested that the evolution of pile secant stiffness (k_N) can be described using a semi-logarithmic relationship, which is expressed as

$$\frac{k_N}{k_{max}} = \frac{k_1}{k_{max}} + B \cdot \ln(N) \qquad \text{Equation 3-4}$$

where B determines the rate of k evolution.

Following the above equations, the ratcheting and pile secant stiffness responses in Figure 3-18 and Figure 3-20 are summarised in Table 3-7.

Table 3-7 Parameters for quantifying ratcheting and the pile secant stiffness.

Soil condition	ζ_b	f (Hz)	A	β	B
Very loose sand	0.4	0.01	0.0088	0.2385	0.0554
		0.5	0.0109	0.2149	0.0548
Dense sand	0.25	0.01	0.0162	0.1946	0.0623
		0.5	0.0175	0.2112	0.0660

3.6.6 Summary of the pile response to cyclic lateral loading

The experimental evidence indicates that the pile response to cyclic lateral loading in dry sand does not show rate dependency. Although only a small number of cyclic loading tests were conducted, sample variations were small, and data are repeatable. Ratcheting and pile secant stiffness also appear to be rate-insensitive. It is found that pile capacity does not reduce due to cyclic loading, which agrees with previous experimental findings by Richards (2019). In *very loose* sand, pile capacity slightly increases by 5% after the cyclic loading compared to the monotonic loading test, which may be due to densification induced by the cyclic loading.

3.7 Pile responses to various vertical loads

3.7.1 Vertical loading on full-scale OWT monopiles in sand

Typical vertical loading on a full-scale monopile is analysed using an illustrative example below. A 3.5-5 MW OWT with a structural weight of approximately 6 MN to 10 MN (Byrne and Houlsby, 2015) and a monopile with $D = 4$ m, $L/D = 4$ and the wall thickness $t = 130$ mm are considered. The weight of the monopile is approximately 2 MN, which gives the total vertical load V of 8 MN to 12 MN. The ultimate vertical bearing capacity (V_u) is estimated using the β method recommended in the design guidance *API 2A-WSD* (API, 2007). V_u may be expressed as

$$V_u = \int_0^L \beta\gamma' z\pi(2D - 2t)\ dz + A_b N_q \gamma' L \qquad \text{Equation 3-5}$$

where β is the shaft friction factor ($\beta = 0.29$ (medium sand) to 0.46 (dense sand)), A_b is the area of the pile steel annulus, and N_q is the end bearing factor ($N_q = 12$ (medium sand) to 40 (dense sand)). Considering that the pile is embedded below the seabed, the effective unit weight of soil γ' is assumed to be 10 kN/m^3. Following the above equation, the ratio of V/V_u is found to fall in a range between 0.25 and 0.83, depending on the soil density and strength properties.

Li *et al*. (2022) conducted laterally-loaded model monopile tests using the centrifuge under 1-g and 100-g, as illustrated in Figure 3-21. Within the range of V/V_u in the illustrative example, pile capacity becomes greater with the increase in V. Following this, experimental investigations into the impact of vertical loading on the lateral pile response are illustrated below.

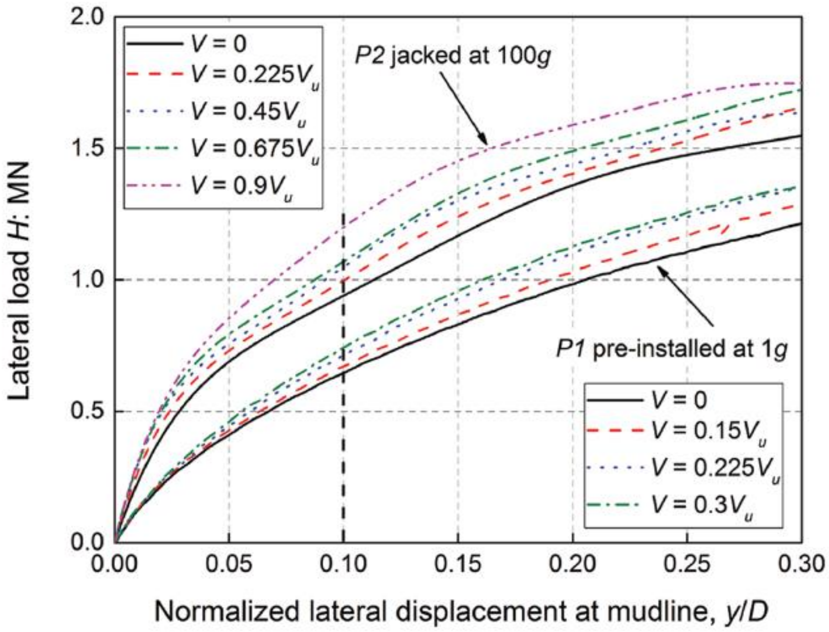

Figure 3-21 Influence of vertical loading on the lateral response of a monopile in sand (V_u: vertical load capacity) (Li *et al*., 2022).

3.7.2 Very loose sand

Figure 3-22 shows the responses of piles under various V in *very loose* sand. It is assumed that the surrounding soil around the model pile is densified during installation. Thus, the ultimate vertical bearing capacity V_u of the model pile in *very loose* sand is approximately 167 N, following Equation 3-5 for medium sand. The range of V/V_u is between 0.41 and 0.83, which is close that for full-scale OWT monopiles. Similar to Li *et al*. (2022), it is evident that increasing vertical loading can lead to a stiffer pile response and higher pile capacity.

Figure 3-22 (b) shows that the rotation-horizontal displacement responses from these tests are similar, and the pile pivot position does not change significantly with vertical loading. Also, as the pile is rigid, the effect of pile distortion is minimal, and thus, the lateral soil deformation response is unlikely to change with V. Therefore, the additional resistance mobilised with the increasing vertical loading may be principally contributed by base resistance.

A monotonic test from Richards (2019) is compared with the monotonic tests under various V (see Figure 3-22 (a)). Because a different test setup is adopted in this research, it is not feasible to reproduce Richards' test ($V = 49$ N; $e = 10D$). The V/V_u ratio in Richards' test is approximately 0.29, within the range for full-scale monopiles, while the tests performed in this research have higher V/V_u values due to the rig design. Although Richards' test was conducted with a higher loading point, the pile response is softer and has a lower capacity than the other tests due to a light weight being applied. Load eccentricity effects are further discussed in Section 3.8.

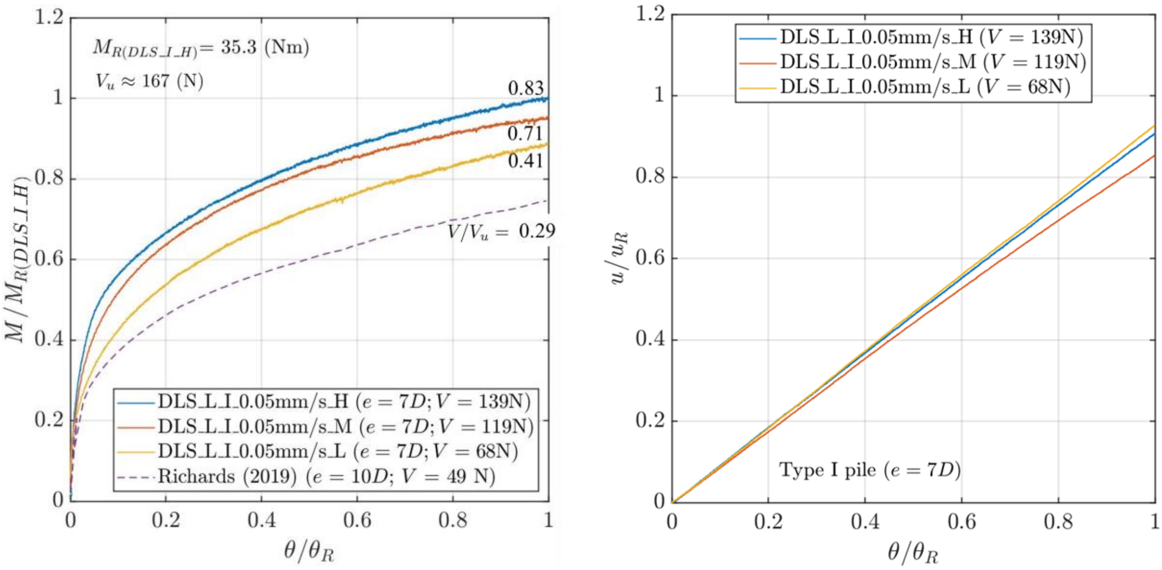

(a) (b)

Figure 3-22 Various vertical loading applied on piles in *very loose* sand: (a) normalised moment-rotation response; (b) normalised horizontal displacement-rotation response.

3.7.3 Dense sand

Although the beneficial influence of vertical loading in *very loose* sand is reported, this phenomenon does not appear in *dense* sand (see Figure 3-23). Following Equation 3-5, the ultimate vertical bearing capacity V_u of the model pile is found to be around 330 N. For the model pile in *dense* sand, the resistance on the pile shaft may be sufficient to resist the vertical load V, and therefore, base resistance does not appear to change with V in the range between 119 N and 139 N. If a greater vertical load could be applied to achieve a high V/V_u ratio, pile capacity might increase accordingly.

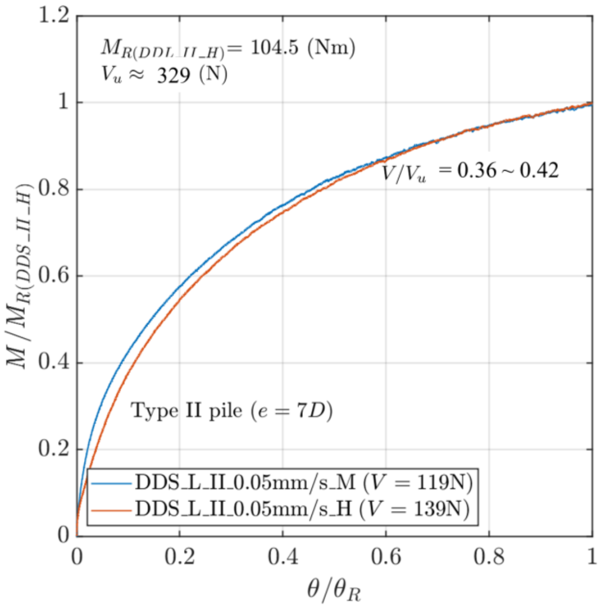

Figure 3-23 Various vertical loading applied on piles in *dense* sand.

3.7.4 Summary of the influence of vertical loading on the lateral pile response

The experimental evidence shows that increasing vertical loading can improve the lateral pile response in *very loose* sand. This beneficial phenomenon may occur in *dense* sand, but the range of experiments was too limited.

It is noticed that the range of vertical loads V applied to the model piles may not reflect precisely the load conditions of full-scale monopiles. Unfortunately, due to the restrictions of the test setup, vertical loading could not be appropriately scaled from the field to the laboratory.

3.8 Pile responses at various load eccentricities

3.8.1 Constant load eccentricity tests

During OWT operation, the load eccentricity e varies with time due to the interactions between wind, waves and turbine excitations. Klinkvort and Hededal (2014) explored load eccentricity effects on monopiles in sand through centrifuge modelling. From their results (see Figure 3-24), it is found that the horizontal load-displacement response of a pile becomes stiffer if e is lower. As discussed in Section 3.4, load eccentricity effects are also observed during the initial loading.

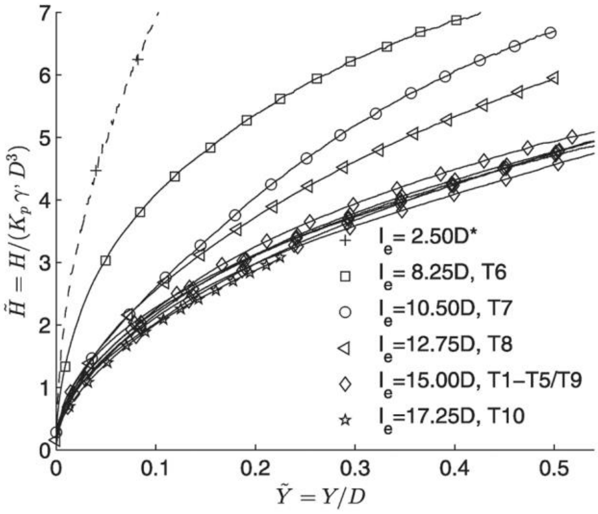

Figure 3-24 Horizontal load-displacement responses at different load eccentricities e in sand (Klinkvort and Hededal, 2014).

Following the above experimental findings, a series of constant load eccentricity tests at $e = 3D$, $7D$ and $20D$ were carried out to large displacement. Both moment-rotation and horizontal load-displacement pile responses in *very loose* and *dense* sand are illustrated in Figure 3-25 and Figure 3-26, respectively. Similar to Klinkvort and Hededal (2014), the horizontal load-displacement response becomes stiffer with decreasing e. On the other hand, the moment-rotation response shows an inverse trend—the moment capacity increases with e. Modelling of different e is shown in Figure 6-9 and Figure 6-10, with further analysis through theoretical development in Chapter 6.

In Figure 3-25 and Figure 3-26, the rotation-horizontal displacement responses at different e demonstrate a similar trend. As discussed in Section 5.2.3, for a rigid pile in sand under the ultimate state, lateral soil stress and base reactions provide resistance against lateral loading. From the data, the pivot position does not hugely change with e, except for the *very loose* sand test at $e = 7D$ due to sample variations. Lateral soil stress distribution may remain the same, while base shear resistance may be more sensitive to e. Following the framework in Section 5.2.3, with the increase in base shear, moment capacity becomes greater, but horizontal load capacity tends to reduce.

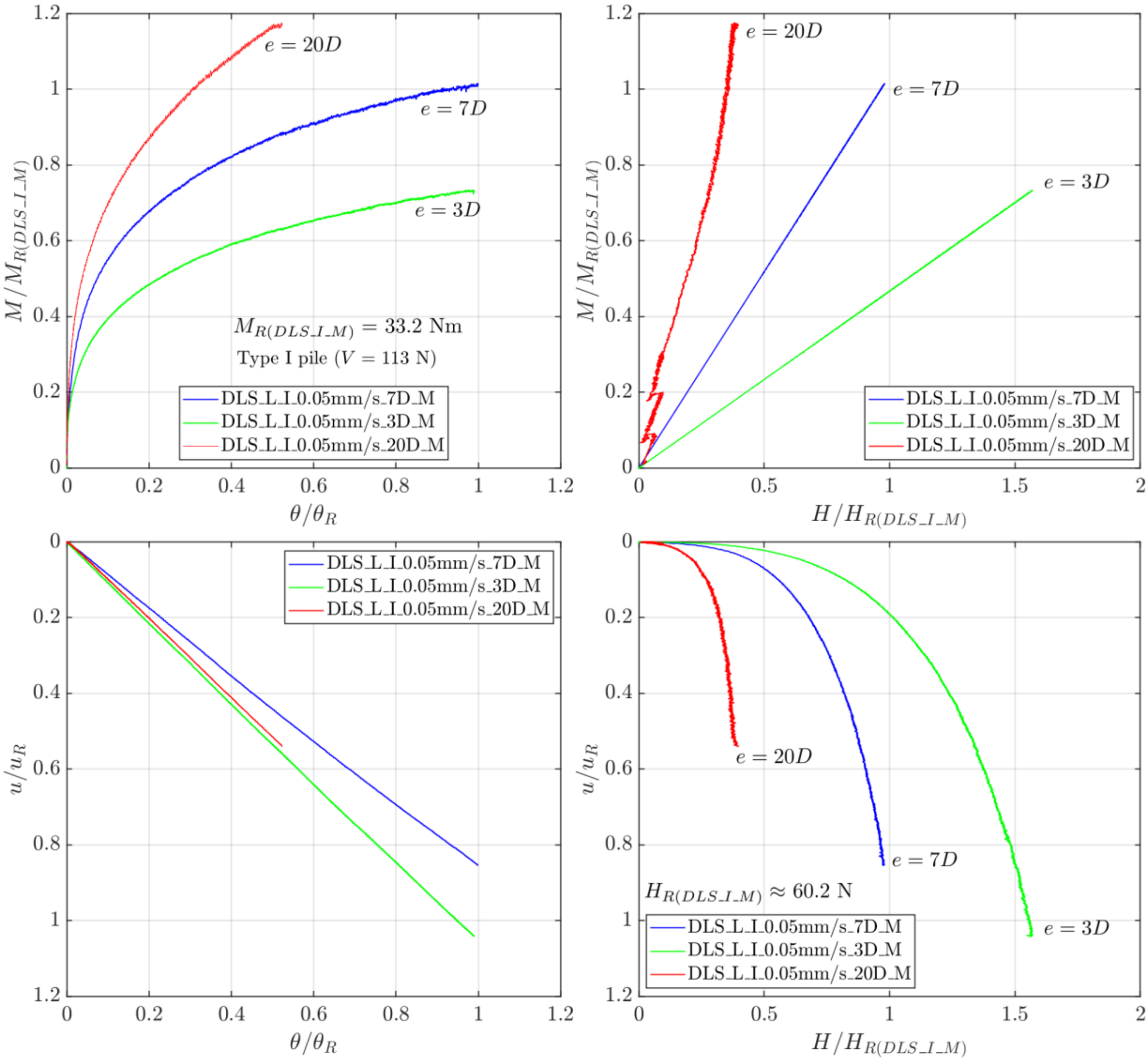

Figure 3-25 Constant load eccentricity tests in *very loose* sand.

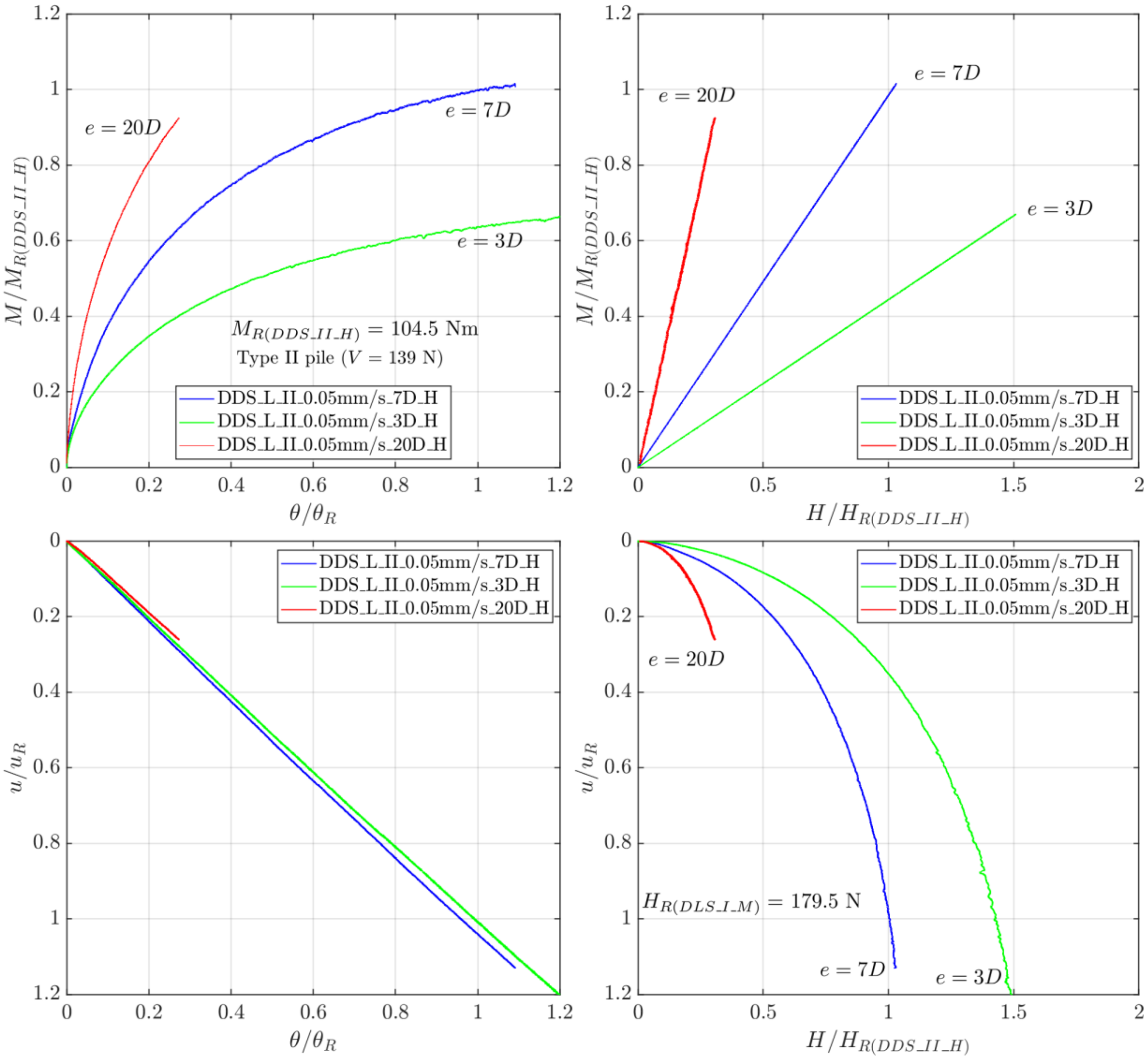

Figure 3-26 Constant load eccentricity tests in *dense* sand.

The results in Figure 3-25 and Figure 3-26 are then expressed in terms of normalised capacities M/M_R and H/H_R. M_R and H_R are obtained individually for each test, and the response at $e = 20D$ are estimated. In Figure 3-27, it can be seen that the normalised M/M_R and H/H_R responses at different *e* seem to be almost identical. Therefore, it is possible to estimate pile responses with other fixed loading points using these normalised relationships.

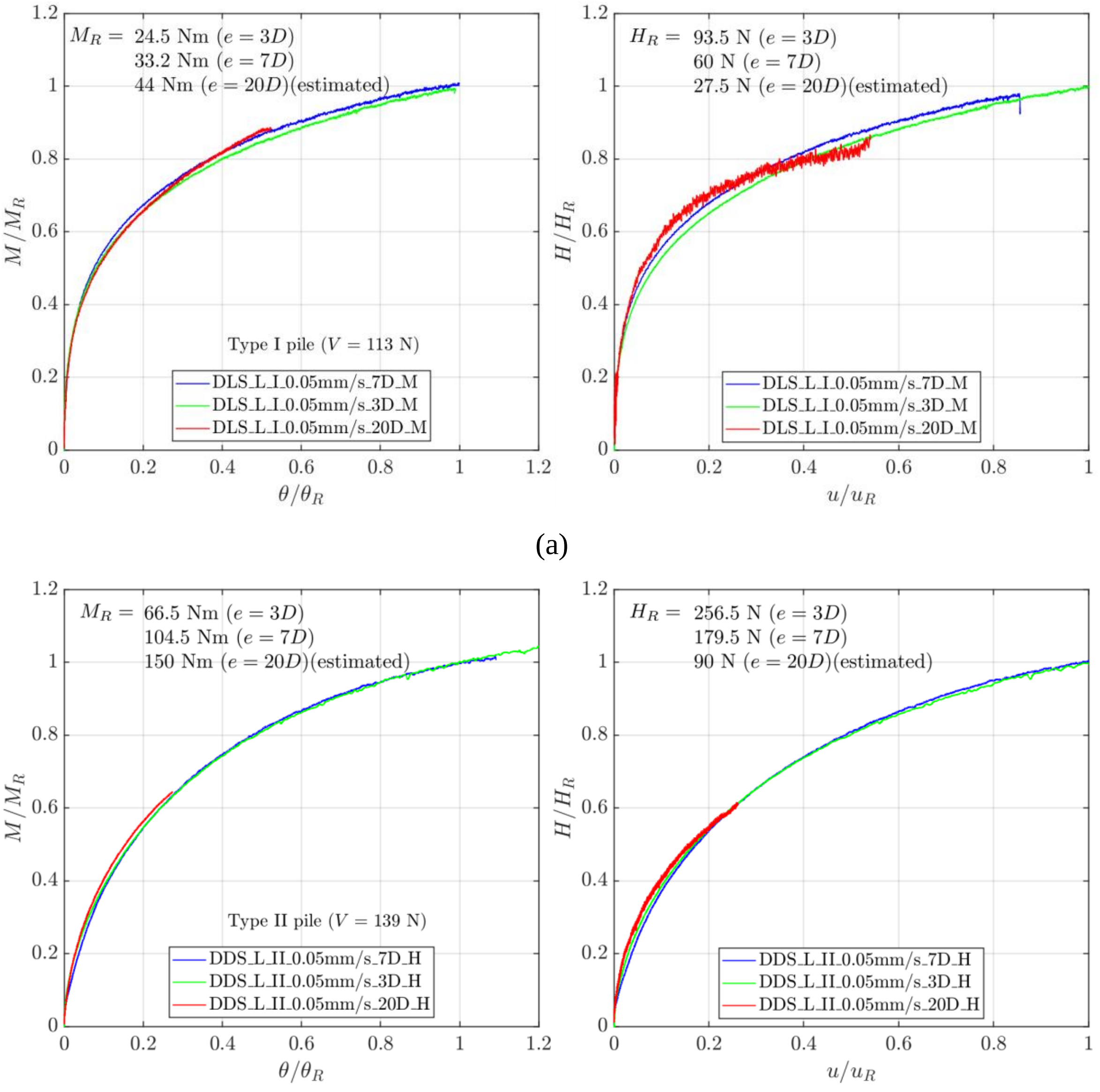

(a)

(b)

Figure 3-27 M/M_R and H/H_R responses: (a) *very loose* sand; (b) *dense* sand.

3.8.2 Time-varying load eccentricity tests

Two example tests were undertaken to investigate the impact of time-varying load eccentricity on pile response. The load inputs are shown in Figure 3-28. H_1 and H_2 are the applied loads for the two actuators, and the resultant horizontal load H is shown dashed. As pile response in dry sand is rate-insensitive, the actuation rate v is not specified in these tests.

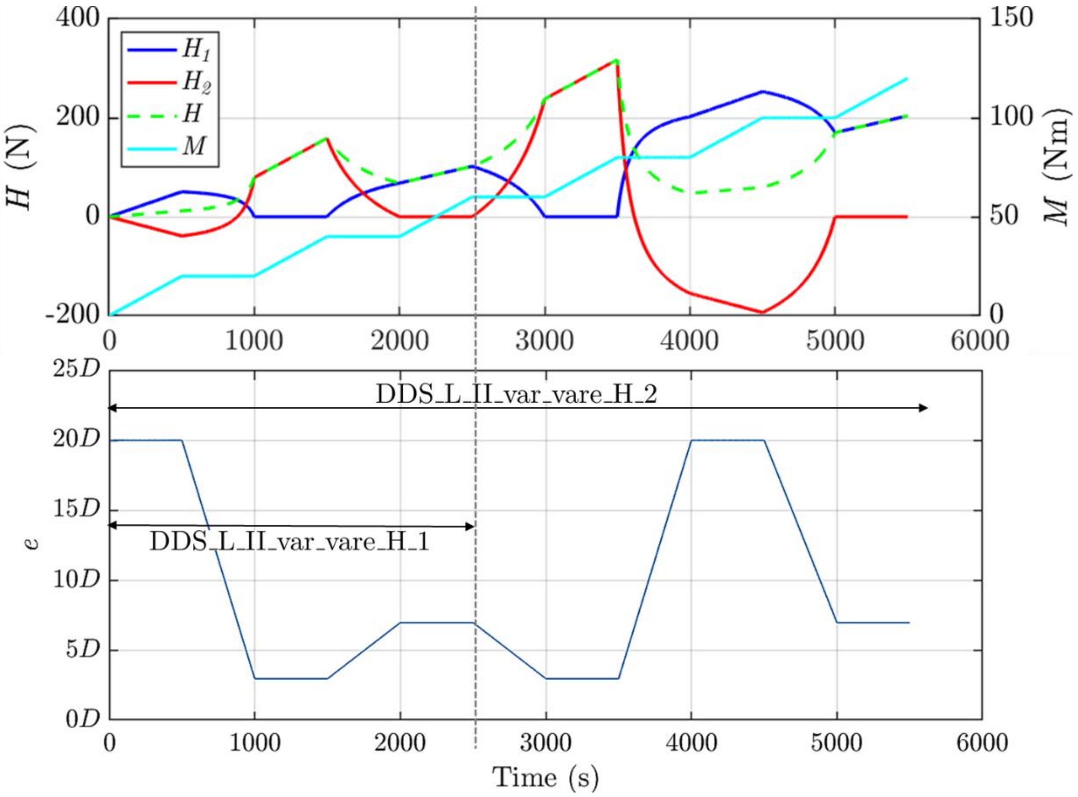

Figure 3-28 Load inputs for the time-varying load eccentricity tests.

In test DDS_L_II_var_vare_H_1, e started at $20D$ for the first 500 s and then decreased to $3D$ during 500 s ~ 1000 s. From 1500 s to 2000 s, e increased to $7D$ and remained constant until the end of the test. M increased at a rate of 0.04 Nm/s and remained fixed during the changes in e.

In test DDS_L_II_var_vare_H_2, from 0 s to 2500 s, the load input was the same as DDS_L_II_var_vare_H_1. After 2500 s, e changed between $3D$ and $20D$, and M increased at the same rate of 0.04 Nm/s and remained constant when e was varying. In order to achieve the specified loading, the actuators may travel in opposite directions, applying an extra bending moment to the model pile. The maximum bending moment induced by the two actuators has minimal influence on the pile response, and the pile can be treated as rigid.

Figure 3-29 shows the responses from the two example tests, from which it can be seen that the small displacement responses are seen to be approximately identical. The influence of sample variations is considered small. Compared to the constant load eccentricity tests, there is no unique load eccentricity response, and the previous loading history can influence the consequent response. The rotation-horizontal displacement response does not significantly change with e.

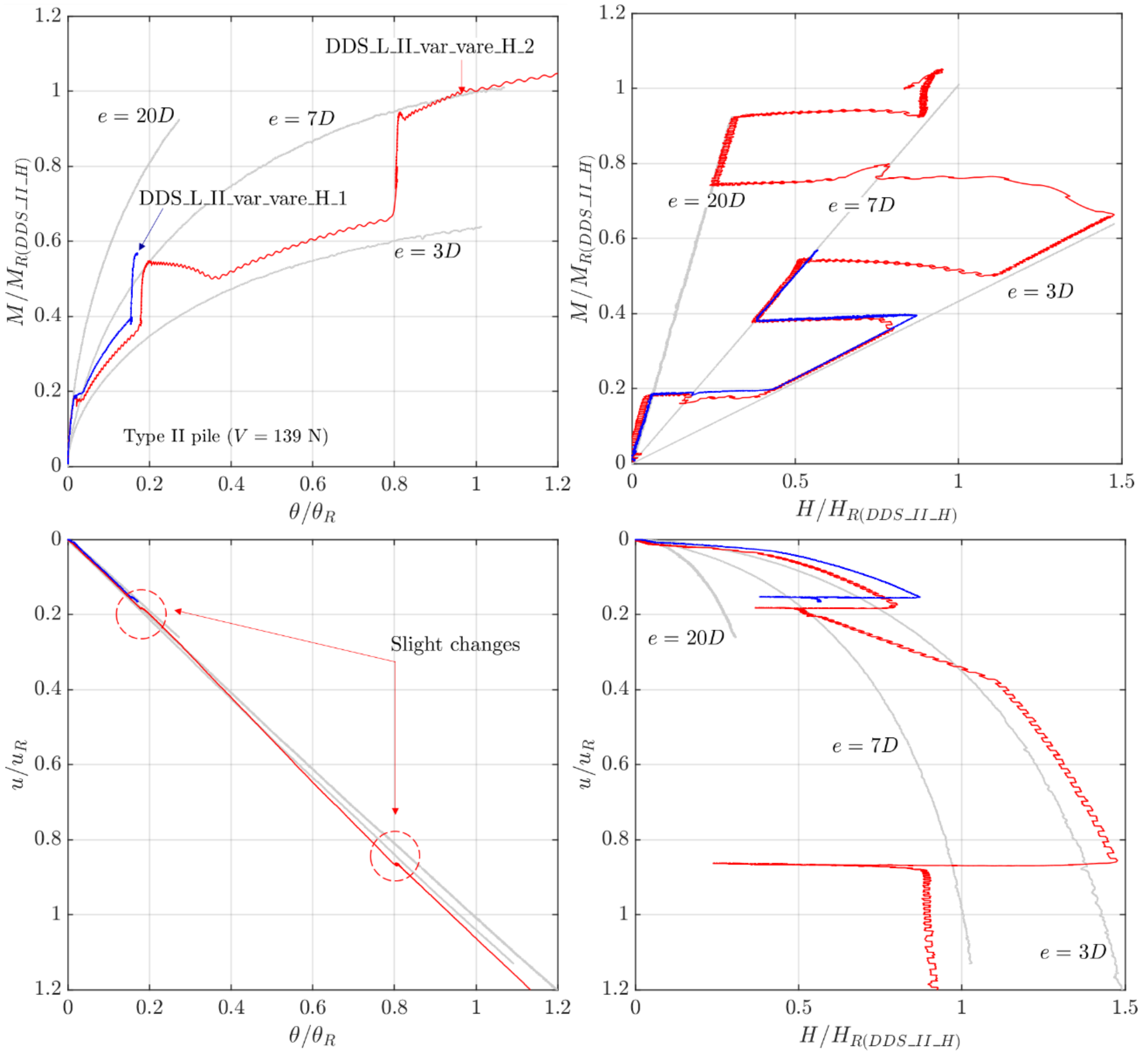

Figure 3-29 Responses of the time-varying load eccentricity tests.

3.8.3 Summary of load eccentricity effects

With the increase in the load eccentricity e, the moment-rotation response becomes stiffer, while the horizontal load-displacement response shows an inverse trend. The time-varying load eccentricity tests do not show a unique load eccentricity response, and the previous loading history may need to be analysed to capture the subsequent pile response.

Load eccentricity effects are complex and may be explained through theoretical analysis using a yield surface approach, which captures the coupled moment-horizontal load response. Details of theoretical development for load eccentricity effects are discussed in Chapter 6.

3.9 Pile uplift under lateral loading

3.9.1 Mechanism

Noticeable pile uplift may occur for the laterally-loaded model piles. As the pile rotates, sand particles beneath the pile may migrate and force the pile to move upwards under low-confining stress on the laboratory floor. This phenomenon was also observed by Richards (2019). Other factors influencing the tendency of pile uplift include the pile geometry, vertical loading and soil density.

3.9.2 Effect of the pile geometry

The amount of pile uplift is influenced by the pile geometry. If the pile wall thickness t is too large relative to the soil particle size, the pile rim may not push into the sand; instead, the pile may tend to climb upwards. For example, Figure 3-30 compares the monotonic responses of Type I and II piles in *very loose* sand. The configurations and capacities of these two tests are identical, and their pile geometries are only slightly different (see Figure 3-10). The data show that the Type I pile is more likely to move upwards than the Type II pile due to the geometry of the pile. In Table 3-2, it can be seen that the t/D_{50} ratio of the Type I pile is greater than that of the Type II pile, and therefore, soil particle size effects become more evident.

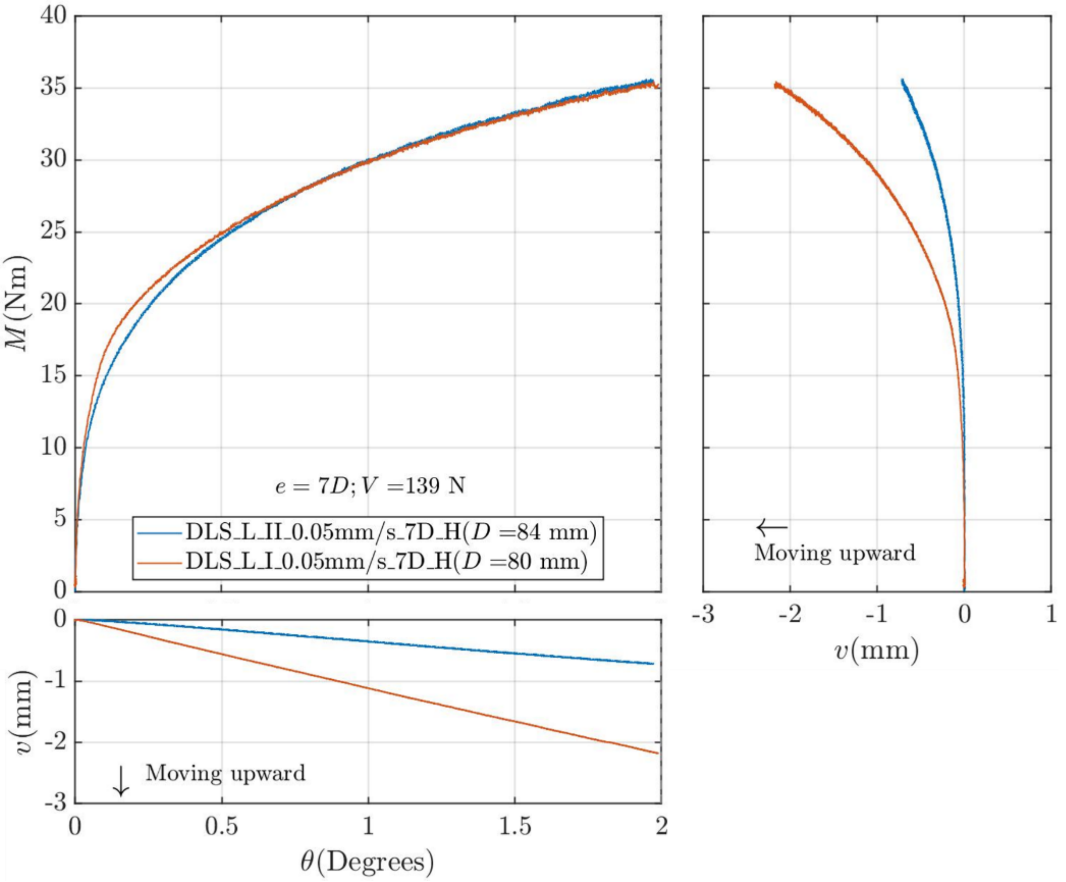

Figure 3-30 Pile uplift responses of Type I and II piles.

3.9.3 Effect of the vertical load

Richards (2019) suggests that increasing vertical loading may suppress the tendency of pile uplift. As illustrated in Figure 3-31, two monotonic tests were undertaken in *dense* sand with different vertical loads V to demonstrate pile uplift response. The amount of uplift decreases by 65%, with the increase in V by 17%.

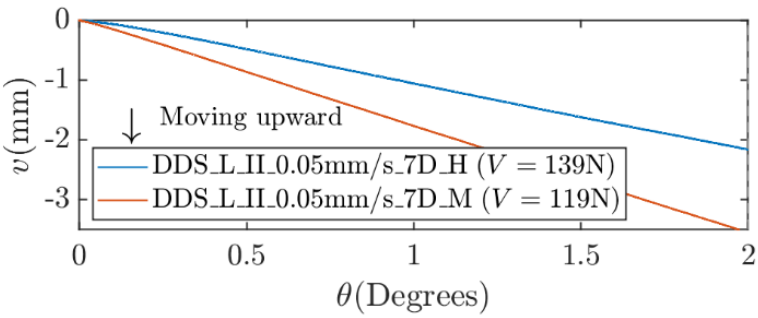

Figure 3-31 Comparison of piles with different vertical loads.

3.9.4 Effect of the soil density

Figure 3-32 shows that pile uplift in *dense* sand is more evident than in *very loose* sand due to soil dilation. However, this phenomenon may not be found in centrifuge testing, in which the tendency of dilation reduces with the increase in the effective stress and gravity, according to Bolton's theory (1986).

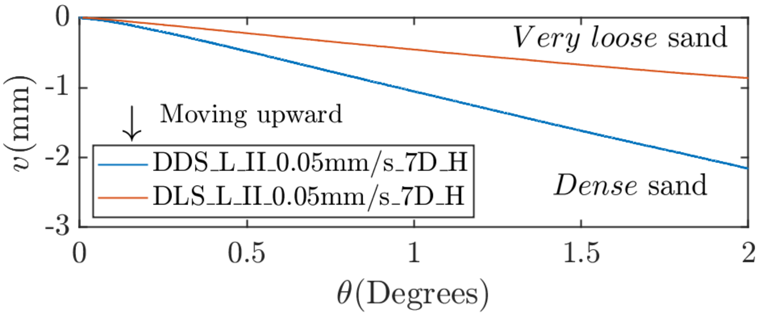

Figure 3-32 Comparison of pile responses in different soil relative densities.

Pile uplift is approximately proportional to θ, which can be interpreted as a vertical movement of the pile rotational point. The slopes of $v - \theta$ for *very loose* sand and *dense* sand are -0.0054D and -0.0128D, respectively.

3.9.5 Summary of pile uplift under lateral loading

Pile uplift occurs in laboratory-floor testing when the model piles are subject to lateral loading. However, this phenomenon may not be seen in a full-scale monopile as the pile shaft may provide sufficient resistance to suppress the tendency of uplift. Furthermore, the amount of vertical movement is less than 4% of the pile diameter, which is unlikely to influence pile response to lateral loading. This thesis compares various test configurations, and factors influencing pile uplift have been identified based on the experimental observations. These factors include the pile geometry, vertical loading and soil relative density.

3.10 Concluding remarks

The test programme involving dry sand provides reliable experimental data to aid the development of theoretical models. Furthermore, experimental observations can broadly reflect the response of full-scale monopiles in dry sand by adopting appropriate scaling techniques. The test results are summarised as follows:

(1) Pile response to monotonic lateral loading in dry sand is almost rate-independent.

(2) Gapping was not found on the active side of the pile but was observed in the PISA field testing in dense marine sand at Dunkirk, France (McAdam *et al*., 2020).

(3) Transient loads were recorded during the rate changes in the variable rate tests. These responses are due to inertial effects induced by the actuation system and not because of soil skeleton effects.

(4) Pile response to cyclic lateral loading in dry sand does not show rate dependency in ratcheting or pile secant stiffness.

(5) Pile capacity in dry sand does not decrease due to cyclic loading, in agreement with the experimental findings by Richards (2019). In *very loose* sand, pile capacity was found to increase by 5% post cyclic loading, possibly due to densification.

(6) Increasing vertical loading can enhance pile capacity in *very loose* sand as shear resistance at the pile base increases. This beneficial influence is also reported in the literature (*e.g.* Li *et al*., 2022) but was not confirmed in the *dense* sand tests at low V.

(7) Pile responses under constant and time-varying load eccentricity are investigated. The coupled moment-horizontal load response is complex and needs to be explained through a yield surface approach, which is discussed in Section 6.3.2.2.

(8) Pile uplift response is influenced by the pile geometry, vertical loading and soil density.

As the testing was undertaken on laboratory-scale model piles, there are some limitations and challenges:

(1) The global response of a pile is modelled, but local soil-pile interactions cannot be detected due to the pile size.

(2) Due to the pile geometry, soil particle size effects may enhance pile uplift response. Excessive vertical movement may be seen if the pile geometry is inappropriate, but this influence appears to be minimal for full-scale monopiles, which have large t/D_{50} and D/D_{50} ratios.

(3) Precise scaling the vertical loading is not feasible due to the test setup. The applied loads on the model piles are below the ultimate vertical capacity, but the load ratios H/V may not reflect full-scale monopile response.

(4) The influence of fines content on pile response needs to be further investigated.

4 Model testing in saturated stiff clay

4.1 Introduction

For physical modelling in clay, soil samples are typically prepared in the laboratory using a consolidation chamber (*e.g.* Bhattacharya *et al*., 2011; Lau, 2015) or a geotechnical centrifuge (Guevara *et al*., 2020) to produce a depth-varying strength profile. However, these preparation methods may take several weeks and are usually physically demanding. Moreover, soil strength is often low and, therefore, cannot simulate realistic offshore wind farm soil conditions.

A novel idea of “bringing the laboratory to the field” was proposed in this research. A mobile laboratory was built for model testing at a stiff clay site instead of using artificial clay samples. The site is located at Cowden, East Yorkshire, England. The soil is a naturally formed, heavily over-consolidated glacial till, broadly representative of multiple offshore wind farm ground conditions in the North Sea (*e.g.* Le *et al*., 2014). This approach is rarely adopted in laboratory-scale model testing but can address the difficulties of obtaining high-strength clay. Primary results from the model tests are reported in Wu *et al*. (2022a).

This chapter reports the model test design and experimental findings at Cowden. Soil rate dependency, cyclic pile response and load eccentricity effects were explored. The magnitude of rate effects under monotonic lateral loading and cyclic characteristics (*e.g.* ratcheting and pile secant stiffness per cycle) are quantified. Additionally, the pile pivot point and gapping were recorded to inform potential future work in detailed numerical modelling. For instance, Zdravkovic *et al*. (2020b) suggested that pile gapping needs to be considered in finite element analysis, including the influence of tension cut-off, to model monopile behaviour more precisely.

4.2 Design of the test programme

4.2.1 Test site

The site (53°50'29.0"N, 0°07'11.9"W) is shared with the PICASO project (Byrne *et al*., 2020a) and is close to the previous PISA Cowden site (see Figure 4-1). The ground conditions of both sites are similar. Detailed soil characterisation for the PISA site can be found in Zdravkovic *et al*. (2020a), Byrne *et al*. (2020b) and Ushev and Jardine (2022a, 2022b). The test site for the laboratory-scale testing was north of the PICASO test site. The PICASO project aims to investigate monopile response to cyclic lateral loading through medium-scale field testing on 1.22 m and 2.5 m diameter piles with aspect ratio L/D of 3 and eccentricity e of $4D$ (Byrne *et al*., 2020a). Data from the PICASO pile testing will be compared with data from the laboratory-scale testing to study scaling effects.

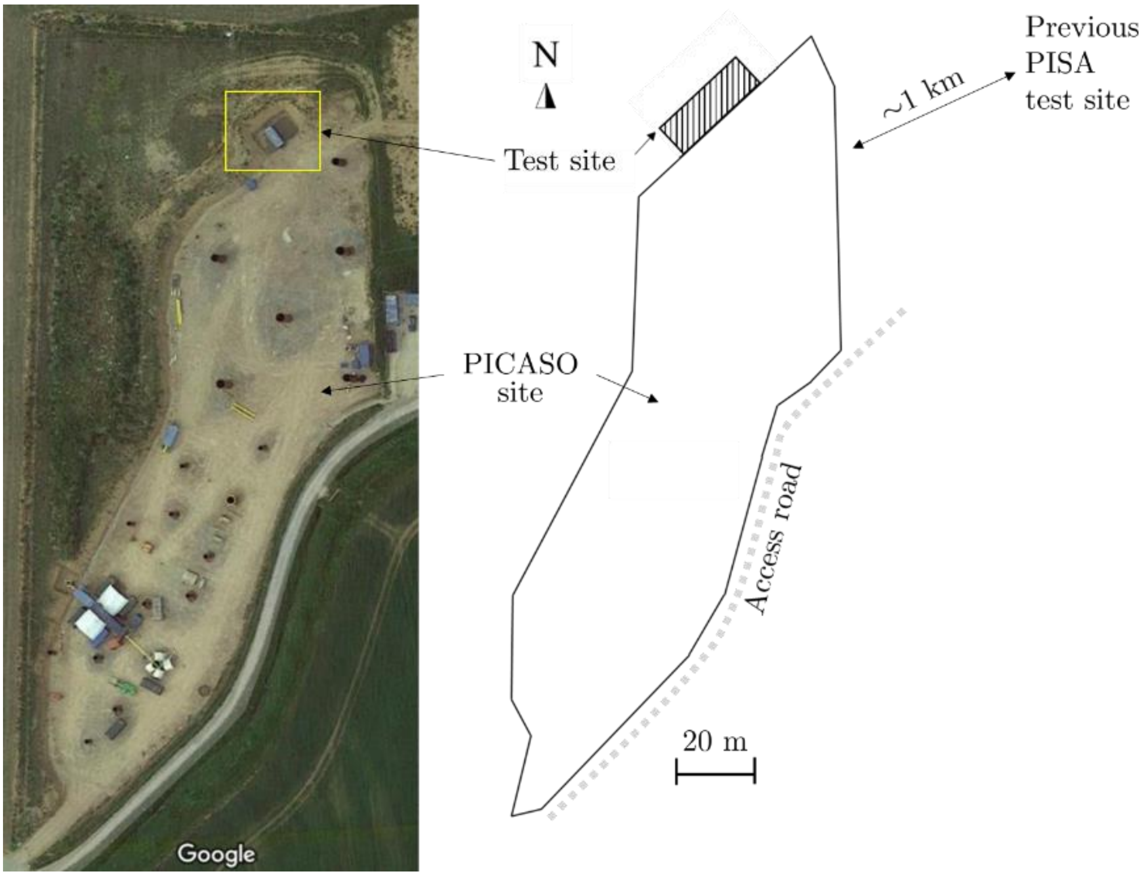

Figure 4-1 Site layout (satellite image retrieved from Google Maps on 01/08/2022).

Figure 4-2 shows the mobile laboratory for the laboratory-scale testing in the Cowden stiff clay. A shipping container was modified into a test cabin with an opening cut into the floor to access the ground and a bespoke grillage anchored to the ground to secure the loading rig. The grillage and rig were isolated from the test cabin to prevent disturbance. The area of the test site is approximately 300 m^2 (10 m × 30 m), in which 50 model tests were conducted. In addition, several tube and block samples were retrieved for laboratory soil element tests. The test area was excavated by approximately 3 m to reach the groundwater level. The water level was maintained during the test campaign to keep the clay saturated.

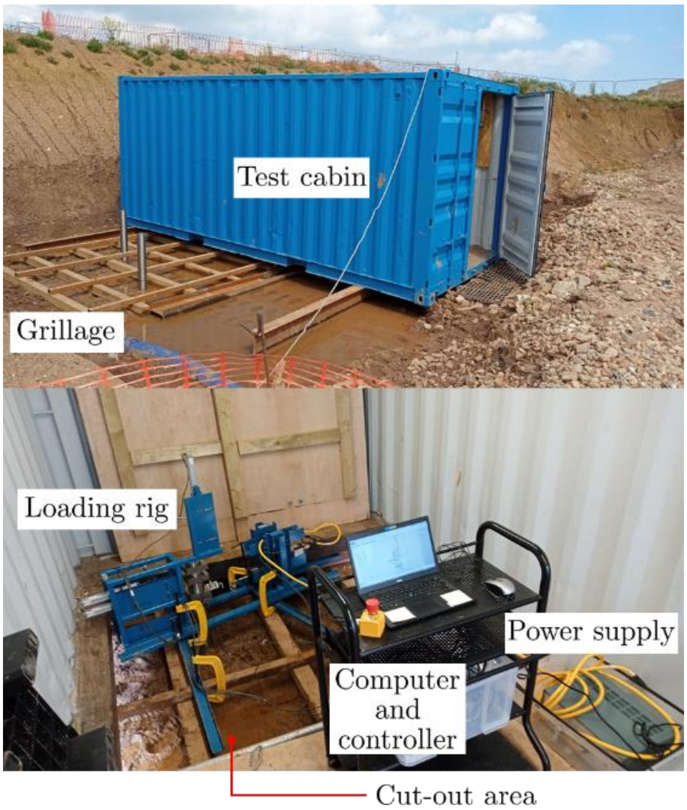

Figure 4-2 On-site mobile laboratory for the experimental work at Cowden.

4.2.2 Soil characterisation

Soil properties of the stiff clay at Cowden are given in Table 4-1. The soil strata is principally composed of a brown, heavily over-consolidated glacial till, with gravel and cobbles being frequently encountered in the soil matrix (see Figure 4-3). Index properties were obtained using soil samples from neighbouring boreholes at the PICASO test site. Several undrainedunconsolidated triaxial compression tests were performed using 38-mm-diameter thin-walled tube samples retrieved from the test site (the height-to-diameter ratio is 2). The triaxial apparatus Digital Tritest 50 by ELE was used. For each triaxial test, the undrained shear strength s_u was determined at approximately 10% ~ 15% strain (ε) when the peak strength occurred under the strain rate $\dot{\varepsilon}$ of 1.3% ε per minute. The near-surface soil (*i.e.* the top 50 mm ~ 150 mm) was found to be softened due to post-excavation swelling, with higher moisture content and lower bulk unit weight. Along with the element test data, 30 vane shear tests (VSTs) were carried out in the field. However, the VST measurements vary considerably and may not be accurate enough for detailed soil characterisation.

Table 4-1 Soil properties of the Cowden till.

Depth (mm)	s_u (kPa)	Moisture content (%)	Bulk unit weight (γ) (kN/m^3)
50 – 150 (0.5D – 1.5D)	26.9 – 35.0	18.2 – 23.2	19.1 – 20.4
200 – 300 (2D – 3D)	80.0 – 95.0 (68.0 – 140.0 from VSTs)	15.6 – 17.7	20.5 – 21.4

Liquid limit (LL) (%)	Plastic limit (PL) (%)	Plasticity index (PI) (%)
35	17	18 (medium plasticity)

Figure 4-3 Appearance of the Cowden stiff clay.

A small number of triaxial compression tests were undertaken at variable $\dot{\varepsilon}$ between 1.3% ε per minute and 6.5% ε per minute to quantify the magnitude of rate effects η_{10} at the element scale. The clay exhibits isotach type viscous behaviour, similar to the rate effects pile test reported in Byrne *et al*. (2020b). Based on the test data (see Figure 4-4), the η_{10} value of the Cowden stiff clay is approximately 0.1 (*i.e.* a 10% increase in strength per log-10 cycle of $\dot{\varepsilon}$). η_{10} does not appear to change with s_u.

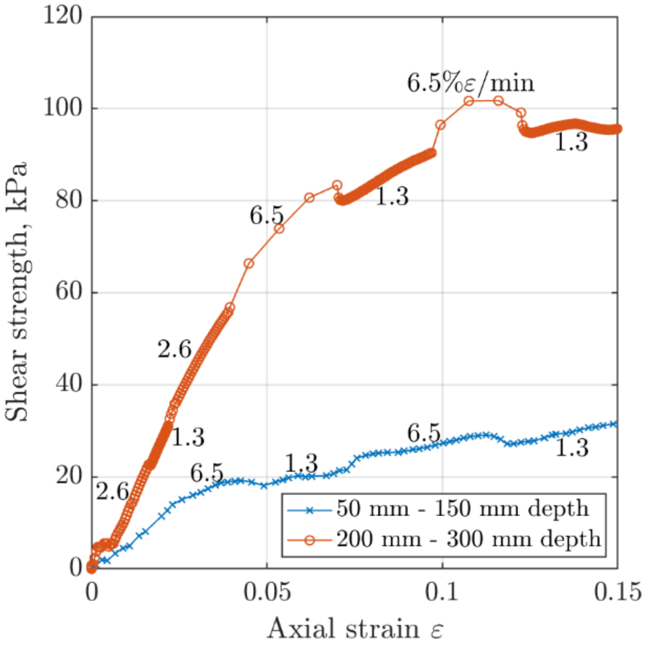

Figure 4-4 Variable strain rate triaxial compression tests on the Cowden till.

Comprehensive soil characterisation is underway for the PICASO testing at Cowden. A site geotechnical investigation has been conducted prior to the testing campaign, including 23 cone penetration tests (CPTs). The shear modulus G_{max} near the ground level is approximately 100 kPa, based on seismic CPT data (Buckley *et al*., 2020; Martin *et al*., 2022). In addition, a series of advanced soil element tests are planned at Oxford University to further investigate the mechanical behaviour and cyclic response of the Cowden till (Qiu, 2022).

4.2.3 Pile installation process

The pile installation process is illustrated in Figure 4-5, and each step is described as follows:

(1) A 254 mm diameter tube (= 2.5D) is inserted into the ground until the target soil surface is reached.

(2) A soil scraper removes the top soft soil (*i.e.* the top 40 mm to 50 mm) and trims the soil surface inside the tube. The soil surface is the reference plane for solving pile pose at the ground level.

(3) The pile is installed using the drop hammer (3000 ~ 3500 blows) and connected to the sensors and actuator(s) (following steps 1 ~ 6 in Figure 3-5). Unlike the pile installation process in dry sand, soil subsidence does not occur in stiff clay.

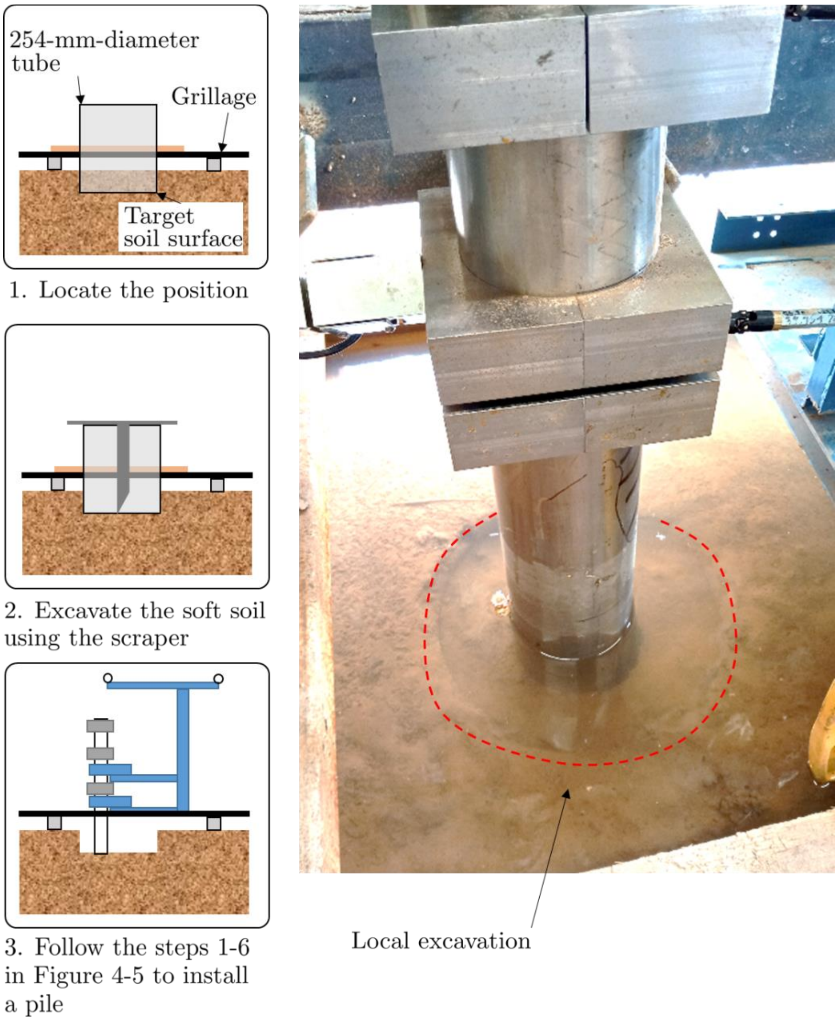

1. Locate the position

2. Excavate the soft soil using the scraper

3. Follow the steps 1-6 in Figure 4-5 to install a pile

Figure 4-5 Pile installation process for the test programme at Cowden.

4.2.4 Test programme

Figure 4-6 illustrates the design of the experimental work on saturated stiff clay. The test programme primarily explores rate and load eccentricity effects on pile response. As little work has been published exploring pile response in stiff clay through model pile testing, a wide range of tests were conducted to allow experimental observations, including high-cycle and pseudo-random cyclic loading responses, to be reported. The work packages are described as follows:

(I) Constant loading and actuation rate tests were conducted at a fixed e of $4D$ to establish reference pile responses and investigate soil rate dependency. Piles remained undisturbed for different periods after installation to explore the effect of pile setup. Selected tests were repeated to identify the influence of soil variations. Load-controlled test data were processed to obtain pile rotation rate ($\dot{\theta}$) with time for comparison with displacement-controlled test data.

(II) Variable loading and actuation rate tests explored rate-dependent pile response and isotach type viscous behaviour. The responses of $\dot{\theta}$ with time from the variable loading rate tests were obtained.

(III) Uni-directional one-way cyclic loading tests under various load frequencies f and cyclic load magnitudes ζ_b were performed to explore rate effects and cyclic characteristics for the model pile. Ratcheting and pile secant stiffness responses at different f were measured. In addition, high-cycle response and post-cyclic monotonic behaviour were explored.

(IV) One-way pseudo-random cyclic lateral loading tests were conducted to simulate realistic load conditions on OWT monopiles. The other purpose of these tests is to compare with data from the PICASO testing on the medium-scale piles at Cowden. The load input file was designed based on modified OWT monitoring data by McAdam (2021).

(V) Load eccentricity effects were investigated by applying various load eccentricities ($e = 4D$, $6D$ and $10D$). As the shaft resistance of the model pile in stiff clay is sufficient to resist the pile weight, the impact of vertical loading on lateral pile response is considered minimal and not discussed in this thesis.

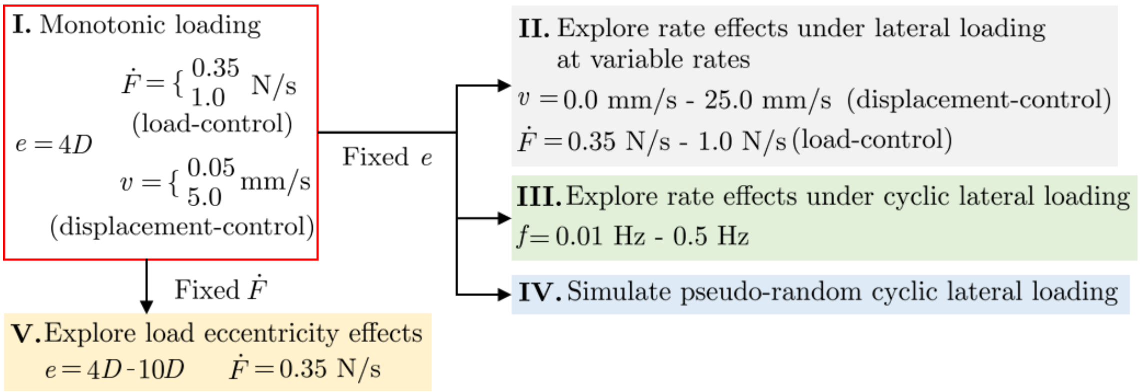

Figure 4-6 Design of testing in the stiff clay.

The nomenclature system in Figure 4-7 is adopted for uniquely identifying test results, and the list of the model tests in the Cowden till under monotonic and cyclic lateral loading is given in Table 4-2. Most tests were used to aid theoretical development in Chapter 6. Similar to the nomenclature system for dry sand, the soil condition, loading pattern, loading/actuation rate $\dot{F}$, v (or the cyclic load frequency f) and load eccentricity e are specified. Although a significant number of tests were planned, some failed due to cobbles and gravel being encountered around the piles, and only selected tests which obtained reliable results are presented in this thesis.

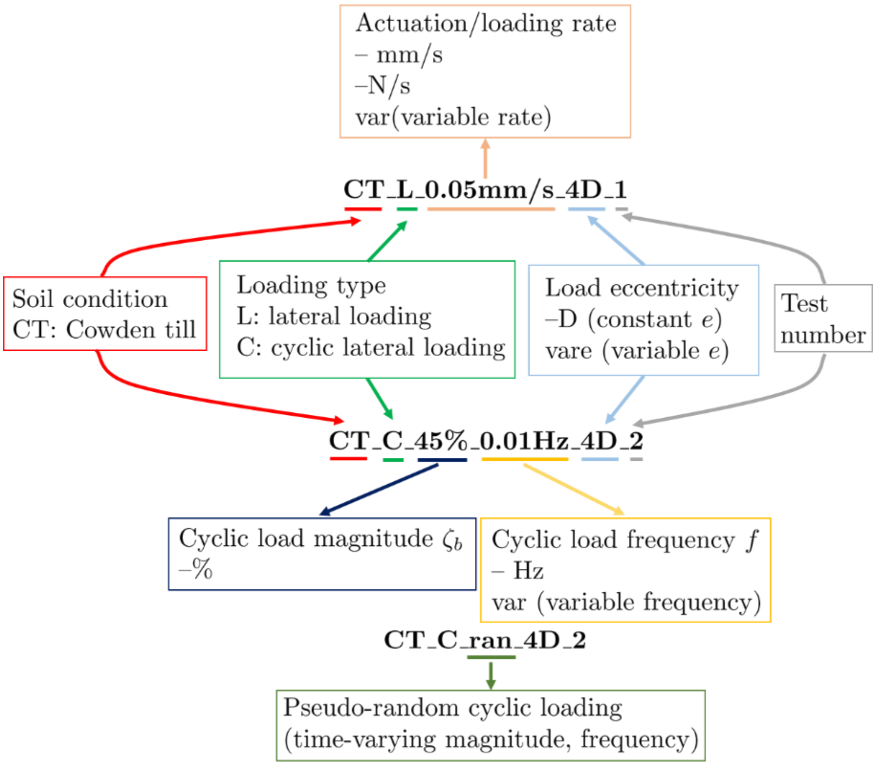

Figure 4-7 Nomenclature for stiff clay.

Table 4-2 List of the model tests in the Cowden till

Test list		Theoretical modelling
I. Constant rate monotonic loading		Section 6.4.1
CT_L_0.35N/s_4D_1 ~ CT_L_0.35N/s_4D_2†	Load-control	
CT_L_1N/s_4D_1 ~ CT_L_1N/s_4D_4		
CT_L_0.05mm/s_4D_1 ~ CT_L_0.05mm/s_4D_2	Displacement-control	
CT_L_5mm/s_4D_1		
II. Variable rate tests		Section 6.4.2
CT_L_var_4D_1 ~ CT_L_var_4D_3	Load-control	
CT_L_var_4D_4 ~ CT_L_var_4D_6	Displacement-control	
III. Load eccentricity effects		Section 6.4.3
CT_L_0.35N/s_6D_1†	Load-control	
CT_L_0.35N/s_10D_1†		
CT_L_0.35N/s_var_1		
IV. Pseudo-random loading		Section 6.4.5
CT_C_ran_4D_1 ~ CT_C_ran_4D_2		
V. Cyclic loading response		Section 6.4.4
CT_C_22.5%_0.5Hz_4D_1	Small magnitude	
CT_C_22.5%_0.01Hz_4D_1		
CT_C_45%_0.5Hz_4D_1	Large magnitude	
CT_C_45%_0.1Hz_4D_1		
CT_C_45%_0.1Hz_4D_2‡		
CT_C_45%_0.01Hz_4D_1		

† : $e = 4D$, $6D$ and $10D$ were compared for load eccentricity effects.

‡ : high-cycle loading ($N > 5000$).

The test programme covers a variety of tests to investigate different phenomena. Test specifications, including the undisturbed period between installation and testing, actuation/loading rate $\dot{F}$, v and ultimate capacities M_R and H_R for each type of testing are described in the following sections.

4.3 Monotonic lateral loading

4.3.1 Monotonic loading under load control

4.3.1.1 Constant loading rate tests

Table 4-3 describes the constant loading rate tests. In these tests, the load eccentricity e was fixed at $4D$, and the loading rate $\dot{F}$ was set to 0.35 N/s (slow loading rate) or 1 N/s (fast loading rate). Excess pore water pressures are expected to be generated during installation for driven piles in clay, followed by subsequent consolidation. The periods between installation and testing for these tests were from six days to four weeks to observe any potential time-dependent increase in pile resistance.

Table 4-3 Descriptions of constant loading rate tests.

Test name	Days between installation and testing	$\dot{F}$ (N/s)	M_R (Nm)	H_R (N)
CT_L_0.35N/s_4D_1	12	0.35	193	504
CT_L_0.35N/s_4D_2	6		309	841
CT_L_1N/s_4D_1	11	1	396[1]	1021[1]
CT_L_1N/s_4D_2	7		323	754
CT_L_1N/s_4D_3	28		370	1030
CT_L_1N/s_4D_4	29		338	858

Note: [1] The test ended at θ = 1.6° due to the load limit setting; M_R and H_R are estimated.

Figure 4-8 shows the responses of H, θ and $\dot{\theta}$ with time from the slow loading rate tests ($\dot{F} = 0.35$ N/s). Under a constant rate of loading, $\dot{\theta}$ increases non-linearly with time. The $\dot{\theta}$ response with time can be fitted using a power-law function (see the yellow curve in Figure 4-8). In test CT_L_0.35N/s_4D_1, a temporary increase in $\dot{\theta}$ temporarily was observed from approximately 900 to 1000 seconds. This phenomenon is recognised as an indicator of existing soft clay or potential localised yielding.

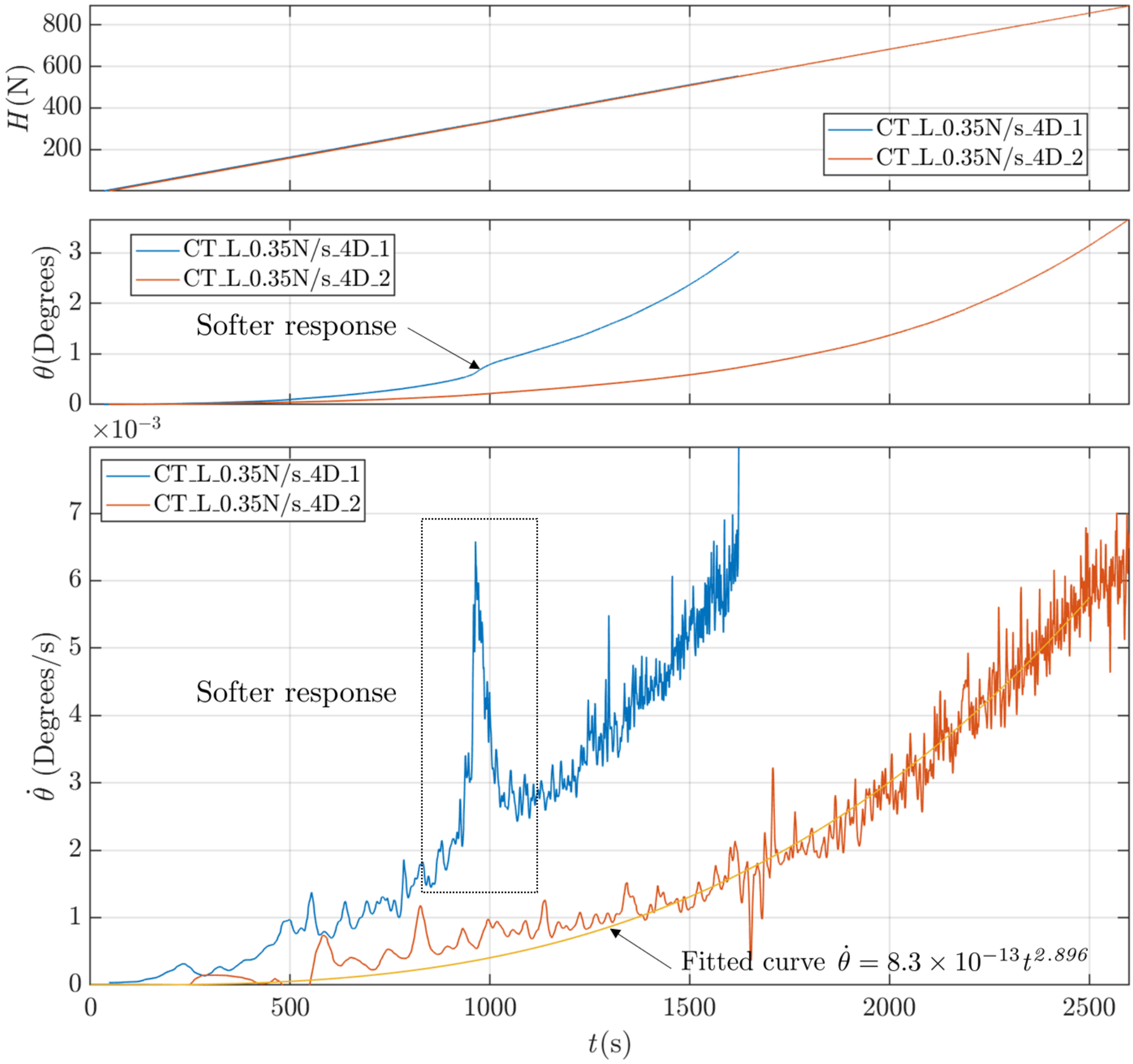

Figure 4-8 H, θ and $\dot{\theta}$ with time of the slow loading rate tests ($\dot{F} = 0.35$ N/s).

Figure 4-9 shows the results of the slow loading rate tests. Both moment-rotation and horizontal load-displacement responses are explored. Similar to the testing in dry sand, the horizontal displacement u and rotation θ are linearly dependent. Conventional monopiles may have a slightly greater L/D ratio around 4 (see *e.g.* Byrne, 2020), and when $u_R = 0.1D$, θ is close to θ_R (see example of the constant actuation rate tests in *very loose* sand in Figure 4-10). The model pile in stiff clay, however, has a smaller L/D ratio of 3, leading to a different rotation-horizontal displacement response. At $\theta = \theta_R = 2°$, u falls within the range between $0.65u_R$ and $0.89u_R$.

The response from test CT_L_0.35N/s_4D_1 is soft compared to the other tests in Table 4-3. As shown in Figure 4-9, the capacity of CT_L_0.35N/s_4D_2 is approximately 50% more than that of CT_L_0.35N/s_4D_1. Soft clay may have been encountered around the pile in test CT_L_0.35N/s_4D_1, causing localised yielding and a soft response. Besides, the rotational-horizontal displacement responses from the two tests show different trends, which may be due to soil variability.

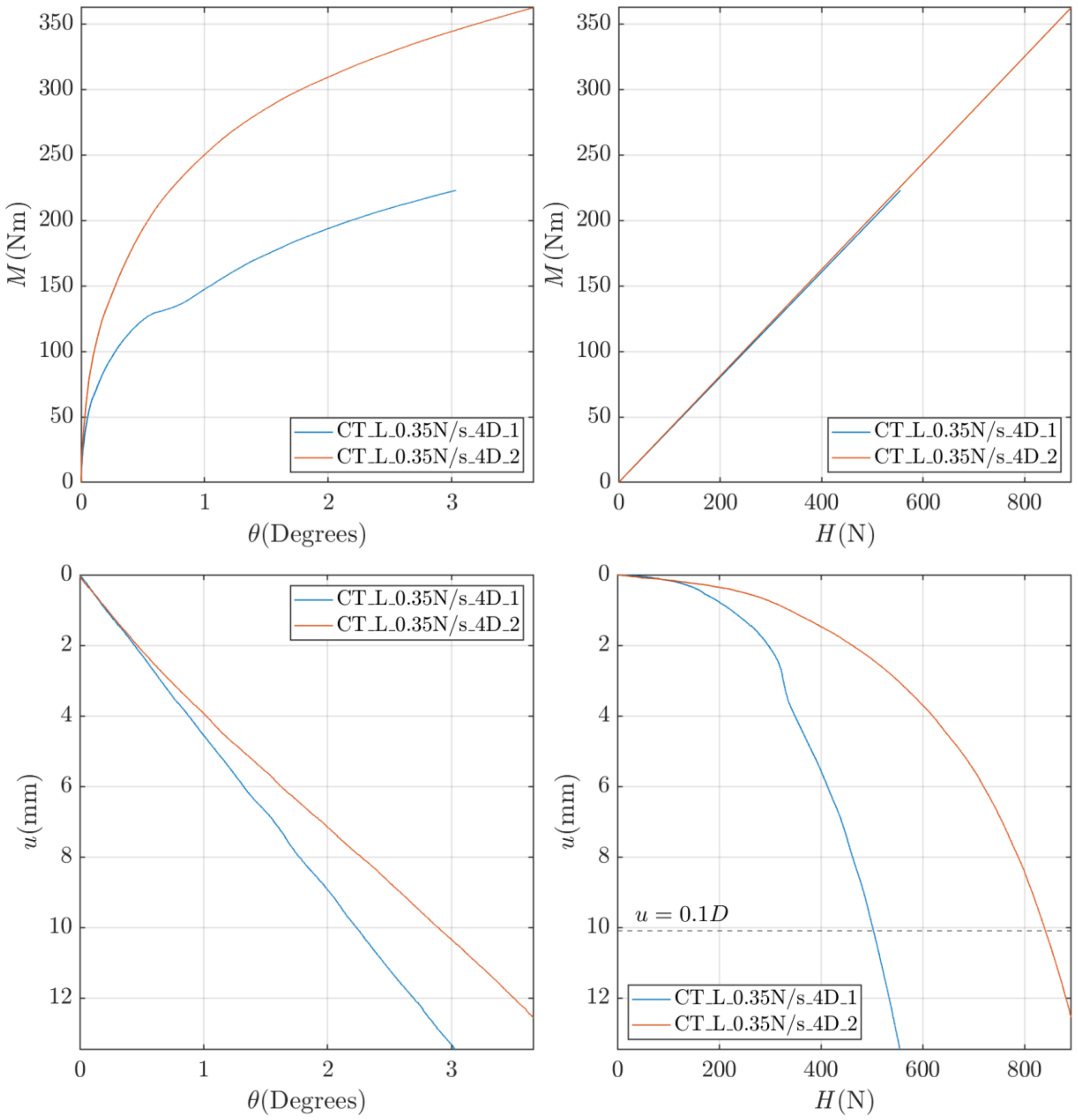

Figure 4-9 Results from the slow loading rate tests.

Figure 4-10 shows H, θ and $\dot{\theta}$ with time from the fast loading rate tests ($\dot{F} = 1$ N/s). Similar to the slow loading rate tests, the $\dot{\theta} - t$ response can be fitted using a power-law function. Amongst the tests, test CT_L_1N/s_4D_2 demonstrates a softer response, and a temporary increase in $\dot{\theta}$ at $t = 400$ s is observed. In test CT_L_1N/s_4D_4, the coupling fell off at $\theta = 0.9°$, immediately followed by unloading. Displacement measurements during the unloading are inaccurate and not shown. After this issue was solved, the test continued under the same loading rate $\dot{F}$ of 1 N/s.

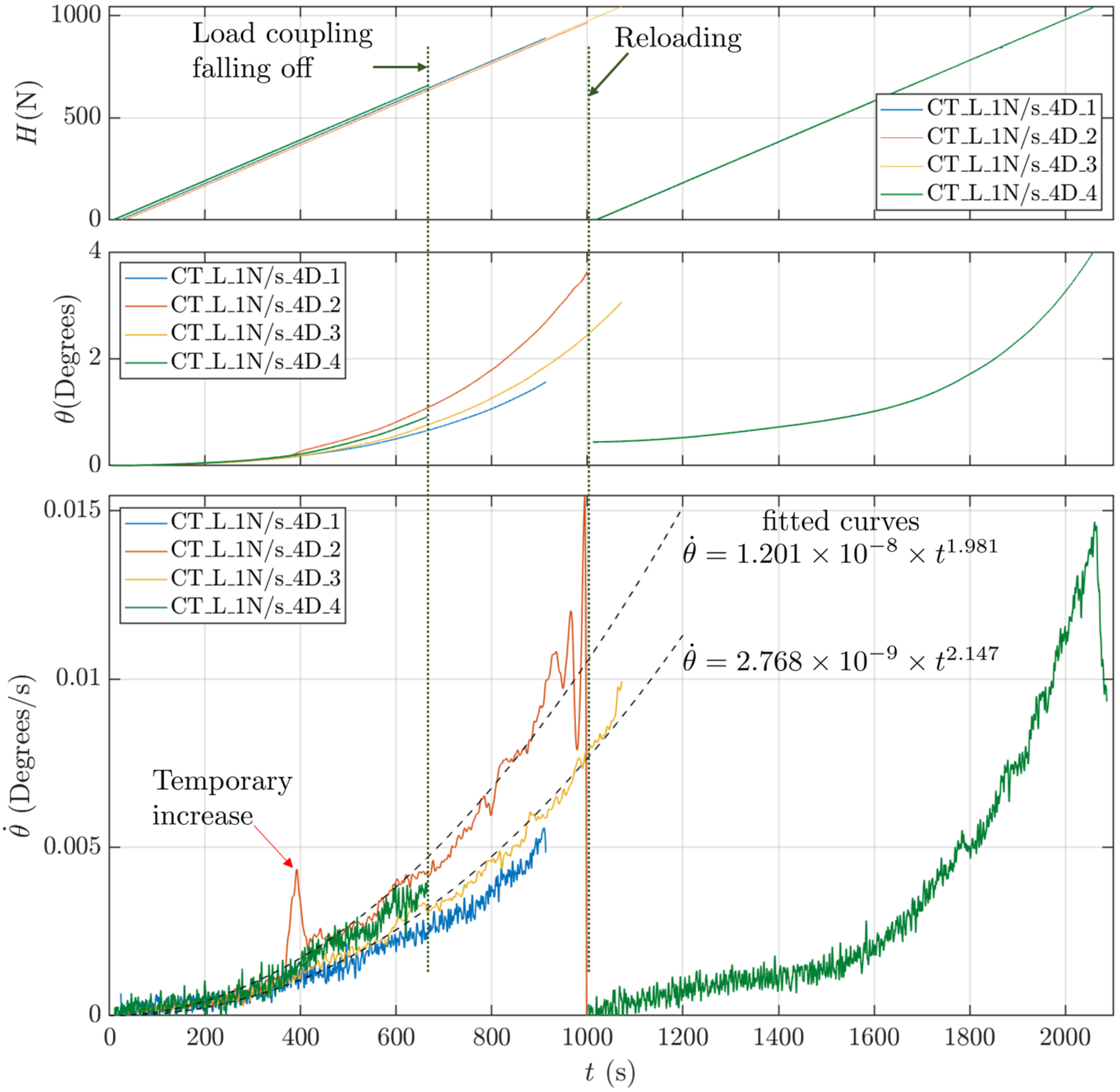

Figure 4-10 H, θ and $\dot{\theta}$ responses with time of the fast loading rate tests.

Figure 4-11 shows the results from the fast loading rate tests. As shown in the data and Table 4-3, it can be seen that the piles with different undisturbed periods between installation and testing show no clear variation with time from installation, indicating that the variation is due to some other cause, such as soil variability. The rotation-horizontal displacement responses from these tests also slightly differ. Excess pore water pressures due to installation may have fully dissipated in all cases, but this is uncertain as pore water pressure measurements were unavailable. An average response curve is obtained from these tests (see red dashed curve in Figure 4-11).

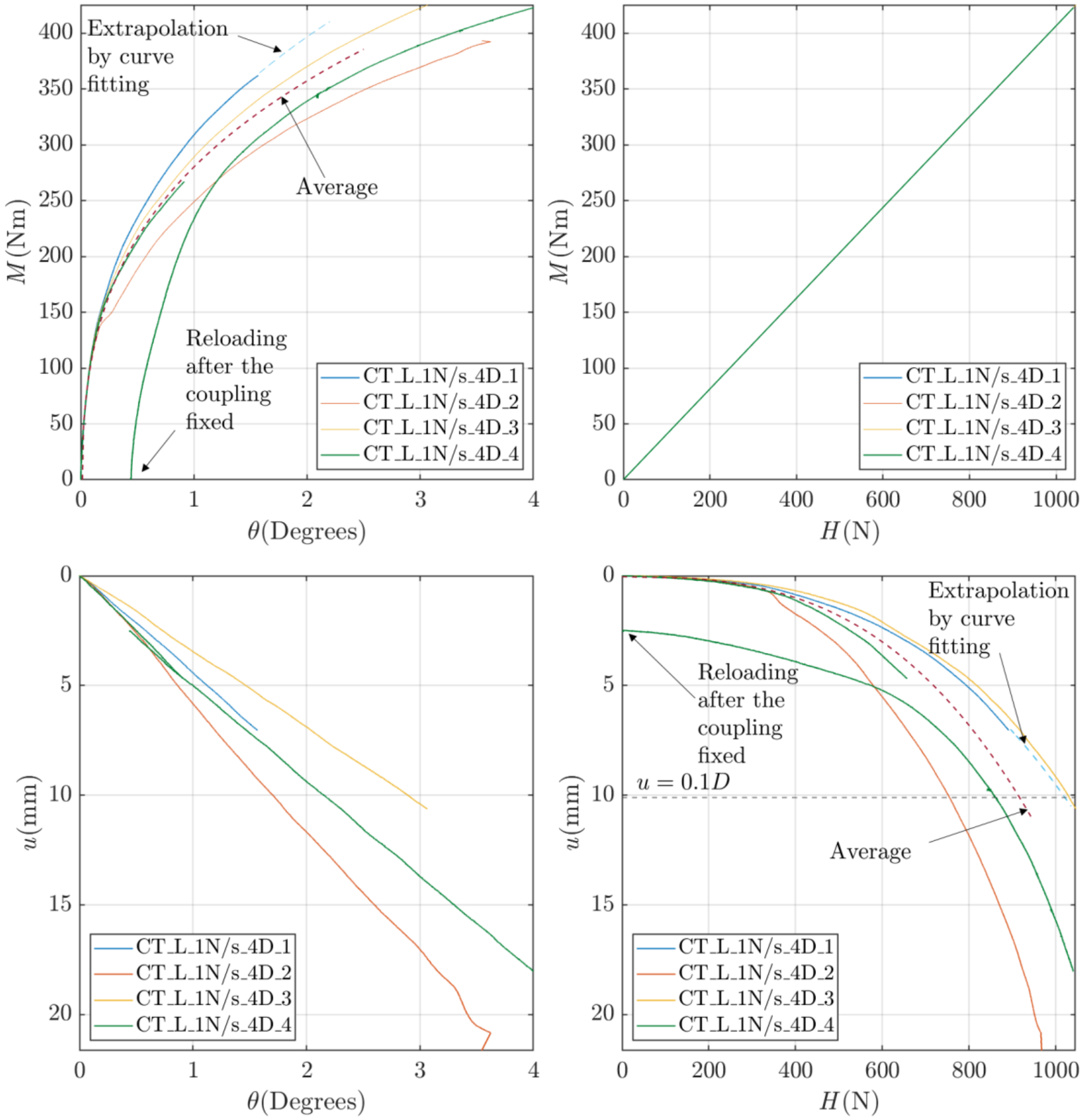

Figure 4-11 Results from the fast loading rate tests ($\dot{F} = 1$ N/s).

4.3.1.2 Reference loads and normalisation for load-controlled monotonic tests

Figure 4-12 compares the M/M_R and H/H_R responses at the slow and fast loading rates. These normalised forms were adopted by Richards (2019) for laboratory-scale testing in dry sand. The results show that the difference due to rate effects does not appear after normalisation, although it is evident that pile capacity increases with $\dot{F}$.

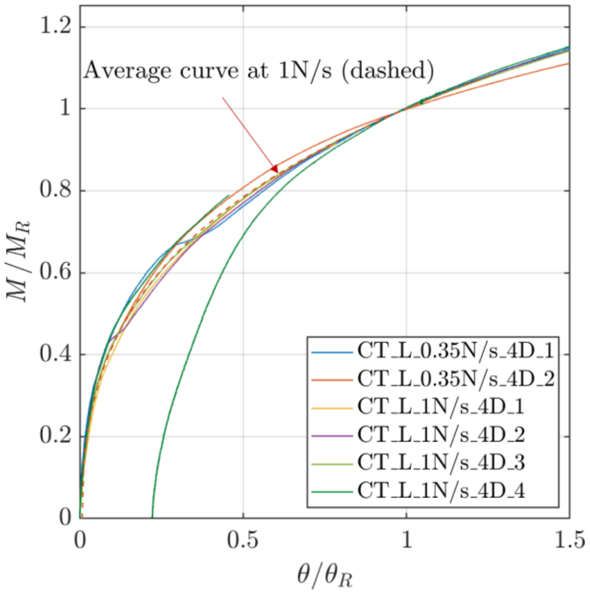

Figure 4-12 Comparing M/M_R and H/H_R responses at different loading rates.

The influence of soil variations is omitted. For example, the M/M_R and H/H_R responses of the slow loading rate tests are approximately identical, despite the variation between the tests. Similarly, the M/M_R and H/H_R responses from the fast loading rate tests are nearly identical, and the influence of soil variations is eliminated by the normalisation.

The constant loading rate tests are used to establish reference responses for normalisation. At the slow loading rate, the response from test CT_L_0.35N/s_4D_2 is adopted, and at the fast loading rate, the average response is used (see Table 4-4).

Table 4-4 Reference loads of the constant loading rate tests in saturated stiff clay.

Loading rate $\dot{F}$ (N/s)	M_R ($\theta = \theta_R = 2°$) (Nm)	H_R ($u = u_R = 0.1D$) (N)
0.35 (slow loading rate)	309	841
1 (fast loading rate)	357	916

4.3.1.3 Variable loading rate tests

The variable loading rate tests with stepwise changes in $\dot{F}$ are described in Table 4-5 and shown in Figure 4-13. Although isotach type viscous behaviour is not observed, possibly due to the small range of rates tested, the response curves become steeper with the increase in $\dot{F}$. The load inputs for tests CT_L_var_4D_1 and CT_L_var_4D_2 are the same, but their responses differ slightly due to soil strength variability. During test CT_L_var_4D_1, the load control was unstable while $\dot{F}$ was varied from 1 N/s to 0.35 N/s, but the issue was immediately fixed by tuning the controller with lower gain values.

Table 4-5 Descriptions of the monotonic loading tests under variable loading rates.

Test name	Days between installation and testing	$\dot{F}$ (N/s)	M_R (Nm)	H_R (N)
CT_L_var_4D_1	11	0.35 ~ 1	-	-
CT_L_var_4D_2	12		290	-
CT_L_var_4D_3	8	0.35 ~ 4	346	884

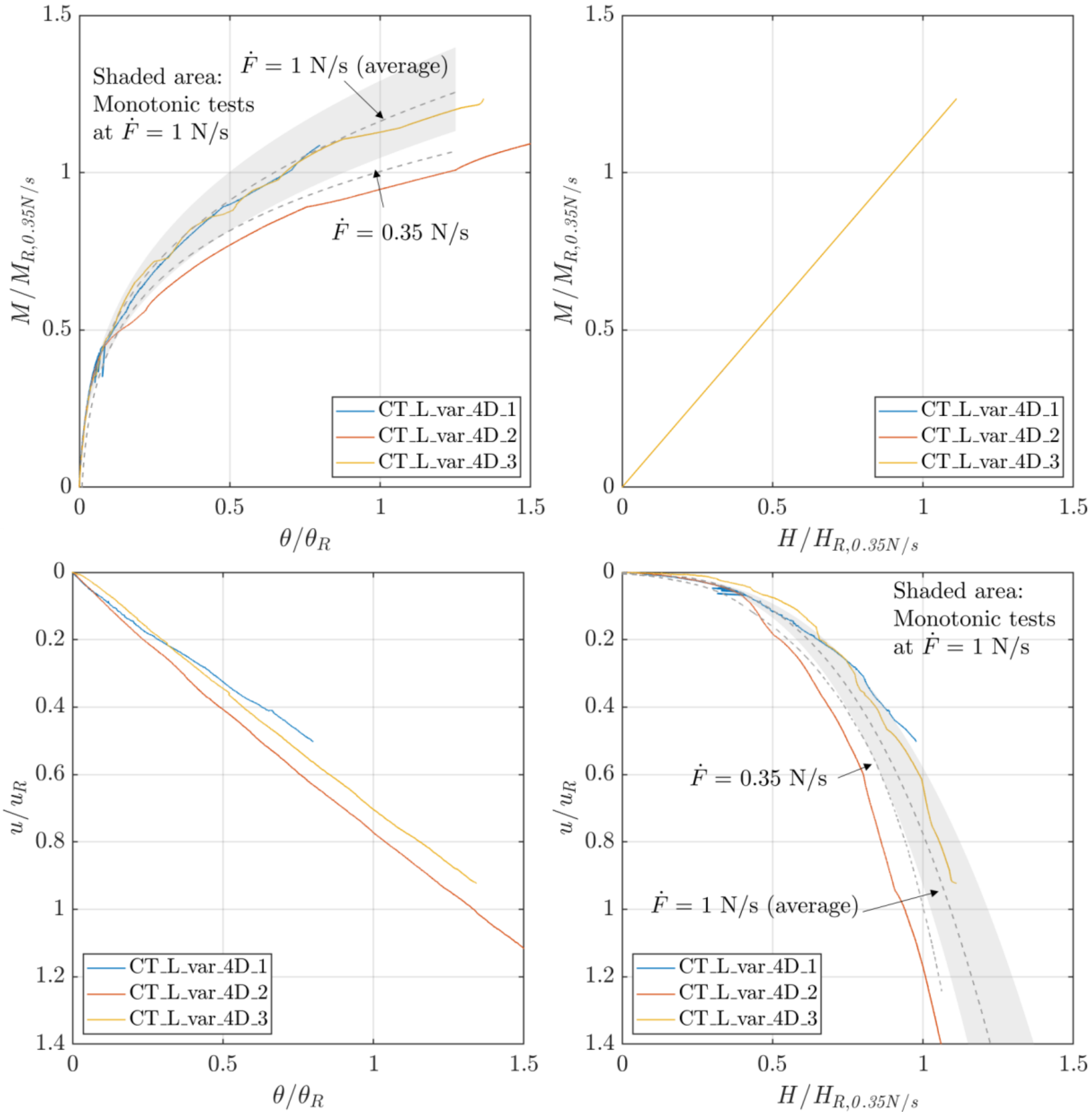

Figure 4-13 Normalised results from the variable loading rate tests.

4.3.2 Monotonic loading under displacement control

4.3.2.1 Constant actuation rate tests

Table 4-6 summarises the constant actuation rate tests. In these tests, the actuation rate v was set to 0.05 mm/s (slow actuation rate, denoted as v_o) or 5 mm/s (fast actuation rate, $100v_o$). The H and θ responses with time from the constant actuation rate tests are compared in Figure 4-14, and the average monotonic response at $v = v_o$ is shown dashed. The pile rotation rate $\dot{\theta}$ (the slope of θ response with time) is linearly proportional to v. When $v = v_o$, $\dot{\theta}$ is approximately 0.00413 Degrees/s, denoted as $\dot{\theta}_o$. By comparing the test results, soil rate effects are evident (see Figure 4-15). The responses from the slow actuation rate tests are approximately identical. In test CT_L_0.05mm/s_4D_2, cobbles and gravel were encountered around the pile, slightly influencing the pile response.

Table 4-6 Descriptions of the monotonic loading tests under displacement control.

Test name	Days between installation and testing	v (mm/s)	M_R (Nm)	H_R (N)
CT_L_0.05mm/s_4D_1	8	0.05	325	831
CT_L_0.05mm/s_4D_2	7		326	882
CT_L_5mm/s_4D_1	17	5	399	1090

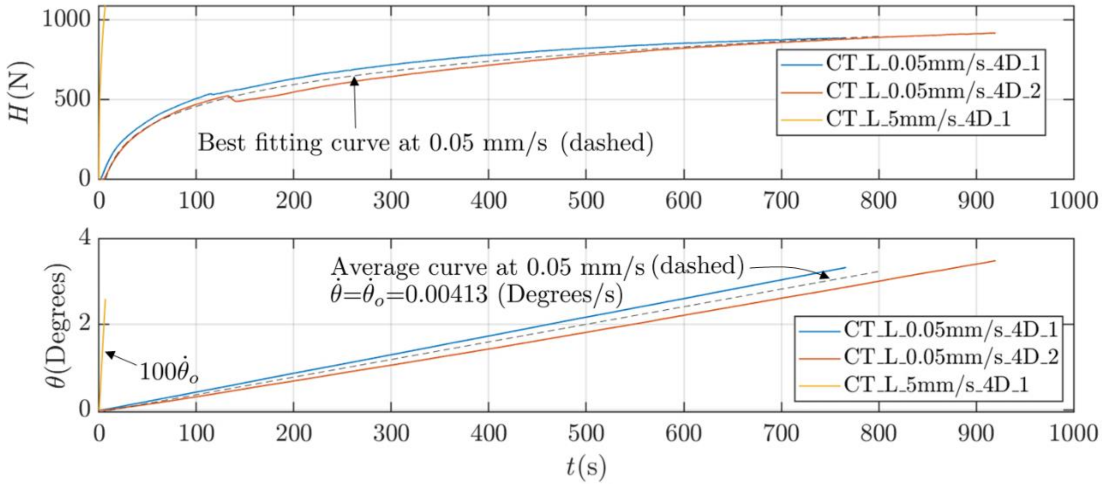

Figure 4-14 H and θ responses with time of the constant actuation rate tests.

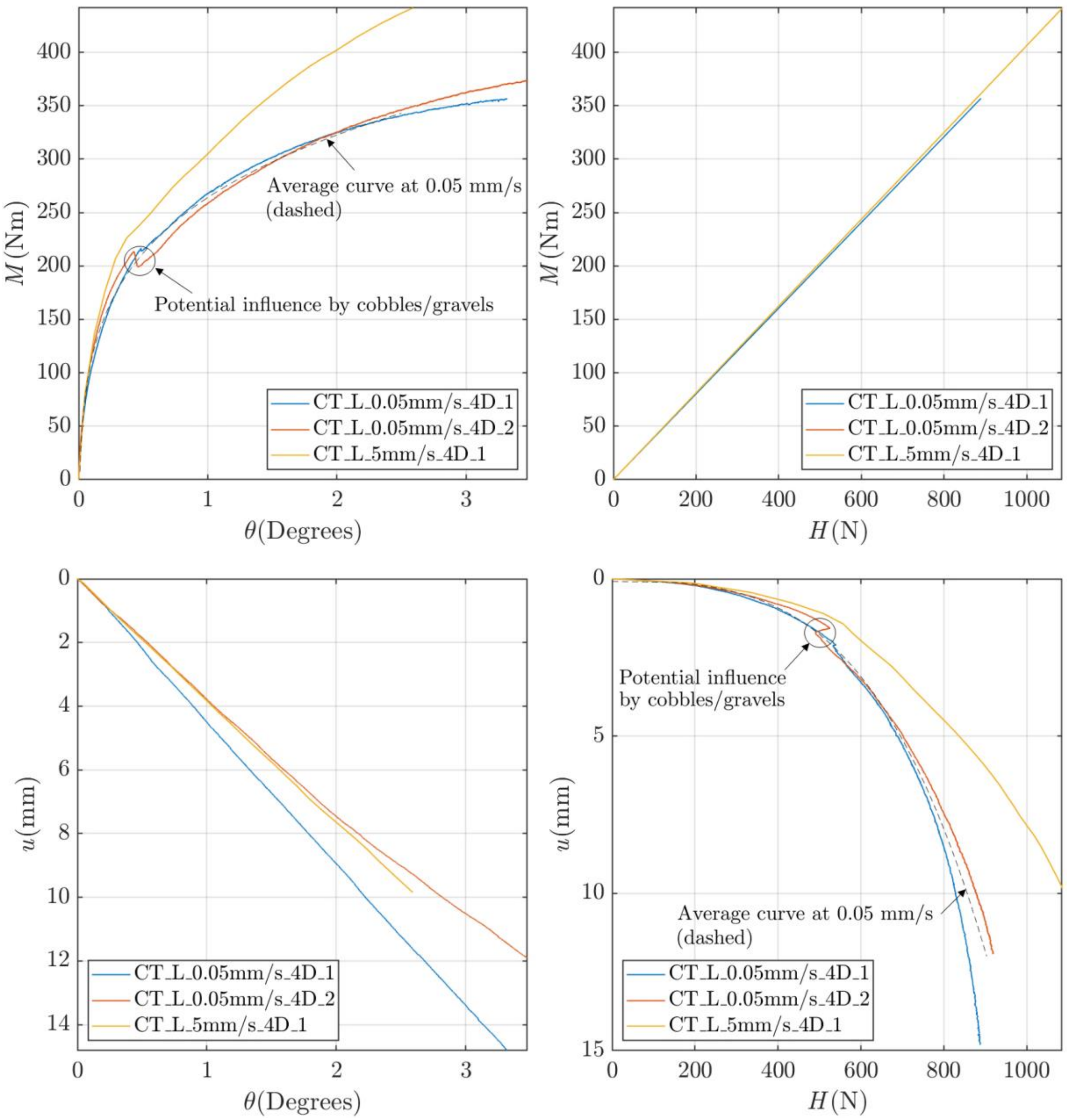

Figure 4-15 Results of the constant actuation rate tests.

4.3.2.2 Reference loads and normalisation for displacement-controlled monotonic tests

The normalised M/M_R and H/H_R responses from the constant actuation rate tests are shown in Figure 4-16. These normalised results are similar, like the constant loading rate tests in Section 4.3.1.1, and do not show rate dependency.

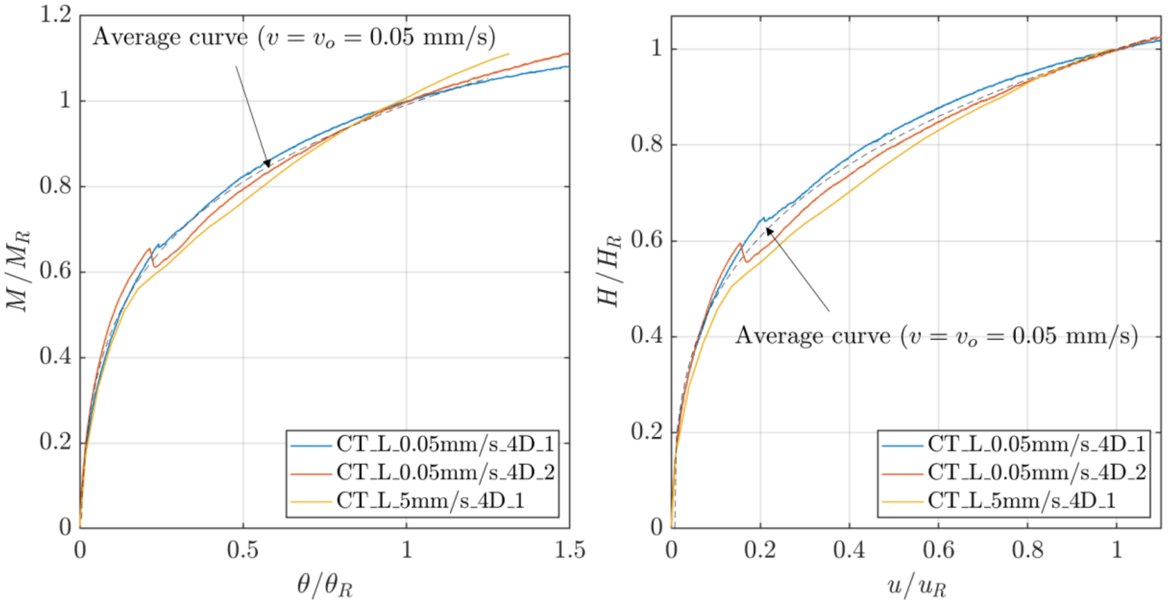

Figure 4-16 M/M_R and H/H_R responses of the constant actuation rate tests.

The reference loads for different actuation rates are given in Table 4-7. The ultimate capacities at the slow actuation rates ($M_{R,0.05mm/s}$ and $H_{R,0.05mm/s}$) are determined by the average response from the corresponding tests. In the next section, a series of variable actuation rate tests are described, and their responses are normalised using $M_{R,0.05mm/s}$ and $H_{R,0.05mm/s}$ for comparison with the constant actuation rate tests.

Table 4-7 Reference loads of the displacement-controlled monotonic tests in saturated stiff clay.

Loading rate v (mm/s)	M_R ($\theta = \theta_R = 2°$) (Nm)	H_R ($u = u_R = 0.1D$) (N)
0.05 (slow actuation rate = v_o)	325.5	856.5
5 (fast loading rate = $100v_o$)	399	1090

4.3.2.3 Variable actuation rate tests

The descriptions of the variable actuation rate tests are given in Table 4-8. The $\dot{\theta}$ responses with time are illustrated in Figure 4-17. Similar to the constant actuation rate tests, v and $\dot{\theta}$ are linearly dependent. In test CT_L_var_4D_4, $\dot{\theta}$ gradually increased with time until $\dot{\theta} = \dot{\theta_o}$, and the response became close to that from the constant actuation rate test at $v = v_o$. During test CT_L_var_4D_5, when v dropped to 0 mm/s (θ remained constant), M decreased by 27% over 50 seconds. In test CT_L_var_4D_6, the M/M_R ratios when $v = v_o$ and $100v_o$ are approximately identical to the constant actuation rate responses at v_o and $100v_o$, respectively.

The normalised responses using $M_{R,0.05mm/s}$ and $H_{R,0.05mm/s}$ are shown in Figure 4-18. Isotach viscous behaviour is evident by applying step changes in v, and a unique $M - \theta - \dot{\theta}$ (or $M - \theta - v$) response is observed. The rotation-horizontal displacement response is linear and does not change with v. The responses from the constant actuation rate tests are compared with the data (see dashed lines in Figure 4-18). Amongst the tests, test CT_L_var_4D_5 has high capacity, possibly due to stiffer clay around the pile. With that exception, the responses of CT_L_var_4D_4 and CT_L_var_4D_6 can be characterised using the constant actuation rate responses at v_o and $100v_o$.

Table 4-8 Descriptions of the monotonic loading tests under displacement-control

Test name	Days between installation and testing	v (mm/s)	M_R (Nm)	H_R (N)
CT_L_var_4D_4	7	0 to v_o	320	-
CT_L_var_4D_5	9	Step changes 0 and $400v_o$	409	1125
CT_L_var_4D_6	7	Step changes between $0.2v_o$ and $100v_o$	368	857

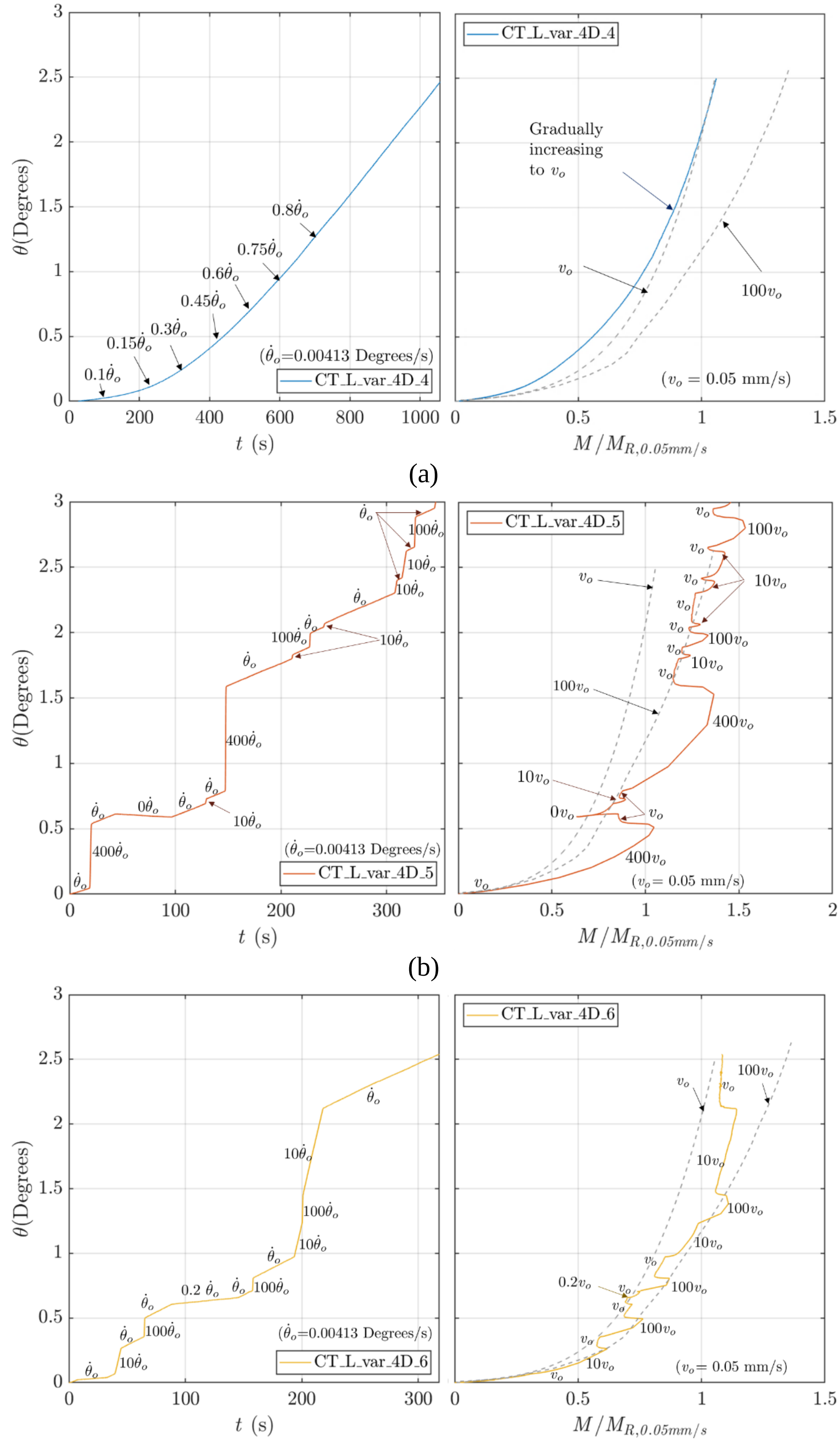

(a)

(b)

(c)

Figure 4-17 θ with time from the variable actuation rate tests:

(a) CT_L_var_4D_4; (b) CT_L_var_4D_5; (c) CT_L_var_4D_6.

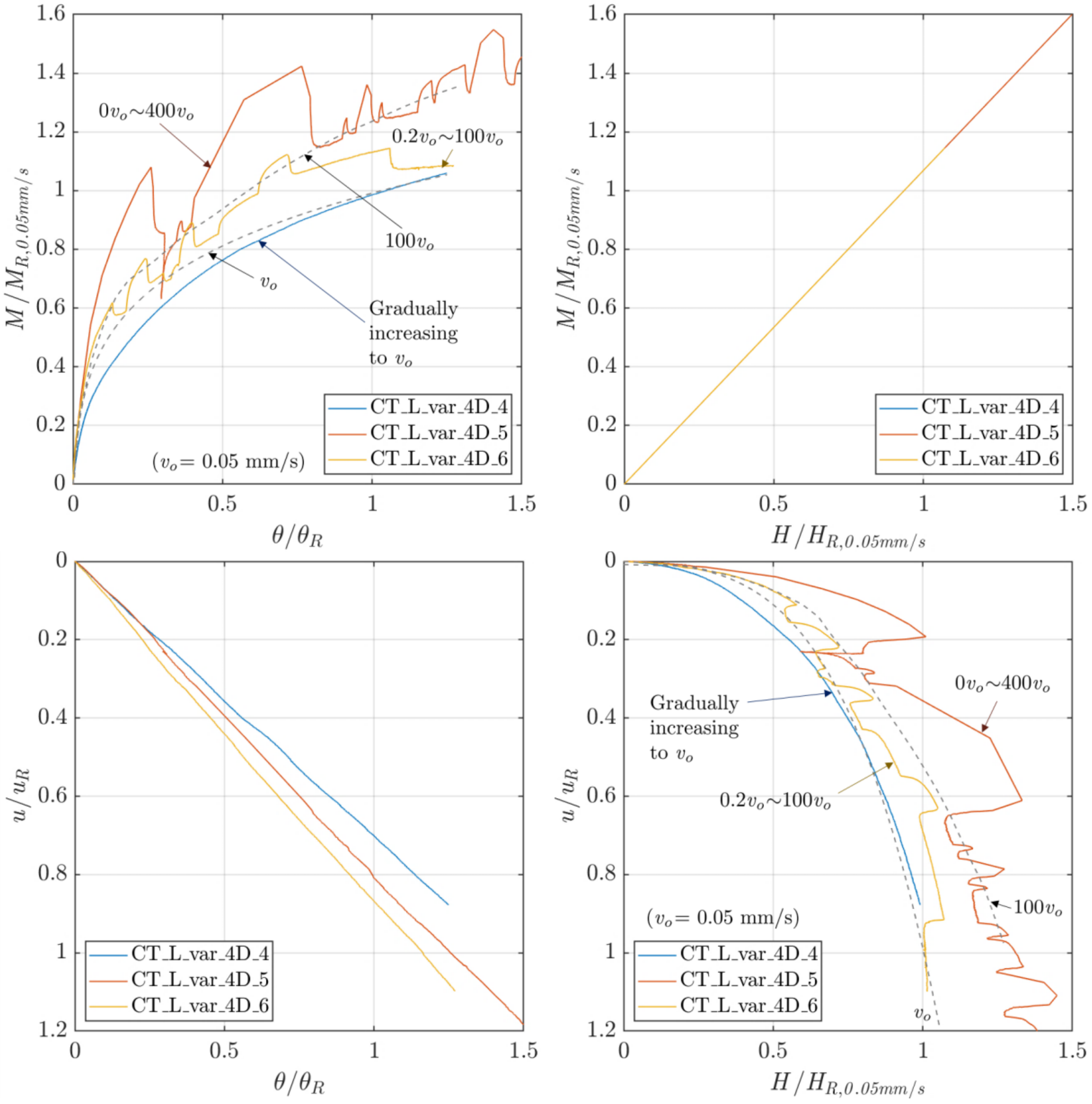

Figure 4-18 Normalised responses from the variable actuation rate tests.

4.3.3 Quantification of rate effects for monopiles under lateral loading

4.3.3.1 Initial pile response

Initial pile responses at different rates are given in Table 4-9. Data are obtained from multiple tests. Load-controlled and displacement-controlled tests are shown separately for clarity. In a similar way to the testing in dry sand, the initial pile response of the model pile in saturated stiff clay is not purely elastic. Although the mean values of k_{max} indicate that the initial pile response is rate-sensitive, a large variation throughout the tests is observed. Therefore, quantifying rate effects for the initial pile response may be inappropriate.

Table 4-9 k_{max} under different rates.

Rate		Range of k_{max} (Nm/°)		
		Lower bound	Mean	Upper bound
$\dot{F}$ (N/s)	0.35	2413	3267	4696
	1	2477	3638	4989
v (mm/s)	0.005	1344	1566	1975
	0.05	2448	3214	4619
	5	-	4022	-

4.3.3.2 Quantification of the rate parameter

The magnitude of rate effects for monopiles is obtained using a semi-logarithmic relationship between the pile rotational rate $\dot{\theta}$ and moment capacity M, where $\dot{\theta}$ can be replaced with the actuation rate v. At the element scale, the relationship between shear strain rate $\dot{\varepsilon}$ and shear strength τ is obtained using the rate parameter η_{10} (see Section 1.2.3). Similarly, the rate parameter for the rotational rate ($\eta_{10\dot{\theta}}$) can be expressed as

$$\eta_{10\dot{\theta}} = \frac{(M_{fast} - M_{slow})/M_{slow}}{\log_{10} v_{fast} - \log_{10} v_{slow}} = \frac{(M_{fast} - M_{slow})/M_{slow}}{\log_{10} \dot{\theta}_{fast} - \log_{10} \dot{\theta}_{slow}}. \qquad \text{Equation 4-1}$$

By comparing the constant actuation rate responses in Figure 4-15, an average $\eta_{10\dot{\theta}}$ value of 0.1 (*i.e.* a 10% increase in M per log-10 cycle of $\dot{\theta}$) is evident and unlikely to change with θ or soil strength properties (*e.g.* s_u). The $\eta_{10\dot{\theta}}$ value is approximately equal to η_{10} from the undrained triaxial compression test, which suggests that the relative magnitude of rate dependency does not change with the scale. The responses from the variable actuation rate tests CT_L_var_4D_5 and CT_L_var_4D_6 are analysed to retrieve data points at v = v_o and $10v_o$. These data points can approximate constant actuation rate responses through curve fitting using power-law functions, eliminating the variation between different tests (see Figure 4-19 and

Figure 4-20). By comparing these estimated responses, an overall $\eta_{10\dot{\theta}}$ of 0.1 is evident. Data and estimated responses match extremely well.

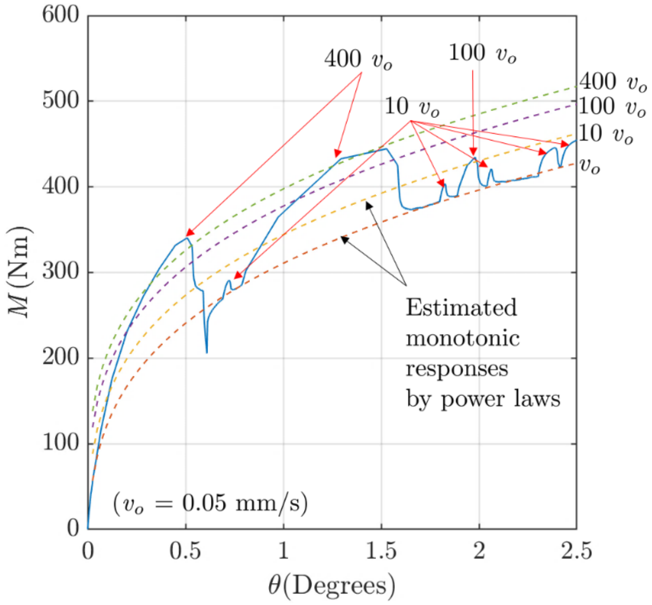

Figure 4-19 Estimated monotonic responses at different v from test CT_L_var_4D_5.

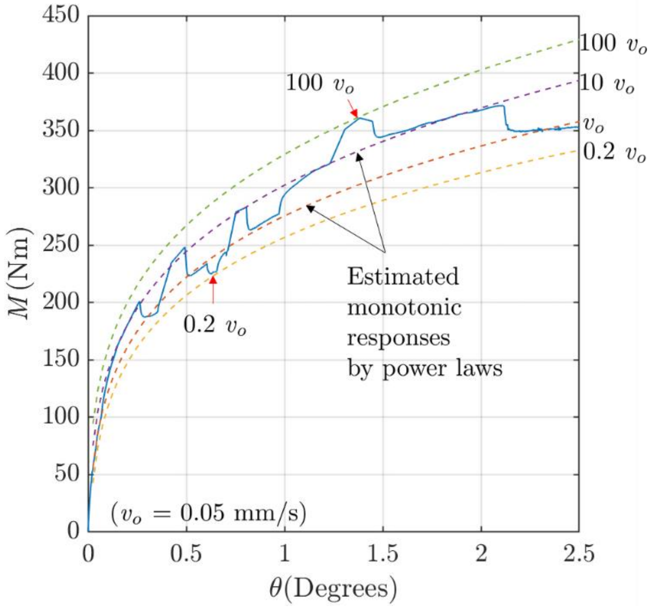

Figure 4-20 Estimated monotonic responses at different v from test CT_L_var_4D_6.

4.3.3.3 Validation of the rate parameter

The $\eta_{10\dot{\theta}}$ value is purely determined by comparing data points at different v and needs to be validated. If isotach type viscous behaviour can characterise pile response, it is possible to capture pile responses at different rates by doing a constant actuation rate test and using $\eta_{10\dot{\theta}}$ to predict results at other rates.

The responses from tests CT_L_var_4D_1 ~ CT_L_var_4D_4 are analysed to examined the $\eta_{10\dot{\theta}}$ through a simple validation approach, as described in Figure 4-21. First of all, a reference rotation rate ($\dot{\theta}_r$) is chosen, and data points at $\dot{\theta} = \dot{\theta}_r$ are retrieved to obtain an estimated response by power-law curve fitting. Secondly, for each θ value, the corresponding $\dot{\theta}$ and monotonic curve are found through the semi-logarithmic relationship in Equation 4-1. Finally, the corresponding M is obtained from the curve to compare with the test data.

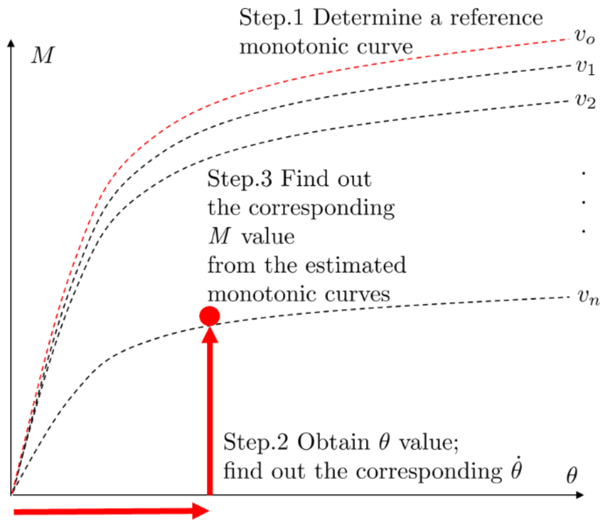

Figure 4-21 Method for validation of the rate parameter $\eta_{10\dot{\theta}}$ with variable loading rate tests.

For each variable loading rate test, an estimated reference monotonic response (red dashed) and $\dot{\theta}_r$ is obtained, and the predicted result (grey) matches closely against the test data (blue), as shown in Figure 4-22.

Figure 4-23 shows the validation of $\eta_{10\dot{\theta}}$ using the data from test CT_L_var_4D_4. In Figure 4-17, v increases to v_o when θ = 1.5°, and the data points from θ = 1.5° to θ = 2.5° are retrieved to obtain a fitted reference monotonic response curve at $v = v_o$. The monotonic curves at the other rates ($0.1v_o$ ~ $0.8v_o$) are estimated using the response at $v = v_o$ and $\eta_{10\dot{\theta}}$ and were found to match the data.

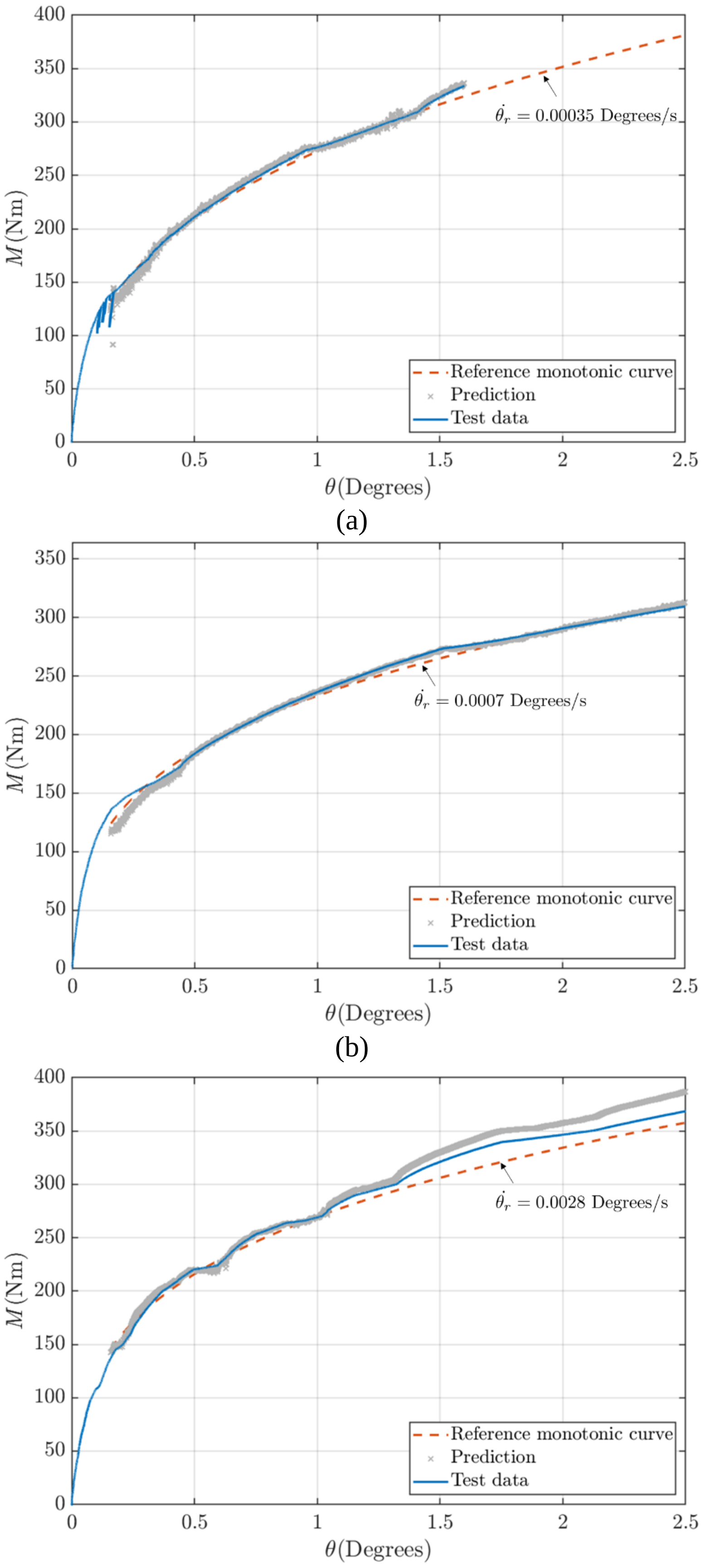

(a)

(b)

(c)

Figure 4-22 Validation of the rate parameter $\eta_{10\dot{\theta}}$ against the load-controlled variable rate tests: (a) CT_L_var_4D_1; (b) CT_L_var_4D_2; (c) CT_L_var_4D_3.

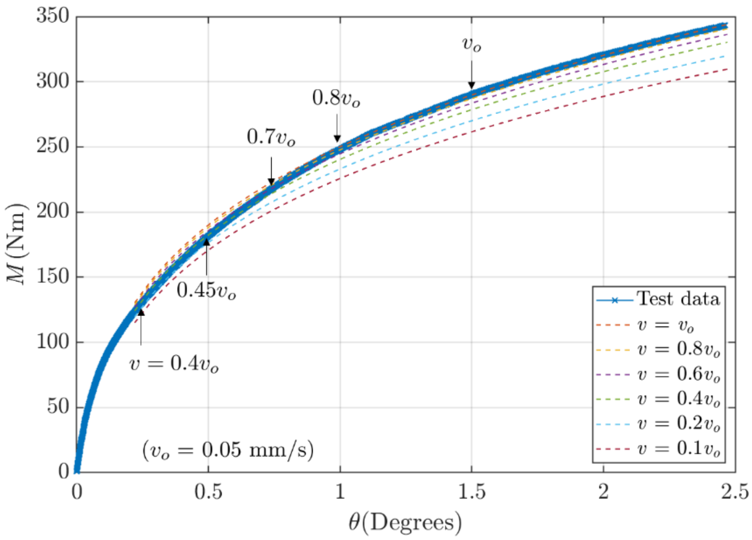

Figure 4-23 Validation of the rate parameter $\eta_{10\dot{\theta}}$ against the test data of CT_L_var_4D_4.

4.3.4 Summary of the pile response to monotonic lateral loading

The monotonic test results show that variation between the tests needs to be assessed for data comparison. Table 4-1 shows that the undrained shear strength s_u varies across the test site, which is expected, given that the soil strata formed naturally. The impact of soil strength variation is eliminated by normalising data in terms of M/M_R or H/H_R. By comparing the tests with different undisturbed periods between installation and testing, it is believed that excess pore pressures induced by impact driving during installation have fully dissipated in all cases, and pile setup was not observed.

As previously reported in the PISA testing at Cowden, pile capacity is enhanced by increasing the loading rate (Byrne *et al*., 2020b). This phenomenon is also seen in the monotonic loading tests at different rates. By comparing the test results, it is found that pile capacity increases by 10% per log-10 cycle of the actuation rate v or rotation rate $\dot{\theta}$ ($\eta_{10\dot{\theta}} = 0.1$), and isotach behaviour is observed in the displacement-controlled tests.

4.4 Cyclic lateral loading

4.4.1 Constant cyclic load magnitude

Uni-directional one-way cyclic lateral loading tests with two different load magnitudes of 22.5% $M_{R,0.35N/s}$ ($\zeta_b = 0.225$) and 45% $M_{R,0.35N/s}$ ($\zeta_b = 0.45$) were conducted to explore (1) cyclic soil rate effects, (2) the effect of load magnitude, (3) high-cycle loading response and (4) post-cyclic behaviour. Descriptions of these tests are given in Table 4-10. Cyclic response is characterised using the key definitions given in Section 3.6.2.

Table 4-10 Descriptions of the constant magnitude cyclic lateral loading.

Test name	Days between installation and testing	f (Hz)	M_R (Nm)	H_R (N)	N
CT_C_45%_0.5Hz_4D_1	9	0.5	367	811	1000
CT_C_45%_0.1Hz_4D_1	8	0.1	321	897	1000
CT_C_45%_0.1Hz_4D_2	13	0.1	-	-	5584
CT_C_45%_0.01Hz_4D_1	8	0.01	-	-	717
CT_C_45%_var_4D_1	12	0.01 ~ 0.5	366	925	1000
CT_C_22.5%_0.5Hz_4D_1	9	0.5	398	1065	1000
CT_C_22.5%_0.01Hz_4D_1	11	0.1	429	1052	1000

The load path in Figure 3-16 is adopted for the cyclic loading tests. For all the tests, the initial loading and unloading rates (Phase I) were performed at $\dot{F} = 0.35$ N/s and -0.35 N/s, respectively, to observe repeatability and variation. During the cyclic loading (Phase II), constant magnitude sinusoidal cyclic loads were applied. The cyclic load frequency f was fixed, except for the illustrative example with time-varying f (CT_C_45%_var_4D_1). In most tests, the maximum cycle number (N) was 1000. In test CT_C_45%_0.1Hz_4D_2, 5584 cycles were completed, while in test CT_C_45%_0.01Hz_4D_1, the cyclic loading ended at N = 717 because θ reached the test limit of 4°. During Phase III, constant rate monotonic loading was applied to explore pile capacity post cyclic loading. For $\zeta_b = 0.45$, the monotonic loading rate $\dot{F}$ was set to 1 N/s, while for $\zeta_b = 0.225$, $\dot{F}$ was set to 0.35 N/s.

4.4.2 Effects of the load frequency and magnitude

4.4.2.1 Moment-rotation responses

Normalised moment-rotation responses at constant f with $\zeta_b = 0.45$ and 0.225 are shown in Figure 4-24, and selected cycles are highlighted in Figure 4-25 and Figure 4-26. When $\zeta_b = 0.45$ and $f = 0.01$ Hz, excessive permanent θ is observed during the cyclic loading, and the maximum N is 717 cycles (see Figure 4-25 (a)). At higher rates (f = 0.1 Hz and 0.5 Hz), the rate of the accumulated θ is slower than that at 0.01 Hz (see Figure 4-25 (b) and (c)). When $\zeta_b = 0.225$, the shape of the hysteresis loop only changes slightly with N, as illustrated in Figure 4-26 (a) and (b).

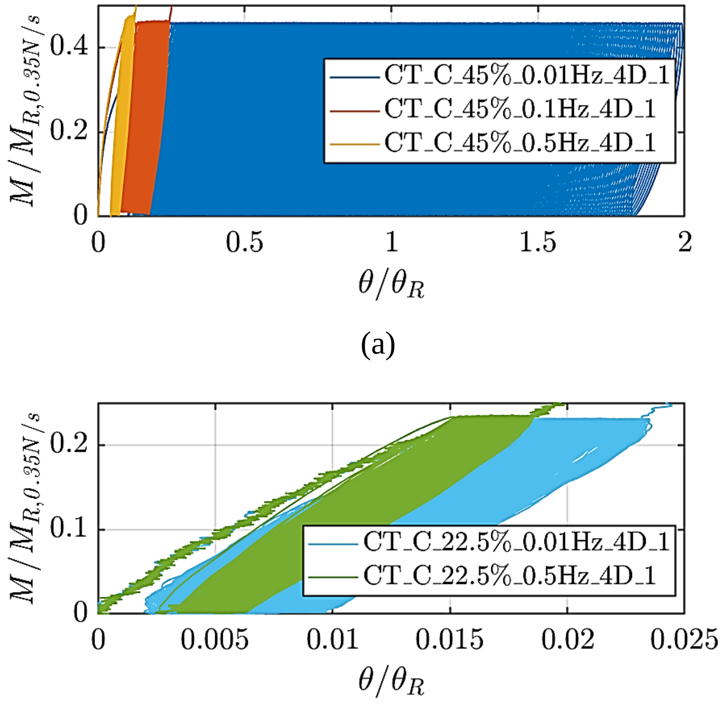

(a)

(b)

Figure 4-24 Comparing normalised moment-rotation responses at constant f:
(a) $\zeta_b = 0.45$ (b) $\zeta_b = 0.225$.

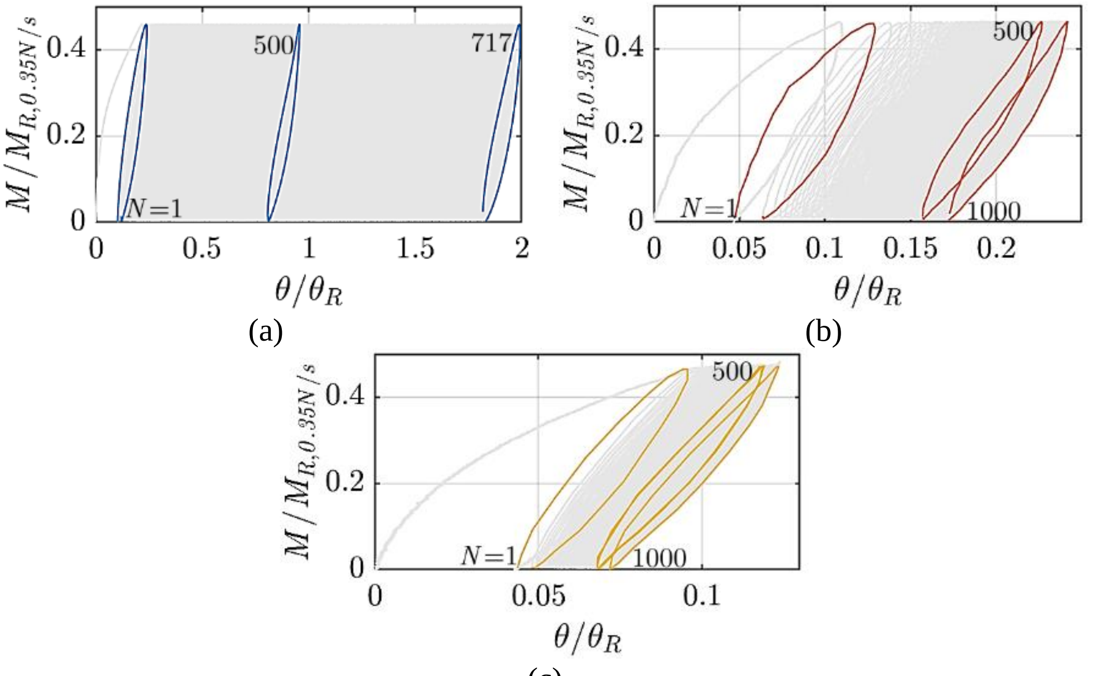

(a) (b)

(c)

Figure 4-25 Normalised moment-rotation responses under constant f with $\zeta_b = 0.45$:

(a) f = 0.01 Hz; (b) f = 0.1 Hz; (c) f = 0.5 Hz.

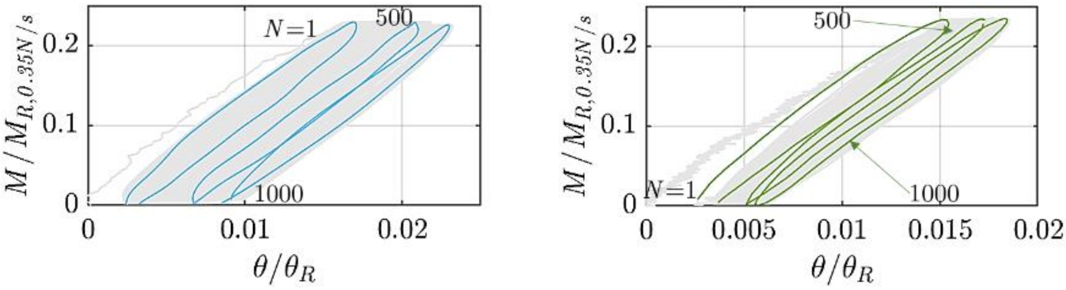

(a) (b)

Figure 4-26 Normalised responses under constant f with $\zeta_b = 0.225$:

(a) f = 0.01 Hz; (b) f = 0.5 Hz.

4.4.2.2 Deformation responses

The relationships of $\Delta\theta/\theta_R$ and $\Delta u/u_R$ with N for the constant magnitude cyclic loading tests are shown in Figure 4-27 (a) and Figure 4-28, respectively. Overall, the responses of $\Delta\theta/\theta_R$ and $\Delta u/u_R$ show a similar trend, and ratcheting is evident. As the tests were conducted in saturated stiff clay, other time-dependent factors (*e.g.* pore pressure dissipation) also influence cyclic characteristics in addition to soil rate effects. Although time-dependent soil behaviour due to partial drainage is not included in the research scope, experimental observations are provided and discussed for further research.

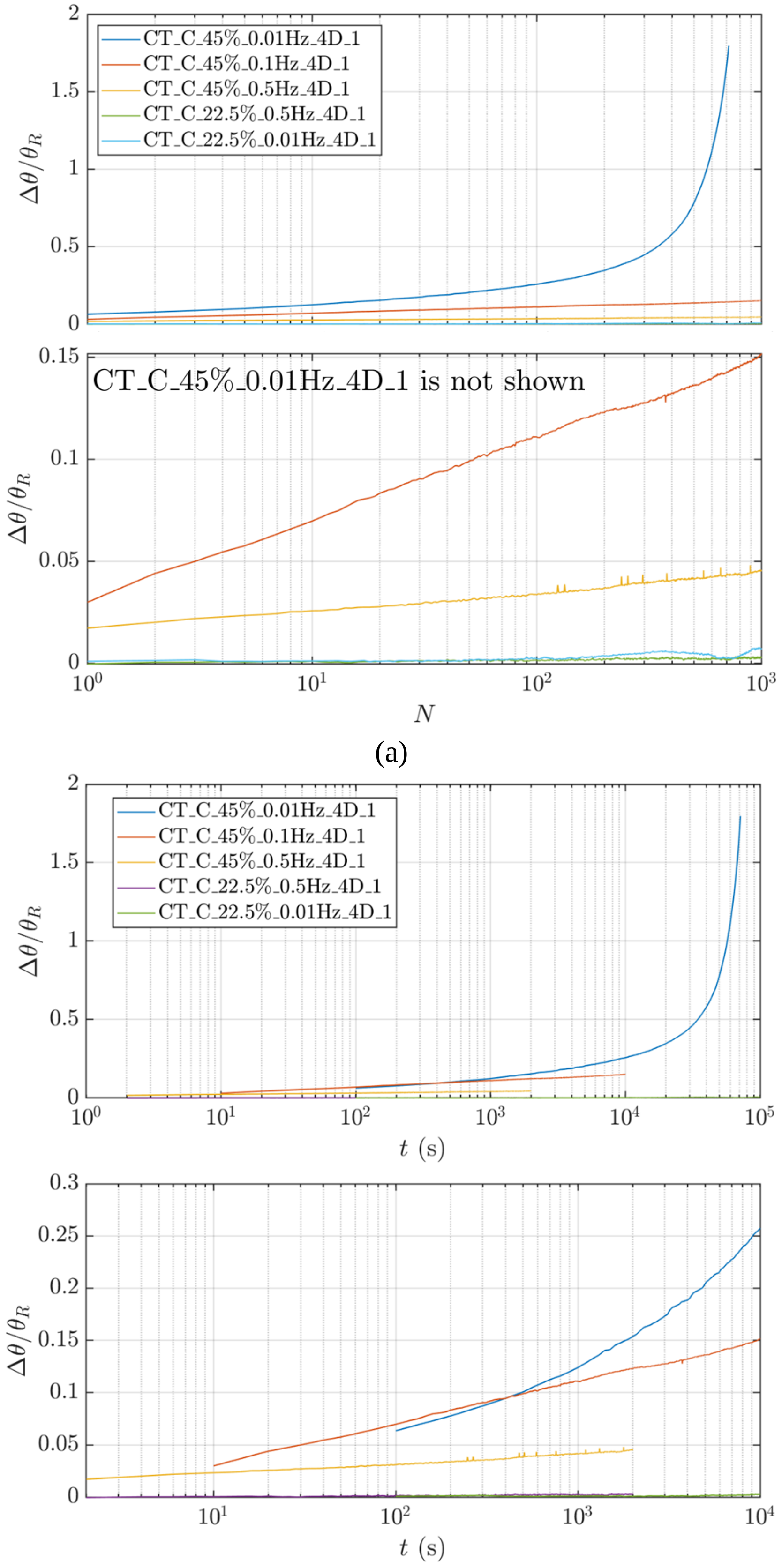

(a)

(b)

Figure 4-27 $\Delta\theta/\theta_R$ responses under constant magnitude cyclic lateral loading at different f: (a) $\Delta\theta/\theta_R$ versus N; (a) $\Delta\theta/\theta_R$ versus time t.

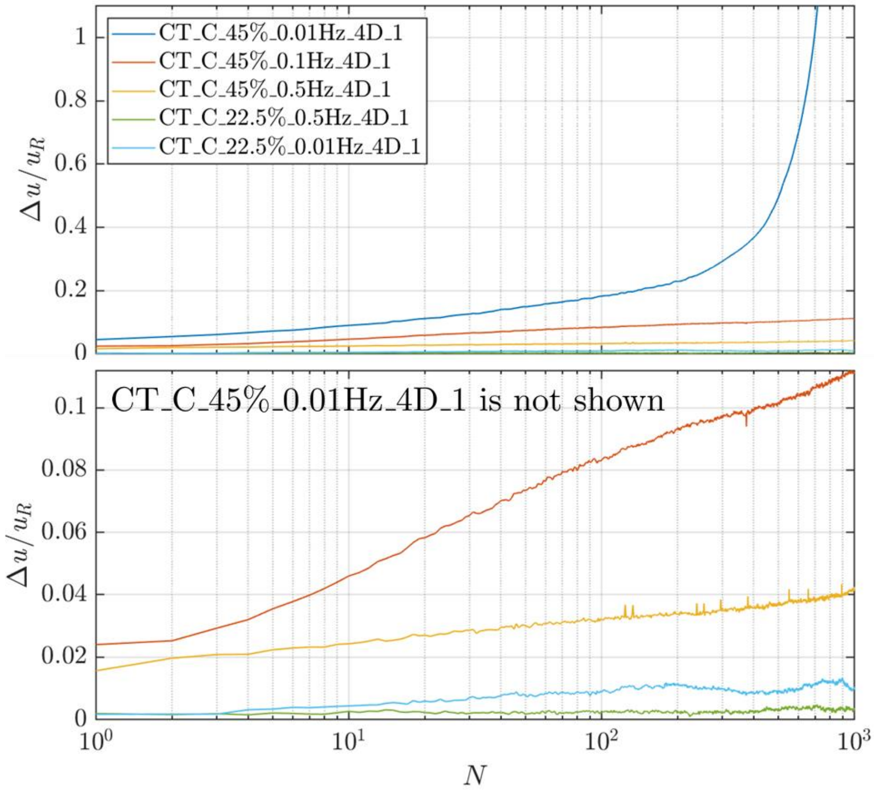

Figure 4-28 $\Delta u/u_R$ responses under constant magnitude cyclic lateral loading at different f.

For the test with $\zeta_b = 0.45$ and $f = 0.01$ Hz, when N = 3 (*i.e.* 300 seconds since the start of the test, see Figure 4-27 (b)), the maximum θ reaches 0.5°, which is often considered the allowable tilt angle for OWTs. This phenomenon may also be time-dependent and influenced by pore pressure response. For the tests with $\zeta_b = 0.45$ and $f = 0.1$ and 0.5 Hz, the rates of accumulated u and θ are much lower than that at 0.01 Hz. After 1000 cycles are complete (the accumulated θ due to the cyclic loading is less than 0.5°. For $\zeta_b = 0.225$, u and θ slightly increase with the cyclic loading. The variation between the two ratcheting responses at different f is minor, and the maximum θ due to cyclic loading reaches approximately 0.04° ~ 0.05°.

4.4.2.3 Pile secant stiffness and energy loss with cyclic loading

The maximum pile stiffness during the initial loading k_{max} ($\Delta\theta$ = 0.003°, $\dot{F}$ = 0.35 N/s) and the secant pile stiffness in the 1st cycle (k_1) are used for normalisation to explore rate effects, as shown in Figure 4-29. The ratio of k/k_{max} represents the stiffness change compared to the initial response. The ratio of k/k_1 focuses on the stiffness change under cyclic loading.

From the data, rate dependency during cyclic loading is evident. During the 0^{th} cycle (Phase I), the "equivalent" f for $\zeta_b = 0.45$ and 0.225 are 0.0005 Hz and 0.001 Hz, respectively, which are much smaller than the range of f tested during the cyclic loading (Phase II). Unlike the testing in dry sand (see Sections 3.6.3 and 3.6.4), the k/k_{max} ratio does not increase during cyclic loading, but does appear to increase with f. The magnitude of k is stable throughout the cyclic loading, except for the test with $\zeta_b = 0.45$ and $f = 0.01$ Hz, in which softening occurred with excessive pile deformation. Otherwise, no deterioration of k with cyclic loading was observed.

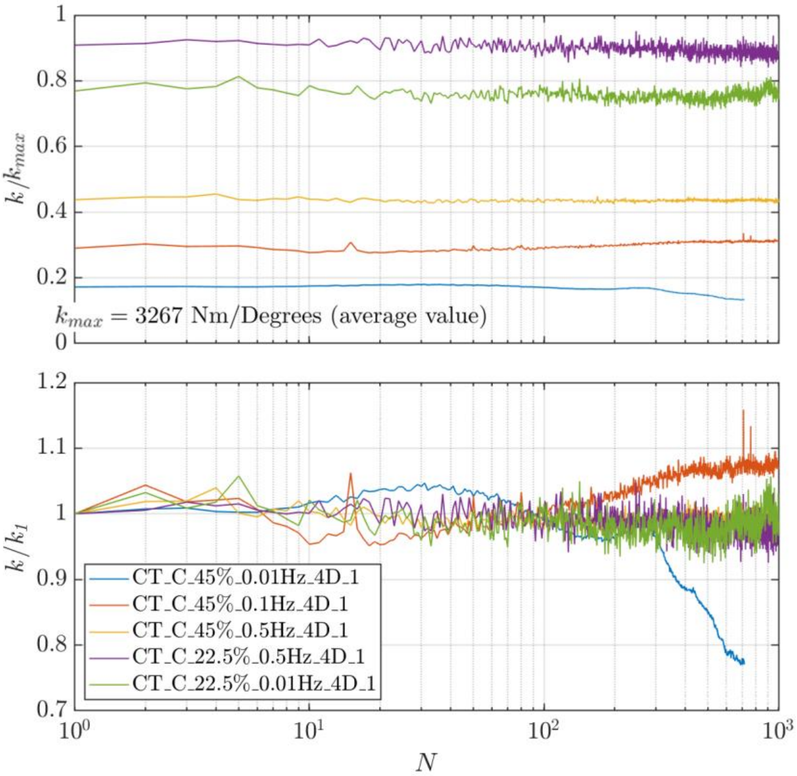

Figure 4-29 Normalised k/k_{max} and k/k_1 responses with N under constant magnitude cyclic lateral loading at different f.

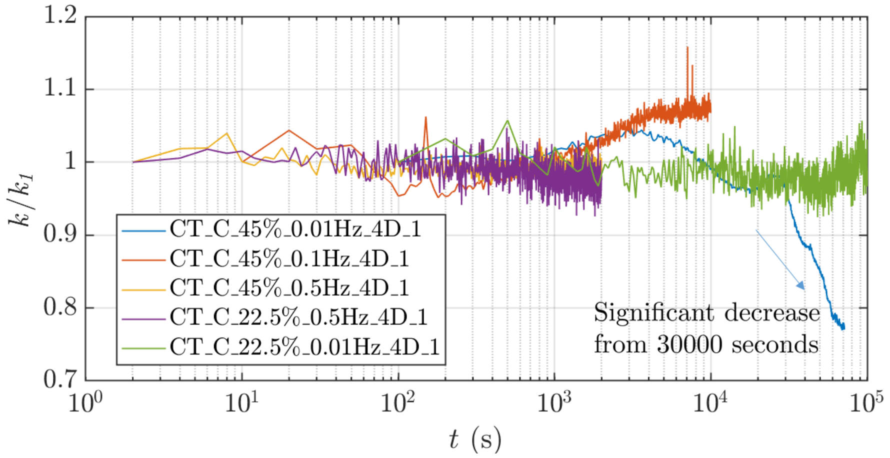

Figure 4-30 Normalised k/k_1 responses with time
under constant magnitude cyclic lateral loading at different f.

With $\zeta_b = 0.45$ and $f = 0.01$ Hz, k begins to drop significantly from $N = 80$ and becomes 25% lower than k_1 when $N = 717$. k starts to decrease from approximately 30000 seconds since the start (see Figure 4-30). This phenomenon does not appear when $\zeta_b = 0.225$ and $f = 0.01$ Hz. Although these two tests were performed at the same f, the difference in behaviour is possibly due to the variation in ζ_b producing different pore pressure responses, or due to some threshold stress for degradation to occur.

Kim (1991) reports that the damping ratio (or energy loss per cycle) is rate-sensitive in clay based on element test research (see Figure 1-16), observing it to become greater with increasing f. However, Figure 4-31(a) shows an inverse trend—η becomes larger with decreasing f. It is noted that the element tests, including the torsional shear and resonant column tests conducted by Kim (1991), were strain-controlled under two-way cyclic loading. The tests shown in Figure 4-31 were subject to uni-directional one-way load-controlled cyclic loading. Thus, the energy dissipation behaviour may differ from that reported by Kim (1991). Except for $\zeta_b = 0.45$ at $f = 0.01$ Hz, the energy loss factor η steadily decreases with N. For $\zeta_b = 0.45$ at $f = 0.01$ Hz, η decreases until $N = 200$, after which it increases significantly (see Figure 4-31 (b)).

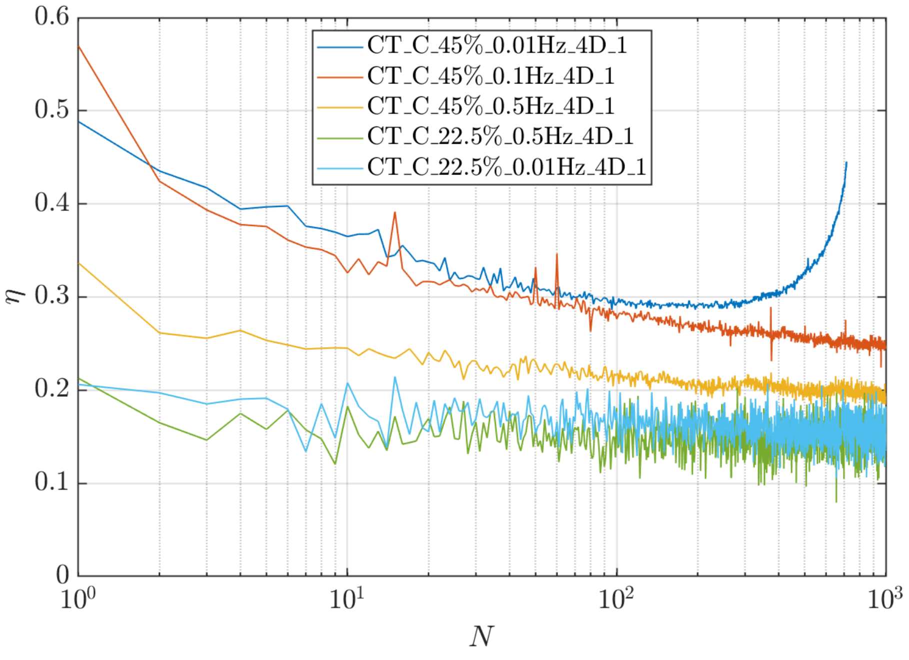

(a)

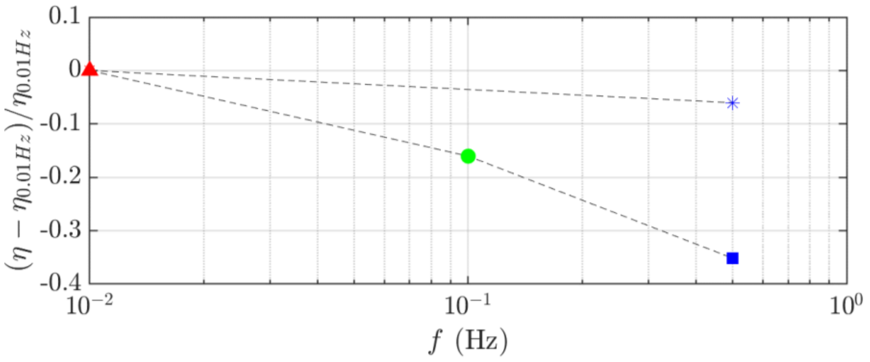

(b)

Figure 4-31 η responses from the constant magnitude cyclic lateral loading tests at different f: (a) η versus N; (b) comparing η with η measured at 0.01 Hz ($\eta_{0.1Hz}$).

4.4.2.4 Variable load frequency

In test CT_C_45%_var_4D_1, f was varied stepwise between 0.01 Hz, 0.1 Hz and 0.5 Hz for every hundred cycles, as detailed in Table 4-11. This test illustrates how a sudden change in f can influence cyclic characteristics. The hysteresis loops during the changes in f are shown in Figure 4-32. When f suddenly increases, the change in θ in the cycle is reduced, leading to a stiffer pile response (see, *e.g.* f increases from 0.01 Hz to 0.5 Hz when N = 300 ~ 301 and 900 ~ 901). Inversely, if f becomes slower (see N = 100 ~ 101, 200 ~ 201, 400 ~ 401, 500 ~501, 700 ~ 701 and 800 ~ 801), the hysteresis loop deforms with more change in θ during the cycle. This phenomenon suggests that if rapid cyclic loading is being applied to the OWT structure, the foundation stiffness can suddenly change, which may also influence and dynamic properties of the structure.

Table 4-11 f changed for every 100 cycles during test CT_C_45%_var_4D_1.

f	0.5 Hz	0.1 Hz	0.01 Hz
N	1-100; 301-400; 601-700; 901-1000	101-200; 401-500; 701-800	201-300; 501-600; 801-900

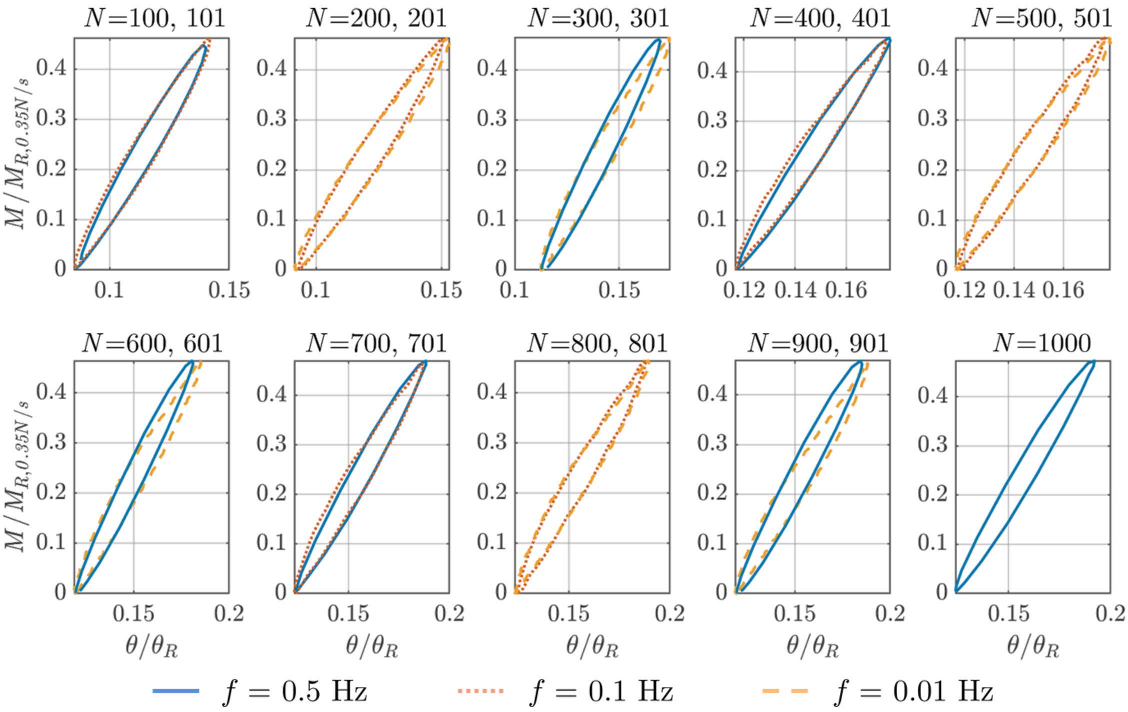

Figure 4-32 Hysteresis loops for every 100 cycles from test CT_C_45%_var_4D_1.

The pile deflection response to variable f is shown in Figure 4-33. It is noted that during the first ten cycles at f = 0.5 Hz, the cyclic loads did not reach the target load magnitude ζ_b of 0.45, and therefore the response when $N < 10$ is not shown for clarity. Overall, the $\Delta\theta_N/\theta_R$ and $\Delta u_N/u_R$ responses show a similar trend. With f decreasing, the rates of accumulated θ and u per cycle increase.

The slopes of $\Delta\theta_N/\theta_R$ in the semi-logarithmic plot in Figure 4-33 at $f = 0.01$, 0.1 and 0.5 Hz are similar to the slopes from the constant cyclic frequency tests with $\zeta_b = 0.45$ (see β values in Table 4-13). However, it is noted that only limited data are available for this case, and the pile response is also influenced by other time-dependent factors (*e.g.* pore pressure dissipation).

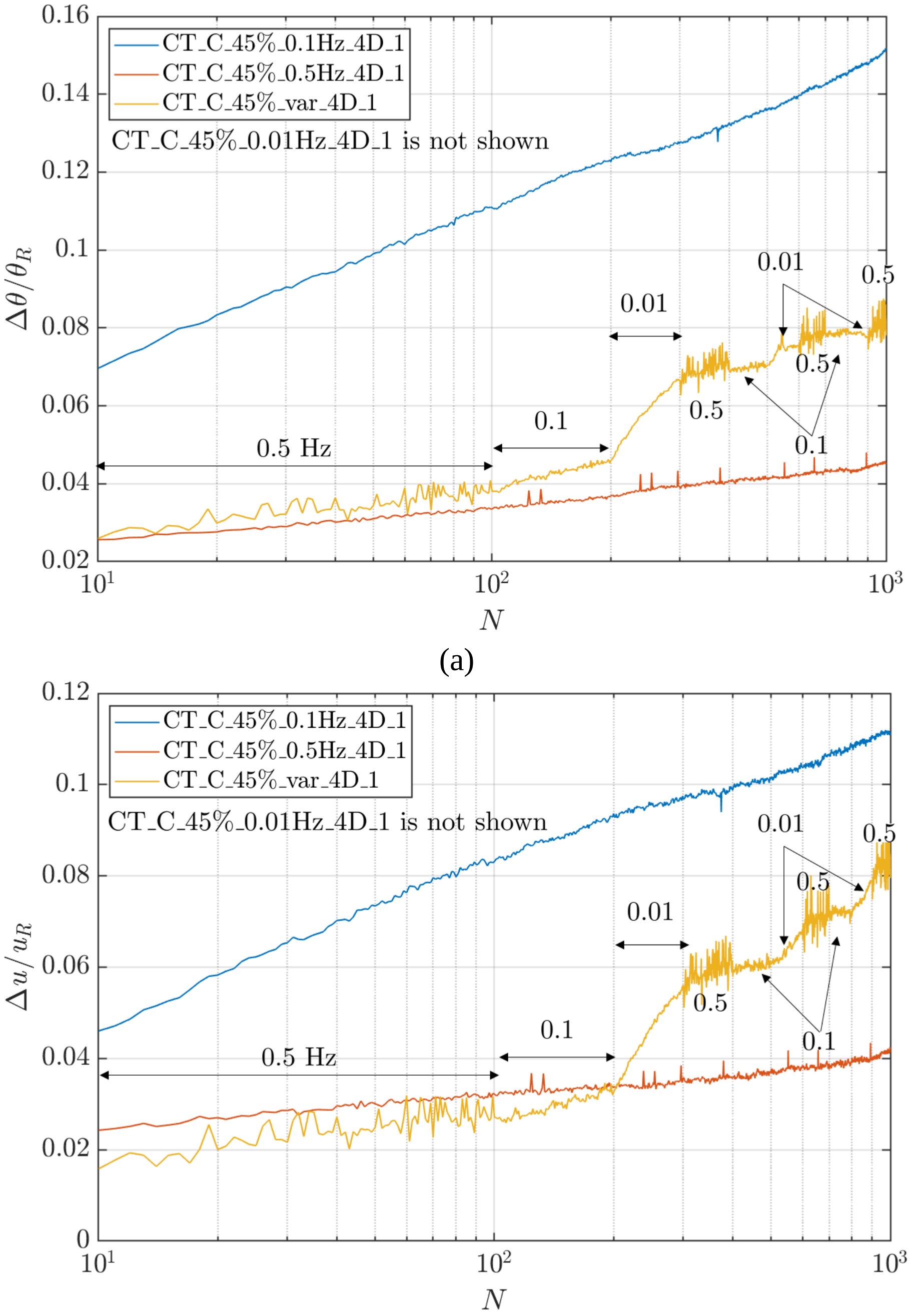

(a)

(b)

Figure 4-33 Deflection response to the large magnitude cyclic lateral loading from test CT_C_45%_var_4D_1: (a) $\Delta\theta/\theta_R$ with N; (b) $\Delta u/u_R$ with N.

The response of k is normalised using k_{max} and the pile secant stiffness for the 10th cycle (k_{10}). The response of the first ten cycles is omitted due to the load-controlled issue. In Figure 4-34, it can be seen that k increases with f. The η response is also rate-sensitive, as illustrated in Figure 4-35. With the rise in f, η tends to become smaller with less energy loss in the hysteresis loop.

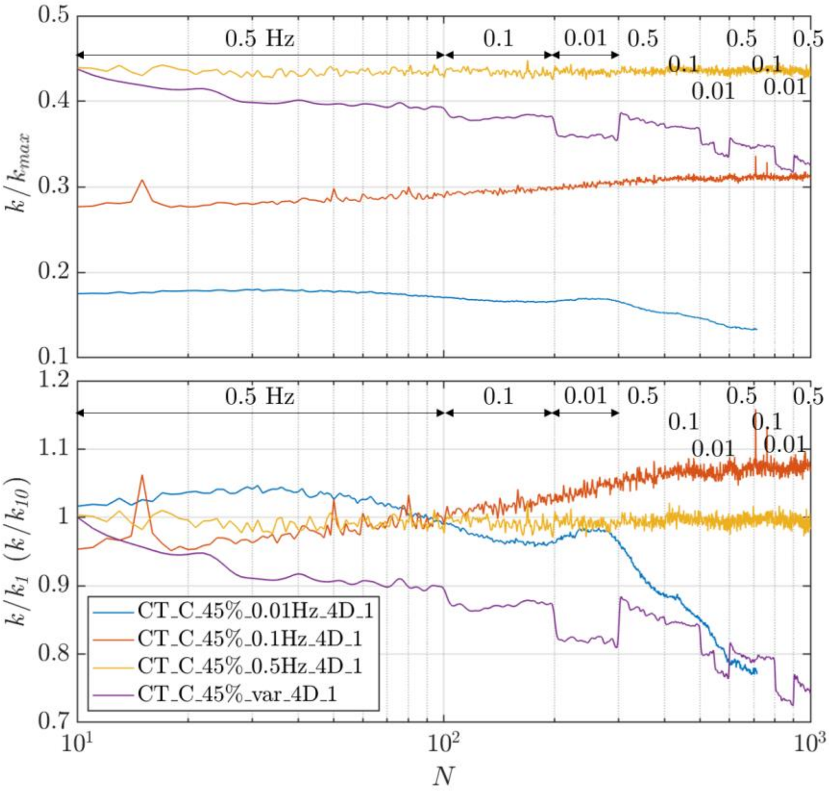

Figure 4-34 Normalised pile secant stiffness responses from test CT_C_45%_var_4D_1.

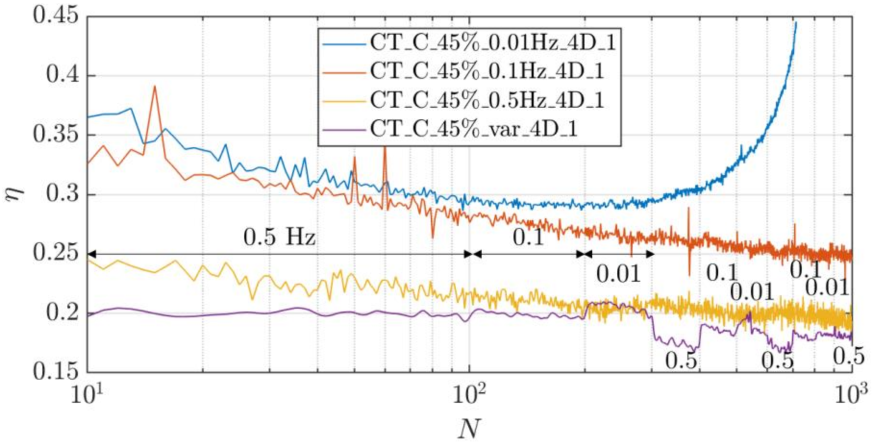

Figure 4-35 η response from test CT_C_45%_var_4D_1.

Although rate effects are observed in the responses of k and η, it is not straightforward to quantify these cyclic characteristics for the variable frequency test. This is because other factors, such as ratcheting, pore pressure dissipation and loading history, can influence cyclic behaviour.

4.4.3 Effect of high-cycle loading

A test with $\zeta_b = 0.45$ and $f = 0.1$ Hz was conducted to explore high-cycle response, as shown in Figure 4-36. The maximum accumulated rotation $\Delta\theta$ occurred when N = 900. At N = 5585, although $\Delta\theta$ is not greater than that at N = 900, pile secant stiffness k becomes observably softer.

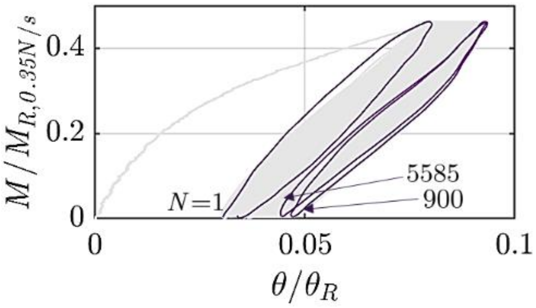

Figure 4-36 Normalised moment-rotation response of the high-cycle loading test ($\zeta_b = 0.45$; $f = 0.1$ Hz).

The deformation response and temperature measurements with N are illustrated in Figure 4-37. Compared with the constant magnitude cyclic loading responses with $N = 1000$ and $\zeta_b = 0.45$, the high-cycle test has a stiffer response and less ratcheting, possibly due to local soil variability. θ increases from N = 1 to 900, followed by a slight decrease with N, while u increases continuously until N = 3000.

The sensors and rig can be affected by temperature fluctuations during the test. Although the soil temperature (see Figure 4-37 (c)) was generally stable throughout the test, a slight temperature change above ground can slightly influence the measured $\Delta u/u_R$ response. During the cyclic loading, the travel distances of the LDTs were small, so the impact of temperature fluctuations can become evident, and the change in apparent response after $N = 3000$ may be related to the temperature change.

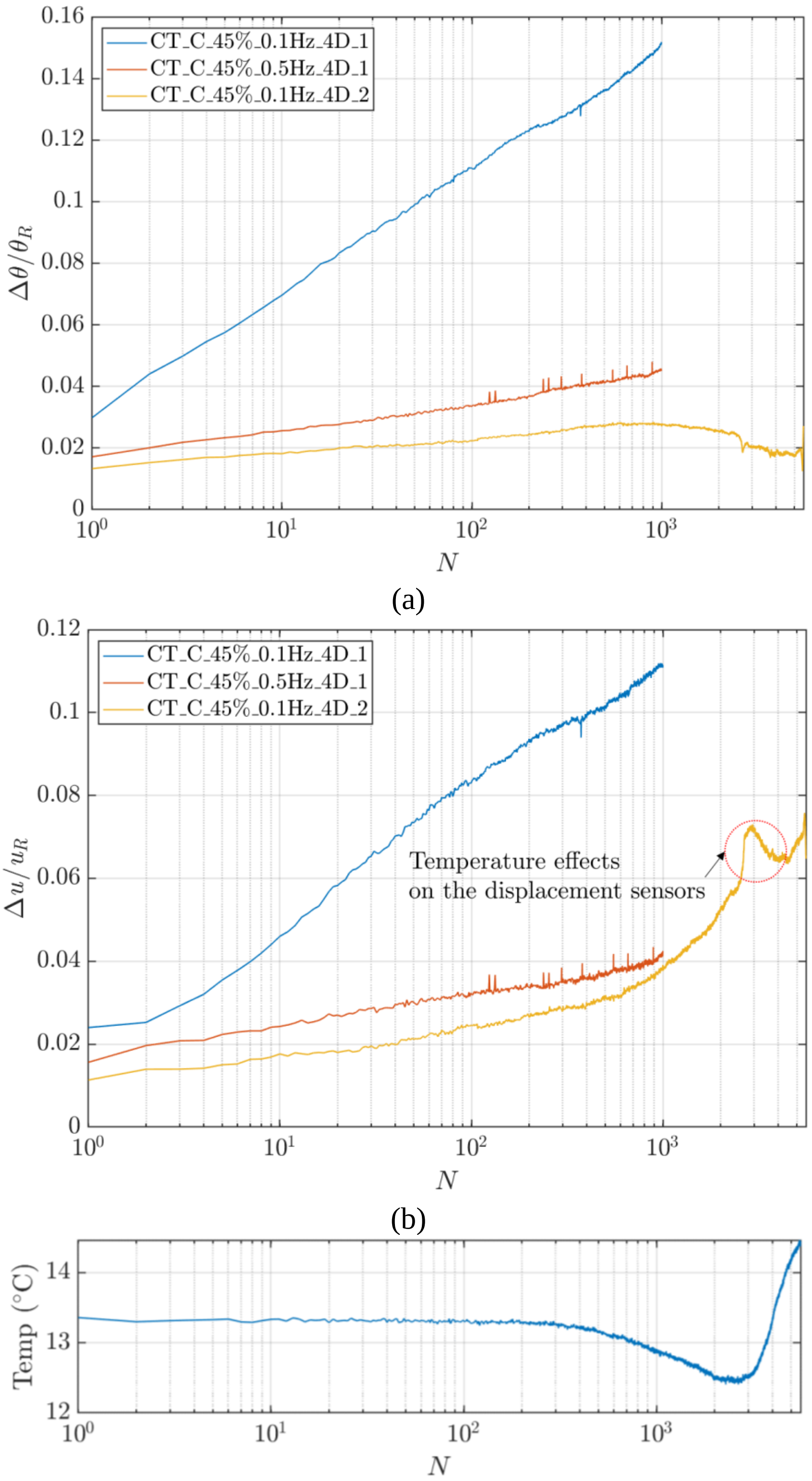

(a)

(b)

(c)

Figure 4-37 Deformation response and temperature measurements under high-cycle loading ($\zeta_b = 0.45$; $f = 0.1$ Hz): (a) $\Delta\theta/\theta_R$ with N; (b) $\Delta u/u_R$ with N; (c) temperature measurements.

The rotational mechanism of the model pile may change under high-cycle loading (see Figure 4-38). $\Delta\theta$ does not increase after N = 900, while u shows a continuous ratcheting response. The ratcheting was found much more in terms of u than in terms of θ. The slope of $u/u_R - \theta/\theta_R$ does not significantly change with N (*i.e.* the pile pivot point was unlikely to change substantially during the test).

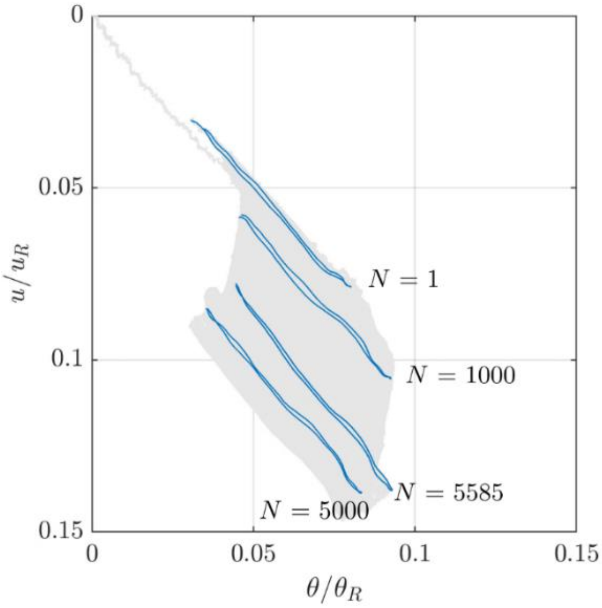

Figure 4-38 Normalised relationship between θ and u under high-cycle loading ($\zeta_b = 0.45$; $f = 0.1$ Hz).

Figure 4-39 shows the normalised responses of k/k_{max} and k/k_1, and the response of η is illustrated in Figure 4-40. In a similar way to the tests with $\zeta_b = 0.45$ and $f = 0.1$ Hz and 0.5 Hz, k is stable for the first 1000 cycles. With the further increase in N, k continues to decrease slowly; at N = 5585, k is 4% smaller than that at the first cycle. η steadily decreases by 25% over the cyclic loading, and the slope of the curve is similar to that of the tests with $\zeta_b = 0.45$ and $f = 0.1$ Hz and 0.5 Hz.

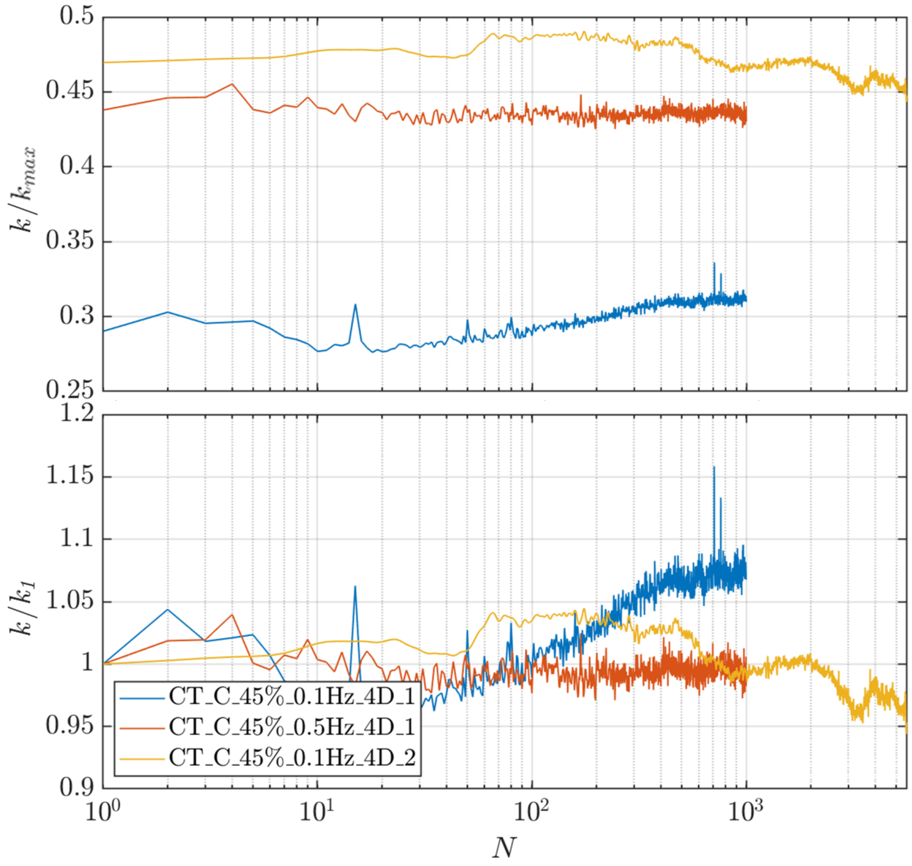

Figure 4-39 Normalised k response to high-cycle loading with N ($\zeta_b = 0.45$; $f = 0.1$ Hz).

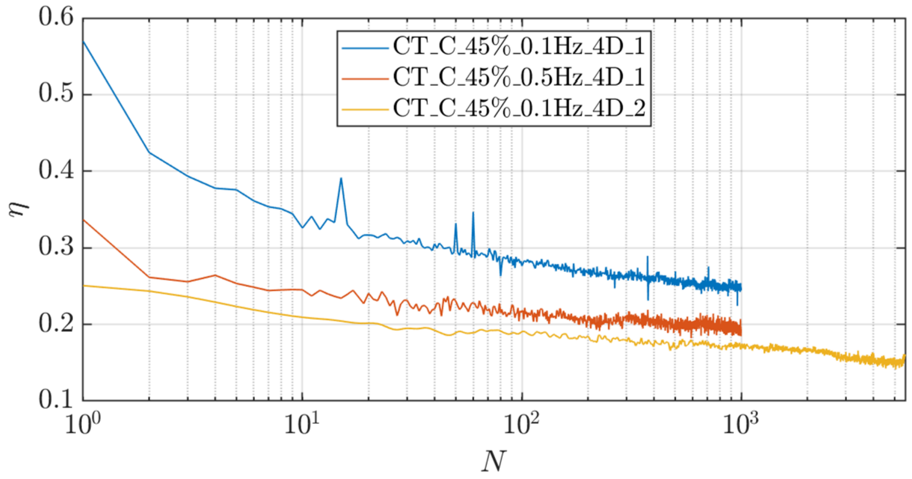

Figure 4-40 η response to high-cycle loading ($\zeta_b = 0.45$; $f = 0.1$ Hz).

4.4.4 Post-cyclic monotonic loading

The post-cyclic monotonic response from the cyclic tests is shown in Figure 4-41. During the post-cyclic monotonic loading, fast ($\dot{F}$ = 1 N/s) and slow (0.35 N/s) rates were applied to tests with $\zeta_b = 0.45$ and 0.225, respectively. As previously mentioned, the test with $\zeta_b = 0.45$ and $f = 0.01$ Hz ended at $N = 717$ and could not continue to move forward to the post-cyclic monotonic loading phase due to the excessive permanent pile deformation. Amongst the post-cyclic monotonic tests, only the response of $\zeta_b = 0.45$ and $f = 0.1$ Hz shows slightly reduced capacity. Pile capacity does not appear to decline for all other cases due to their cyclic loading history; this is an important observation with implications for pile design.

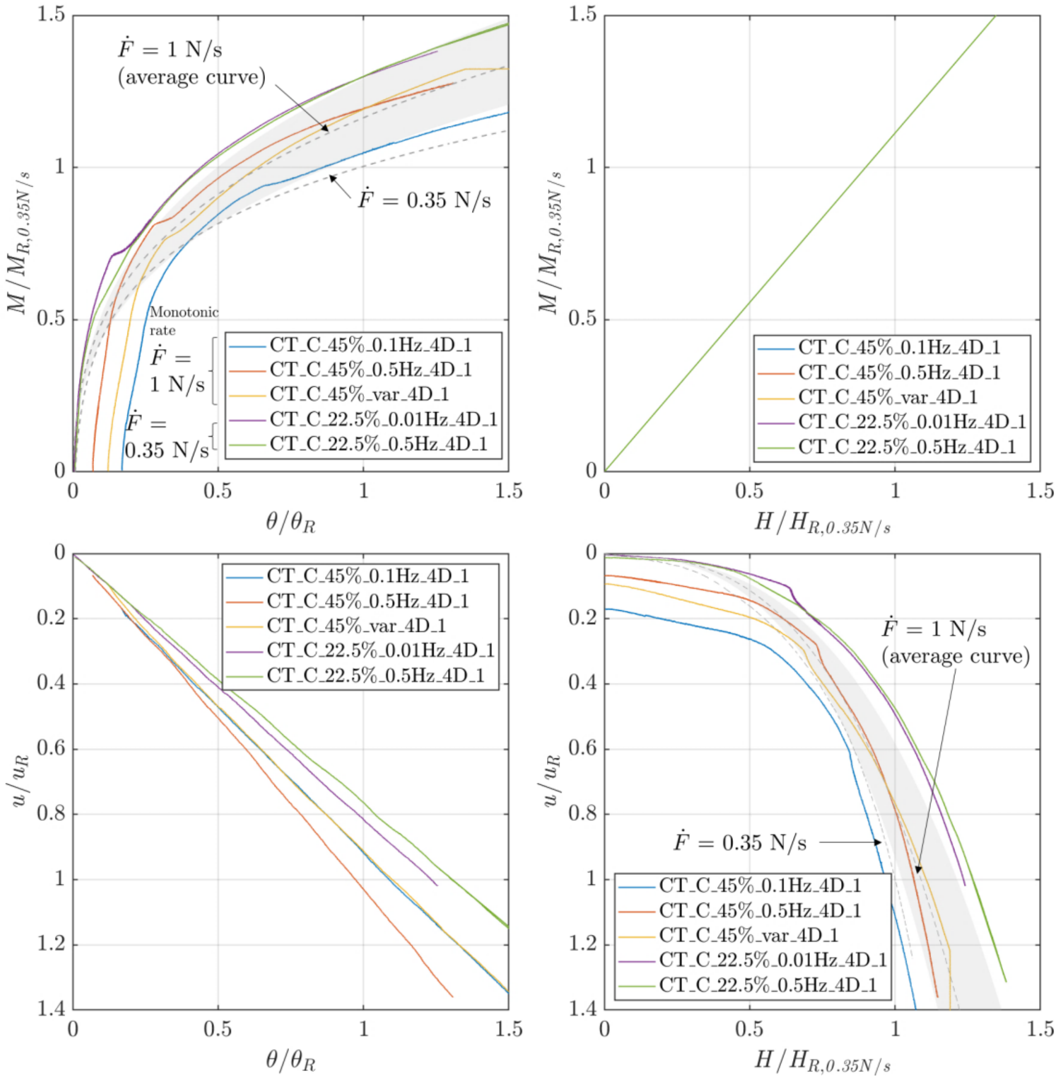

Figure 4-41 Normalised responses of the post-cyclic monotonic loading.

In the $p - y$ method, pile capacity is considered to be reduced due to cyclic loading. However, cyclic rate effects are not considered in the $p - y$ analysis, and data on stiff clay are limited in the literature to inform monopile design.

It is also noted that two-way and multi-directional cyclic responses are not discussed in this thesis, and their post-cyclic responses may differ from that under one-way cyclic loading.

4.4.5 Pseudo-random cyclic lateral loading

Two pseudo-random cyclic lateral loading tests (see Table 4-12) were conducted to simulate realistic time-varying cyclic lateral loads being applied on an OWT. The input load data were designed based on modified OWT monitoring data by McAdam (2021) and can be categorised by the maximum loads used to scale the load sequence (H_{max}):

(1) small magnitude loading (H_{max} = 100 N, 11% $M_{R,1N/s}$),

(2) medium magnitude loading (H_{max} = 235 N, 27% $M_{R,1N/s}$),

(3) large magnitude loading (H_{max} = 591 N, 68% $M_{R,1N/s}$).

In test CT_C_ran_4D_1, only the large magnitude loading was applied, while in test CT_C_ran_4D_2, all three types of loading were performed to evaluate the impacts of various cyclic load magnitudes on the overall pile response.

Table 4-12 Descriptions for the pseudo-random cyclic lateral loading tests

Test name	Days between installation and testing	M_R (Nm)	H_R (N)
CT_C_ran_4D_1	6	-	-
CT_C_ran_4D_2	8	317	894

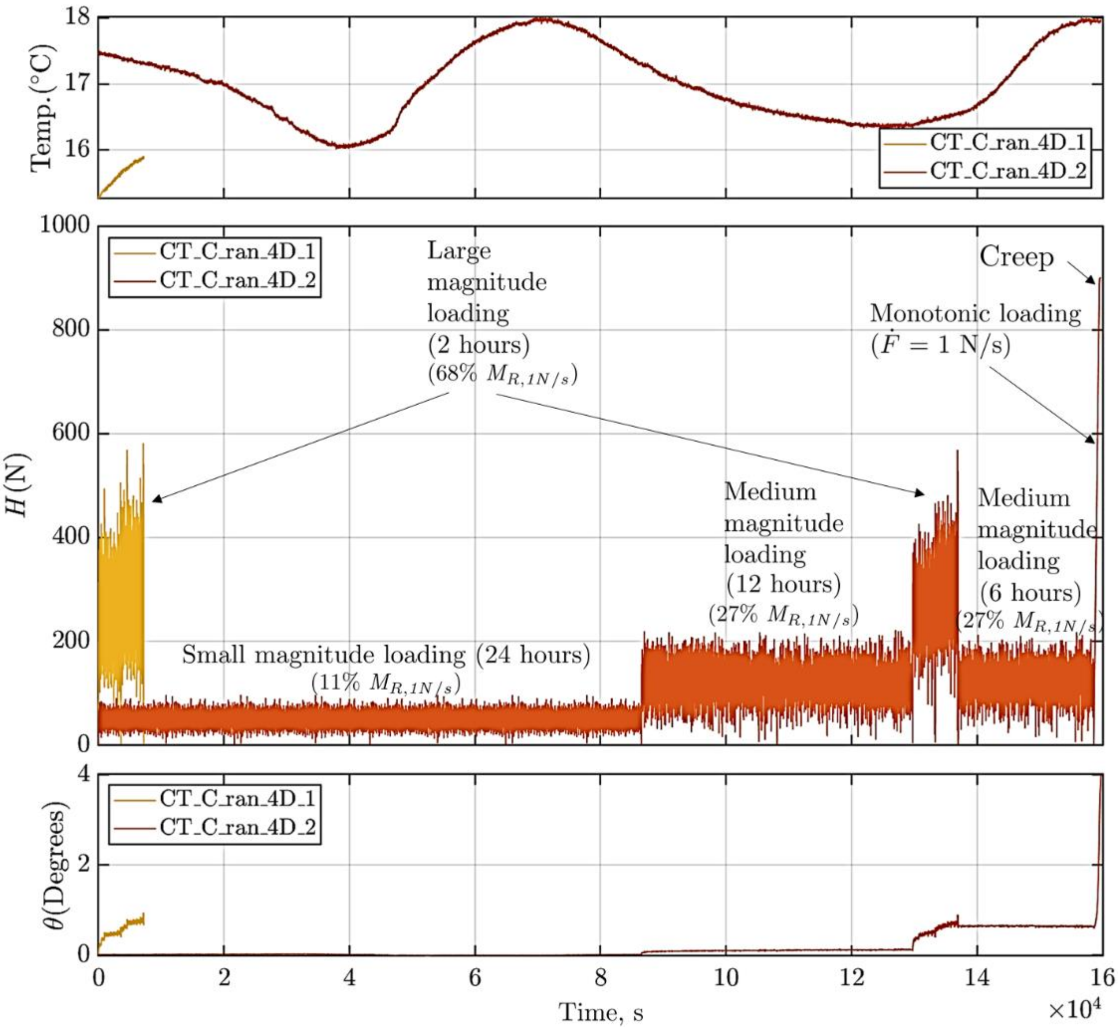

Figure 4-42 Temperature, H and θ with time
from the pseudo-random cyclic lateral loading tests.

Figure 4-42 shows the temperature, H and θ responses with time from the pseudo-random cyclic lateral loading tests. In both tests, the soil temperature was stable. In test CT_C_ran_4D_1, the large magnitude loading was applied for 2 hours. In CT_C_ran_4D_2, the small magnitude loading was first performed for 24 hours, followed by the 12-hour medium magnitude loading and the 2-hour large magnitude loading. Afterwards, the medium magnitude loading was performed for 6 hours, followed by monotonic loading at $\dot{F}$ = 1N/s.

For both tests, the maximum θ due to the cyclic loads is approximately 0.9°, suggesting that the small and medium magnitude loading do not strongly impact the ultimate response. In test

CT_C_ran_4D_2, after the large magnitude loading, the 6-hour medium magnitude loading was applied, but the permanent pile deformation did not continue to increase.

During the cyclic loading, the overall responses from the two tests are similar, and the small and medium magnitude loading influences appear to be minimal, as shown in Figure 4-43. In test CT_C_ran_4D_2, θ only reached 7% θ_R when the pile was subject to the medium magnitude loading, but it went up to 45% θ_R when the large magnitude loading was applied. Under the large magnitude loading, permanent pile rotation $\Delta\theta$ exceeds the SLS limit ($\theta = 0.5°$). It is unclear whether this phenomenon is also seen in full-scale monopiles, and care is required when assessing cyclic effects in design.

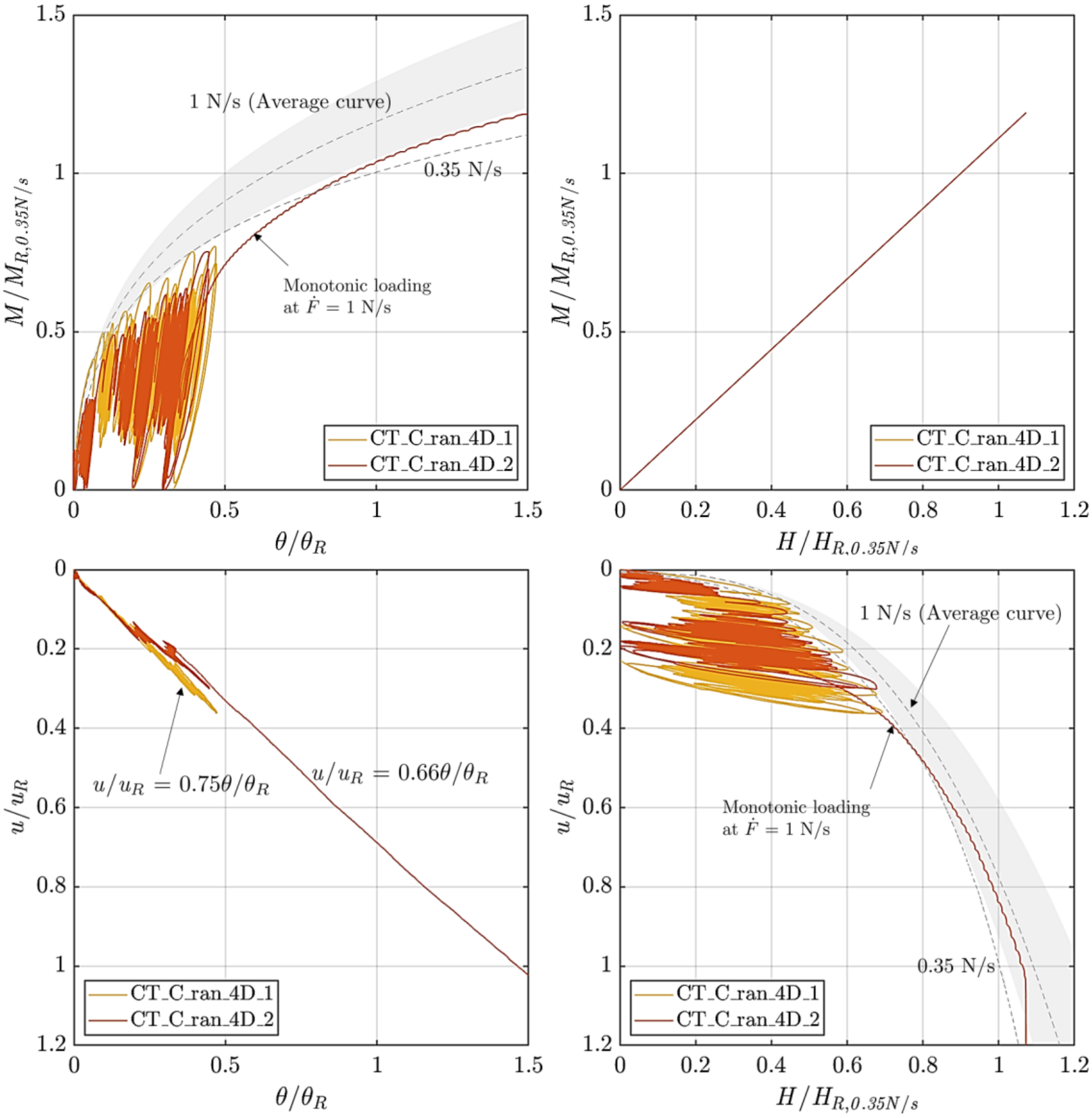

Figure 4-43 Normalised responses of the pseudo-random cyclic lateral loading tests.

The input loads for the model tests were scaled down from the design loads for the medium-scale piles in the PICASO project, but details are not discussed in this thesis. Further information can be found in the PICASO Project Test Manual (PICASO AWG, 2022).

4.4.6 Quantification of rate effects for monopiles under cyclic lateral loading

4.4.6.1 Ratcheting

In a similar way to the tests in dry sand, the ratcheting behaviour from the constant frequency tests in saturated stiff clay can be fitted using Equation 3-3. For $\zeta_b = 0.45$ and $f = 0.01$ Hz, plastic deformation sharply increases when $N > 100$ ($i.e.$ after 10000 seconds from the start of the test), and only the small-cycle response ($N < 100$) is quantified. Overall, with the increase in f, the constants A (the initial increment of $\Delta\theta_N$) and β (the rate of increasing θ with N) decrease.

Table 4-13 Parameters for quantifying ratcheting.

ζ_b	f (Hz)	A	β
0.45	0.5	0.0194	0.1221
	0.1	0.0571	0.1406
	0.01	0.0602 (only applicable when $N < 100$)	0.3137
0.225	0.5	0.000139	0.2193
	0.01	0.000753	0.2813

4.4.7 Summary of the pile response to cyclic lateral loading

The test data demonstrate cyclic rate effects for the model pile in stiff clay in terms of ratcheting and stiffness per cycle, and the magnitude of cyclic rate effects depends on the cyclic load magnitude. With the increase in the load frequency f, pile secant stiffness k becomes greater, and less evolution of permanent pile deformation occurs. Except for the test with $\zeta_b = 0.45$ and $f = 0.01$Hz, the other tests show that k does not significantly decrease with the cycle number N, and pile capacity is unlikely to reduce due to cyclic loading.

In addition to rate effects, other time-dependent phenomena, such as pore pressure dissipation, need to be assessed in monopile design in stiff clay. However, pore pressure response is complex and depends on various factors (*e.g.* the cyclic load magnitude, pile size, etc.). Unfortunately, due to the testing scale, it was impossible to investigate pore pressure response in detail.

An illustrative example of variable load frequency shows that the rate of ratcheting may be estimated from the constant frequency tests. However, the response of k cannot be assessed in the same way, as the load history and pore pressure response also appear to affect the response.

An example of pseudo-random cyclic loading demonstrates that the pile response is more sensitive to large-magnitude cyclic loads, such as storm loading. The influence of small and medium magnitude loads is considered minimal. The load input was also used for the PICASO testing on the medium-scale piles. Data from different sizes of piles can be compared to study scaling issues.

4.5 Load eccentricity effects

Load eccentricity tests are summarised in Table 4-14. In the constant load eccentricity tests (e = $6D$ and $10D$), $\dot{F}$ was set to the same rate (= 0.35 N/s) to minimise rate effects. For achieving e = $10D$, both the actuators are used, and the allowable load limits for the actuators are expected to reach at $\theta = 0.5\theta_R$. In test CT_C_0.35N/s_10D_1, after θ = $0.5\theta_R$, the pile was unloaded to zero loads at $e = 10D$, followed by reloading at $e = 6D$. This was to prevent over-loading on the actuators while continuing to test the pile until $\theta = \theta_R$. M_R and H_R at $e = 10D$ are estimated. In the variable load eccentricity test, e is between $4D$ and $10D$. Details of the variable load eccentricity test can be found in Section 4.5.3.

Table 4-14 Descriptions for the load eccentricity tests.

Test name	Days between installation and testing	e	M_R (Nm)	H_R (N)
CT_C_0.35N/s_6D_1	11	$6D$	431	814
CT_C_0.35N/s_10D_1	11	$10D$	450[1]	470[1]
CT_C_0.35N/s_vare_1	8	$4D$ ~ $10D$	-	-

Note: [1] M_R and H_R are estimated by curve fitting using power-law functions.

4.5.1 Initial pile response

In the previous findings in dry sand, it was found that the moment-rotation response of the model piles was enhanced by increasing e, and this phenomenon is also found in clay. However, the initial response at $e = 10D$ is softer than at $e = 4D$ and $6D$ (see Figure 4-44). In the test at $e = 10D$, a low control gain was chosen to prevent the system from becoming unstable. Unfortunately, it also led to a soft response at the beginning of loading, and a longer response time was required to reach the target load and achieve the target e.

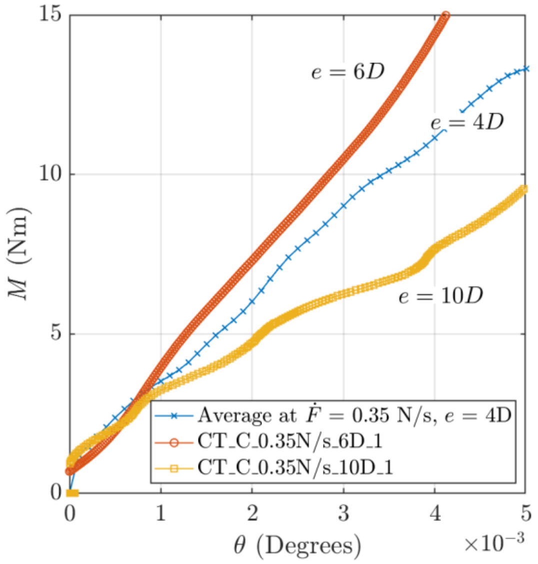

Figure 4-44 Initial pile responses at various e.

4.5.2 Constant load eccentricity tests at large pile movement

Figure 4-45 shows the responses of H and θ with time from the constant load eccentricity tests. All the tests were conducted at the same $\dot{F}$ to reduce the impact of soil rate effects. In test

CT_C_0.35N/s_10D_1, the control setting was adjusted when $H = 320$ N to minimise the influence of unstable control (see the spiky response in Figure 4-45).

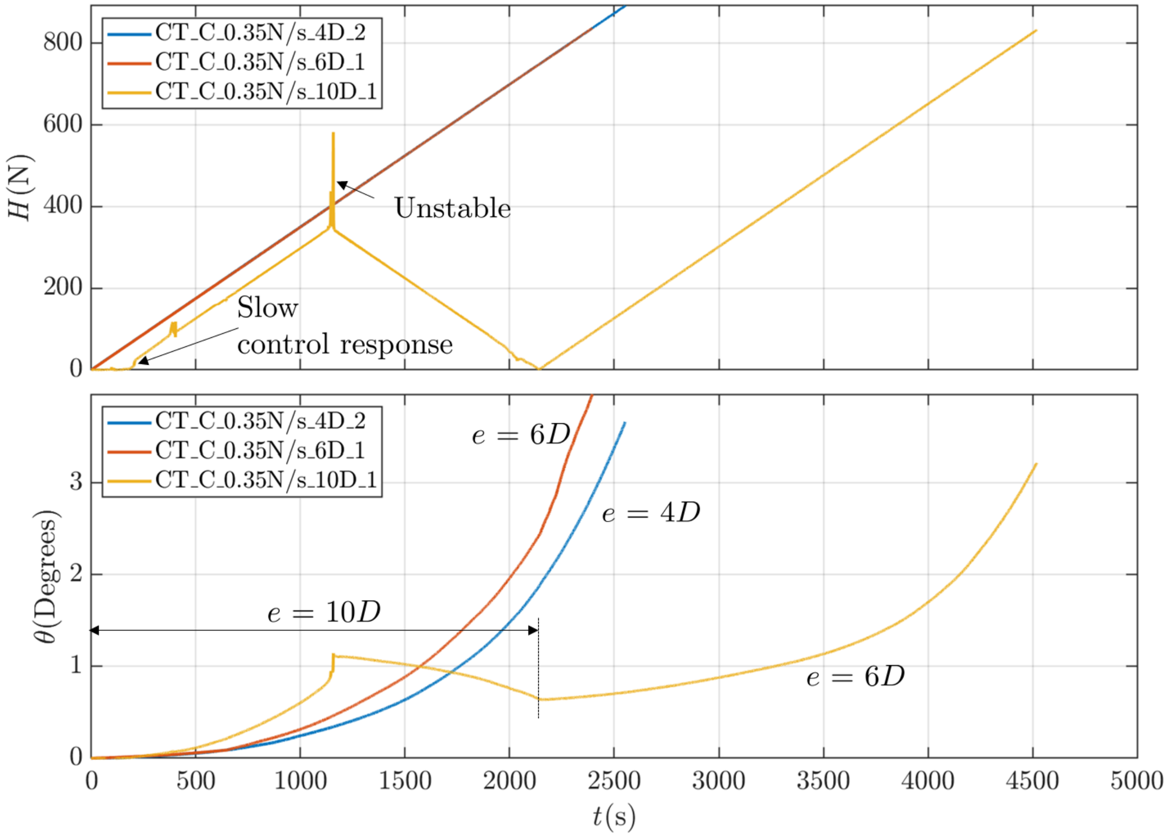

Figure 4-45 H and θ responses with time from the constant load eccentricity tests.

Normalised responses at $e = 4D$, $6D$ and $10D$ under large pile movement are shown in Figure 4-46. Similar to the testing in dry sand, the moment-rotation response of the model pile is enhanced with the increase in e (except for $e = 10D$ initially, see Figure 4-44), while the lateral load-displacement response becomes softer simultaneously.

The rotation-horizontal displacement response is approximately linear and shows dependency on e. During test CT_C_0.35N/s_10D_1, the horizontal displacement-rotation response altered during the change in e from $10D$ to $6D$. Further analysis using a yield surface approach is discussed in Chapter 6 to explain load eccentricity effects in stiff clay theoretically (see Figure 6-21).

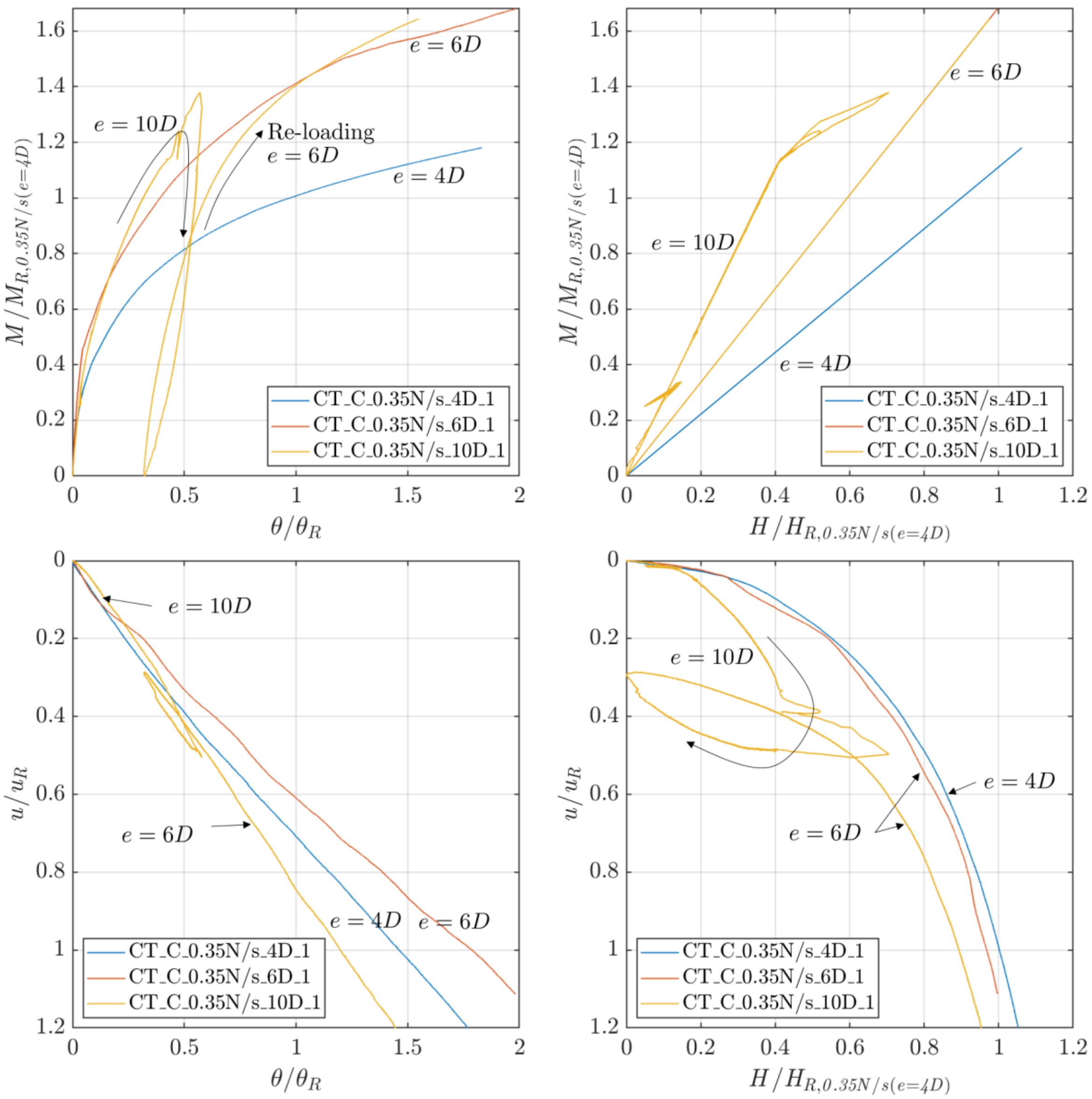

Figure 4-46 Normalised responses of the constant load eccentricity tests.

The normalised M/M_R and H/H_R responses at $e = 4D, 6D$ and $10D$ are shown in Figure 4-47. Similar to the previous findings in dry sand, these normalised responses do not vary with the height of the loading point, except for the spike at $e = 10D$ due to the control issue. Therefore, it may be possible to estimate the pile response with a fixed loading point through these normalised data.

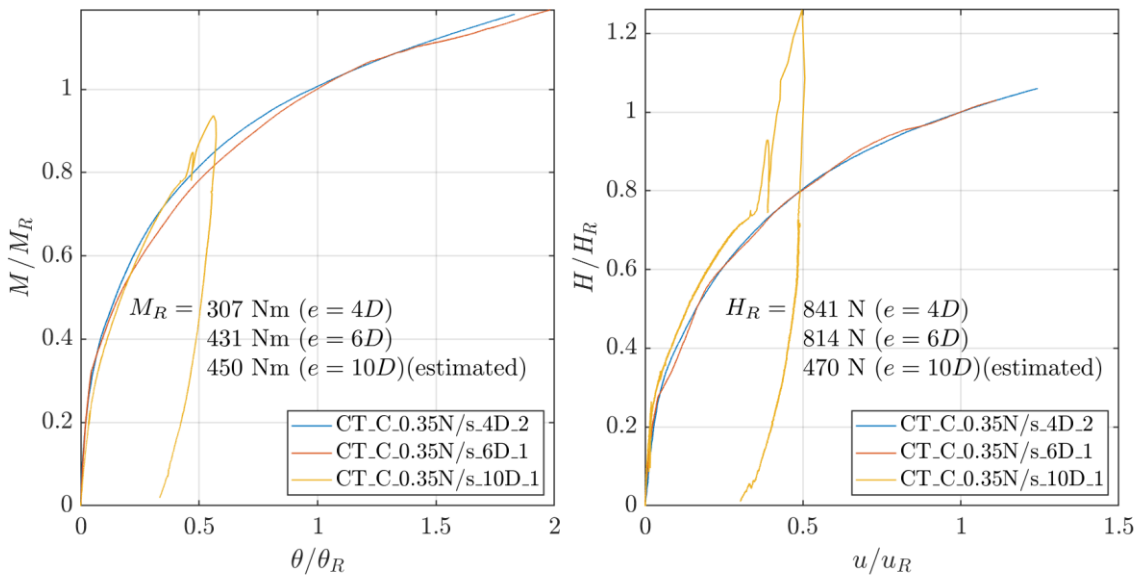

Figure 4-47 M/M_R and H/H_R responses from the constant eccentricity tests.

4.5.3 Variable load eccentricity

The H, M, e and θ responses from test CT_C_0.35N/s_vare_1 with time are illustrated in Figure 4-48. During the changes in e between $4D$ and $10D$, H is fixed; when e = $4D$ and $10D$, $\dot{F}$ = 0.35 N/s and -0.35 N/s, respectively. Figure 4-49 illustrates the response of the variable load eccentricity test, in comparison with the constant eccentricity tests at e = $4D$ and $10D$ with $\dot{F}$ = 0.35 N/s.

Similar to the variable load eccentricity test in dry *dense* sand (see Figure 3-29), pile response to variable e cannot be estimated by comparing constant load eccentricity tests. The load history also needs to be considered. The rotation-horizontal displacement response appears to change with e. The responses at $e = 4D$ and $10D$ are found to be estimated using the two parallel dashed lines in Figure 4-49. During the changes in e, θ appears to vary more significantly than u.

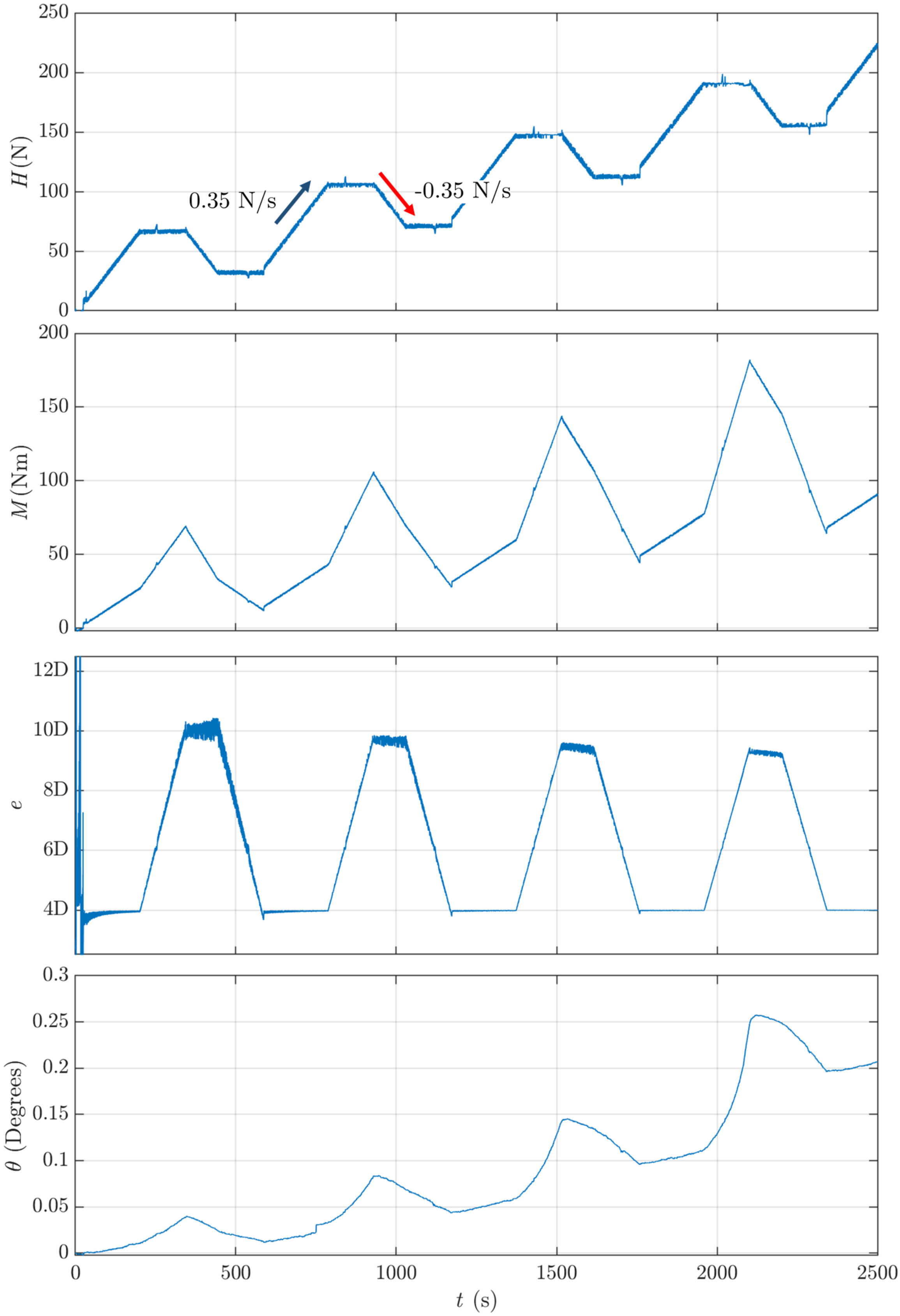

Figure 4-48 H, M, e and θ with time.

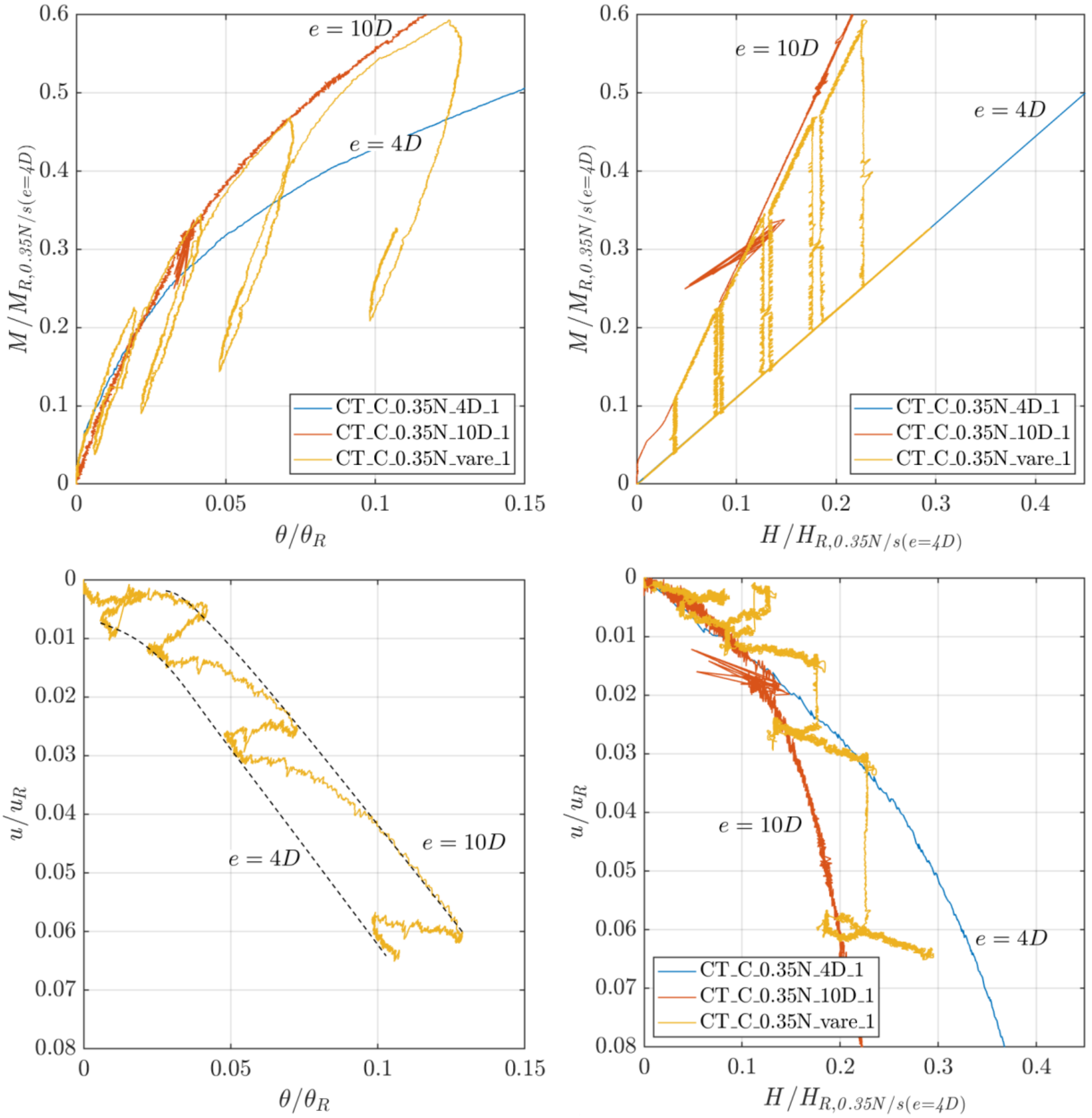

Figure 4-49 Normalised responses of the variable load eccentricity test.

In general, the deformation or load responses from the variable load eccentricity test are complex and cannot be characterised by constant eccentricity tests. Furthermore, the yielding behaviour may change, and the moment-rotation and horizontal load-displacement may show different trends with *e* varying with time.

4.5.4 Summary of load eccentricity effects

Similar to the testing in dry sand, with increasing e, the moment-rotation response becomes stiffer, and moment capacity is enhanced, while simultaneously, horizontal load capacity decreases. However, in contrast to the findings in dry sand, it is found that the rotation-horizontal displacement response in clay is dependent on e, which suggests that the pile pivot position can also change with e. The case of variable load eccentricity is assessed through theoretical explanations in Section 6.4.3.2.

4.6 Pile gapping and pivot position

Gapping forms on the active side of the model pile, as shown in Figure 4-50. The gap is filled with water, but due to the scale, the influence of hydrostatic pore water pressure may be insignificant. Previous centrifuge research also indicates that a pile gap will develop under cyclic lateral loading (Lau, 2015). Similarly, Byrne *et al*. (2020b) reported pile gapping in the PISA pile testing in stiff clay at Cowden.

By considering gapping, the lateral response of a pile can be more precisely modelled. For instance, Zdravković *et al.* (2020b) performed comprehensive finite element modelling to simulate the PISA piles at Cowden, accounting for the influence of gapping. Their analysis specifies the depth of gap and tension cut-off, which is relevant to full-scale offshore monopiles where gapping is likely to occur, and the gap will be filled with water.

The dimensions of the gap can only be measured after each test. Overall, the depth of pile gapping was found to be approximately $2.31D$ ~ $2.49D$ (= $0.77L$ ~ $0.83L$) at $e = 4D$; when $e = 6D$, the gap depth was shorter (~$0.52L$). Unfortunately, the measurement at $e = 10D$ is unavailable, as the final stage of test (CT_L_0.35N/s_10D_1) was completed at $e = 6D$.

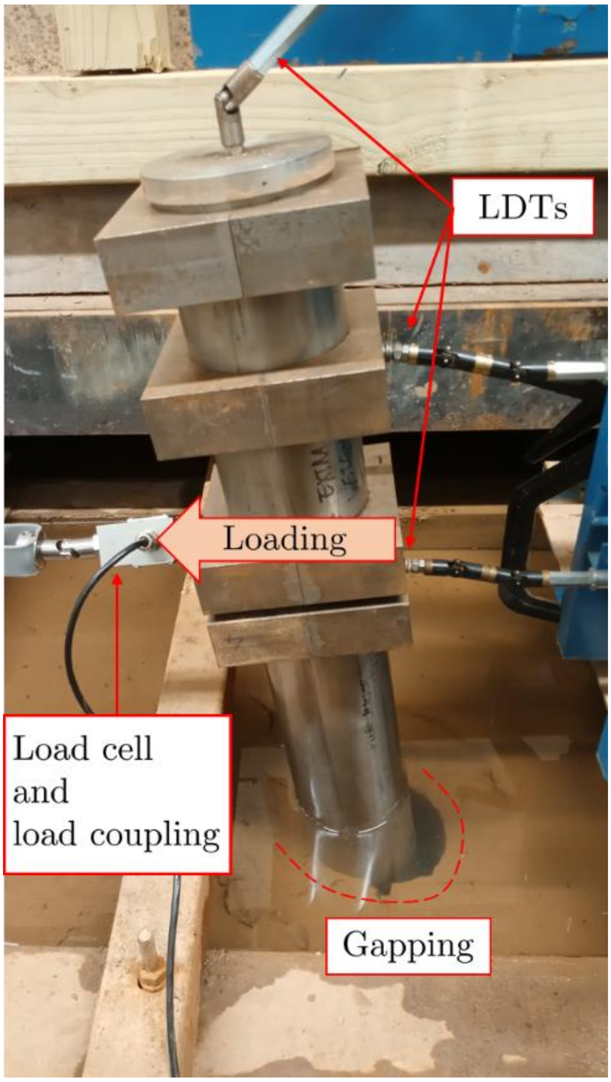

Figure 4-50 Illustration of pile gapping (shown exaggerated (θ = 4°)).

The pile pivot position at $e = 4D$ is obtained by processing the pile movement data. As the pile is considered rigid, the pile pivot position can be solved through the measurements of u, v and θ. By analysing all the available data, including the monotonic and cyclic lateral loading tests, it is found that pile uplift is negligible compared to the testing in dry sand. In Figure 4-51, it can be seen that the pivot point is approximately 2.29D (= 0.76L) below the ground-level, and a wide range between 1.79D and 3.28D (=0.6L ~ 1.09L) is observed due to soil variations. In centrifuge testing, for example, Lau (2015) reported that the pile rotational point is approximately 0.7L for a prototype monopile with the L/D ratio of 5.22 and e of 7.83D. These values may be considered appropriate to simulate monopile response.

Data at $e = 6D$ and $10D$ are insufficient to evaluate the pile pivot position. For $e = 4D$, there is some evidence that gapping occurs all the way down to the pile pivot elevation. In Chapter 6, the pile pivot positions at different load eccentricities are explored through theoretical methods.

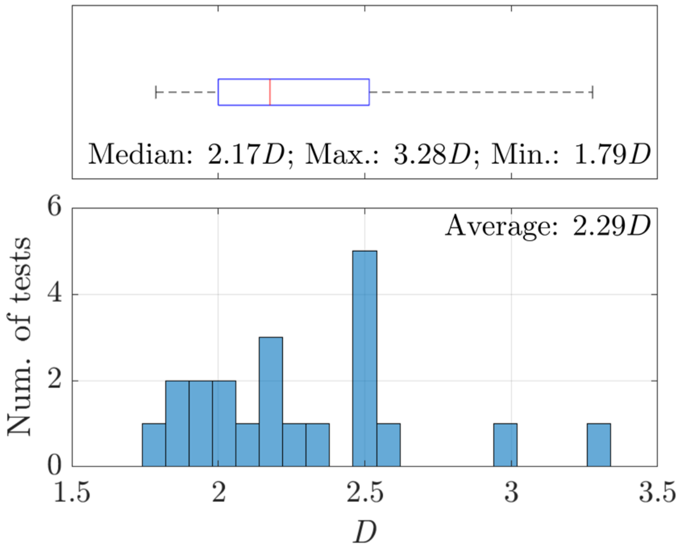

Figure 4-51 Statistics of the pile pivot position when $e = 4D$.

4.7 Concluding remarks

The completed Cowden laboratory-scale test programme provides a dataset to inform monopile design in glacial till. Key research contributions are summarised below:

(1) The novel idea of "bringing the laboratory to the field" was exploited in this research. High-strength clay is available at a suitable site with significantly less sample preparation and sources required than for laboratory-made clay samples. The clay used for the model tests is similar to the ground conditions found at multiple North Sea wind farms. By applying appropriate scaling techniques, the experimental observations can give insights into the response of full-scale monopiles.

(2) Soil property variations are reported in some of the tests, but the influence of soil variations can be avoided in the normalised forms M/M_R and H/H_R. The detailed characterisation

for the PICASO test site is ongoing, with advanced element testing methods being applied to investigate soil properties (Qiu, 2022).

(3) Rate effects in the Cowden till were found in the triaxial and model testing, and the relative magnitudes of rate effects are approximately the same. Under monotonic loading, with a tenfold increase in the strain rate $\dot{\varepsilon}$ or the actuation rate v, soil resistance and pile capacity are enhanced by 10%.

(4) The effect of pile set-up is not found in the test results. Due to the pile size, the time for excess pore pressure dissipation after installation is shorter than that of full-scale monopiles.

(5) Cyclic loading response is driven by the load magnitude, load history, ratcheting and the dissipation of excess pore water pressures. Secant stiffness k increases with load frequency f. The rate of ratcheting ($\Delta\theta$ or Δu) per cycle increases when f becomes slower.

(6) The pseudo-random cyclic loading tests indicate that large cyclic loads (*e.g.* storm loading) dominate the pile response, and the influence of small and medium magnitude cyclic loads is minimal.

(7) The monotonic response after cyclic loading shows that pile capacity does not decrease, which indicates that the $p-y$ method with cyclic degradation, a commonly used design approach for monopiles, may be too conservative and needs to be updated.

(8) Load eccentricity effects in clay and dry sand are similar. The moment-rotation response becomes stiffer with increasing load eccentricity e, and the pile pivot point changes slightly.

(9) Under lateral loading, pile gapping is observed on the active side of the pile, and the pivot point under e = $4D$ loading is approximately $2.29D$ (= $0.76L$) below the soil surface.

During the test campaign, challenges and limitations were recorded for future research, as described below:

(1) Cobbles and gravel are frequently found in the glacial till at Cowden and can influence pile response due to the pile size. For example, the diameter of a cobble can be up to 25 mm, which is relatively large compared to the diameter of a model pile. Therefore, care is required in the assessment of data.

(2) Pore pressure response is an essential element for evaluating pile response in clay. Unfortunately, due to the pile size, it was not straightforward to implement instrumentation for monitoring pore pressure dissipation around the pile. However, detailed analyses of pore pressure response may be done by element testing or field pile testing (*e.g.* the PICASO project) with pore pressure measurements.

(3) In this thesis, only uni-directional one-way cyclic loading was applied. The effects of two-way and multi-directional loading are not included in the research scope. A wider range of cyclic loading tests is required to investigate cyclic pile response under general loading more rigorously.

5 Analytical equations and scaling issues for monopiles

5.1 Introduction

Following previous laboratory investigations into offshore foundations (*e.g.* Kelly *et al.*, 2006; LeBlanc *et al.*, 2010), analytical pile responses to lateral loading in dry sand and clay are explored to aid theoretical development and scaling. Firstly, elastic pile response is derived considering lateral soil resistance along the pile and base shear. As highlighted in the PISA method, base shear and moment can provide significant resistance against lateral loading for monopiles (Byrne *et al.*, 2017). The influence of base resistance on lateral pile response is discussed. Next, ultimate response is derived by incorporating ultimate lateral soil resistance and base reactions in the analysis. Factors influencing soil strength parameters are also taken into account for scaling. Finally, non-dimensional equations for both elastic and ultimate responses are derived, and lateral and rotational pile responses are illustrated in normalised forms. By scaling the pile geometry and considering the ground conditions, the response of a full-scale monopile can be estimated.

Rate effects and drainage conditions at different scales are analysed to explore scaling issues further. As the experimental work was conducted on the laboratory floor (*i.e.* under 1-g), viscous properties of the soil and pore fluid do not change with the pile size. However, drainage response is influenced by the scale. Examples of drainage times for full-scale piles and model piles in clay are demonstrated in this chapter.

5.2 Analytical equations for piles in dry sand

5.2.1 Soil stiffness and stress level

In the laboratory, sand samples are prepared at low confining stress. To correlate the shear stiffness (G) to a test condition, it is assumed that pile response is governed by the isotropic stress level. Following the scaling framework by Kelly *et al*. (2006) and LeBlanc *et al*. (2010), G is expressed as

$$\frac{G}{p_a} = c_1 \left(\frac{\sigma_v'}{p_a}\right)^n \qquad \text{Equation 5-1}$$

where p_a is the atmospheric pressure, c_1 is a dimensionless constant, σ_v' is the effective vertical stress, and n is defined as the pressure exponent (Kelly *et al*., 2006).

σ_v' below the seabed is described below:

$$\sigma_v'(z) = \gamma' z \qquad \text{Equation 5-2}$$

where z is the depth below the seabed, and γ' is the effective unit weight of soil. n = 0.5 was suggested by Wroth and Houlsby (1985) and proven by Kelly *et al*. (2006) through physical modelling of caisson foundations.

5.2.2 Elastic response

For rigid piles subject to lateral loading, the ground-level lateral and rotation angle (u, θ) are measured, and the lateral movement at a given depth z (u_z) is approximately expressed as

$$u_z = u - \theta z. \qquad \text{Equation 5-3}$$

It is assumed that the net lateral pressure (σ) on the pile can be estimated using a Winkler-type expression below:

$$\sigma = kG \cdot \frac{u_z}{D} \qquad \text{Equation 5-4}$$

where k is a dimensionless factor.

Considering base shear, the ground-level horizontal load H is calculated as

$$H = \int_0^L \sigma D \, dz + k_b \cdot G_L \cdot \underbrace{\frac{u - \theta L}{D}}_{\substack{\text{Elastic}\\\text{strain}\\\text{at}\\\text{pile base}}} \cdot \frac{\pi D^2}{4}$$

$$= \int_0^L kG(u - \theta z) \, dz + k_b \cdot G_L \cdot \frac{u - \theta L}{D} \cdot \frac{\pi D^2}{4}$$

$$= \int_0^L kc_1(\gamma' z p_a)^{0.5}(u - \theta z) \, dz + k_b \cdot G_L \cdot \frac{u - \theta L}{D} \cdot \frac{\pi D^2}{4} \qquad \text{Equation 5-5}$$

$$= kc_1 \cdot \sqrt{\gamma' L \cdot p_a} \cdot L \left[\frac{2}{3}u - \frac{2}{5}\theta L\right] + k_b \cdot G_L \cdot \frac{u - \theta L}{D} \cdot \frac{\pi D^2}{4}$$

$$= kL \cdot G_L \left[\frac{2}{3}u - \frac{2}{5}\theta L\right] + kL \cdot G_L \cdot \frac{D}{L} \cdot \frac{k_b}{k} \cdot \frac{\pi}{4}[u - \theta L]$$

in which G_L is the shear stiffness of sand at the pile base ($z = L$), and k_b is the base shear stiffness, and the base shear factor $f_b = \frac{D}{L} \cdot \frac{k_b}{k} \cdot \frac{\pi}{4}$. The response of base shear can be approximately analysed as a rigid circular plate subject to horizontal force, k_b is found to be $16/[\pi(2 - \nu)]$ (*e.g.* Veletsos and Verbic, 1974), and ν is Poisson's ratio of soil.

Similarly, the ground-level moment M can be expressed as

$$M = -\int_0^L \sigma D z \, dz - k_b \cdot G_L \cdot \frac{u - \theta L}{D} \cdot \frac{\pi D^2}{4} \cdot L + \underbrace{k_\theta \cdot G_L \cdot \theta \cdot D^3}_{\text{rotational response}}$$

$$= -\int_0^L kG(uz - \theta z^2) \, dz - k_b \cdot G_L \cdot \frac{u - \theta L}{D} \cdot \frac{\pi D^2}{4} \cdot L + k_\theta \cdot G_L \cdot \theta \cdot D^3 \qquad \text{Equation 5-6}$$

$$= kL^2 \cdot G_L \left[\left(-\frac{2}{5} - f_b\right)u + \left(\frac{2}{7} + f_b\right)\theta L\right] + kL^2 \cdot G_L \cdot \frac{k_\theta}{k} \cdot \left(\frac{D}{L}\right)^3 \cdot \theta L$$

$$= kL^2 \cdot G_L \left[\left(-\frac{2}{5} - f_b\right)u + \left(\frac{2}{7} + f_b + f_\theta\right)\theta L\right]$$

in which the rotational stiffness (k_θ) at the pile base and the base moment factor $f_\theta = \frac{k_\theta}{k} \cdot \left(\frac{D}{L}\right)^3$ are considered. The magnitude of k_θ is approximately $1/[3(1-\nu)]$ (Veletsos and Verbic, 1974).

By combining the load and moment responses, the following equation can be derived:

$$\begin{bmatrix} \frac{M}{L} \\ H \end{bmatrix} = kL \cdot G_L \begin{bmatrix} \left(\frac{2}{7} + f_b + f_\theta\right) & -\left(\frac{2}{5} + f_b\right) \\ -\left(\frac{2}{5} + f_b\right) & \left(\frac{2}{3} + f_b\right) \end{bmatrix} \begin{bmatrix} \theta L \\ u \end{bmatrix} = DG_L \begin{bmatrix} k_1 & k_2 \\ k_2 & k_3 \end{bmatrix} \begin{bmatrix} \theta L \\ u \end{bmatrix} \qquad \text{Equation 5-7}$$

where k_1, k_2 and k_3 are constants.

Inversely, the rotation and displacement responses at the ground level can be derived as

$$\begin{bmatrix} \theta L \\ u \end{bmatrix} = \frac{1}{DG_L(k_1k_3 - k_2^2)} \begin{bmatrix} k_3 & -k_2 \\ -k_2 & k_1 \end{bmatrix} \begin{bmatrix} \frac{M}{L} \\ H \end{bmatrix}. \qquad \text{Equation 5-8}$$

The moment-rotation relationship is expressed as

$$M = \left[\frac{DG_L L^2 (k_1k_3 - k_2^2)}{k_3 - k_2\left(\frac{HL}{M}\right)} \right] \cdot \theta. \qquad \text{Equation 5-9}$$

For scaling, the above relationship can be re-written as

$$\begin{aligned} \frac{M}{DL^3\gamma'} &= \frac{k_1k_3 - k_2^2}{k_3 - k_2(\frac{HL}{M})} \cdot c_1(\gamma' L p_a)^{0.5} \cdot \frac{1}{L\gamma'} \cdot \theta \\ &= \frac{c_1(k_1k_3 - k_2^2)}{k_3 - k_2\left(\frac{L}{e}\right)} \cdot \sqrt{\frac{p_a}{L\gamma'}} \cdot \theta. \end{aligned} \qquad \text{Equation 5-10}$$

Then, non-dimensional groups $\widetilde{M} = \frac{M}{DL^3\gamma'}$, $\widetilde{k_M} = \frac{c_1(k_1k_3-k_2^2)}{k_3-k_2(\frac{L}{e})}$ and $\tilde{\theta} = \sqrt{\frac{p_a}{L\gamma'}} \cdot \theta$ can be defined.

The moment response is normalised by considering the pile geometry and γ', the stiffness is influenced by the L/e ratio, and the rotation response is dependent on the stress level.

Similarly, from Equation 5-8, the lateral load-displacement relationship is found below:

$$H = \left[\frac{DG_L L(k_1 k_3 - k_2^2)}{-k_2\left(\frac{M}{HL}\right) + k_1}\right] \cdot u.$$ Equation 5-11

By normalising the load, stiffness and displacement, the above equation can be re-written as

$$\frac{H}{DL^2\gamma'} = \frac{(k_1 k_3 - k_2^2)}{-k_2\left(\frac{M}{HL}\right) + k_1} \cdot c_1\sqrt{c_2 L\gamma' p_a} \cdot \frac{1}{L^2\gamma'} \cdot u$$

Equation 5-12

$$= \frac{c_1(k_1 k_3 - k_2^2)}{-k_2\left(\frac{e}{L}\right) + k_1} \cdot \sqrt{\frac{p_a}{L\gamma'}} \cdot \frac{u}{L}.$$

from which non-dimensional groups $\widetilde{H} = \frac{H}{DL^2\gamma'}$, $\widetilde{k_H} = \frac{c_1(k_1 k_3 - k_2^2)}{-k_2(e/L) + k_1}$, and $\tilde{u} = \sqrt{\frac{p_a}{L\gamma'}} \cdot \frac{u}{L}$ can be defined. As illustrated in the normalised groups ($\widetilde{M}, \widetilde{H}, \widetilde{k_M}, \widetilde{k_H}, \tilde{\theta}$ and $\tilde{u}$), tests with the same L/D and e/L ratios are comparable if factors influencing the stiffness are constant.

5.2.3 Ultimate limit state

Figure 5-1 illustrates the stress distribution for a laterally-loaded rigid pile in sand under the ultimate limit state. In addition to the external lateral and moment loading (H, M), the self-weight of a pile V is considered in the analysis.

For the model testing in dry sand, the embedded length L is short (less than 336 mm), and shaft resistance itself is found insufficient to support the pile weight. Most of the vertical load V and the weight of the soil plug are transferred to the pile base. A few assumptions are made to derive pile response in the ultimate limit state:

(1) The vertical bearing capacity at the pile base is enough to support the pile;

(2) Shaft resistance against moment loading is negligible;

(3) Shaft resistance against vertical loading is small.

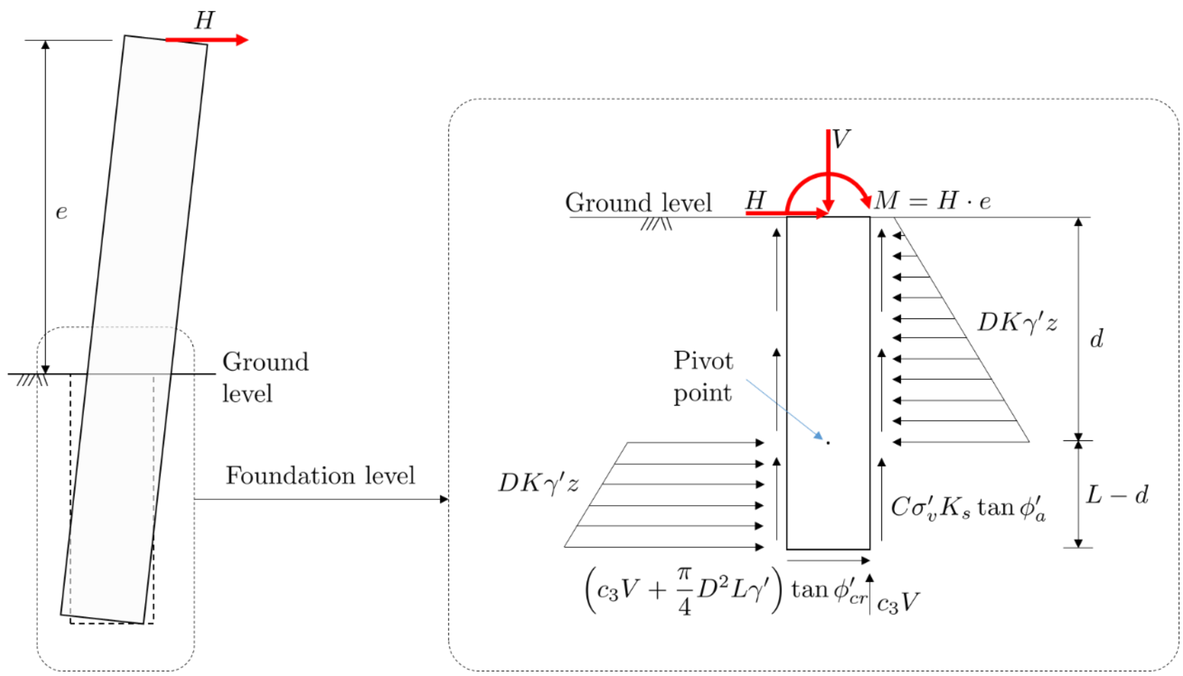

Figure 5-1 Stress distribution for a rigid pile in sand principally subject to lateral loading ($C = \pi D$; $K_S \approx 0.7$; ϕ'_a = effective pile-soil friction angle).

In the ultimate limit state, horizontal load pressure is determined by $KD\gamma' z$, and K is dependent on the friction angle (Broms, 1964). The pile rotational point is located at $z = d$. At the pile base, the friction angle is assumed to be the critical state friction angle ϕ'_{cr} as large strains are expected to occur. For a full-scale pile, the confining stress is higher, and soil strength properties (*e.g.* dilation) may differ from those in the laboratory. For instance, Chapter 3 introduces the mechanical behaviour of the sand for model testing, including the influence of the stress level on the drained friction angle (ϕ'). The base shear is contributed by the transferred vertical load c_3V (often concentrated on the pile edge) and the overburden soil $\frac{\pi}{4}D^2L\gamma'$. c_3 is between 0 and 1 due to the contribution of shaft resistance.

Based on the above assumptions, the ultimate lateral load and moment responses can be expressed as

$$H + \left(c_3V + \frac{\pi}{4}D^2L\gamma'\right)\tan\phi'_{cr} + \frac{DK\gamma'(L^2 - 2d^2)}{2} = 0 \qquad \text{Equation 5-13}$$

and

$$M-\left(c_3V+\frac{\pi}{4}D^2L\gamma'\right)L\tan\phi'_{cr}-\frac{DK\gamma'(L^3-2d^3)}{3}-c_3V\cdot\frac{D}{2}=0. \qquad \text{Equation 5-14}$$

By combining the above two equations and eliminating d, the following relationship can be derived:

$$\left[\frac{1}{K}\cdot\frac{H}{DL^2\gamma'}+\frac{1}{K}\cdot\frac{\left(c_3V+\frac{\pi}{4}D^2L\gamma'\right)\tan\phi'_{cr}}{DL^2\gamma'}+\frac{L^2}{2}\right]^3$$

Equation 5-15

$$=\left[\frac{3}{2K}\cdot\frac{M}{DL^3\gamma'}-\frac{3}{2K}\cdot\frac{\left(c_3V+\frac{\pi}{4}D^2L\gamma'\right)L\tan\phi'_{cr}+c_3V\cdot\frac{D}{2}}{DL^3\gamma'}-\frac{L^3}{2}\right]^2.$$

Then, $\tilde{V}=\frac{V}{DL^2\gamma'}$ can be found, and Equation 5-15 can be presented using the normalised terms $\tilde{M},\tilde{H},\tilde{V},\tilde{u}$ and $\tilde{\theta}$ for elastic response. These key non-dimensional parameters are summarised in Table 5-1.

It is recommended that normalisation of displacement or rotation in dry sand needs to be explored further through testing at different scales or under an enhanced gravity. The normalised terms $\tilde{u}$ and $\tilde{\theta}$ terms are dependent on the scale and the atmospheric pressure (*i.e.* the term $\sqrt{\frac{p_a}{L\gamma'}}$). Although LeBlanc *et al.* (2010) suggested that $\tilde{u}$ and $\tilde{\theta}$ can be used for comparison between laboratory and full-scale tests, experimental evidence is required. On the other hand, in the literature, normalised lateral displacement and rotation may be expressed as u/u_R and θ/θ_R, and these terms are adopted in this thesis. However, it is noted that u_R or θ_R values are arbitrarily defined, and their definition by different researchers varies (Richards, 2019).

Table 5-1 Non-dimensional parameters for scaling pile tests in sand.

Aspect ratio	Load eccentricity ratio	Normalised moment $\widetilde{M}$	Normalised horizontal load $\widetilde{H}$	Normalised vertical load $\tilde{V}$	Normalised lateral displacement $\tilde{u}$	Normalised rotation $\tilde{\theta}$
$\frac{L}{D}$	$\frac{e}{L}$	$\frac{M}{DL^3\gamma'}$	$\frac{H}{DL^2\gamma'}$	$\frac{V}{DL^2\gamma'}$	$\frac{u}{L}\sqrt{\frac{p_a}{L\gamma'}}$	$\theta\sqrt{\frac{p_a}{L\gamma'}}$

5.3 Analytical equations for piles in stiff clay

5.3.1 Strength properties

The scaling framework for clay is derived considering constant and variable strength profiles. A similar approach for a single rigid pile in homogenous overconsolidated clay is proposed by Chiou and Chien (2021).

For clay with a strength profile varying with depth, the undrained shear strength s_u can typically be expressed as

$$s_u = s_{u0} + \rho z \qquad \text{Equation 5-16}$$

where s_{u0} is the undrained shear strength at the soil surface, and ρ is the strength factor. ρ can be characterised using a non-dimensional term r below:

$$r = \rho L / s_{uL} \qquad \text{Equation 5-17}$$

in which s_{uL} is the undrained shear strength at the pile base. r = 1 is often seen in soft, normally consolidated clay, while in stiff clay, r may be 0 (*i.e.* a uniform shear strength profile with depth).

The shear modulus G is approximately proportional to s_u in clay, which can be expressed as

$$\frac{G}{s_u} = I_r \qquad \text{Equation 5-18}$$

where I_r is the rigidity index.

5.3.2 Elastic response

Similar to sand, $u_z = u - \theta z$ and $\sigma = \frac{kGu_z}{D}$. Considering base shear, the horizontal load and moment responses can be written as

$$H = \int_0^L \sigma D\, dz + k_b \cdot G_L \cdot \frac{u - \theta L}{D} \cdot \frac{\pi D^2}{4}$$

$$= \int_0^L kG(u - \theta z)\, dz + k_b \cdot G_L \cdot \frac{u - \theta L}{D} \cdot \frac{\pi D^2}{4} \qquad \text{Equation 5-19}$$

$$= kI_r L\left[\left(s_{uL} - \frac{rs_{uL}}{2}\right)u + \left(-\frac{s_{uL}}{2} + \frac{rs_{uL}}{6}\right)\theta L\right] + k_b \cdot G_L \cdot \frac{u - \theta L}{D} \cdot \frac{\pi D^2}{4}$$

$$= kLG_L\left[\left(1 - \frac{r}{2}\right)u - \left(\frac{1}{2} - \frac{r}{6}\right)\theta L\right] + kLG_L \cdot f_b \cdot [u - \theta L]$$

and

$$M = -\int_0^L \sigma Dz\, dz - k_b \cdot G_L \cdot \frac{u - \theta L}{D} \cdot \frac{\pi D^2}{4} \cdot L + k_\theta \cdot G_L \cdot \theta \cdot D^3$$

$$= -\int_0^L kG(u - \theta z)z\, dz - k_b \cdot G_L \cdot \frac{u - \theta L}{D} \cdot \frac{\pi D^2}{4} \cdot L + k_\theta \cdot G_L \cdot \theta \cdot D^3 \qquad \text{Equation 5-20}$$

$$= kL^2 G_L\left[-\left(\frac{1}{2} - \frac{r}{6} - f_b\right)u + \left(\frac{1}{3} - \frac{r}{12} + f_b + f_\theta\right)\theta L\right].$$

By combining the above equations, the following relationship is derived:

$$\begin{bmatrix} \frac{M}{L} \\ H \end{bmatrix} = kL \cdot G_L \begin{bmatrix} \left(\frac{1}{3} - \frac{r}{12} + f_b + f_\theta\right) & -\left(\frac{1}{2} - \frac{r}{6} + f_b\right) \\ -\left(\frac{1}{2} - \frac{r}{6} + f_b\right) & \left(1 - \frac{r}{2} + f_b\right) \end{bmatrix} \begin{bmatrix} \theta L \\ u \end{bmatrix} \qquad \text{Equation 5-21}$$

$$= DG_L \begin{bmatrix} k_4 & k_5 \\ k_5 & k_6 \end{bmatrix} \begin{bmatrix} \theta L \\ u \end{bmatrix}$$

where k_4, k_5 and k_6 are functions of r.

The above equation can be re-arranged as

$$\begin{bmatrix}\theta L\\ u\end{bmatrix}=\frac{1}{DG_L(k_4k_6-k_5^2)}\begin{bmatrix}k_6 & -k_5\\ -k_5 & k_4\end{bmatrix}\begin{bmatrix}\frac{M}{L}\\ H\end{bmatrix}.$$ Equation 5-22

Then, the moment-rotation response can be re-written as

$$M=\left[\frac{DL^2G_L(k_4k_6-k_5^2)}{k_6-\frac{k_5L}{e}}\right]\cdot\theta$$

$$=\left[\frac{DL^2I_r(s_{u0}+\rho z)(k_4k_6-k_5^2)}{k_6-\frac{k_5L}{e}}\right]\cdot\theta=\left[\frac{DL^2I_rs_{u_L}(k_4k_6-k_5^2)}{k_6-\frac{k_5L}{e}}\right]\cdot\theta.$$ Equation 5-23

By re-arranging the above equation, M can be normalised as follows:

$$\frac{M}{DL^2s_{u_L}}=\left[\frac{I_r(k_4k_6-k_5^2)}{k_6-\frac{k_5L}{e}}\right]\cdot\theta$$ Equation 5-24

from which non-dimensional groups $\widetilde{M}=\frac{M}{DL^2s_{u_L}}$, $\widetilde{k_M}=\frac{I_r(k_4k_6-k_5^2)}{k_6-\frac{k_5L}{e}}$ and $\tilde{\theta}=\theta$ can be defined to illustrate normalised moment-rotation response.

The lateral load-displacement response can be expressed as

$$H=\left[\frac{DLG_L(k_4k_6-k_5^2)}{-k_5e+k_4L}\right]\cdot u$$

$$=\left[\frac{DLI_r(s_{u0}+\rho z)(k_4k_6-k_5^2)}{-k_5e+k_4L}\right]\cdot u=\left[\frac{DLI_rs_{u_L}(k_4k_6-k_5^2)}{-k_5e+k_4L}\right]\cdot u.$$ Equation 5-25

By normalising H,

$$\frac{H}{DLs_{u_L}}=\left[\frac{I_r(k_4k_6-k_5^2)}{-k_5e/L+k_4}\right]\cdot\frac{u}{L}.$$ Equation 5-26

Similarly, normalised terms $\widetilde{H}=\frac{H}{DLs_{u_L}}$, $\widetilde{k_H}=\frac{I_r(k_4k_6-k_5^2)}{-k_5e/L+k_4}$ and $\tilde{u}=\frac{u}{L}$ can be adopted to represent normalised horizontal load-displacement response.

5.3.3 Ultimate limit state

Figure 5-2 shows stress distribution around a rigid pile in clay. The maximum vertical resistance along the pile shaft:

$$\int_0^L C\alpha_{s_u} s_u \, dz = \int_0^L \pi D\alpha_{s_u} s_u \, dz \approx \pi DL\alpha_{s_u}\left(s_{u0} + \frac{\rho L}{2}\right) \text{ (stiff clay).} \qquad \text{Equation 5-27}$$

where α_{s_u} is the cohesion factor between the pile and soil. α_{s_u} often falls in the range of 0.4 ~ 0.8 for stiff clay.

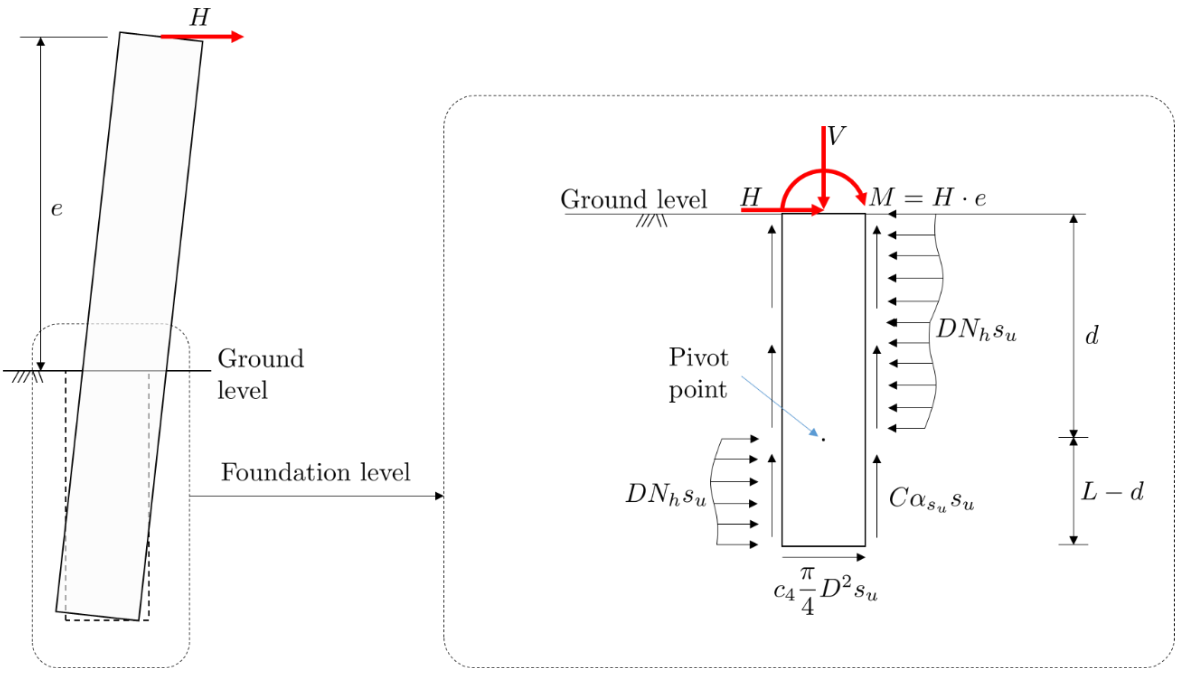

Figure 5-2 Stress distribution for a rigid pile in clay principally subject to lateral loading (C: perimeter).

Compared to sand, the pile weight and the soil plug are countered by shaft resistance for the model pile (D = 101.6 mm, L/D = 3), and vertical resistance at the pile base may be ignored. The contribution of shaft resistance against moment loading is assumed to be negligible.

At the ultimate state, $\sigma = N_h s_u = N_h(s_{u0} + \rho z) = N_h s_{uL}\left(1 - r + r\frac{z}{L}\right)$, and N_h is a dimensionless factor varying between 9 and 12, depending on the pile roughness (Randolph and Houlsby, 1984). N_h may vary with depth, as suggested by Randolph and Houlsby (1984) considering wedge failure around the pile, but the influence of this variation is assumed to be minor for laboratory-scale model piles and is not considered in the analysis.

It is assumed that the pile pivot point is located at the depth d. The ultimate lateral resistance is expressed as

$$H = 2DdN_h\left(s_{u0} + \frac{\rho d}{2}\right) - DLN_h\left(s_{u0} + \frac{\rho L}{2}\right) - c_4\frac{\pi}{4}D^2 s_{uL} \qquad \text{Equation 5-28}$$

where c_4 is a constant between 0 and 1.

The ultimate moment resistance is expressed as follows:

$$M = -2DN_h\left(\frac{s_{u0}d^2}{2} + \frac{\rho d^2}{3}\right) + DN_h\left(\frac{s_{u0}L^2}{2} + \frac{\rho d^2}{3}\right) + c_4\frac{\pi}{4}D^2 L s_{uL}. \qquad \text{Equation 5-29}$$

For stiff clay, $s_u(z) = s_{u_0} = s_{u_L}$, $\rho = 0$ so that

$$H = 2DdN_h s_{u0} - DLN_h s_{u0} - c_4\frac{\pi}{4}D^2 s_{u0} \qquad \text{Equation 5-30}$$

and

$$M = -DN_h s_{u0} d^2 + \frac{DL^2\, N_h s_{u0}}{2} + c_4\frac{\pi}{4}D^2 L s_{u0}. \qquad \text{Equation 5-31}$$

$\widetilde{H} = \frac{H}{DLs_{u0}}$ and $\widetilde{M} = \frac{M}{DL^2 s_{u0}}$ are defined. By eliminating d in the above equations:

$$\widetilde{M} = -N_h\left[\frac{1}{2N_h}\widetilde{H} + \frac{c_4\pi}{8N_h}\cdot\frac{D}{L} + \frac{1}{2}\right]^2 + \frac{N_h}{2} + \frac{c_4\pi}{4}\cdot\frac{D}{L}. \qquad \text{Equation 5-32}$$

The normalised loads and displacements for the ultimate limit state and elastic response are identical. Thus, one can illustrate pile response in terms of $\widetilde{M}, \widetilde{H}, \tilde{u}$ and $\tilde{\theta}$. The influence of vertical loading seems to be minimal in clay compared to sand for the laboratory-floor testing. Key normalised terms for scaling piles in clay are summarised in Table 5-2. These non-dimensional parameters are also adopted for analysing large-scale pile test data from the

PICASO project, which will be reported later as part of the DPhil thesis by Martin (2023) to compare with the data reported in this thesis (see Chapter 4).

Table 5-2 Non-dimensional parameters for scaling pile tests in clay.

Aspect ratio	Load eccentricity ratio	Normalised moment $\widetilde{M}$	Normalised horizontal load $\widetilde{H}$	Normalised lateral displacement $\tilde{u}$	Rotation $\tilde{\theta}$
$\frac{L}{D}$	$\frac{e}{L}$	$\frac{M}{DL^2 s_u}$	$\frac{H}{DLs_u}$	$\frac{u}{L}$	θ

5.4 Normalisation

Although the scaling frameworks for sand and clay indicate that pile response can be illustrated using the non-dimensional parameters, in this thesis, data are normalised using reference values of load and pile movement. This approach is suggested by Richards (2019) for model testing, as it is considered more intuitive. For the moment-rotation response of a pile, M is normalised using the reference moment (M_R) when θ reaches the reference rotation (θ_R) of 2°. For the horizontal load-displacement response, the horizontal reference load H_R and displacement u_R of $0.1D$ are used to normalise H and u, respectively. In laboratory-scale model testing, θ_R and u_R are determined arbitrarily and may not reflect the actual design pile movement for a full-scale pile. Comparisons between the two normalisation methods of sand and clay using test data are illustrated in Figure 5-3 and Figure 5-4. For sand, p_a is set to 100 kPa, which approximately represents the atmospheric pressure. For clay, normalised results shall be compared with pile testing at different scales (*e.g.* the PICASO medium-scale pile testing). The normalised forms proposed in Table 5-2 may be also adopted for centrifuge modelling, and further validation is needed.

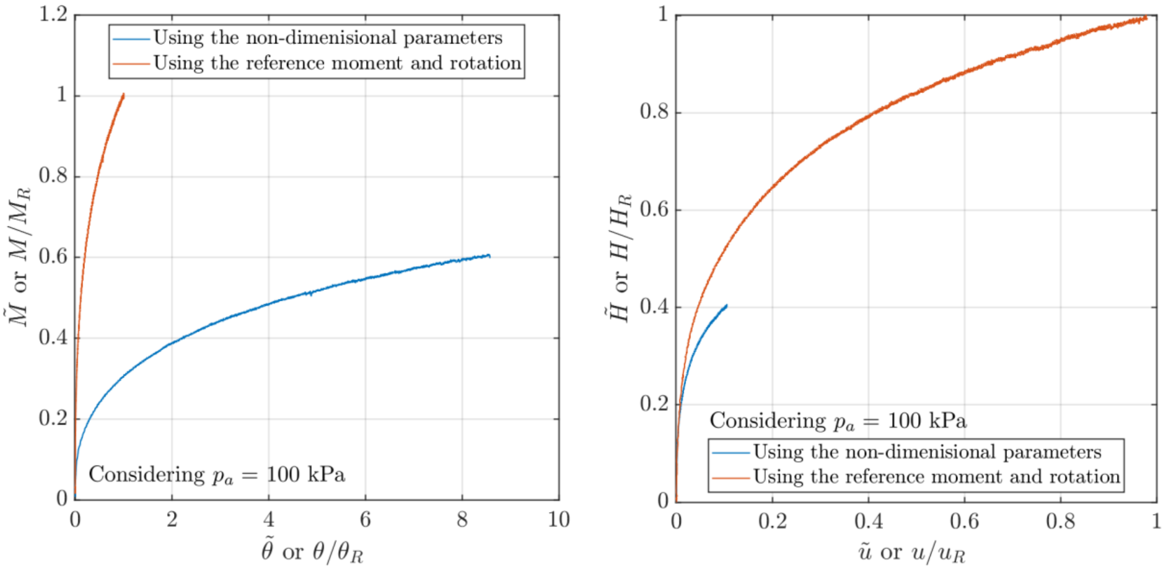

(a) (b)

Figure 5-3 Illustration of the two normalisation approaches for model testing in sand: (a) moment-rotation response; (b) horizontal load-displacement response.

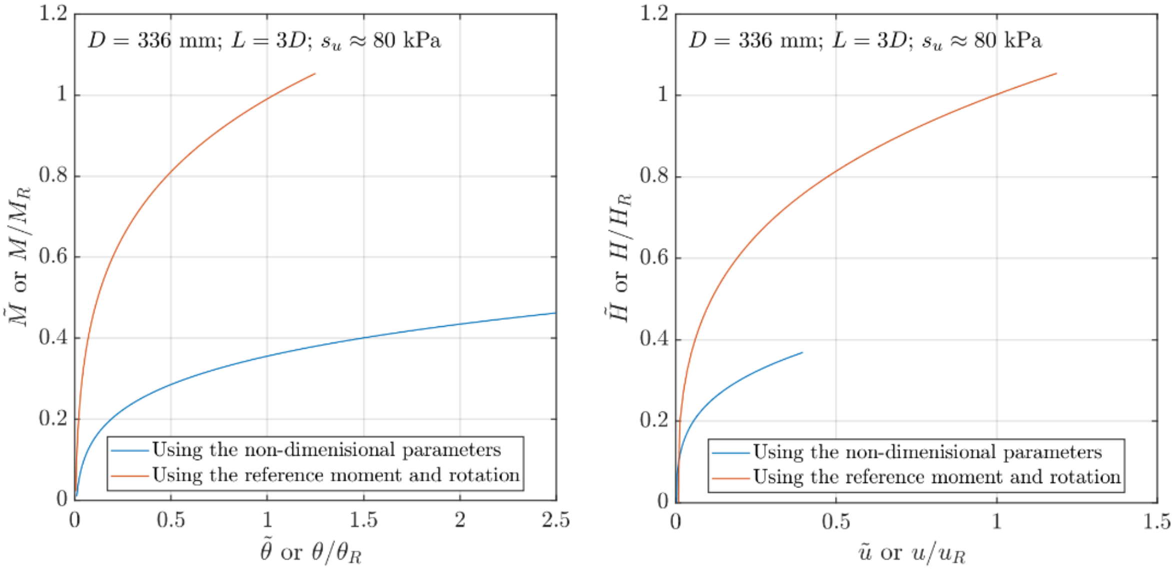

(a) (b)

Figure 5-4 Illustration of the two normalisation approaches for model testing in clay: (a) moment-rotation response; (b) horizontal load-displacement response.

5.5 Scaling of soil rate dependency

The relative magnitude of soil rate effects does not change with the pile size based on previous experimental evidence. For example, the relative magnitude of rate effects does not change with element test methods (Kiyota and Tatsuoka, 2006). Furthermore, Balaam (2020) also showed that the rate parameter determined by element testing could be used to estimate rate-dependent pile response. Similarly, in this thesis, it is found that the relative magnitudes of rate effects measured from element testing and model testing are identical in clay. Experimental observations on soil rate effects are shown in Chapters 3 and 4.

5.6 Drainage conditions

Drainage conditions are analysed in the monopile design, and on some occasions, partial drainage may occur and lead to decreasing resistance. For instance, Jostad *et al*. (2020) reported that when piles in saturated dense sand are subject to large magnitude cyclic loading within a few seconds, the drainage condition may become undrained or partially drained. Pore pressure dissipation response around a monopile is complex and not included in the research scope; however, some considerations could be considered to differentiate drainage and rate-dependent responses.

It is known that the drainage response of a pile is dependent on the pile size. For example, for a full-scale monopile foundation, the affected dimensions of the surrounding soil are a hundred times larger than those of a model pile. As a result, drainage paths around the model pile are expected to be much shorter by a factor of 100, and excess pore water pressures dissipate faster by a factor of 10^4.

To evaluate drainage response, it could be hypothesised that when the overall degree of consolidation (U) is less than 10 % for a drainage path of $1D$, the surrounding soil is considered approximately undrained. The time factor for 10 % of consolidation (T_{10}) is estimated using the equation suggested by (Sivaram and Swamee 1977):

$$T_{10}=\frac{\frac{\pi}{4}\left(\frac{U(\%)}{100}\right)^2}{\left[1-\left(\frac{U(\%)}{100}\right)^{5.6}\right]^{0.357}}=\frac{\frac{\pi}{4}\left(\frac{10}{100}\right)^2}{\left[1-\left(\frac{10}{100}\right)^{5.6}\right]^{0.357}}=0.007854. \qquad \text{Equation 5-33}$$

Following the above equation, it is found that the time factors for approximately 50 % of consolidation (T_{50}) and 90 % consolidation (T_{90}) are 0.1978 and 0.849, respectively.

Model tests in dry sand and saturated stiff clay were conducted in this research. Further research on exploring pile response in saturated sand is ongoing at Oxford University through laboratory testing (Keane, 2022). Drainage response in dry sand can be treated as fully drained, and the influence of excess pore air pressures is negligible. A simplified drainage analysis for saturated stiff clay is demonstrated as follows.

The tests in saturated stiff clay were undertaken at a field site in Cowden, northeast England. Details about the site are discussed in Chapter 4. The site is approximately 1 km from the PISA pile testing test area, and the ground conditions at both sites are approximately identical. Therefore, along with the oedometer test on the clay retrieved from the test site, soil characteristics from the PISA Cowden site (Zdravković *et al*., 2020a; Ushev and Jardine, 2022b) are also considered to analyse drainage response, as illustrated in Table 5-3. γ' was measured from tube samples retrieved from the test area. A wide range of k estimated for glacial till are adopted (Zdravkovic *et al*., 2020a). m_v suggested by Carter and Bently (2016) and measured from the oedometer test are considered, but it is much influenced by the initial voids ratio, as well as the initial and final pressures during compression. c_v is estimated using γ', k and m_v, and the range of c_v is close to that obtained from the oedometer tests by Ushev and Jardine (2022b).

Table 5-3 Estimations of consolidation for different pile sizes.

	Full-scale pile (D = 8 m)	Model pile (D = 0.101 m)
Unit weight of soil (γ') (kN/m^3)	21.2	
Coefficient of compressibility (m_v) (m^2/MN)	0.05 ~ 0.1 (stiff glacial till) (Carter and Bently, 2016) 0.084 (measured from the odometer test)	
Permeability (k) (mm/s)	1.6×10^{-6} (weathered) ~ 1.6×10^{-8} (unweathered) (Zdravkovic *et al.*, 2020a)	
Coefficient of consolidation (c_v) (m^2/s)	7.6×10^{-9} ~ 1.5×10^{-6}	
Length of drainage path (m) (assuming 1D)	8	0.101
Time for 10 % consolidation (hours)	92 ~ 18490	0.2~ 3.0
Time for 50 % consolidation (hours)	2330 ~ 46600	0.4 ~ 74.3
Time for 90 % consolidation (hours)	10000 ~ 200000	1.6 ~ 318.8

In Table 5-3, it can be seen that the time for 10 % consolidation for a full-scale pile (D = 8 m) is much longer than that for the model pile (D = 0.101 m). If a model test takes more than three hours, the surrounding soil may become partially drained, and therefore, pore pressure dissipation response may need to be assessed.

Excess pore pressures accumulate during pile installation, and pile resistance gradually grows with pore pressures dissipating over time. Based on the analysis in Table 5-3, model piles need to stay undisturbed for 75 hours after installation to achieve 50 % consolidation. In Chapter 4, pile responses with different undisturbed periods are compared to validate the estimated time of consolidation.

Although the above analysis provides some simplified estimations of consolidation, evaluating pore pressure response during dynamic testing is still challenging. As reported throughout in Chapter 4, long-term pile testing, such as high cycle loading under a slow rate, in addition to soil skeleton behaviour (*i.e.* rate effects), time-dependent pore pressure response may also influence pile response. This issue is not addressed in this thesis due to lack of pore pressure measurements during testing. Further research is needed to tackle this issue.

5.7 Summary

This chapter elaborates on scaling issues for the laboratory-floor model pile testing. Analysis of pile behaviour in dry sand and clay is discussed, and factors influencing soil strength properties are described. Non-dimensional load and displacement parameters are proposed to compare different-scale pile tests.

Is it believed that the test scale does not influence the relative magnitude of soil rate effects. In Chapter 4, rate effects in saturated stiff clay from element and model testing are studied for comparison.

Drainage conditions for full-scale and model piles are evaluated. Soil properties from the test site and the PISA Cowden site are considered. For the model pile, the consolidation time is much shorter than that for a full-scale pile, and the surrounding soil may partially drain if a test runs over several hours.

Piles installed in glacial till need to be undisturbed for a sufficient period to allow excess pore water pressures to dissipate. In practice, full-scale piles are left for several months for consolidation and gaining resistance. Considering the scale of the model pile, excess pore water pressures may take several days to dissipate after installation.

6 Theoretical development

6.1 Introduction

A new macro-element model using a yield surface approach, developed by Houlsby (2022a), was implemented and extended to explore pile response to general lateral loading, considering combined $V - H - M$ loading, soil rate effects and cyclic effects. Macro-element (0-D) modelling techniques have been used to capture monopile behaviour (*e.g.* Abadie, 2015; Page *et al.*, 2018; Richards, 2019), which integrate soil reactions along the pile into a macro element. Observations in pile testing, such as non-linearity, kinematic hardening and ratcheting, can be simulated using 0-D models. Also, compared to 3-D finite element modelling, 0-D modelling can save a significant amount of time on computation. Furthermore, as offshore wind farm design is time-critical, such 0-D modelling techniques can help to accelerate the design process for OWT monopiles.

The model was developed under the hyperplasticity framework. Previous work shows that hyperplasticity models provide a sound theoretical basis and capture pile response accurately. For instance, Balaam (2020) calibrated models in hyperplasticity to describe non-linearity under monotonic loading, rate dependency and cyclic response of clay with good confidence. Similarly, Abadie (2015) and Richards (2019) demonstrated that hyperplasticity models can rigorously capture monopile responses to monotonic and cyclic lateral loading in sand. In general, these case studies show that pile response can be precisely modelled under the hyperplasticity framework.

This chapter elaborates on the development and performance of the model, based on the original work by Houlsby (2022a). First of all, theoretical derivations and model formulation are introduced in hyperplasticity. Secondly, selected tests in dry sand are compared with simulations to examine the performance of the model under general lateral loading without considering rate dependency. Finally, data from the saturated stiff clay testing are compared with modelling results to evaluate soil rate effects and general lateral loading.

6.2 Model formulation

This section introduces the formulation of the macro-element model. The concept of the model for general lateral loading of monopiles was provided in the notes by Houlsby (2022a). In this thesis, the model was validated and extended to include (1) base resistance, (2) soil rate effects and (3) ratcheting under cyclic loading so that a wider range of experimental observations can be simulated. The modelling approach, features of the model, structure and hyperplasticity framework are described below, with the supplementary materials in the Appendix.

6.2.1 Macro-element modelling approach

The macro-element (0-D) modelling approach adopted by Abadie *et al*. (2019) is extended to consider various load eccentricities e, aspect ratios L/D and soil reactions. The macro response of a rigid pile can be described in terms of the horizontal load H_e and displacement (u_e) at the loading point (see Figure 6-1). The pile motion is analysed as the plane motion of a rigid body. u_e is obtained through the ground-level displacements θ and u:

$$u_e = e \cdot \theta + u \approx e \tan \theta + u \qquad \text{Equation 6-1}$$

where θ is small (*i.e.* usually less than 2°), and the vertical pile displacement v is negligible. In the macro-element model, H_e is equal to H at the ground level, and the moment load M at the ground level can be expressed as $H_e \cdot e$ or $H \cdot e$.

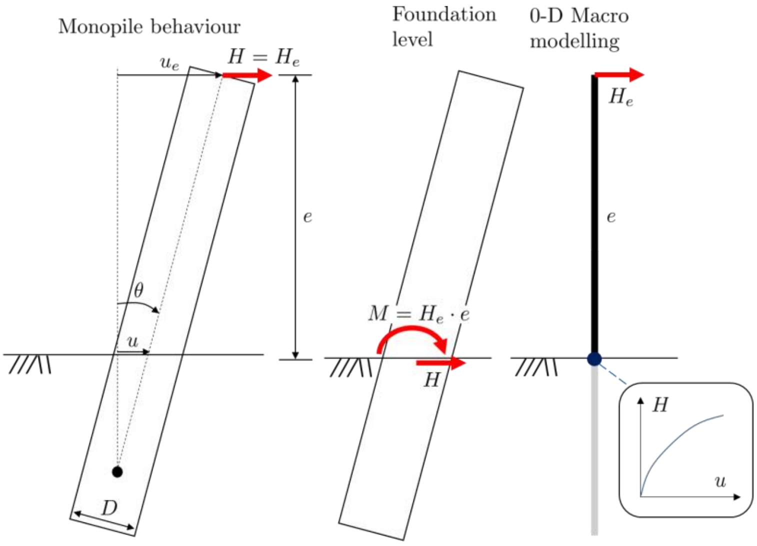

Figure 6-1 Illustration of macro-element modelling of monopile behaviour (after Abadie *et al*., 2019).

6.2.2 Model features

6.2.2.1 Combined loading

Combined $V - H - M$ loading is considered in the model, following the analytical derivations in Chapter 5. The failure surface in the $H - M$ space is specified under a constant V. For OWT monopile design, the allowable pile rotation θ and horizontal displacement u are often prescribed. Therefore, both moment-rotation and horizontal load-displacement responses need to be analysed to inform monopile design, and are integrated in this model.

In the model, various $H - M$ combinations can be modelled, and V was assessed to determine whether it would enhance lateral resistance (*e.g.* the impact of vertical loading on pile response in dry *very loose* sand, see Section 3.7.2). For evaluating the model under various combined $H - M$ loading, data from the load eccentricity tests in dry sand (Section 3.8) and saturated stiff clay (Section 4.5) were analysed.

6.2.2.2 Impact of base reactions on pile capacity

The influence of base resistance on lateral pile capacity is discussed in Chapter 5. The original Houlsby model was extended to include base resistance components, such as base shear and moment, in the analysis. Data from the monotonic loading tests (Sections 3.5.1 and 4.3.1) were used to demonstrate the impact of base reactions.

6.2.2.3 Rate dependency

Soil rate effects are observed in clay under monotonic and cyclic lateral loading. The model can implement linear viscosity and rate process theory to capture soil rate dependency, following the work by Houlsby and Puzrin (2006). Data from Sections 4.3 and 4.4 were utilised to calibrate the model and examine its performance.

6.2.2.4 Ratcheting under cyclic lateral loading

The hyperplasticity model, HARM, developed by Houlsby *et al.* (2017), can be implemented to capture ratcheting under cyclic loading. The HARM analysis in this thesis followed the previous work by Houlsby *et al.* (2017) and Richards (2019). Data from the dry sand (Section 3.6) and saturated stiff clay testing (Section 4.4) were used to calibrate the HARM parameters.

6.2.3 Structure of the model

In Chapter 5, analytical equations for elastic response and the ultimate condition are derived considering the coupled moment-horizontal load pile behaviour. These equations form the basis of the model.

The model considers two idealised soil conditions:

(1) fully drained sand (dry sand) with a strength proportional to the effective stress level $\gamma' z$,

(2) clay with a linear undrained shear strength profile $s_u = s_{u0} + \rho z$.

Following the original work by Houlsby (2022a), the forms of the elastic stiffness and ultimate response considering base resistance are described below.

6.2.3.1 Elastic stiffness

For drained sand, following Equation 5-7, the elastic stiffness matrix for the coupled moment-horizontal load response is shown below:

$$\begin{bmatrix} H \\ M' \end{bmatrix} = kL \cdot G_L \begin{bmatrix} \left(\frac{2}{3} + f_b\right) & -\left(\frac{2}{5} + f_b\right) \\ -\left(\frac{2}{5} + f_b\right) & \left(\frac{2}{7} + f_b + f_\theta\right) \end{bmatrix} \begin{bmatrix} u \\ \vartheta \end{bmatrix} \qquad \text{Equation 6-2}$$

where $M' = M/L$ and $\vartheta = \theta L$ are defined.

For clay, from Equation 5-21, the elastic stiffness matrix can be expressed as

$$\begin{bmatrix} H \\ M' \end{bmatrix} = kL \cdot G_L \begin{bmatrix} \left[\left(1 - \frac{r}{12}\right) + f_b\right] & -\left[\left(\frac{1}{2} - \frac{r}{6}\right) + f_b\right] \\ -\left[\left(\frac{1}{2} - \frac{r}{6}\right) + f_b\right] & \left[\left(\frac{1}{3} - \frac{r}{12}\right) + f_b + f_\theta\right] \end{bmatrix} \begin{bmatrix} u \\ \vartheta \end{bmatrix}. \qquad \text{Equation 6-3}$$

where $r = \rho L/s_{uL}$, and $r = 0$ for stiff overconsolidated clay with uniform s_u.

The above two matrices can be re-written in a general form below (Houlsby, 2022a):

$$\begin{bmatrix} H \\ M' \end{bmatrix} = f_0 \cdot kL \cdot G_L \begin{bmatrix} 1 & -f_1 f_2 \\ -f_1 f_2 & f_1^2 \end{bmatrix} \begin{bmatrix} u \\ \vartheta \end{bmatrix}. \qquad \text{Equation 6-4}$$

Inversely, the above equation can be expressed as

$$\begin{bmatrix} u \\ \vartheta \end{bmatrix} = \frac{1}{f_0 \cdot kL \cdot G_L \cdot f_1^2 \cdot (1 - f_2^2)} \begin{bmatrix} f_1^2 & f_1 f_2 \\ f_1 f_2 & 1 \end{bmatrix} \begin{bmatrix} H \\ M' \end{bmatrix} \qquad \text{Equation 6-5}$$

where f_0, f_1 and f_2 are dimensionless factors and related soil strength properties. If base resistance is considered in the analysis, f_0, f_1 and f_2 are also influenced by f_b and f_θ.

The model used here is expressed in terms of the load (H, M') and displacement (u, ϑ) variables. Following Section 6.2.1, $H = H_e$ and $u_e = e \cdot \theta + u$ can be found. The power input to the system is $H \cdot \dot{u}$ (horizontal displacement rate at the ground level) $+M \cdot \dot{\theta}$ (rotation rate), which can be re-written as $H\left(e\dot{\theta} + \dot{u}\right) = H_e \cdot \dot{u_e}$ (horizontal displacement rate at the loading point).

Therefore, from the $H_e - u_e$ response at the loading point, the coupled $H - M'$ response can be found.

6.2.3.2 Ultimate response and failure surface

For drained sand, Equation 5-13 and Equation 5-14 can be normalised as

$$\frac{H}{DK\gamma' L^2} = \frac{(2\delta^2 - 1)}{2} - \underbrace{\frac{\left(c_3 V + \frac{\pi}{4} D^2 L\gamma'\right)\tan\phi'_{cr}}{DK\gamma' L^2}}_{f_{s_s}} \qquad \text{Equation 6-6}$$

and

$$\frac{M}{DK\gamma' L^3} = \frac{M'}{DK\gamma' L^2}$$

$$= \frac{(1 - 2\delta^3)}{3} + \left[\underbrace{\frac{\left(c_3 V + \frac{\pi}{4} D^2 L\gamma'\right)\tan\phi'_{cr}}{DK\gamma' L^2}}_{f_{s_s}} + \underbrace{\frac{\frac{c_3 V}{2}}{DK\gamma' L^2} \cdot \frac{D}{L}}_{f_{s_v}}\right] \qquad \text{Equation 6-7}$$

in which $\delta = d/L$ (between 0 and 1), $K = 3K_p$ (coefficient of passive lateral earth pressure) (Broms, 1964), f_{s_s} is the ultimate base shear factor for sand, and f_{s_v} is the ultimate base moment factor for sand due to vertical loading.

Based on the above equations, it is found that that K is 9.967 for dry *very loose* sand and 14.116 for dry *dense* sand. The f_{s_s} and $f_{s_s} + f_{s_v}$ values for the model piles used for the dry sand testing are shown in Figure 6-2. The type I and II piles have $D = 80$ mm and 84 mm, respectively. The aspect ratio L/D for dry sand is 4, and γ' values for different soil conditions are given in Table 3-3. The magnitude of base resistance depends on V, the aspect ratio D/L as well as pile shaft resistance. $c_3 = 1$ is assumed for extreme cases (*i.e.* pile shaft resistance is negligible and V is all transmitted to the pile base). The coupled normalised moment-horizontal load response can be expressed in terms of the failure surface, as described in Section 6.2.3.3.

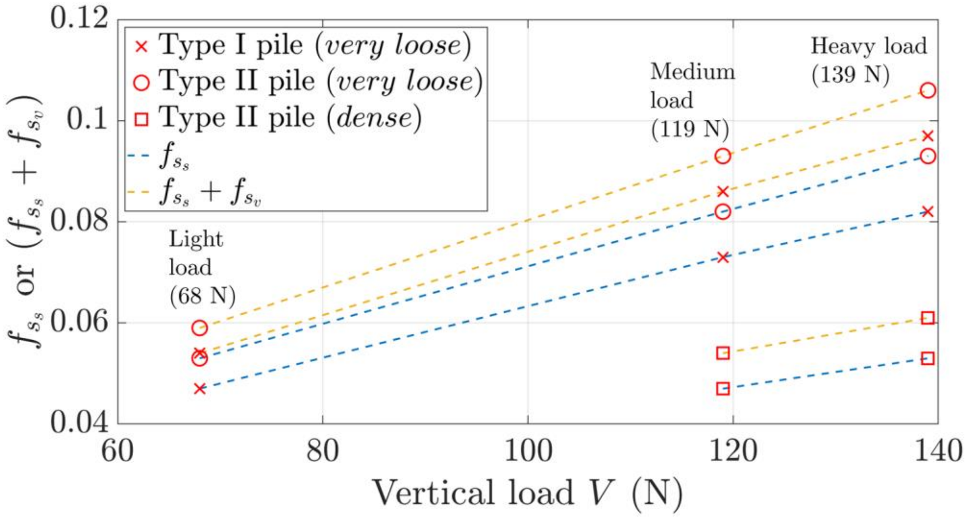

Figure 6-2 f_{s_s} and $f_{s_s}+f_{s_v}$ values for the testing in dry sand.

Following Equation 5-28 and Equation 5-29, the ultimate response in clay can be normalised as

$$\frac{H}{N_h s_{uL} DL} = (1-r)(2\delta-1) + \frac{r(2\delta^2-1)}{2} - \underbrace{\frac{c_4\pi}{4N_h}\cdot\frac{D}{L}}_{f_{c_s}} \qquad \text{Equation 6-8}$$

and

$$\frac{M'}{N_h s_{uL} DL} = \frac{(1-r)}{2}(1-2\delta^2) + \frac{r(1-2\delta^3)}{3} + \underbrace{\frac{c_4\pi}{4N_h}\cdot\frac{D}{L}}_{f_{c_s}} \qquad \text{Equation 6-9}$$

where f_{c_s} is the ultimate base shear factor for clay. It is noted that the above equation assumes that pile shaft resistance is sufficient to withstand V, so there is no additional moment resistance due to vertical loading at the pile base.

Similar to sand, the coupled normalised moment-horizontal load response in clay can be found using the failure surface (see discussions in Section 6.2.3.3). With the consideration of base shear, an additional term f_{c_s} is included in the normalised response. The maximum value of f_{c_s} is 0.029 when $c_4 = 1$, $N_h = 9$ and $L/D = 3$.

6.2.3.3 Failure surfaces

Following Equation 6-6 and Equation 6-7, the failure surfaces for sand with and without base resistance are shown in Figure 6-3. The failure surface enlarges distinctly and becomes "opened" for δ between 0 and 1 with base resistance being incorporated into the analysis. f_{s_s} and $(f_{s_s} + f_{s_v})$ are 0.093 and 0.1 (the maximal values for the model testing), respectively. With different test conditions in terms of V, pile geometry and relative density D_r, f_{s_s} and f_{s_v} will vary and result in differing failure surfaces.

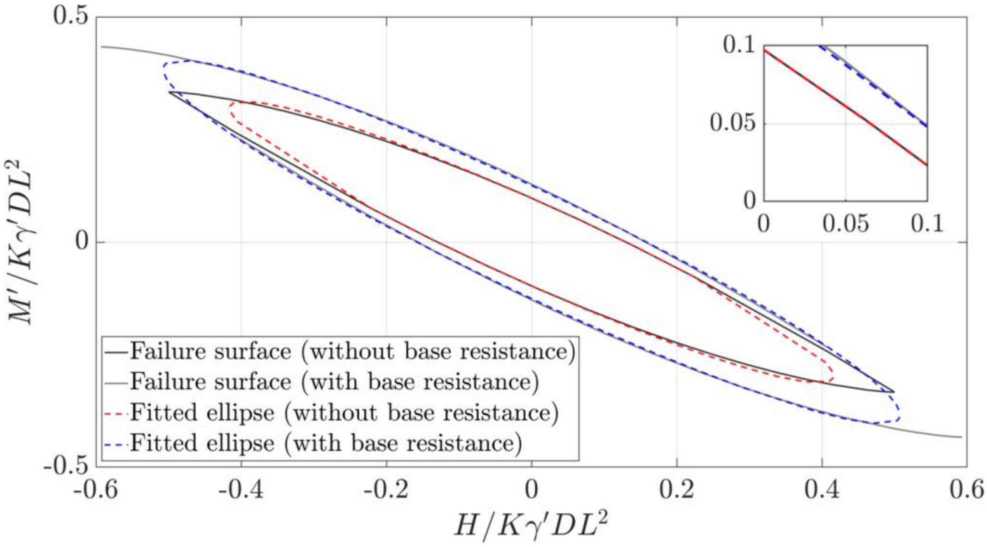

Figure 6-3 Failure surfaces for sand ($f_3 = 0.80$ when considering base resistance).

Figure 6-4 shows the failure surfaces of the normalised ultimate response in clay with and without base shear ($f_{c_s} = 0.029$). Similar to sand, by adding base shear into the analysis, the failure surface becomes larger; for $\delta = 0 \sim 1$, the surface is opened.

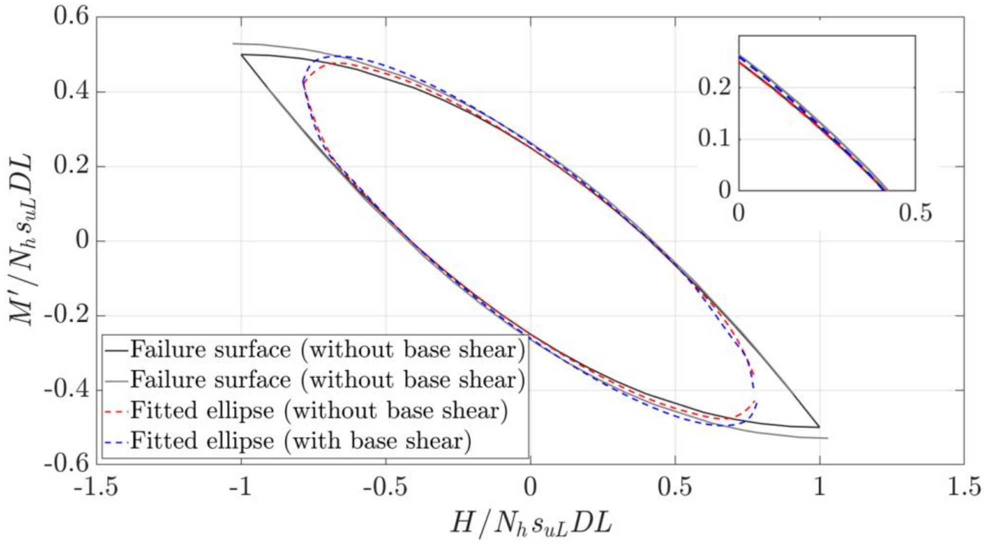

Figure 6-4 Failure surfaces for clay.

For numerical implementation, the failure surfaces for sand and clay can be approximately described using ellipses (see dashed in Figure 6-3 and Figure 6-4). The following elliptical function is used to describe the failure surface (Houlsby, 2022a):

$$\left(\frac{H}{H_0}\right)^2 + 2f_4 \cdot \left(\frac{H}{H_0}\right) \cdot \left(\frac{M'}{f_3 H_0}\right) + \left(\frac{M'}{f_3 H_0}\right)^2 - 1 = 0 \qquad \text{Equation 6-10}$$

in which H_0 is the intercept on the H-axis, and f_3 and f_4 are constants. From the data, it is found that the rotation point of a pile often falls between $0.7L$ and $0.9L$ ($\delta = 0.7$ ~ 0.9). Within this range, the failure surfaces are well-fitted by the ellipses.

For both soil conditions, the eccentricity of the originally fitted ellipse (red dashed) does not change if base resistance is added to the analysis (*i.e.* f_4 remains fixed). By decreasing f_3, the originally fitted ellipse becomes smaller. The f_3 and f_4 values for different test conditions are given below in Section 6.2.3.4.

It is noted that these failure surfaces and fitted ellipses were only examined for $L/D = 3$ ~ 4, and other considerations may be required for extreme L/D ratios (*e.g.* $L/D < 1$ for shallow foundations or footings).

6.2.3.4 Fitting parameters

Table 6-1 lists the input parameters for dry sand and saturated stiff clay without incorporating base resistance into design. It is noted that these parameters have physical meanings and cannot be arbitrarily calibrated to fit test data. The values of f_1 and f_2 are given by the derivations of elastic stiffness in Section 6.2.3.1. For saturated stiff clay, soil strength properties are assumed to be uniform, and therefore, $r = 0$ is taken for f_1 and f_2. The parameters f_3 and f_4 are determined using approximated elliptical failure surfaces for the ultimate condition, as described in Section 6.2.3.3. Considering base resistance, the contribution of f_b can improve horizontal load response, and f_θ appears to enhance moment capacity in dry sand. For both soil conditions, f_1 and f_3 are modified (see Table 6-2) with considering base resistance. f_1 for dry and clay are approximately 0.735 and 0.675 , respectively. f_3 for dry sand is dependent on V.

Table 6-1 Input parameters for the model without considering base resistance.

	Dry sand	Saturated stiff clay ($r = 0$)
f_1	$\sqrt{\frac{2}{7}\cdot\frac{3}{2}} = \sqrt{\frac{3}{7}}$ 0.65	$\sqrt{\frac{\left(\frac{1}{3}-\frac{r}{12}\right)}{\left(1-\frac{r}{12}\right)}}$ 0.58
f_2	$\frac{2}{5}\cdot\frac{3}{2}\cdot\sqrt{\frac{7}{3}} = \frac{\sqrt{21}}{5}$ 0.92	$\frac{\left(\frac{1}{2}-\frac{r}{6}\right)\cdot\sqrt{\left(1-\frac{r}{12}\right)}}{\sqrt{\left(\frac{1}{3}-\frac{r}{12}\right)}}$ 0.87
f_3	0.75	0.60
f_4	0.95	0.85

Table 6-2 Input parameters for the model with base resistance.

	Dry sand	Saturated stiff clay ($r = 0$)
f_b	0.15 ($D/L = 4$; $\nu = 0.3 \sim 0.4$)	0.22 ($D/L = 3$; $\nu = 0.49$)
f_θ	0.002 ($D/L = 4$; $\nu = 0.3 \sim 0.4$)	0.006 ($D/L = 3$; $\nu = 0.49$)
f_1	$\sqrt{\dfrac{\left(\frac{2}{7} + f_b + f_\theta\right)}{\left(\frac{2}{3} + f_b\right)}}$ 0.735	$\sqrt{\dfrac{\left[\left(\frac{1}{3} - \frac{r}{12}\right) + f_b + f_\theta\right]}{\left[\left(1 - \frac{r}{12}\right) + f_b\right]}}$ 0.675
f_2	$\dfrac{\left(\frac{2}{5} + f_b\right)}{\sqrt{\left(\frac{2}{3} + f_b\right) \cdot \left(\frac{2}{7} + f_b + f_\theta\right)}}$ 0.92	$\dfrac{\left(\frac{1}{2} - \frac{r}{6}\right) + f_b}{\sqrt{\left[\left(1 - \frac{r}{12}\right) + f_b\right] \cdot \left[\left(\frac{1}{3} - \frac{r}{12}\right) + f_b + f_\theta\right]}}$ 0.87
f_3	0.78 ($V = 68$ N) 0.795 ($V = 139$ N) (*very loose*) 0.78 (*dense*)	0.63
f_4	0.95	0.85

6.2.4 Modelling under the hyperplasticity framework (Houlsby and Puzrin, 2006)

The hyperplasticity approach for describing constitutive behaviours of non-linear materials (*e.g.* soils) is presented by Houlsby and Puzrin (2006), following the original work by Ziegler (1963). The hyperplasticity framework obeys the First and Second Laws of Thermodynamics, which allows a compact development of plasticity theories (Puzrin and Houlsby, 2001). The First Law describes energy conservation, and the Second Law illustrates dissipation, expressed by the Clausius-Duhem inequality. Hyperplasticity also allows the modelling of both rate-dependent (*e.g.* clay) and rate-independent (*e.g.* dry sand) mechanical behaviours.

The hyperplasticity modelling approach uses internal variables (often plastic strains) to memorise the loading history. For a dissipative material, the constitutive behaviour can be fully described by two potential functions: (1) either the Gibbs free energy (g) or the Helmholtz free energy (f) and (2) a dissipation function (d) or a yield function (y). In elasticity theory, the Gibbs free energy g represents complementary energy, and the Helmholtz free energy f means strain energy. A dissipation function d describes dissipation as a function of the state, rate of the internal variables and heat flow. Further information on the formulation of hyperplasticity, including the theoretical background and mathematical transforms, can be found in Houlsby and Puzrin (2006) and the hyperplasticity website (Houlsby, 2022b).

6.2.4.1 Kinematic hardening

The model utilises a multi-surface plasticity approach to describe kinematic hardening, as illustrated in Figure 6-5. Conceptually, the model implements a series of yield surfaces, each of which is the same shape as the failure surface described in Section 6.2.3.3 above. Each element has a parallel spring, slider and dashpot, representing elastic, plastic and rate-dependent properties, respectively. The subscript e in the model specifies that the parameters of the model are related to a given load eccentricity e. Without considering soil rate effects, the viscous terms μ_{e1}, $\mu_{e2}\ldots\mu_{eN}$ (*i.e.* the dashpots in Figure 6-5) are omitted, and in this case the model would obey Masing's hypothesis for one-dimensional cyclic loading. The properties of these components are described in the following sections, and the derivation of the kinematic hardening model in hyperplasticity is provided in Appendix A.1.

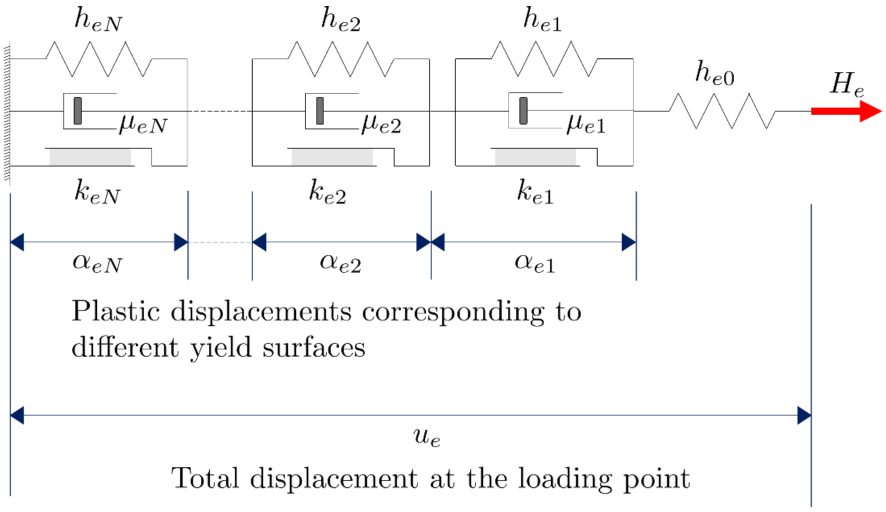

Figure 6-5 Conceptual model for kinematic hardening considering rate effects.

6.2.4.2 Calibration and formulation of the general loading model

The general loading model is calibrated using a data-driven approach. For the cyclic testing in clay, data from each test are analysed to obtain a backbone curve (*i.e.* the initial loading response) of the $H_e - u_e$ response individually to avoid the influence of variation throughout the tests. If the variation between different tests is minimal or they have a similar reaction curve (*e.g.* the dry sand testing), one may be used for calibration to simulate the other. For calibration, (N+1) data points were retrieved to obtain a discrete $H_e - u_e$ reaction curve, as illustrated in Figure 6-6. For modelling monotonic response, approximately 20 data points were acquired.

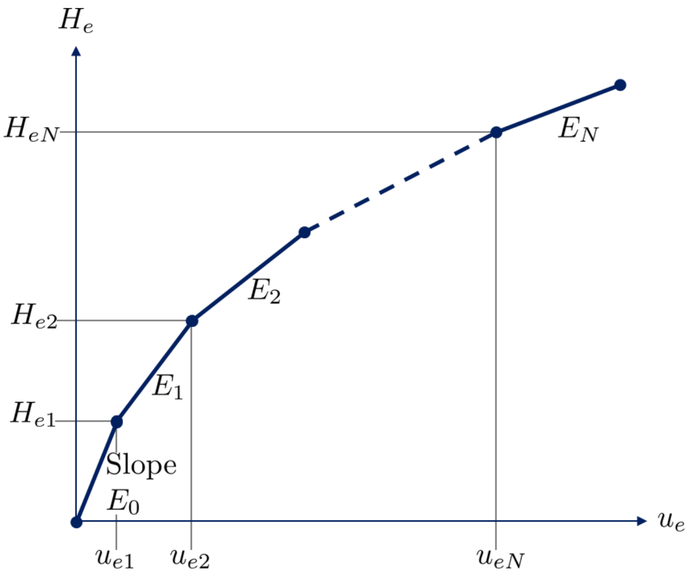

Figure 6-6 Calibration of $H_e - u_e$ response for modelling.

From the calibration curve, it is found that

$$H_{en} = k_{en}, n = 1 \dots N \qquad \text{Equation 6-11}$$

$$u_{en} = \sum_{i=0}^{n-1} \frac{k_{en} - k_{ei}}{h_{ei}}, n = 0 \dots N \qquad \text{Equation 6-12}$$

and

$$\frac{1}{E_n} = \sum_{i=0}^{n} \frac{1}{h_{ei}}, n = 0 \dots N. \qquad \text{Equation 6-13}$$

Conversely, k_{en} and h_{en} can be expressed as

$$k_{en} = H_{en}, n = 1 \dots N \qquad \text{Equation 6-14}$$

and

$$h_{e0} = E_0;\ h_{en} = \frac{E_{n-1}E_n}{E_{n-1} - E_n}, n = 1 \dots N. \qquad \text{Equation 6-15}$$

The formulation of the general loading model by Houlsby (2022a) is given in Appendix A.2. Following the above calibration procedure, the g and y functions based on the kinematic hardening model are derived by incorporating macro pile response illustrated in Figure 6-1. Physical quantities and their derived relationships in hyperplasticity are given in Table 6-3, and fitting parameters f_1, f_2, f_3 and f_4 can be found in Table 6-1 and Table 6-2.

Table 6-3 Physical quantities and their corresponding formula.

Physical quantity	u	ϑ	$\bar{\chi}_{un}$	$\bar{\chi}_{\vartheta n}$	$\dot{\alpha}_{un}$ (rate of α_{un})	$\dot{\alpha}_{\vartheta n}$ (rate of $\alpha_{\vartheta n}$)
Derived relationship	$-\frac{\partial g}{\partial H}$	$-\frac{\partial g}{\partial M'}$	$-\frac{\partial g}{\partial \alpha_{un}}$	$-\frac{\partial g}{\partial \alpha_{\vartheta n}}$	$\lambda_n \frac{\partial y_n}{\partial \chi_{un}}$	$\lambda_n \frac{\partial y_n}{\partial \chi_{\vartheta n}}$

6.2.4.3 Rate effects

To incorporate rate effects into the general loading model, linear viscosity and RPT are derived in hyperplasticity in Appendix A.3 and A.4, based on the previous work by Houlsby and Puzrin (2006). As illustrated at the element-scale in Figure 1-22, linear viscosity may occur near the upper yield, while the semi-logarithmic relationship (*e.g.* RPT) is observed at a faster rate. Since the determination of the upper yield for monopile response is unclear, both rate-dependent expressions are considered in this thesis.

For numerical implementation in hyperplasticity, in addition to the g and y functions given in the general loading model, the flow potential function w is introduced to simulate rate effects, with μ_{e1}, μ_{e2},… μ_{eN} being included in Figure 6-5. With w, $\partial w/\partial\chi_{un}$ and $\partial w/\partial\chi_{\vartheta n}$ functions implemented, rate effects for monopiles in idealised soils can be simulated.

6.2.4.4 HARM (Houlsby et al., 2017)

The HARM is extended from the kinematic hardening model described in Section 6.2.4.1 by adding the ratcheting factor at the loading point, R_e. Its series form is illustrated conceptually in Figure 6-7. To include the HARM features in the model, following Appendix B3 in Houlsby *et al.* (2017), Equation A-12 and Equation A-13 are re-written as

$$\begin{aligned} g = &-\frac{f_1^2H^2+2f_1f_2HM'+M'^2}{2h_0} \\ &-\left[\sum_{n=1}^{N}(H\alpha_{un}+M'\alpha_{\vartheta n})\right]\underbrace{-(H\alpha_{ur}+M'\alpha_{\vartheta r})}_{\text{Ratcheting}} \\ &+\sum_{n=1}^{N}\frac{h_n}{2f_1^2(1-f_2^2)}\left(\alpha_{un}^2-2f_1f_2\alpha_{un}\alpha_{\vartheta n}+f_1^2\alpha_{\vartheta n}^2\right) \end{aligned}$$

Equation 6-16

and

$$\begin{aligned} y_n = &\frac{\sqrt{f_3^2\chi_{un}^2+2f_3f_4\chi_{un}\chi_{\vartheta n}+\chi_{\vartheta n}^2}}{k_n}-1 \\ &\underbrace{+R_e\left(\frac{\sqrt{f_3^2\chi_{ur}^2+2f_3f_4\chi_{ur}\chi_{\vartheta r}+\chi_{\vartheta r}^2}}{k_n}-\frac{\sqrt{f_3^2H^2+2f_3f_4HM'+M'^2}}{k_n}\right)}_{\text{Ratcheting}} \end{aligned}$$

Equation 6-17

where α_{ur} and $\alpha_{\vartheta r}$ are the ratcheting displacements in u and ϑ, χ_{ur} and $\chi_{\vartheta r}$ are the generalised ratcheting forces in the $H-u$ and $M'-\vartheta$ domains.

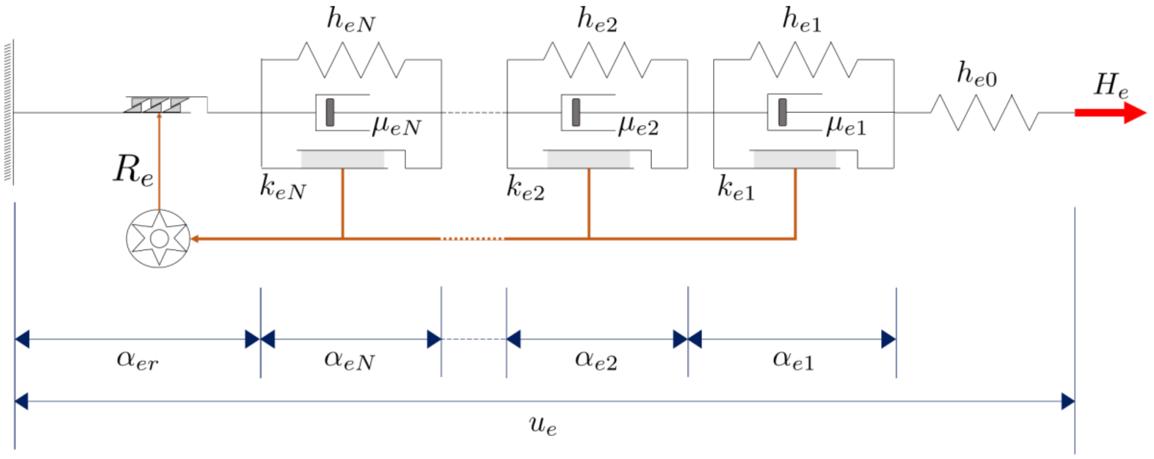

Figure 6-7 Conceptual expression of the HARM
extended from the kinematic hardening model (after Houlsby *et al.*, 2017).

The calibration of the HARM features follows Richards (2019) for laboratory-scale monopile testing in dry sand. Details can be found in Richards' DPhil thesis. In order to capture ratcheting, the ratcheting factor R_e is found to change with the amount of ratcheting at the loading point (α_{er}). R_e can be expressed using a modified power-law function suggested by Richards (2019):

$$R_e = R_{e0}\left\{1 + \frac{\beta}{\beta^*}\left[\left(\frac{R_{e0}}{R_e^*}\right)^{\frac{1}{m_r}} - 1\right]\right\}^{-\frac{1}{m_r}} \qquad \text{Equation 6-18}$$

in which β is the hardening parameter, m_r is the exponent for the R_e equation, R_{e0} is often taken as 1 (R_e values are less than 1), and (β^*, R_e^*) is a selected point specified by the R_e function. The illustration of the power-law function is shown in Figure 6-8. To capture the ratcheting rate, $\dot{\beta}$, it may be expressed as

$$\dot{\beta} = |\dot{\alpha}_{er}|. \qquad \text{Equation 6-19}$$

From the above equation, it is assumed that the ratcheting rates of u and θ are identical. R_{e0}, m_r, β^* and R_e^* need to be calibrated. Examples of the HARM applications for dry sand and saturated stiff clay are illustrated in Sections 6.3.4 and 6.4.4.

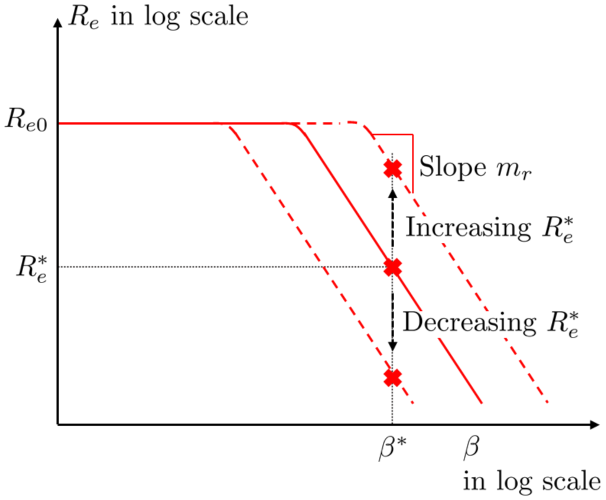

Figure 6-8 Illustration of the R_e function (after Richards, 2019).

6.2.4.5 Numerical implementation

The equations for numerical implementations for general loading are found in Table 6-4. For numerical implementation, these equations were coded using Python and solved incrementally by N steps using the HyperDrive code by Houlsby (2022a). When the model is running, input parameters f_1, f_2, f_3 and f_4 are pre-defined, and k_n and h_n are obtained from the calibration curve. μ (and $\dot{\alpha}_{ref}$) can be added into the model for rate dependency if w, $\partial w/\partial \chi_{un}$ and $\partial w/\partial \chi_{\vartheta n}$ functions are defined. The physical quantities (*e.g.* loads and displacements) are given in Table 6-3, and equations for numerical implementation are derived in Table 6-4.

The time differential functions of u, ϑ, $\bar{\chi}_{un}$, $\bar{\chi}_{\vartheta n}$, $\dot{\alpha}_{un}$ and $\dot{\alpha}_{\vartheta n}$ are derived for $n = 1 \dots N$, which yields 2+4N equations. At each increment, if there is no yield, the time differential function of $\dot{y}_n \neq 0$ but $\lambda_n = 0$; for other conditions, $y_n = y_{n0}$ at the end of the previous increment. $\dot{y}_n$ can be implemented as

$$\dot{y}_n = -\frac{y_{n0}}{\delta t} = \frac{2(f_3^2 \chi_{un}\dot{\chi}_{un} + f_3 f_4 \chi_{un}\dot{\chi}_{\vartheta n} + f_3 f_4 \dot{\chi}_{un}\chi_{\vartheta n} + \chi_{\vartheta n}\dot{\chi}_{\vartheta n})}{k_n^2} \qquad \text{Equation 6-20}$$

where δt is the timestep, and thus further N equations are given. Together with load-controlled data $(\dot{H}, \dot{M}')$, displacement-controlled data $(\dot{u}, \dot{\vartheta})$, or combinations of the two, the equations in

Table 6-4 are solved incrementally. More steps with smaller increments are required to simulate a test more accurately.

Table 6-4 List of equations for numerical implementation for general loading.

$\frac{\partial g}{\partial H}$	$-\frac{f_1^2 H + f_1 f_2 M'}{h_0} - \sum_{n=1}^{N} \alpha_{un}$
$\frac{\partial g}{\partial M'}$	$-\frac{f_1 f_2 H + M'}{h_0} - \sum_{n=1}^{N} \alpha_{\vartheta n}$
$\frac{\partial g}{\partial \alpha_{un}}$	$-H + \frac{h_n}{f_1^2(1-f_2^2)}(\alpha_{un} - f_1 f_2 \alpha_{\vartheta n})$
$\frac{\partial g}{\partial \alpha_{\vartheta n}}$	$-M' + \frac{h_n}{f_1^2(1-f_2^2)}(f_1 f_2 \alpha_{un} + f_1^2 \alpha_{\vartheta n})$
$\begin{bmatrix} \frac{\partial^2 g}{\partial H^2} & \frac{\partial^2 g}{\partial M' \partial H} \\ \frac{\partial^2 g}{\partial H \partial M'} & \frac{\partial^2 g}{\partial M'^2} \end{bmatrix}$	$\begin{bmatrix} -\frac{f_1^2}{h_0} & -\frac{f_1 f_2}{h_0} \\ -\frac{f_1 f_2}{h_0} & -\frac{1}{h_0} \end{bmatrix}$
$\begin{bmatrix} \frac{\partial^2 g}{\partial \alpha_{un}^2} & \frac{\partial^2 g}{\partial \alpha_{\vartheta n} \partial \alpha_{un}} \\ \frac{\partial^2 g}{\partial \alpha_{un} \partial \alpha_{\vartheta n}} & \frac{\partial^2 g}{\partial \alpha_{\vartheta n}^2} \end{bmatrix}$	$\begin{bmatrix} \frac{h_n}{f_1^2(1-f_2^2)} & \frac{-f_1 f_2 h_n}{f_1^2(1-f_2^2)} \\ \frac{-f_1 f_2 h_n}{f_1^2(1-f_2^2)} & \frac{2 f_1 h_n}{f_1^2(1-f_2^2)} \end{bmatrix}$
$\begin{bmatrix} \frac{\partial^2 g}{\partial H \partial \alpha_{un}} & \frac{\partial^2 g}{\partial M' \partial \alpha_{un}} \\ \frac{\partial^2 g}{\partial H \partial \alpha_{\vartheta n}} & \frac{\partial^2 g}{\partial M' \partial \alpha_{\vartheta n}} \end{bmatrix}$	$\begin{bmatrix} -\alpha_{un} & 0 \\ 0 & -\alpha_{\vartheta n} \end{bmatrix}$
$\frac{\partial y_n}{\partial \chi_{un}}$	$\frac{2(f_3 \chi_{un} + f_3 f_4 \chi_{\vartheta n})}{k_n^2}$
$\frac{\partial y_n}{\partial \chi_{\vartheta n}}$	$\frac{2(f_3 f_4 \chi_{un} + \chi_{\vartheta n})}{k_n^2}$
$\begin{bmatrix} \frac{\partial^2 y_n}{\partial \chi_{un}^2} & \frac{\partial^2 y_n}{\partial \chi_{un} \partial \chi_{\vartheta n}} \\ \frac{\partial^2 y_n}{\partial \chi_{\vartheta n} \partial \chi_{un}} & \frac{\partial^2 y_n}{\partial \chi_{\vartheta n}^2} \end{bmatrix}$	$\begin{bmatrix} \frac{2 f_3}{k_n^2} & \frac{2 f_3 f_4}{k_n^2} \\ \frac{2 f_3 f_4}{k_n^2} & \frac{2}{k_n^2} \end{bmatrix}$
$\begin{bmatrix} \frac{\partial w_n}{\partial \chi_{un}} & \frac{\partial w_n}{\partial \chi_{\vartheta n}} \end{bmatrix}$ (linear rate dependency)	$\begin{bmatrix} \frac{y_n}{\mu} \cdot S(\chi_{un}) & \frac{y_n}{\mu} \cdot S(\chi_{\vartheta n}) \end{bmatrix}$
$\begin{bmatrix} \frac{\partial w_n}{\partial \chi_{un}} & \frac{\partial w_n}{\partial \chi_{\vartheta n}} \end{bmatrix}$ (rate process theory)	$\begin{bmatrix} \dot{\alpha}_{ref} \sinh\left(\frac{\chi_{un}}{\dot{\alpha}_{ref}}\right) & \dot{\alpha}_{ref} \sinh\left(\frac{\chi_{\theta n}}{\dot{\alpha}_{ref}}\right) \end{bmatrix}$

To include the HARM features to capture cyclic loading, the g and y functions are re-written, as given in Equation 6-16 and Equation 6-17. Extra terms $\partial g/\partial u_r$, $\partial g/\partial \vartheta_r$, $\partial g/\partial \chi_{ur}$, $\partial g/\partial \chi_{\vartheta r}$, $\partial y/\partial \chi_{ur}$ and $\partial y/\partial \chi_{\vartheta r}$ are required for the analysis, with the additional parameters for the R_e function.

6.3 Modelling pile responses in dry sand

6.3.1 Monotonic response

6.3.1.1 Very loose sand

Figure 6-9 shows the modelling of a monotonic loading test in dry *very loose* sand. In this case, data from test DLS_L_I_0.05mm/s_7D_H were used to calibrate the model and compared with the modelling result. The model inputs f_1, f_2, f_3 and f_4 without considering base resistance are given in Table 6-1. With the consideration of base resistance, f_1 and f_3 are increased to 0.735 and 0.795, respectively (see Table 6-2).

It can be seen from the results in Figure 6-9 that the pile response does not appear to change whether base resistance is considered or not. The reason for this is that the magnitude of vertical loading V is small. In the moment-horizontal load response, the yield surfaces at various loading stages are illustrated and approximately straight lines in the $H-M$ domain (similar to Figure 6-3). These yield surfaces can help identify pile responses at different load eccentricities e. The difference between the yield surfaces with and without base reactions is found to be small (see blue and red dashed in Figure 6-9).

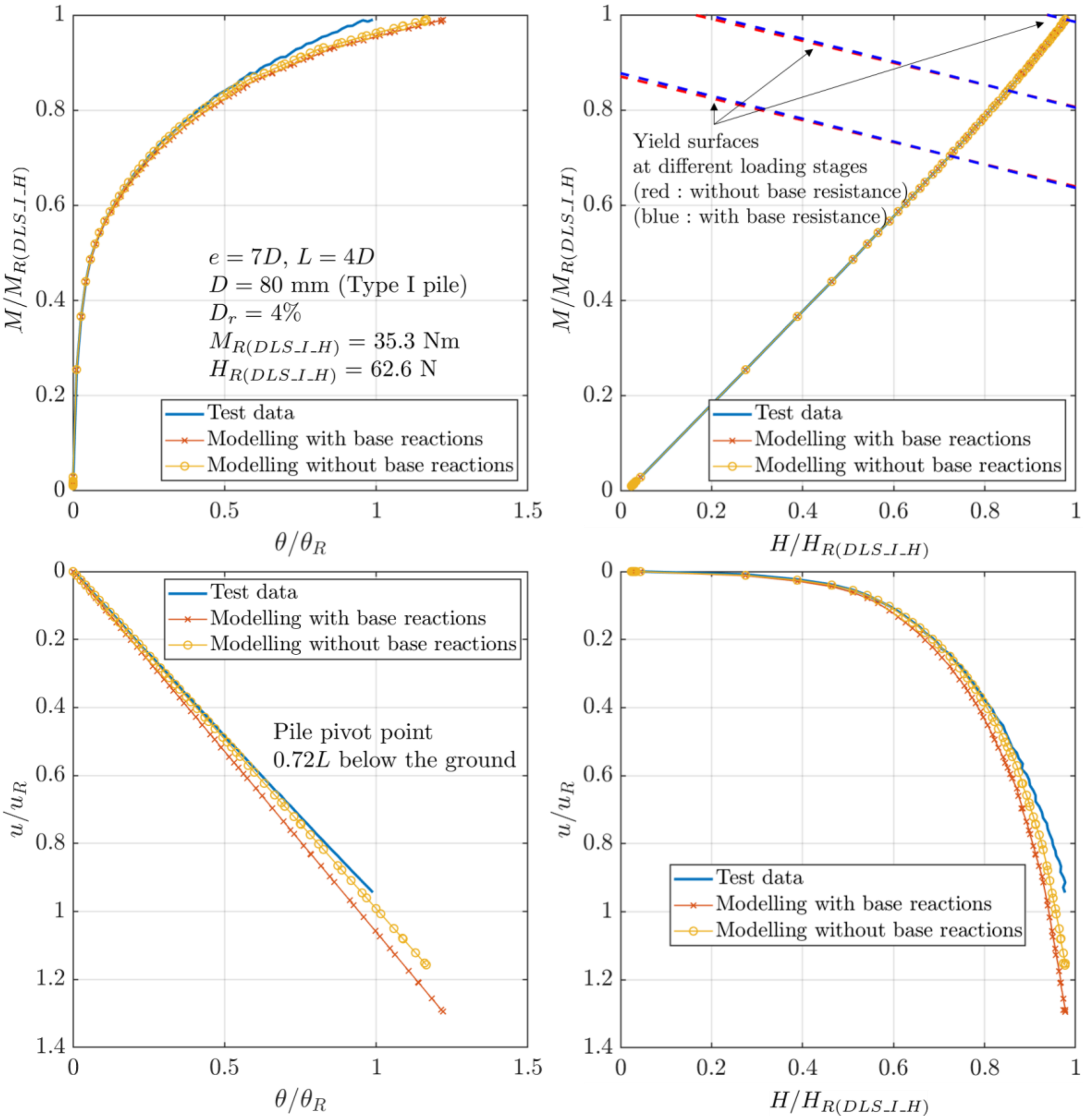

Figure 6-9 Illustration of pile response to monotonic loading in dry *very loose* sand.

Both experimental and modelling results indicate that the pile pivot position is about $0.72L$ below the ground level, as shown in the rotation-horizontal displacement response in Figure 6-9. By comparing the simulations and test data, it can be concluded that the analytical derivations embedded in the model are valid and can capture pile response in dry *very loose* sand with good confidence.

6.3.1.2 *Dense* sand

Figure 6-10 shows the pile response in *dense* sand to monotonic loading using data from test DDS_L_II_50mm/s_7D_H. The model inputs for dry *dense* are given in Table 6-1 and Table 6-2. Again, adding base resistance does not appear to change pile capacity from the results. This phenomenon suggests that the impact of vertical loading on base reactions in dry *dense* sand is negligible.

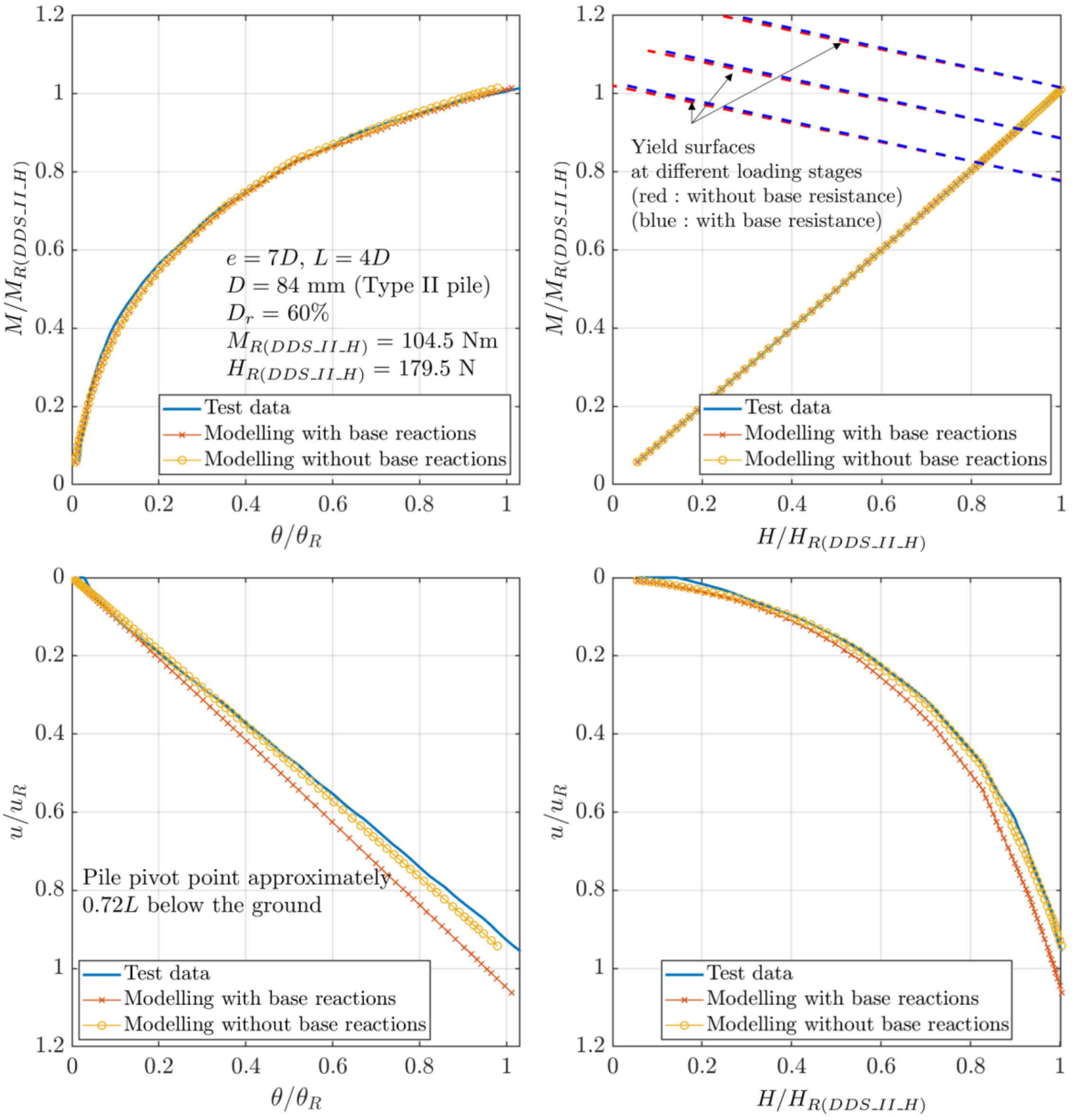

Figure 6-10 Illustration of pile response to monotonic loading in dry *dense* sand.

The yield surfaces at different loads are demonstrated in blue and red dashed (with and without considering base resistance). Similar to dry *very loose* sand, the pile rotational point is about

0.72 L below the ground level, and the model performs well to capture monotonic loading response in dry *dense* sand.

6.3.2 Load eccentricity effects

6.3.2.1 Fixed load eccentricity

Figure 6-11 shows modelling load eccentricity effects in dry *very loose* sand. In the analysis, data at $e = 7D$ (test DLS_L_I_0.05mm/s_7D_M) were retrieved to obtain a calibration curve with the medium pile weight V of 119 N. The input parameters are found in Table 6-2 (considering base resistance), and $f_3 = 0.79$. The modelling results are very close to the actual pile responses from the test data, indicating that the model can accurately predict pile responses at different e. From the test data, it is found that the rotation-horizontal displacement response may change greatly with e, but this phenomenon may be due to sample variations. Only a slight change in the rotation-horizontal displacement response is seen in the modelling results.

The yield surfaces in the moment-horizontal load response at different loading stages are also illustrated to help identify load eccentricity effects (see blue dashed considering base resistance). Along the same yield surface, moment capacity increases with e and less θ, while the horizontal load-displacement response shows an inverse trend.

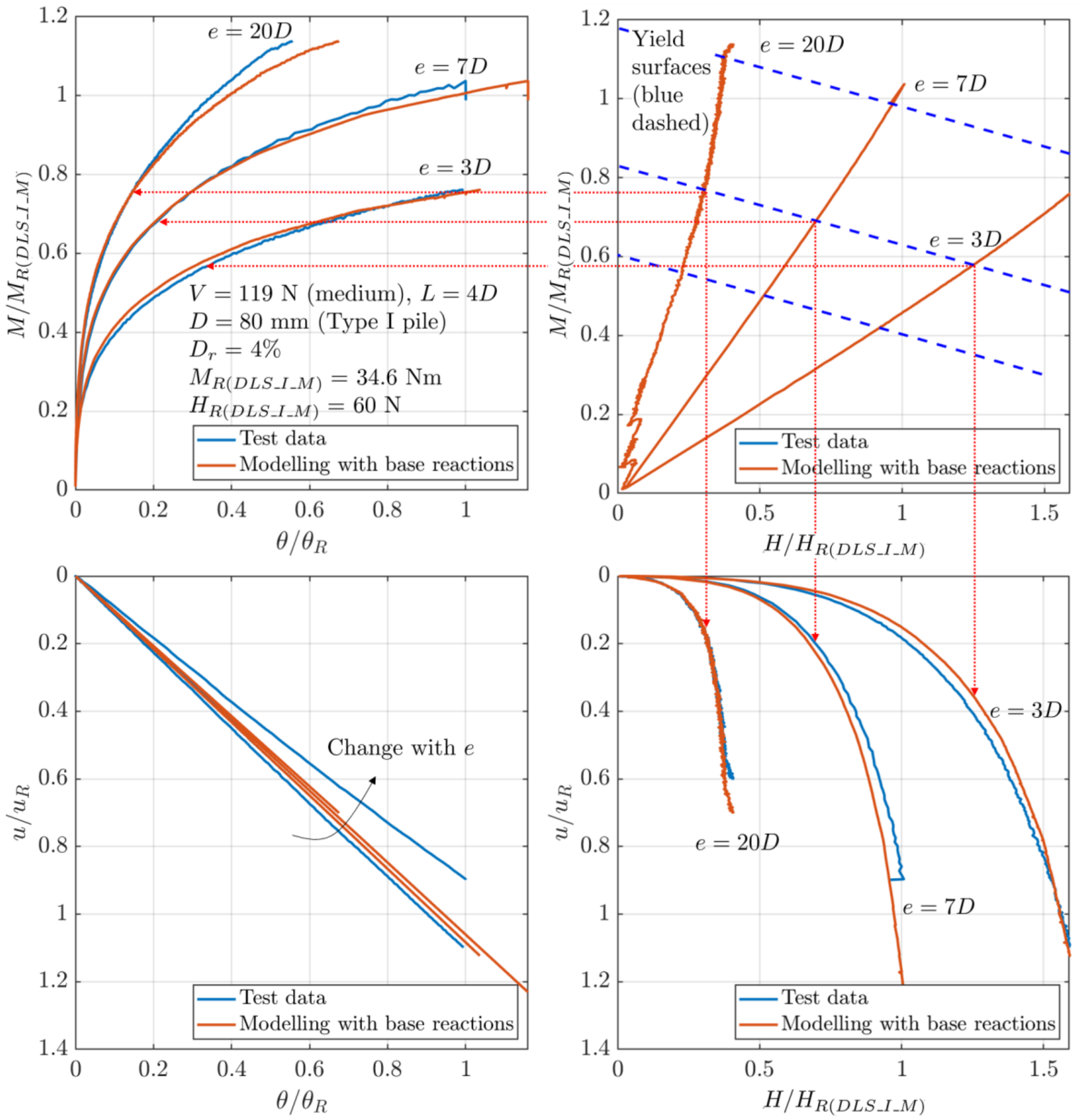

Figure 6-11 Modelling various heights of loading points in dry *very loose* sand.

6.3.2.2 Time-varying load eccentricity

In *dense* sand, data from tests DDS_L_II_var_vare_H_1 and DDS_L_II_var_vare_H_2 are compared with the modelling of time-varying e (see Section 3.8.2 for details of the test inputs and results). The monotonic response in Figure 6-10 was adopted to calibrate a reaction curve for the model, as the soil condition and V across these tests are almost identical. The modelling results are shown in Figure 6-12 and Figure 6-13. Overall, the model captures time-varying combined $H - M$ loading response well, except at large pile movement (*e.g.* $\theta/\theta_R > 0.6$).

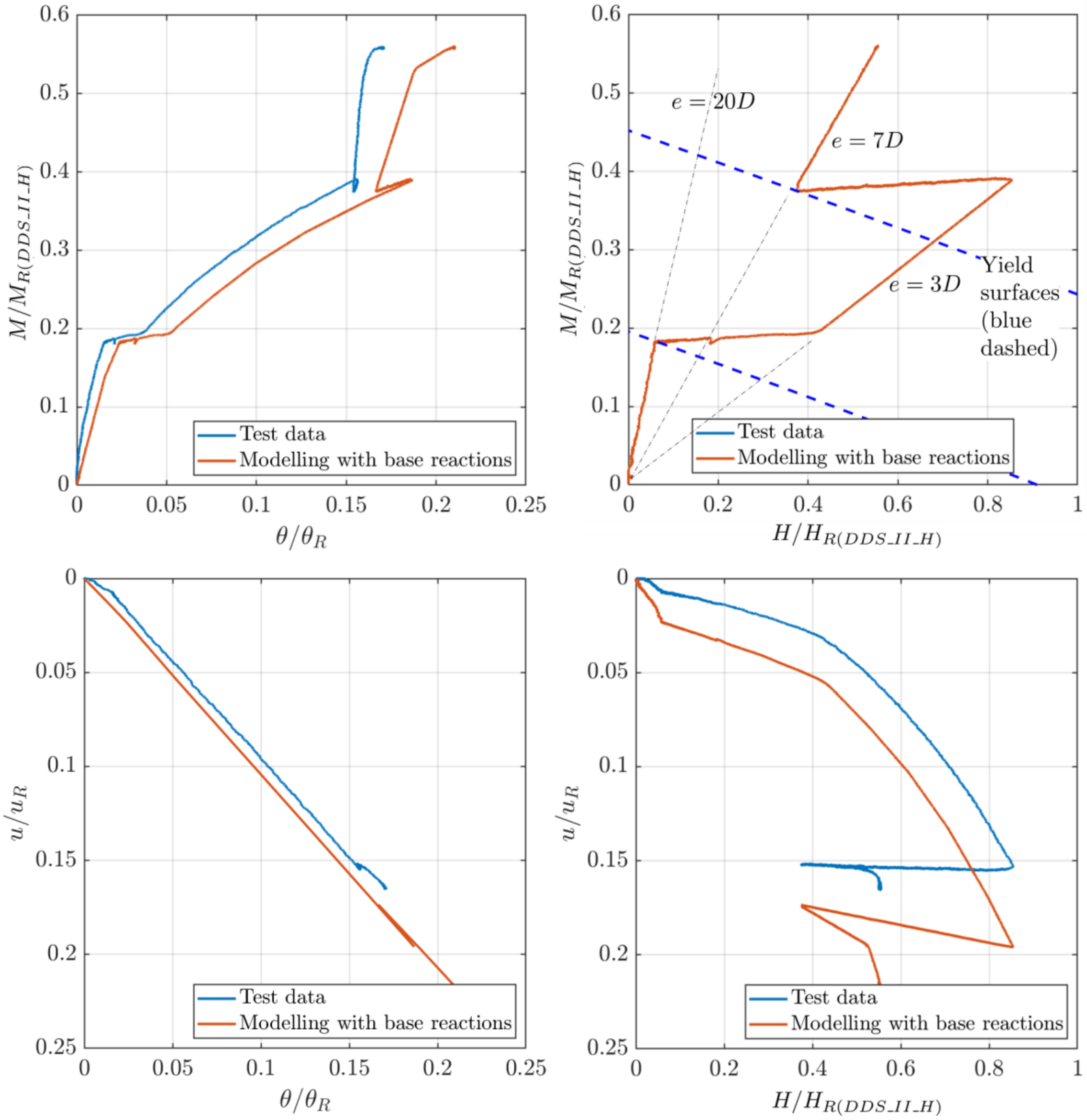

Figure 6-12 Modelling test DDS_L_II_var_vare_H_1.

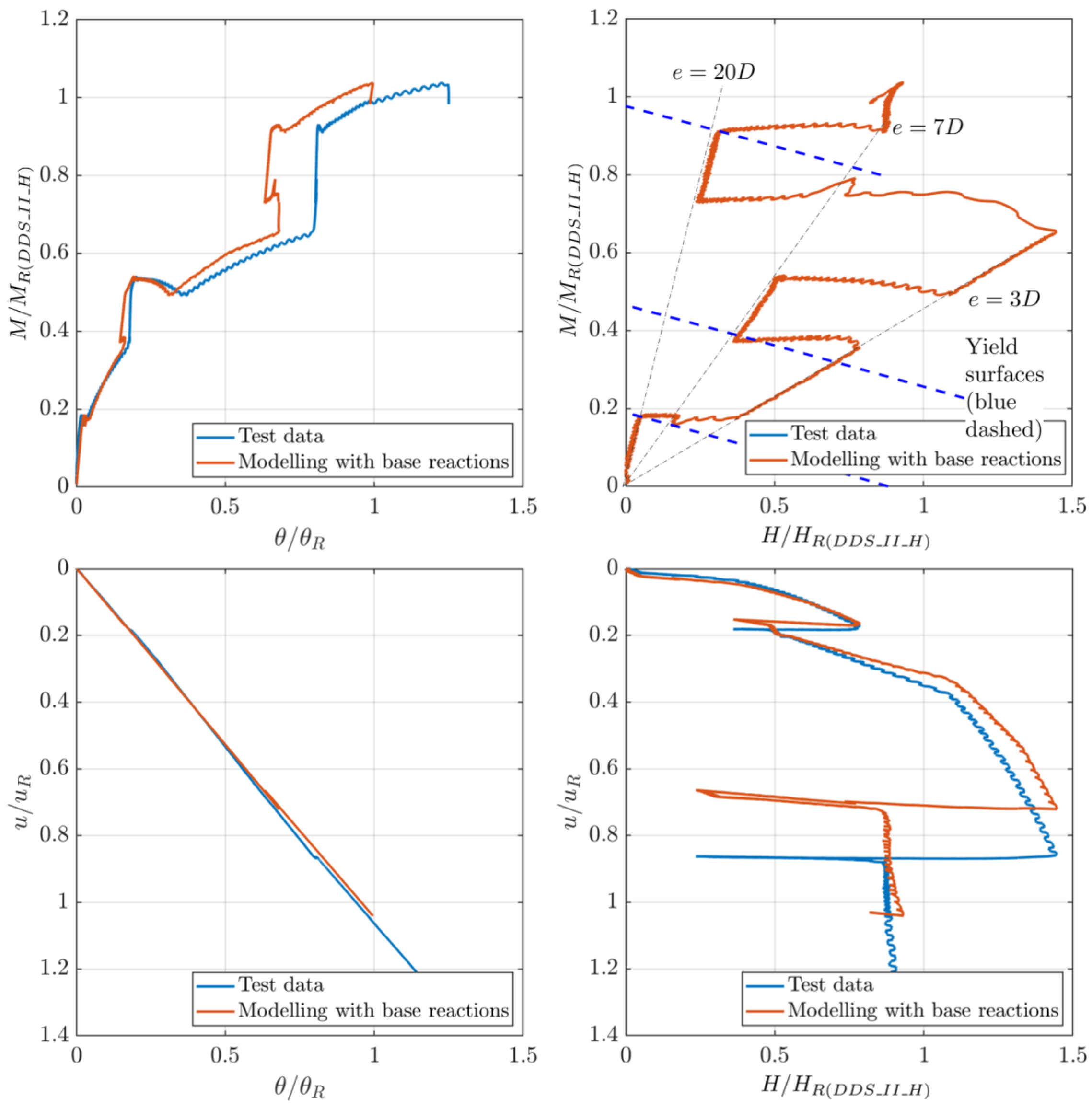

Figure 6-13 Modelling test DDS_L_II_var_vare_H_2.

The shape of the yield surface does not change with e and is only related to the pile aspect ratio L/D. If the $H - M$ loading moves outside the previously established yield surface, pile deformation is expected to increase significantly. By contrast, if the $H - M$ loading moves within the yield surface, the changes in u and θ are minimal, and the response tends to be elastic.

6.3.3 Impact of vertical loading

Data in Figure 6-9 are used to estimate the responses of the same model pile under different V in dry *very loose* sand. With decreasing V, the response becomes softer, and pile capacity is reduced. The analysis in Section 6.3.1 shows that the influence of base resistance on the model pile response in sand is minimal. In this case (see Figure 6-14), f_3 was changed within the range between 0.78 and 0.795 for different V (Table 6-2), but there is no much difference in the two modelling results compared to the test data.

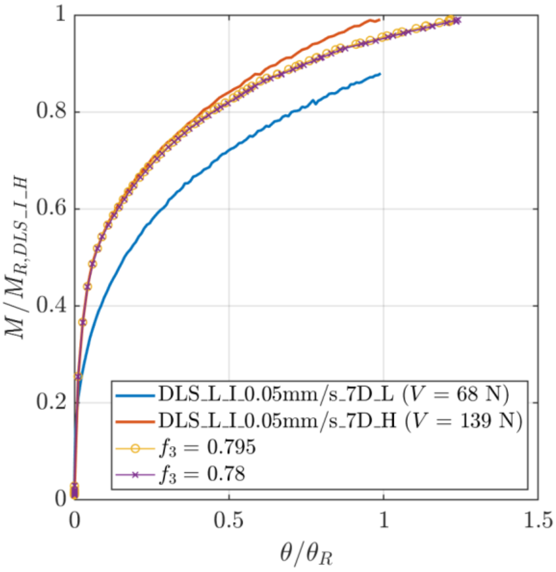

Figure 6-14 Evaluating the impact of vertical loading by changing the input parameter f_3.

6.3.4 Cyclic lateral loading

6.3.4.1 Without modelling ratcheting

An illustrative example of modelling cyclic loading response without the HARM features is presented using data from test DDS_C_II_0.5Hz_7D_H. The initial loading response from the test was used as the calibration curve for modelling. The input parameters f_1, f_2, f_3 and f_4 are given in Table 6-2, considering base resistance. The model captures the pile response with good confidence for the initial loading-unloading (see Figure 6-15). The slight difference between the test data and the modelling result is due to sample variations. However, Figure 6-16 shows that with cyclic loading, ratcheting occurs but cannot be precisely modelled. Therefore, the HARM features are required to include the effect of ratcheting.

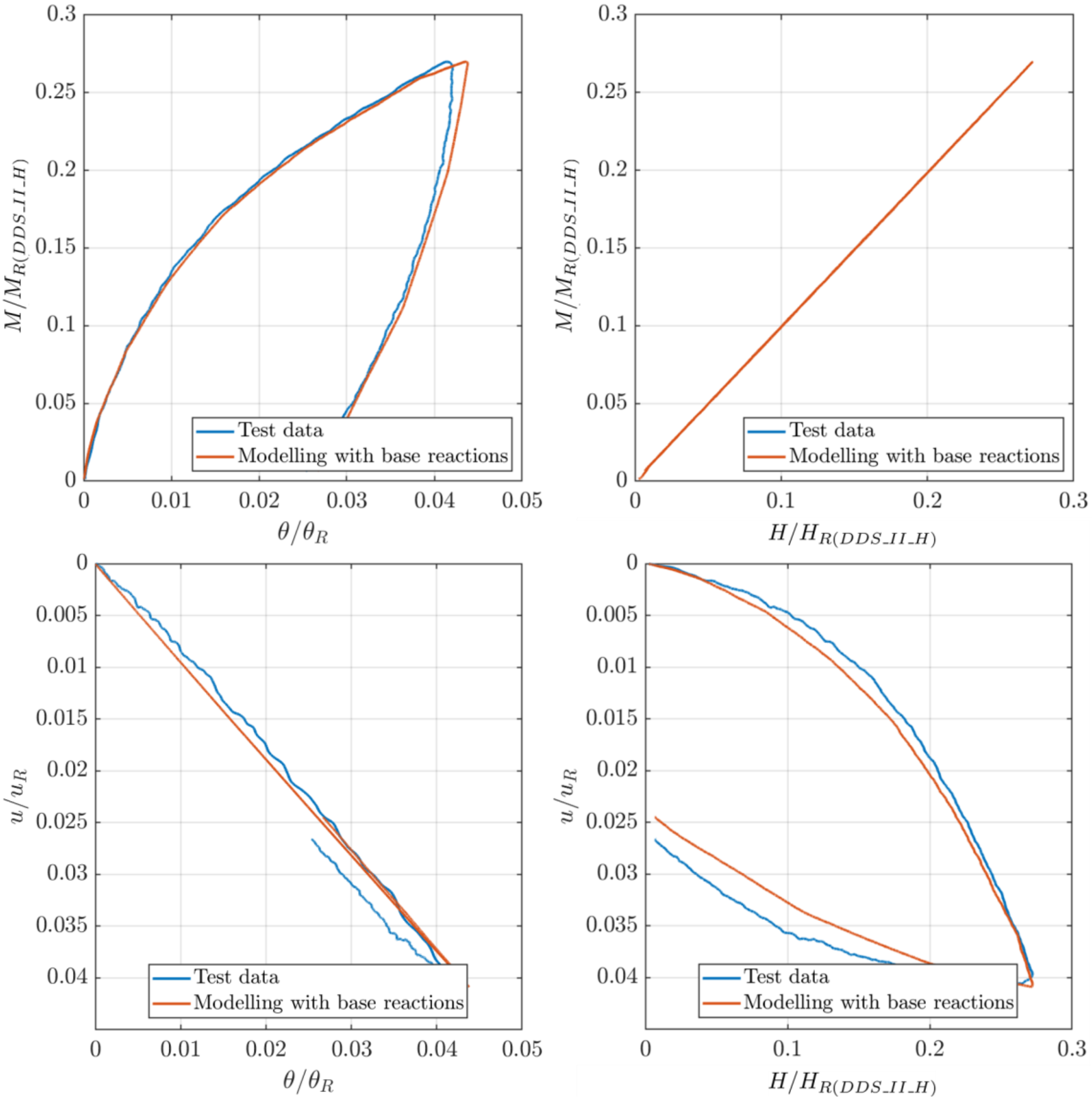

Figure 6-15 Initial loading-unloading response in *dry dense* sand without the HARM features.

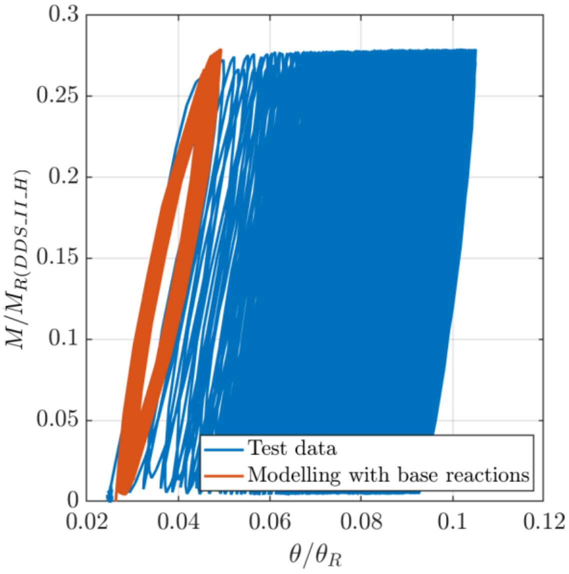

Figure 6-16 Cycling response in *dry dense* sand without the HARM features.

6.3.4.2 Modelling ratcheting with the HARM features

Tests DLS_C_II_0.5Hz_7D_H and DDS_C_II_0.5Hz_7D_H were simulated with the HARM features to capture ratcheting responses in dry *very loose* sand and *dense* sand, respectively (see Figure 6-17). In these cases, base resistance was considered (see the input parameters f_1, f_2, f_3 and f_4 in Table 6-2). The fitting parameters for the R_e function are given Table 6-5. The R_{e0}, m_r and R_e^* values were suggested by Richards (2019) based on experimental data. R_{e0} and m_r were fixed and assumed not to change with the soil density and the cyclic load magnitude. R_e^* and β^* are coupled, and therefore, $R_e^* = 0.08$ was assumed in this case, following Richards (2019), and only changed β^*. Overall, the modelling results are similar to the test data, and the HARM features can be included in the model.

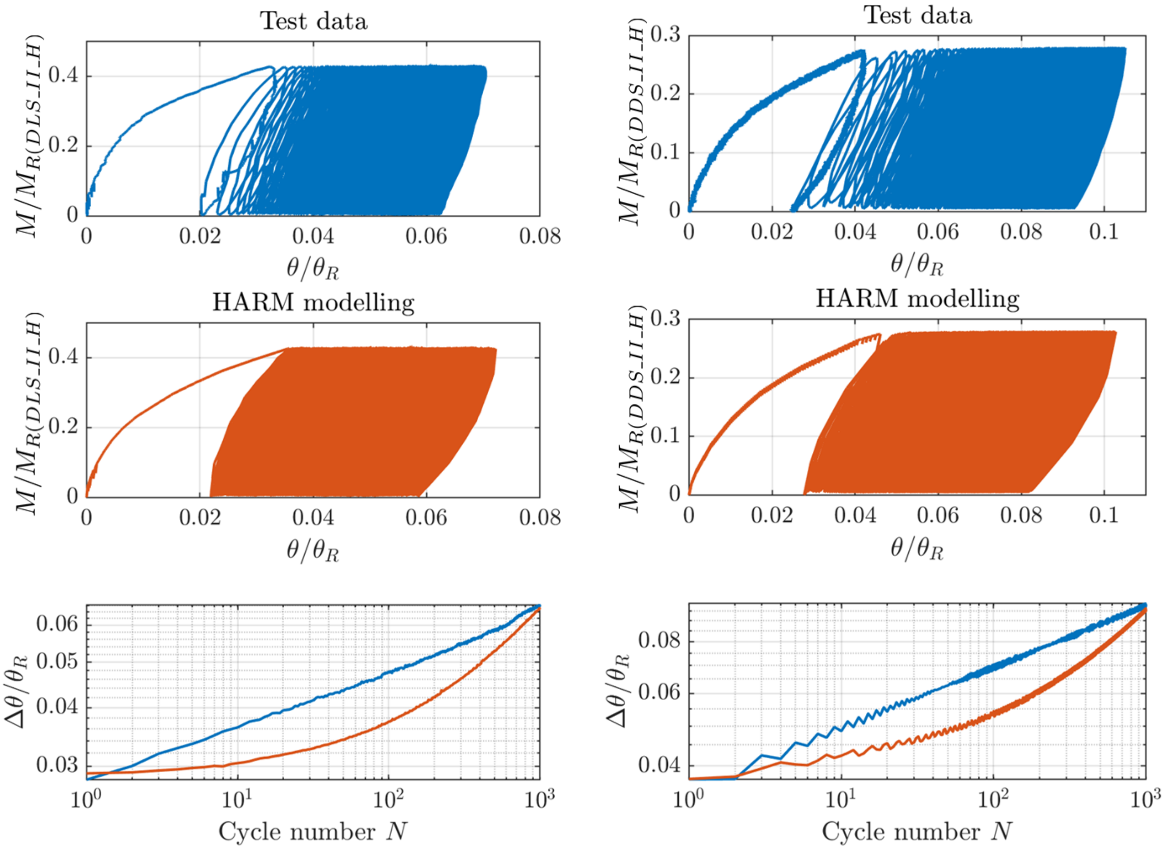

(a) (b)

Figure 6-17 Cycling pile response with the HARM features:

(a) *Very loose* sand; (b) *Dense* sand.

Table 6-5 Parameters of the R_e function in dry sand.

	R_{e0}	m_r	β^*	R_e^*
Very loose sand	1.0	0.65	5×10^{-6}	0.08
Dense sand			2×10^{-6}	

6.3.5 Summary of modelling in dry sand

The model is based on the analytical equations derived in Section 5.2, which were validated and proven by comparing modelling and test results. As rate effects are not seen in dry sand, rate-dependent functions w, $dw/d\chi$ were not implemented in the above cases. The coupled moment-horizontal load response of the model pile under monotonic loading is modelled quite well. Pile responses at different e were also simulated with satisfaction. The impact of vertical loading is evident in the dry *very loose* sand tests, but it does not appear to change the pile response in the model considerably. The HARM features were successfully added to the model. With the HARM implementation, ratcheting under cyclic lateral loading can be well-captured.

6.4 Modelling pile responses in saturated stiff clay

6.4.1 Impact of base reactions

Data from test CT_C_0.35N/s_4D_2 were used to calibrate the model and to study the influence of base reactions on lateral pile response. In this case, it was assumed that undrained shear strength s_u is uniform and does not change with depth (*i.e.* $r = 0$). Without considering the response of base reactions, the input parameters f_1, f_2, f_3 and f_4 are found in Table 6-1. By adding base reactions, f_1 and f_3 become 0.675 and 0.63, respectively (see Table 6-2). Rate dependent functions w, $\partial w/\partial\chi_{un}$ and $\partial w/\partial\chi_{\vartheta n}$ were not implemented in this analysis.

The modelling results and the test data are illustrated in Figure 6-18. For both moment-rotation and horizontal load-displacement responses, modelling with base reactions gets close to the actual pile behaviour, which agrees with the PISA method (see Section 1.1.5.2). In addition, moment capacity is found to be increased by 1% if base resistance is included in the model.

The rotation-horizontal displacement response and the pile pivot point slightly change if base resistance is added to the analysis.

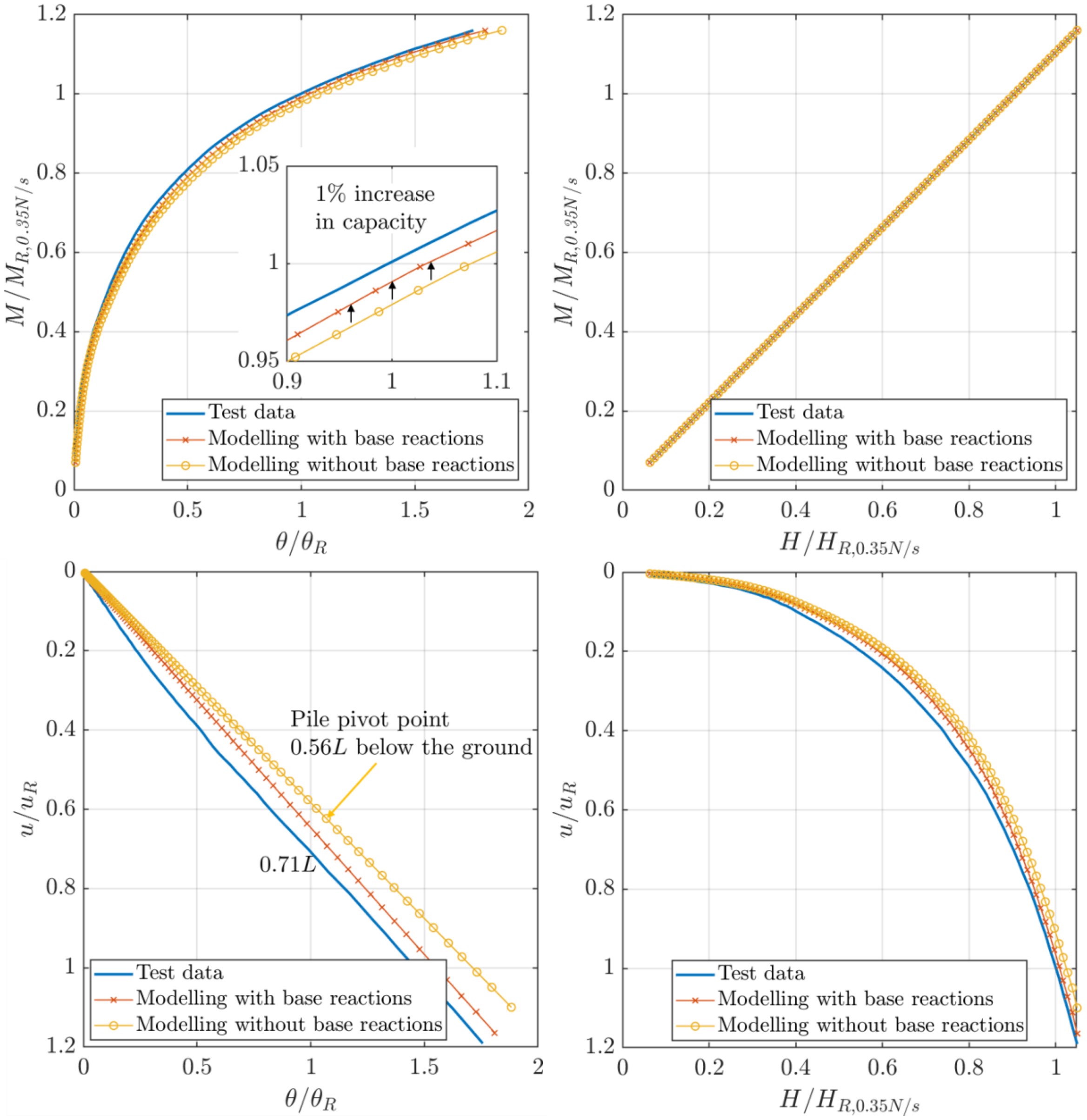

Figure 6-18 Demonstration of the impact of base reactions on piles in saturated stiff clay.

6.4.2 Modelling rate effects under monotonic loading

This section discusses modelling rate effects using linear viscosity and RPT. In terms of time on computation, the linear viscosity model needs less effort to carry out a simulation, while the RPT model runs longer due to the complex hyperbolic w, $\partial w/\partial \chi_{un}$ and $\partial w/\partial \chi_{\vartheta n}$ functions. Illustrative examples are given below.

Data from test CT_L_var_4D_6 were used to determine μ considering linear viscosity, as illustrated in Figure 6-19. A constant rate monotonic curve was obtained from the fitted data at the actuation rate $v = 0.05$ mm/s (see Section 4.3.3.2 for details). The input parameters f_1, f_2, f_3 and f_4 are given in Table 6-2, considering the influence of base shear. In this case, μ was found to be 0.0002 (N·hr/mm). In the $M - \theta$ domain, it can be seen that the modelling result and test data match well. However, the horizontal load-displacement response is a little over-estimated. This deviation is expected given that soil strength properties can be non-uniform in the field.

In the analysis of RPT, the μ value from the previous analysis was adopted, and $\dot{\alpha}_{ref}$ was observed from test data. μ was set to 0.0002 (N·hr/mm) based on the monotonic response at $v = v_o = 0.05$ mm/s, while $\dot{\alpha}_{ref}$ was found to be 0.05/μ (mm/hr) at the loading point when $e = 4D$. The $\mu\dot{\alpha}_{ref}$ value is close to $\eta_{10_{\dot{\theta}}}$ (= 0.1) divided by $\ln 10$, which is similar to the experimental observations in Section 4.3.3.2.

The linear viscosity and RPT models demonstrate a similar response at a slow rate. However, at a faster rate, the reaction curve from the RPT model fits the test data better than the linear viscosity model (see Figure 6-19). Linear viscosity is suitable for slow rates (*i.e.* near the upper yield) before transforming into the semi-logarithmic relationship between the rate and strength. With the rate increase, the RPT model matches the semi-logarithmic relationship better.

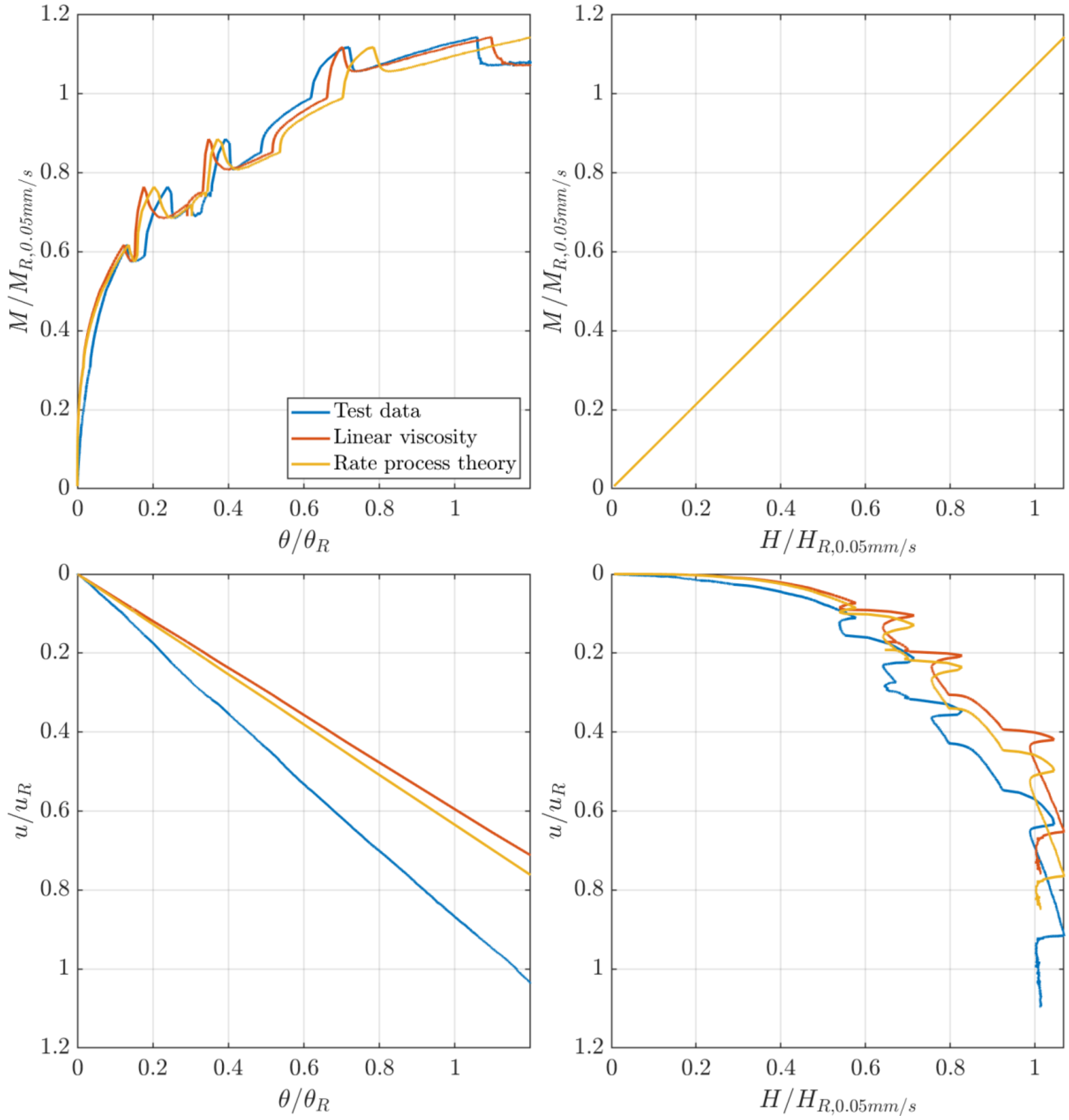

Figure 6-19 Modelling the variable rate response from test CT_L_var_4D_6 using linear viscosity and RPT.

The above μ, $\dot{\alpha}_{ref}$ values were adopted to model test CT_L_var_4D_5 using RPT to examine consistency, as shown in Figure 6-20. In this case, again, the monotonic response curve at $v = v_o$ was obtained for calibration. The modelling result matches the test data quite well, and the μ, $\dot{\alpha}_{ref}$ values are found to be representative.

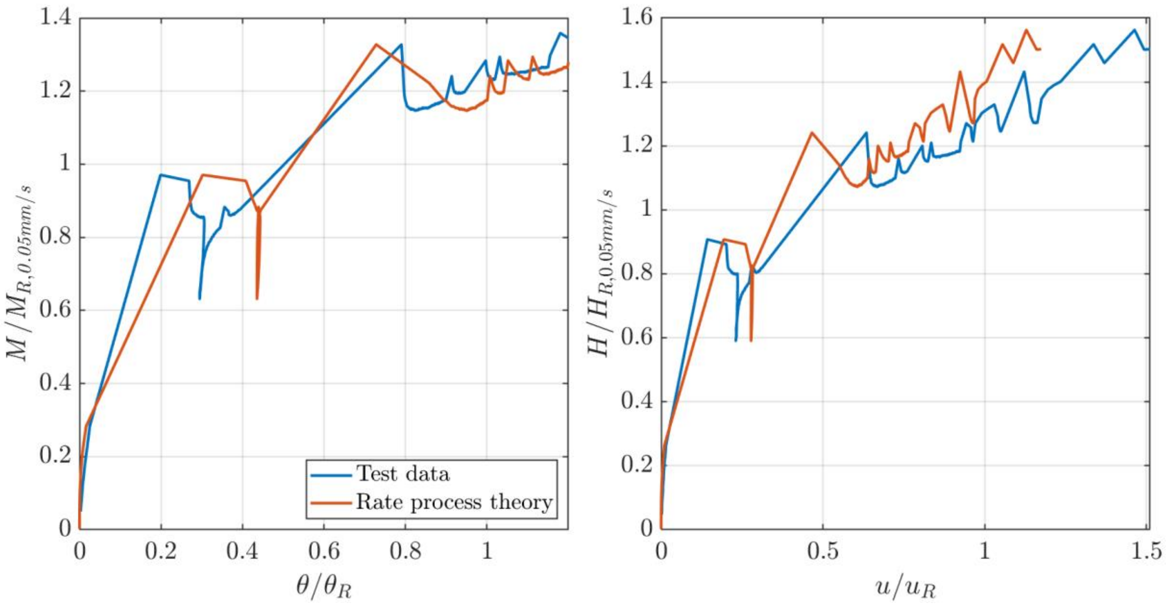

Figure 6-20 Modelling the response from test CT_L_var_4D_5 using RPT.

6.4.3 Load eccentricity effects

6.4.3.1 Fixed load eccentricity

Constant loading rate responses with $e = 4D$, $6D$ and $10D$ were simulated, as illustrated in Figure 6-21. The calibration curve at $e = 4D$ was used. The input parameters f_1, f_2, f_3 and f_4 are given in Table 6-2 (with base resistance). These tests were conducted at the same loading rate $\dot{F} = 0.35$ N/s, so the rate-independent model was implemented in this case study.

In general, the model can capture pile responses at different e, but a slight difference between modelling and test data at $e = 6D$ is observed. The yield surfaces with base resistance are shown in blue dashed in Figure 6-21 to identify the yield behaviour of the pile. Similar to the modelling in dry sand, with increasing e, moment capacity becomes larger with less θ, while the horizontal load-displacement response indicates an inverse trend.

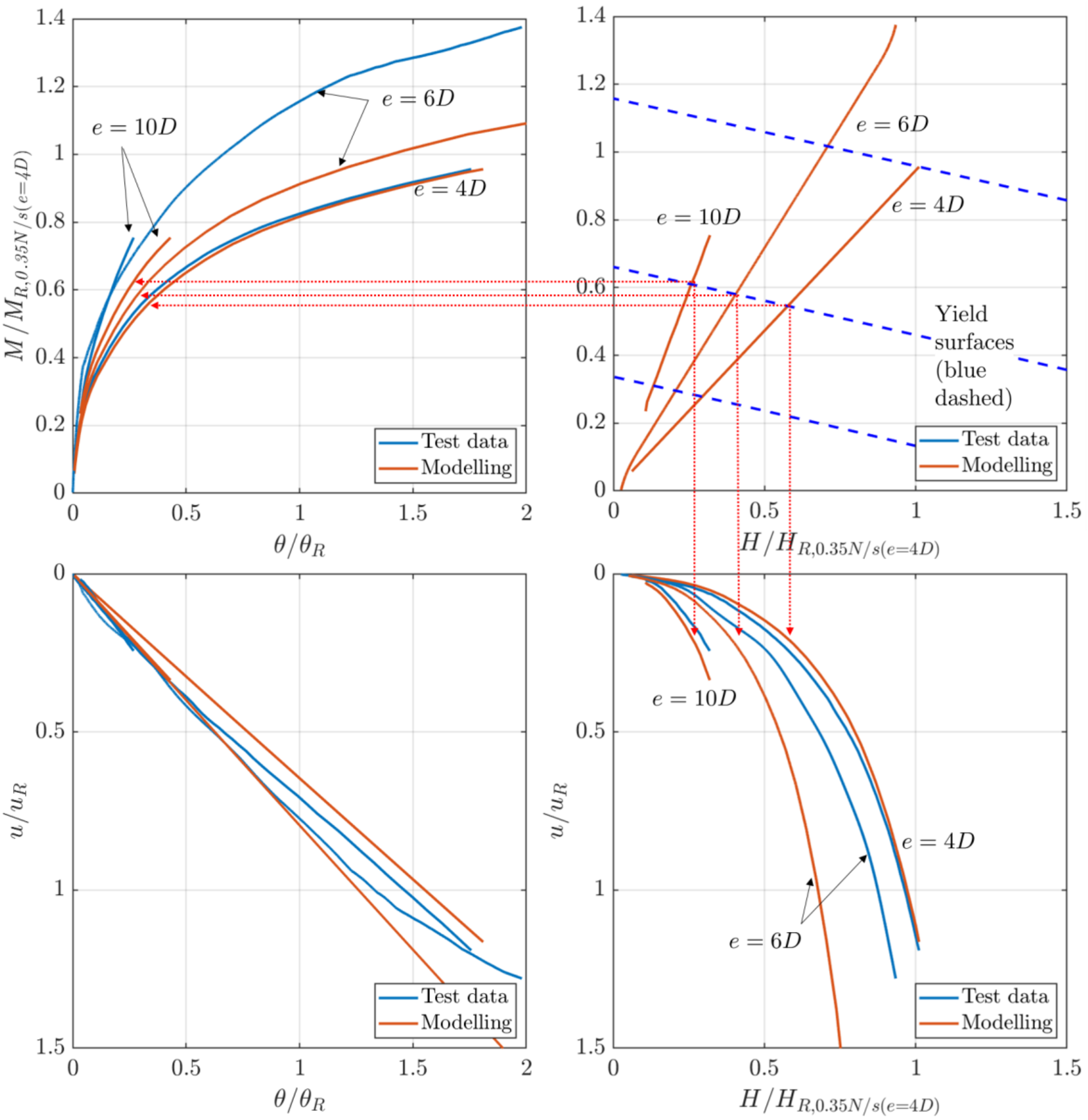

Figure 6-21 Modelling constant loading rate responses with $e = 4D$, $6D$ and $10D$.

6.4.3.2 Time-varying load eccentricity

An example of time-varying e (test CT_L_0.35N/s_vare_1) is illustrated in Figure 6-22. The load input data can be found in Figure 4-48. During the test, e was varying between $4D$ and $10D$. $\dot{F} = 0.35$ N/s when e was maintained constant. Similarly, data from the monotonic response at $e = 4D$ and $\dot{F} = 0.35$ N/s was used to calibrate a reaction curve to determine the stiffness, and the input parameters are the same as previously used in Figure 6-21. The result shows that the pile response can be characterised using the yield surface (see dashed in

Figure 6-22). If the combined $H - M$ loading moves inward from the yield surface, the response is elastic.

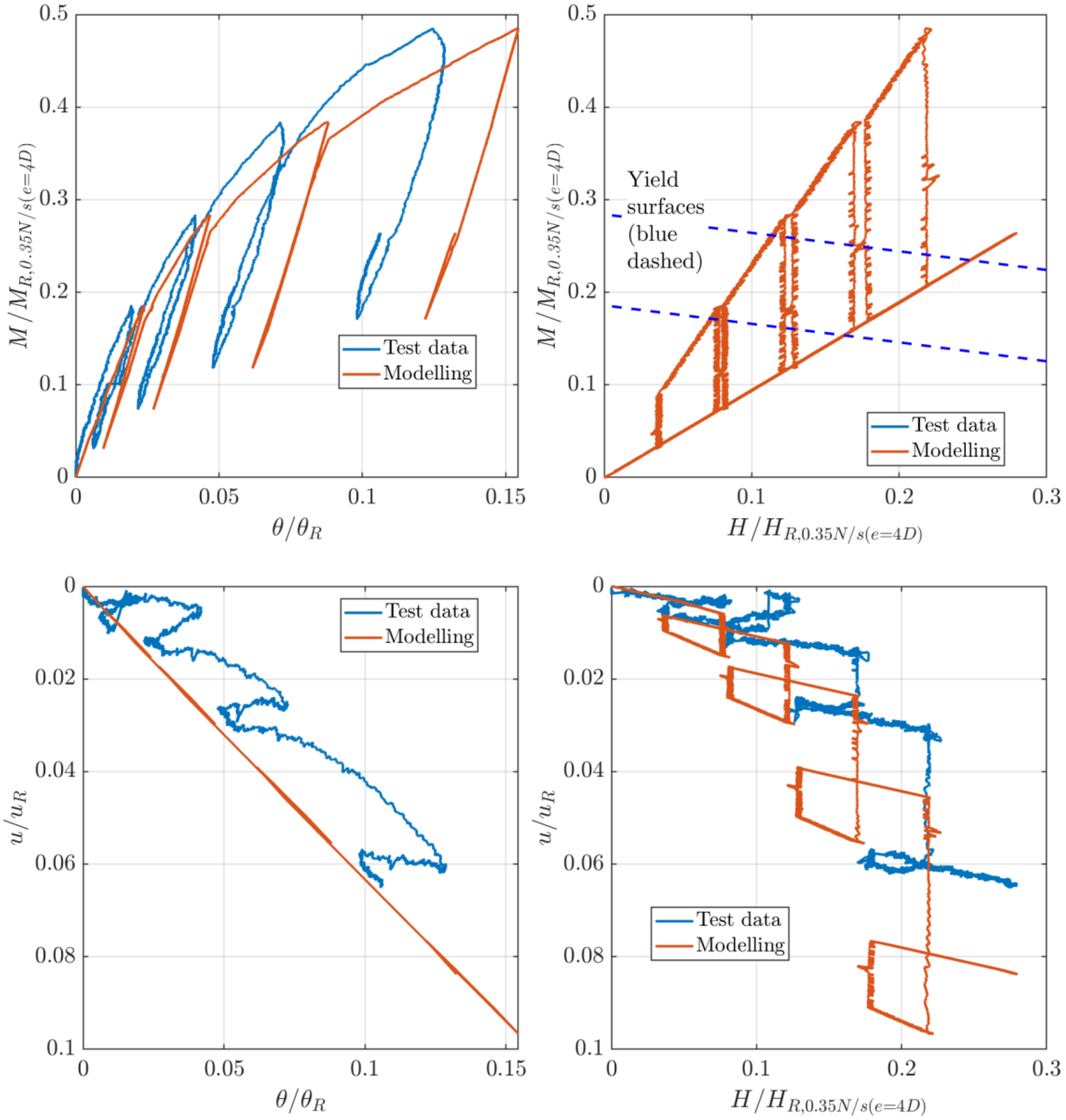

Figure 6-22 Modelling pile response under time-varying e.

6.4.4 Cyclic loading responses at different frequencies

6.4.4.1 Without the HARM implementation

Modelling cyclic loading responses with the rate-dependent characteristics by implementing w, $\partial w/\partial \chi_{un}$ and $\partial w/\partial \chi_{\vartheta n}$ functions can lead to slight permanent pile deformation. Examples of modelling the large magnitude ($\zeta_b = 0.45$) cyclic loading responses at different frequencies f are illustrated in Figure 6-23. In these cyclic loading tests, f_1, f_2, f_3 and f_4 are given in Table

6-2, and μ and $\dot{\alpha}_{ref}$ obtained from the variable tests in Section 6.4.2 were adopted. For each test, a calibration curve obtained from the initial response was used to avoid the influence of soil variations.

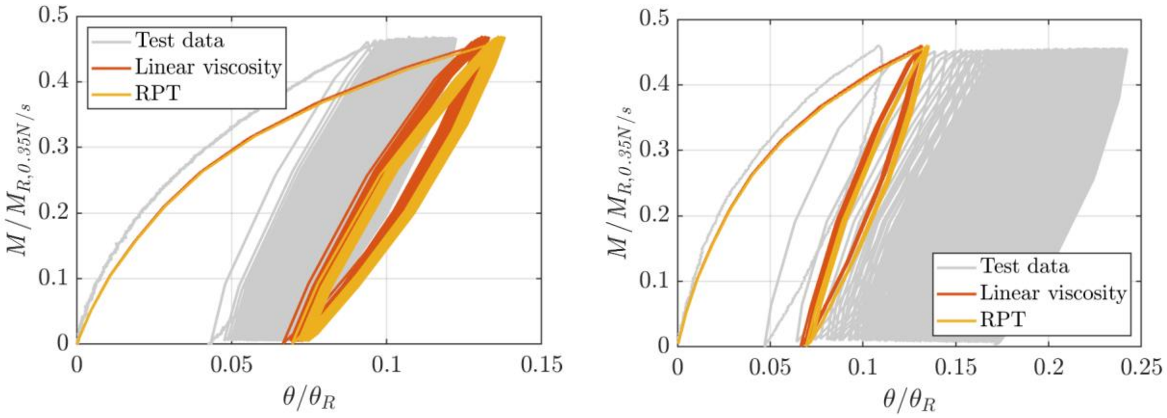

(a) 0.5 Hz (b) 0.1 Hz

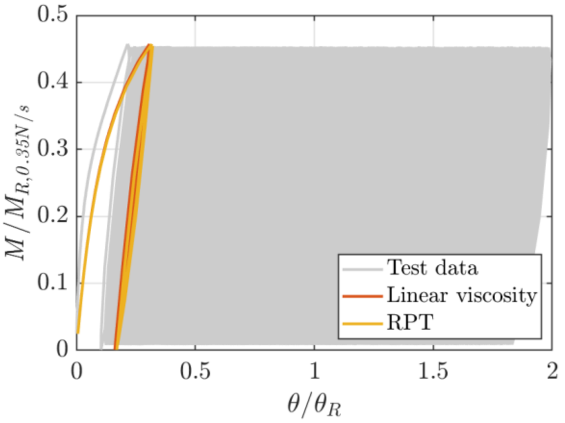

(c) 0.01 Hz

Figure 6-23 Modelling cyclic loading under different f ($\zeta_b = 0.45$) without the HARM application.

From the results, the difference between the linear viscosity and RPT is slight because $\dot{\theta}$ (or $\dot{u}$) is small under cyclic lateral loading. Similar to the dry sand modelling in Figure 6-15, the initial loading-unloading loop can be obtained without the HARM implementation. However, ratcheting during cyclic loading cannot be perfectly simulated, so again the HARM features are required to be added in the analysis of cyclic loading.

6.4.4.2 With the HARM features

The constant magnitude cyclic loading tests with $\zeta_b = 0.45$ and 0.225 under different f (see Section 4.4.2) were modelled with the HARM implementation and rate effects, as illustrated in Figure 6-24 and Figure 6-25. The input parameters for the R_{en} function are given in Table 6-6. Similar to the dry sand testing, for simplicity, the parameters R_{e0}, m_r and R_e^* were fixed for all cases. f_1, f_2, f_3 and f_4 are found in Table 6-2, μ and $\dot{\alpha}_{ref}$ from the variable tests in Section 6.4.2 were used.

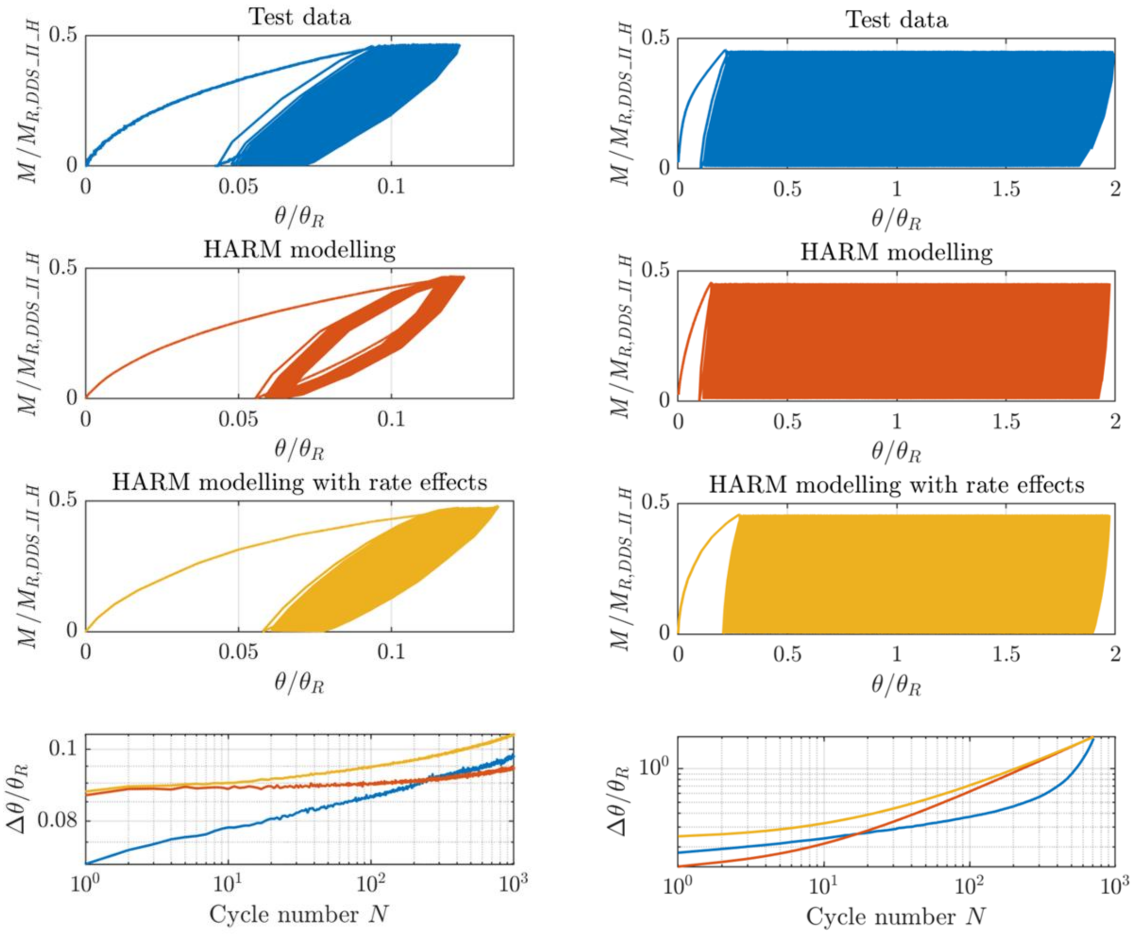

(a) (b)

Figure 6-24 Modelling cyclic loading under different f with the HARM features ($\zeta_b = 0.45$): (a) $f = 0.5$ Hz; (b) $f = 0.01$ Hz.

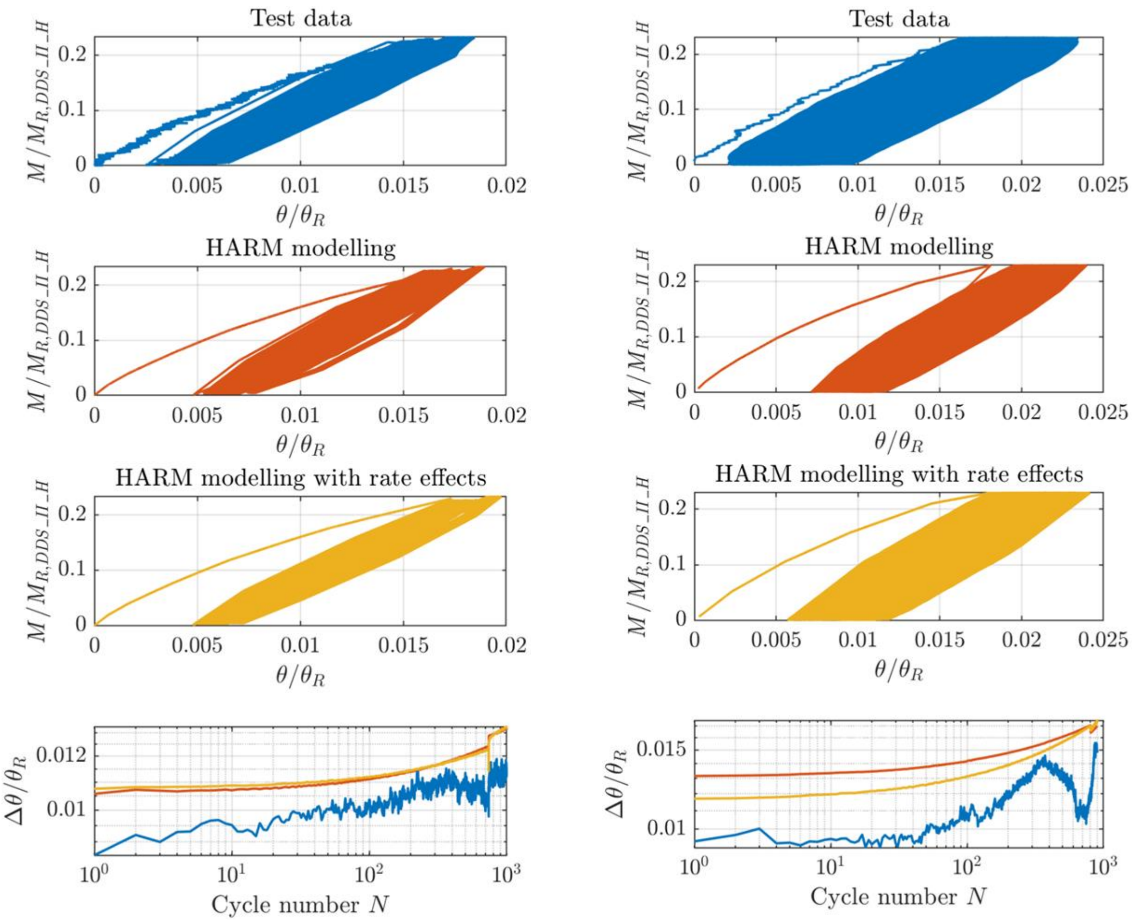

(a) (b)

Figure 6-25 Modelling cyclic loading under different f

with the HARM features ($\zeta_b = 0.225$): (a) $f = 0.5$ Hz; (b) $f = 0.01$ Hz.

Table 6-6 Parameters of the R_e function in saturated stiff clay.

ζ_b	f (Hz)	R_{e0}	m_r	β^* (without rate effects)	β^* (including rate effects)	R_e^*
0.45	0.5	1.0	0.65	1×10^{-7}	9×10^{-7}	0.08
	0.01			4×10^{-1}	2.3×10^{-1}	
0.225	0.5			1×10^{-7}	5×10^{-8}	
	0.01			5×10^{-6}	5×10^{-6}	

In general, with the increase in f, β^* becomes smaller. When $\zeta_b = 0.45$, modelling with rate effects can provide a better result. When $\zeta_b = 0.225$, the difference between modelling with and without rate effects is small and may be negligible.

6.4.5 Modelling pseudo-random cyclic loading

The illustrative example (test CT_C_ran_4D_1) in Section 4.4.5 was studied. In this case, the calibration curve used in Section 6.4.1 was implemented with the consideration of base resistance (see the input parameters in Table 6-2). The R_{e0}, m_r and R_e^* parameters for the R_e function were the same as the other tests (see Table 6-6). β^* was 0.0015 and 0.002 for without and with rate effects. In the analysis of rate effects, similarly, f_1, f_2, f_3 and f_4 are listed in Table 6-2 and the μ and $\dot{\alpha}_{ref}$ values in Section 6.4.2 were used. In general, the modelling results and the test data match closely. Without adding the functions of rate effects, the overall pile response can be approximately captured using the HARM (see Figure 6-26). The pile response can be more accurately simulated if rate dependency is included in the analysis.

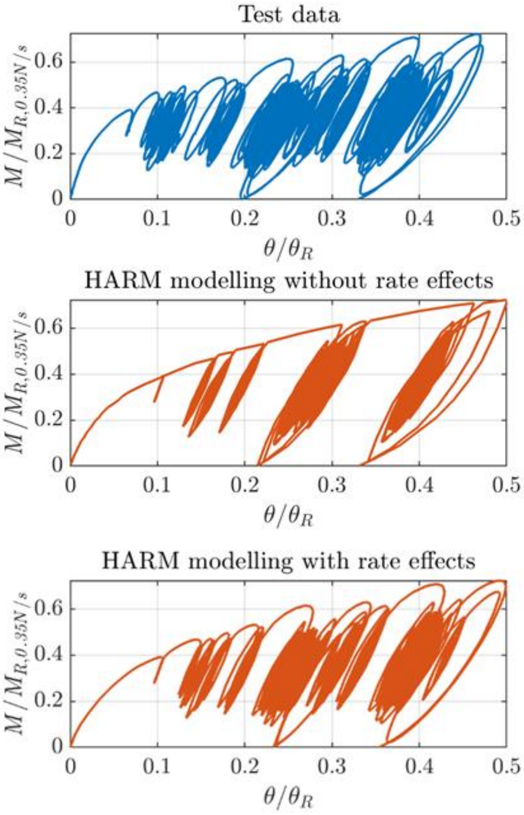

Figure 6-26 Modelling the pile response to pseudo-random cyclic loading.

6.4.6 Summary of modelling in saturated stiff clay

From the above analyses of pile responses in saturated stiff clay to various loading conditions, it was found that modelling with the implementation of base resistance gives a better fit with experimental data. Load eccentricity effects can be simulated, although the influence of soil variations needs to be considered. In addition, the model can capture rate effects using linear viscosity or RPT, and ratcheting under cyclic lateral loading can be modelled by incorporating the HARM features in the analysis. The modelling results show good confidence in comparison with the test data.

6.5 Concluding remarks

The new design model under the hyperplasticity framework was developed for general lateral pile response. The performance of the model is summarised below:

(1) The coupled moment-horizontal load response of a pile is captured, and the pile pivot position is found using the model.

(2) Base reactions (*e.g.* base shear and moment) can be added to the model. Modelling with base reaction components shows a better fit for saturated stiff clay.

(3) Load eccentricity effects were modelled with good confidence. By identifying the yield surface, pile response under time-varying e can be well-estimated.

(4) The model captures rate dependency by implementing linear viscosity and RPT. By comparing modelling results and test data, $\eta_{10_{\dot{\theta}}} = 0.1$ is evident for the Cowden till.

(5) The model can include the HARM features to capture ratcheting response under cyclic lateral loading. For cyclic loading in clay, modelling with rate effects gives a more accurate result.

Overall, the performance of the model is satisfactory, and further examinations using other data sources and different pile test scales are recommended. With the increase in pile size, soil characteristics may significantly vary with depth, and other considerations may be required for the input parameters of the model.

7 Conclusions

7.1 Introduction

Through laboratory-floor model testing, this thesis investigated rate effects for monopile foundations in dry sand and saturated stiff clay under monotonic and cyclic lateral loading. Additionally, combined load effects were explored. Together with the experimental work, a new practical pile design model was developed in hyperplasticity to capture pile response to general lateral loading. Detailed conclusions are given in each chapter, and this chapter summarises the key contributions of this thesis, discusses implications for monopile design and addresses future work.

7.2 Key contributions

1. Development of the loading rig

This thesis proposed a new loading rig design for model monopile testing, as described in Chapter 2. The rig allows rapid loading, multi-amplitude cyclic loading and tests with time-varying load eccentricity to be performed. In addition, the rig adopts the FPGA technology so that the control and data logging system can operate under a fast loop rate to calculate pile pose and achieve precise control in real time.

The rig was fully commissioned and used to perform more than a hundred model tests in this research project. It is also used for ongoing research exploring pile response in saturated sand at Oxford University (Keane, 2022).

2. Identification of inertial effects in dry sand

For piles in dry clean sand, rate effects are negligible. A sudden increase or decrease in lateral loading is observed with increasing or decreasing the pile loading rate. Previous element research suggests that such behaviour may be acceleration-sensitive (Tatsuoka *et al.*, 2008).

However, by examining the testing device, this phenomenon was found to be due to inertial effects induced by the actuator instead of soil skeleton behaviour, as reported in Section 3.5.4.

3. Using naturally formed clay for laboratory-scale model testing

The completion of the testing at Cowden shows an alternative to laboratory-prepared samples for performing laboratory-scale testing in clay. The stiff clay at Cowden broadly represents the ground conditions of multiple North Sea wind farms. In contrast to conventional sample preparation methods in the laboratory, using clay in the field can save a significant amount of time and effort, and a large number of tests can be conducted. In addition, high-strength clay is achievable if a suitable site is chosen. At the Cowden site, the undrained shear strength s_u was found to be 80 kPa ~ 95 kPa (see Section 4.2.2). Along with the element test data in this research, a field investigation and a series of laboratory tests were conducted for the PICASO project to inform detailed soil characterisation.

4. Identification of rate effects in saturated stiff clay

Rate effects in clay were observed under both monotonic and cyclic lateral loading. Under monotonic loading, pile capacity increases by approximately 10% with a tenfold increase in the pile actuation or rotation rate, and isotach type viscous behaviour is observed, as discussed in Section 4.3.

In Section 4.4, pile secant stiffness is shown to increase with cyclic load frequency under cyclic lateral loading, while the rate of the accumulated pile deformation (*i.e.* ratcheting) shows an inverse trend. Softening may become evident with excessive permanent pile deformation if the frequency is slow under the large cyclic load magnitude (*e.g.* test CT_C_45%_0.01Hz_4D_1). Conversely, if the frequency is higher than 0.1 Hz, potentially due to rate effects, pile secant stiffness may not decrease with cyclic loading, and softening may not occur.

5. Exploring combined load effects on lateral response

Load eccentricity effects are demonstrated in terms of the coupled moment-horizontal load response and the failure surface. Experimental evidence is reported in Sections 3.8 and 4.5, and theoretical modelling is discussed in Sections 6.3.2 and 6.4.3. If the coupled loading path moves outward from the failure surface, plastic deformation occurs. By contrast, if the path is inward from the failure surface, the response becomes more elastic.

The impact of vertical loading on the lateral response of a pile was found to be significant in dry *very loose* sand (see Section 3.7.2), as increasing vertical loading may enhance base resistance against lateral loading. However, it is noted that scaling vertical loading from the field to the laboratory may not be possible due to the test setup. At full scale, the influence of vertical loading may be minor and needs to be assessed further.

6. Other experimental observations

The pile pivot position, pile uplift and gapping are reported in this thesis to inform detailed numerical modelling and future experimental design. The vertical, horizontal and rotational pile displacements were measured during each test to capture the planar pile movement. For the testing in dry sand, in some cases (see Section 3.9), pile uplift was evident but did not appear to influence the overall pile response. For the testing in saturated stiff clay, pile gapping was observed on the active side of the pile, as discussed in Section 4.6. The depth of pile gapping was found to be close to the pile pivot position (approximately $0.8L$ below the ground level).

7. Theoretical development to inform monopile design

A new hyperplasticity-based model for general lateral loading of monopiles was developed in this thesis, based on the notes by Houlsby (2022a) (see Section 6.2.3). Following the PISA design method, base resistance can be included in the model. The elastic stiffness includes additional shear and moment components at the pile base, considering a rigid circular plate subject to general lateral loading. The failure surface enlarges if base resistance is considered. Besides, rate dependency using a linear viscous dashpot (Appendix A.3) or RPT (Appendix A.4) can be added to the model. With further development, other features, such as ratcheting under cyclic loading, can be simply incorporated into the model (see, *e.g.* the HARM application in Section 6.2.4.4).

The above features were validated against test data in this thesis. Overall, the performance of the model is satisfactory, providing an efficient way to simulate monopile response to general lateral loading. For example, in practice, if the soil conditions across an offshore wind farm are uniform or can be idealised, this model may be implemented to examine quickly all OWT locations, and various combined load scenarios can be validated.

7.3 Implications for monopile design

1. Post-cyclic monotonic response

In current design practice (see discussions in Section 1.1.5.3), pile capacity is reduced due to cyclic loading in sand and clay. However, from the uni-directional one-way cyclic tests in Sections 3.6 and 4.4, pile capacity does not decrease in most cases due to cyclic loading. Pile capacity can even increase in dry *very loose* sand because cyclic loading may densify the surrounding soil around the pile (see Section 3.6.3).

2. Assessment of load eccentricity effects

If the history of load eccentricity is assessed, it is possible to simulate the pile response more accurately. For example, during OWT operation, various lateral loads are applied at different heights (*e.g.* wind and waves). Also, the time-varying load eccentricity tests (see Sections 3.8.2 and 4.5.3) show that pile response may become more elastic or plastic according to the load history.

The theoretical model developed in Chapter 6 can be used to assess the history of the coupled loading and its influence on the pile response. The analyses of the time-varying load eccentricity tests are found in Sections 6.3.2.2 and 6.4.3.2.

3. Assessment of the response to multi-amplitude cyclic lateral loading

The illustrative examples of multi-amplitude (pseudo-random) cyclic lateral loading are given in Section 4.4.5. The load input data can be categorised as small, medium and large magnitude loads. The experimental results show that the large magnitude loads significantly influence the pile response. In contrast, the small and medium magnitude loads do not cause additional pile deformation after the large magnitude loads. Similarly, Liu *et al.* (2022a, 2022b) examined different load packages in terms of the cyclic load magnitude, to evaluate load history effects through direct simple shear testing and numerical modelling in sand. Their results indicate that the average stress controls ratcheting, and the ordering of loading packages has a minor influence on the pile response. Therefore, large magnitude loads may be more critical to determine the pile response to multi-amplitude cyclic loading, and the influence of small magnitude loads may be minimal.

7.4 Future work

1. Exploring pile response in coarse-grained soils with fines

This thesis explored the pile behaviour in clean sand; thus, the influence of fines content was found to be negligible. However, silty sand and sandy silt are commonly found in offshore wind farm sites in the Asian Pacific region, and the influence of fines content needs careful consideration (Yang *et al.*, 2022). Also, in the PISA pile testing at Dunkirk, northern France, it was found that fines content may cause cementation, leading to rate-sensitive pile response (see Zdravkovic *et al.*, 2020a; McAdam *et al.*, 2020). As a result, further research could be done to investigate pile response in coarse-grained soils with fines.

2. Investigating scaling effects in clay

The testing in saturated clay was performed on the model piles with an aspect ratio L/D of 3 and load eccentricity ratio e/D of 4, in line with the PICASO test piles (Byrne *et al.*, 2020a). The two test programmes shared the same area, and a field investigation and laboratory soil element tests were carried out for soil characterisation. Work is underway to interpret data from the PICASO pile tests, and the results will be reported in due course as part of the DPhil project at Oxford University by Martin (2023). Together with the PICASO test results, further work on scaling effects will be done to examine the normalisation procedure for clay using the dimensionless terms in Table 5-2.

3. Investigating pore pressure response in clay

The cyclic loading tests in clay (see Section 4.4) show that permanent pile deformation under cyclic lateral loading increases with the decrease in the cyclic load frequency. In addition to soil rate effects, this phenomenon may also be related to other time-dependent phenomena (*e.g.* pore pressure dissipation). However, as pore pressure measurements were unavailable in these tests, it is challenging to differentiate rate effects and time-dependent pore pressure response. This complex phenomenon could be investigated further through advanced element testing at different rates or large-scale testing with real-time pore pressure measurements.

4. Examination of the theoretical model using data from other sources

Although the theoretical model works well at the laboratory scale, it has not been validated against large-scale pile test data. In addition, soil conditions may become more complex with the increase in scale, and other considerations, such as the impact of shaft friction on lateral pile capacity, may need to be considered. Therefore, it would be useful to examine the performance of the theoretical model using data from other sources with different pile geometries and sizes, soil conditions and load eccentricities.

7.5 Overview

Rate effects are not often considered in monopile design, and design guidelines do not include soil rate dependency. However, increasing soil loading rate may enhance soil resistance, leading to a stiffer response and a higher pile capacity. If these beneficial phenomena are considered, design may be optimised, and savings could be made. This thesis forms part of a series of research activities on optimising monopile design for the next generation OWTs at Oxford University, following previous work to provide a broader range of experimental observations. This research project has provided new insights into rate-dependent pile responses to monotonic and cyclic lateral loading, as well as combined load effects through physical modelling on the laboratory floor. Besides, bringing the laboratory to the field at Cowden was a great success, providing an alternative way to achieve high-strength clay for physical modelling. The new pile design model in hyperplasticity was developed to capture the coupled moment-horizontal load response of a pile. The influence of base resistance, rate effects and ratcheting under cyclic lateral loading can be simulated by incorporating additional parameters.

References

Abadie, C.N. 2015. Cyclic lateral loading of monopile foundations in cohesionless soils. DPhil Thesis. University of Oxford.

Abadie, C.N., Houlsby, G.T., and Byrne, B.W. 2019. A method for calibration of the Hyperplastic Accelerated Ratcheting Model (HARM). Computers and Geotechnics, 112: 370–385. doi:10.1016/j.compgeo.2019.04.017.

Abdellaziz, M., Karray, M., Betegard, J., Locat, P., Ledoux, C., Mompin, R., and Chekired, M. 2022. Strain rate effect on static and dynamic behaviors of eastern Canada fine-grained soils. Canadian Geotechnical Journal, 59(7): 1083–1095. doi:10.1139/cgj-2021-0140.

Andersen, K.H. 2015. Cyclic soil parameters for offshore foundation design. In Frontiers in Offshore Geotechnics III : Proceedings of the 3rd International Symposium on Frontiers in Offshore Geotechnics (ISFOG 2015). Oslo, Norway. pp. 5–82.

API. 2007. API recommended practice 2A-WSD (RP 2A-WSD) planning, designing, and constructing fixed offshore platforms—working stress design.

Arshad, M., and O’Kelly, B.C. 2017. Model studies on monopile behavior under long-term repeated lateral loading. International Journal of Geomechanics, ASCE, 17(1): 04016040. doi:10.1061/(ASCE)GM.1943-5622.0000679.

Augustesen, A., Liingaard, M., and Lade, P. V. 2004. Evaluation of time-dependent behavior of soils. International Journal of Geomechanics, ASCE, 4(3): 137–156. doi:10.1061/(ASCE)1532-3641(2004)4:3(137).

Balaam, T.D. 2020. Development and calibration of cyclic loading models for monopile foundations in clay. DPhil Thesis. University of Oxford.

Beuckelaers, W.J.A.P. 2017. Numerical modelling of laterally loaded piles for offshore energy applications. DPhil Thesis. University of Oxford.

Bhattacharya, S. 2019. Design of foundations for offshore wind turbines. Wiley, Hoboken, NJ, USA.

Bhattacharya, S., Lombardi, D., and Muir Wood, D. 2011. Similitude relationships for physical modelling of monopile-supported offshore wind turbines. International Journal of Physical Modelling in Geotechnics, 11(2): 58–68. doi:10.1680/ijpmg.2011.11.2.58.

Bolton, M.D. 1986. The strength and dilatancy of sands. Géotechnique, 36(1): 65–78. doi:10.1680/geot.1986.36.1.65.

Bolton, M.D. 1987. Discussion: The strength and dilatancy of sands. Géotechnique, 37(2): 219–226. doi.org:10.1680/geot.1987.37.2.219.

Bolton, M.D., Gui, M.W., Garnier, J., Corte, J.F., Bagge, G., Laue, J., and Renzi, R. 1999. Centrifuge cone penetration tests in sand. Géotechnique, 49(4): 543–552. doi:10.1680/geot.1999.49.4.543.

Broms, B.B. 1964. Lateral resistance of piles in cohesionless soils. Journal of the Soil Mechanics and Foundations Division, ASCE, 90(3): 123–156. doi:10.1061/JSFEAQ.0000614.

Brown, M.J., and Hyde, A.F.L. 2008. Rate effects from pile shaft resistance measurements. Canadian Geotechnical Journal, 45(3): 425–431. doi:10.1139/T07-115.

Buckley, R.M., Byrne, B.W., Martin, S.C., Mcadam, R.A., Sheil, B.B., Aghakouchak, A., and Rene, L. 2020. Large diameter pile testing for offshore wind applications with a focus on cyclic lateral loading and rate effects. In 4th International Symposium on Frontiers in Offshore Geotechnics (ISFOG 2020). Austin, Texas.

Byrne, B., McAdam, R., Burd, H., Houlsby, G., Martin, C., Beuckelaers, W., Zdravkovic, L., Taborda, D., Potts, D., Jardine, R., Ushev, E., Liu, T., Abadias, D., Gavin, K., Igoe, D., Doherty, P., Gretlund, J.S., Andrade, M.P., Wood, A.M., Schroeder, F., Turner, S., and Plummer, M. 2017. PISA: New design methods for offshore wind turbine monopiles. In Offshore Site Investigation Geotechnics 8th International Conference Proceedings. Society of Underwater Technology, London, United Kingdom. pp. 142–161. doi:10.3723/OSIG17.142.

Byrne, B., McAdam, R., Burd, H., Houlsby, G., Martin, C., C, L., Taborda, D., Potts, D., Jardine, R., Sideri, M., Schroeder, F., Gavin, K., Doherty, P., Igoe, D., Wood, A., Kallehave, D., and Gretlund, J. 2015. New design methods for large diameter piles under lateral loading for offshore wind applications. In Frontiers in Offshore Geotechnics III : Proceedings of the 3rd International Symposium on Frontiers in Offshore Geotechnics (ISFOG 2015). Oslo, Norway. pp. 705–710.

Byrne, B.W. 2020. Editorial: geotechnical design for offshore wind turbine monopiles. Géotechnique, 70(11): 943–944. doi:10.1680/jgeot.2020.70.11.943.

Byrne, B.W., Aghakouchak, A., Buckley, R.M., Burd, H.J., Gengenbach, J., Houlsby, G.T., Mcadam, R.A., Martin, C.M., Schranz, F., Sheil, B.B., and Suryasentana, S. 2020a. PICASO: Cyclic lateral loading of offshore wind turbine monopiles. In 4th International Symposium on Frontiers in Offshore Geotechnics (ISFOG 2020). Austin, Texas.

Byrne, B.W., and Houlsby, G.T. 2006. Assessing novel foundation options for offshore wind turbines. In The World Maritime Technology Conference (WMTC 2006). London, United Kingdom.

Byrne, B.W., and Houlsby, G.T. 2015. Helical piles: an innovative foundation design option for offshore wind turbines. Philosophical Transactions of the Royal Society A: Mathematical, Physical and Engineering Sciences, 373(2035): 20140081. doi:10.1098/rsta.2014.0081.

Byrne, B.W., McAdam, R.A., Burd, H.J., Beuckelaers, W.J.A.P., Gavin, K.G., Houlsby, G.T., Igoe, D.J.P., Jardine, R.J., Martin, C.M., Muir Wood, A., Potts, D.M., Skov Gretlund, J., Taborda, D.M.G., and Zdravković, L. 2020b. Monotonic laterally loaded pile testing in a stiff glacial clay till at Cowden. Géotechnique, 70(11): 970–985. doi:10.1680/jgeot.18.PISA.003.

Carter, M., and Bently, S.P. 2016. Soil properties and their correlations, 2nd edition. Wiley, West Sussex, UK.

Chiou, J.-S., and Chien, H.-Y. 2021. Analytical interaction diagram for lateral responses of a rigid pile in homogeneous overconsolidated clay. Journal of Geotechnical and Geoenvironmental Engineering, ASCE, 147(9): 05021008. doi:10.1061/(ASCE)GT.1943-5606.0002602.

Cox, W.R., Reese, L.C., and Grubbs, B.R. 1974. Field testing of laterally loaded piles in sand. In Offshore Technology Conference. Houston, Texas. pp. 459–464. doi:10.4043/2079-MS.

Dadras-Ajirloo, D., Grimstad, G., and Amiri, S.A.G. 2022. On the isotache viscous modelling of clay behaviour using the hyperplasticity approach. Géotechnique,: 1–13. doi:10.1680/jgeot.21.00245.

DNV. 2014. DNV-OS-J10:1 Design of offshore wind turbine structures.

DNV GL. 2016a. DNVGL-ST-0126: Support structures for wind turbines.

DNV GL. 2016b. DNVGL-ST-0437: Loads and site conditions for wind turbines.

EEW. 2022. EEW website. Available from https://eew-group.com/about/news/detail/eew-spc-has-produced-the-worlds-heaviest-monopile/ [accessed 1 May 2022].

European Commission. 2022. Boosting offshore renewable energy for a climate neutral Europe. Available from https://ec.europa.eu/commission/presscorner/detail/en/IP_20_2096 [accessed 1 May 2022].

Fodil, A., Aloulou, W., and Hicher, P.Y. 1997. Viscoplastic behaviour of soft clay. Géotechnique, 47(3): 581–591. doi:10.1680/geot.1997.47.3.581.

Global Wind Energy Council. 2020. Global offshore wind report 2020.

Graham, J., Crooks, J.H.A., and Bell, A.L. 1983. Time effects on the stress-strain behaviour of natural soft clays. Géotechnique, 33(3): 327–340. doi:10.1680/geot.1983.33.3.327.

Great.gov.uk. 2022. Offshore wind. Available from https://www.great.gov.uk/international/content/investment/sectors/offshore-wind/#:~:text=The UK government has a,for growth of the sector. [accessed 11 April 2022].

Grimstad, G., Degago, S.A., Nordal, S., and Karstunen, M. 2010. Modeling creep and rate effects in structured anisotropic soft clays. Acta Geotechnica, 5(1): 69–81. doi:10.1007/s11440-010-0119-y.

Guevara, M., Doherty, J., Watson, P.G., and White, D.J. 2020. Key features impacting soil-conductor lateral behaviour as illustrated by centrifuge tests. In 4th International Symposium on Frontiers in Offshore Geotechnics (ISFOG 2020). Austin, Texas.

Houlsby, G.T. 2022a. Personal Communication.

Houlsby, G.T. 2022b. Hyperplasticity. Available from https://hyperplasticity.wordpress.com/ [accessed 11 August 2022].

Houlsby, G.T., Abadie, C.N., Beuckelaers, W.J.A.P., and Byrne, B.W. 2017. A model for nonlinear hysteretic and ratcheting behaviour. International Journal of Solids and Structures, 120: 67–80. doi:10.1016/j.ijsolstr.2017.04.031.

Houlsby, G.T., and Puzrin, A. 2006. Principles of hyperplasticity. Springer London, London. doi:10.1007/978-1-84628-240-9.

Jeanjean, P., Zakeri, A., Zhang, Y., and Andersen, K.H. 2022. The new ISO/API P-Y curves in clays and their reconciliation with the PISA framework. In Offshore Technology Conference. Houston, USA. doi:10.4043/31860-MS.

Jostad, H.P., Dahl, B.M., Page, A., Sivasithamparam, N., and Sturm, H. 2020. Evaluation of soil models for improved design of offshore wind turbine foundations in dense sand. Géotechnique, 70(8): 682–699. doi:10.1680/jgeot.19.TI.034.

Kallehave, D., Byrne, B.W., LeBlanc Thilsted, C., and Mikkelsen, K.K. 2015. Optimization of monopiles for offshore wind turbines. Philosophical Transactions of the Royal Society A: Mathematical, Physical and Engineering Sciences, 373(2035): 20140100. doi:10.1098/rsta.2014.0100.

Keane, R.A. 2022. Personal Communication.

Kelly, R.B., Houlsby, G.T., and Byrne, B.W. 2006. A comparison of field and laboratory tests of caisson foundations in sand and clay. Géotechnique, 56(9): 617–626. doi:10.1680/geot.2006.56.9.617.

Kim, D.-S. 1991. Deformational characteristics of soils at small to intermediate strains from cyclic tests. PhD Thesis, University of Texas at Austin.

Kiyota, T., and Tatsuoka, F. 2006. Viscous property of loose sand in triaxial compression, extension and cyclic loading. Soils and Foundations, 46(5): 665–684. doi:10.3208/sandf.46.665.

Klinkvort, R.T., and Hededal, O. 2013. Lateral response of monopile supporting an offshore wind turbine. Proceedings of the Institution of Civil Engineers - Geotechnical Engineering, 166(2): 147–158. doi:10.1680/geng.12.00033.

Klinkvort, R.T., and Hededal, O. 2014. Effect of load eccentricity and stress level on monopile support for offshore wind turbines. Canadian Geotechnical Journal, 51(9): 966–974. doi:10.1139/cgj-2013-0475.

Kulhawy, F.H., and Mayne, P.W. 1990. Manual on estimating soil properties for foundation design (No. EPRI-EL-6800).

Kutter, B.L., and Sathialingam, N. 1992. Elastic-viscoplastic modelling of the rate-dependent behaviour of clays. Géotechnique, 42(3): 427–441. doi:10.1680/geot.1992.42.3.427.

Lau, B.H. 2015. Cyclic behaviour of monopile foundations for offshore wind farms. PhD Thesis, University of Cambridge.

Le, T.M.H., Eiksund, G.R., Strøm, P.J., and Saue, M. 2014. Geological and geotechnical characterisation for offshore wind turbine foundations: A case study of the Sheringham Shoal wind farm. Engineering Geology, 177: 40–53. doi:10.1016/j.enggeo.2014.05.005.

LeBlanc, C., Houlsby, G.T., and Byrne, B.W. 2010. Response of stiff piles in sand to long-term cyclic lateral loading. Géotechnique, 60(2): 79–90. doi:10.1680/geot.7.00196.

Lee, J., Kyung, D., Hong, J., and Kim, D. 2011. Experimental investigation of laterally loaded piles in sand under multilayered conditions. Soils and Foundations, 51(5): 915–927. doi:10.3208/sandf.51.915.

Lefebvre, G., and LeBoeuf, D. 1987. Rate effects and cyclic loading of sensitive clays. Journal of Geotechnical Engineering, ASCE, 113(5): 476–489. doi:10.1061/(ASCE)0733-9410(1987)113:5(476).

Leroueil, S., Kabbaj, M., Tavenas, F., and Bouchard, R. 1985. Stress–strain–strain rate relation for the compressibility of sensitive natural clays. Géotechnique, 35(2): 159–180. doi:10.1680/geot.1985.35.2.159.

Li, Q., Gavin, K.G., Askarinejad, A., and Prendergast, L.J. 2022. Experimental and numerical investigation of the effect of vertical loading on the lateral behaviour of monopiles in sand. Canadian Geotechnical Journal, 59(5): 652–666. doi:10.1139/cgj-2020-0769.

Liu, H., Pisanò, F., Jostad, H.P., and Sivasithamparam, N. 2022a. Impact of cyclic strain accumulation on the tilting behaviour of monopiles in sand: An assessment of the Miner's rule based on SANISAND-MS 3D FE modelling. Ocean Engineering, 250: 110579. doi:10.1016/j.oceaneng.2022.110579.

Liu, H., Sivasithamparam, N., Suzuki, Y., and Jostad, H.P. 2022b. Load history idealisation effects for design of monopiles in clay. Géotechnique. Available Online. doi:10.1680/jgeot.22.00010.

Lu, W., Kaynia, A.M., and Zhang, G. 2021. Centrifuge study of p–y curves for vertical–horizontal static loading of piles in sand. International Journal of Physical Modelling in Geotechnics, 21(6): 275–294. doi:10.1680/jphmg.19.00030.

Lu, W., and Zhang, G. 2018. Influence mechanism of vertical-horizontal combined loads on the response of a single pile in sand. Soils and Foundations, 58(5): 1228–1239. doi:10.1016/j.sandf.2018.07.002.

Martin, S.C. 2023 (expected). Medium scale field testing of monopile foundations under cyclic lateral loading. DPhil Thesis, Univerisity of Oxford.

Martin, S.C., Buckley, R.M., Mcadam, R.A., and Byrne, B.W. 2022. Enhanced stress wave analysis of scaled monopiles in glacial till at Cowden. In 11th international conference on stress wave theory and design and testing methods for deep foundations (SW22). Rotterdam, The Netherlands.

Matešić, L., and Vucetic, M. 2003. Strain-rate effect on soil secant shear modulus at small cyclic strains. Journal of Geotechnical and Geoenvironmental Engineering, ASCE, 129(6): 536–549. doi:10.1061/(ASCE)1090-0241(2003)129:6(536).

Matlock, H. 1970. Correlation for design of laterally loaded piles in soft clay. In Offshore Technology Conference. Houston, Texas. doi:10.4043/1204-MS.

Mayne, P.W., Kulhawy, F.H., and Trautmann, C.H. 1995. Laboratory modeling of laterally-loaded drilled shafts in clay. Journal of Geotechnical Engineering, ASCE, 121(12): 827–835. doi:10.1061/(ASCE)0733-9410(1995)121:12(827).

McAdam, R.A. 2021. Personal Communication.

McAdam, R.A., Byrne, B.W., Houlsby, G.T., Beuckelaers, W.J.A.P., Burd, H.J., Gavin, K.G., Igoe, D.J.P., Jardine, R.J., Martin, C.M., Muir Wood, A., Potts, D.M., Skov Gretlund, J., Taborda, D.M.G., and Zdravković, L. 2020. Monotonic laterally loaded pile testing in a dense marine sand at Dunkirk. Géotechnique, 70(11): 986–998. doi:10.1680/jgeot.18.PISA.004.

Mitchell, J.K., Campanella, R.G., and Singh, A. 1968. Soil creep as a rate process. Journal of the Soil Mechanics and Foundations Division, ASCE, 94(1): 231–253. doi:10.1061/JSFEAQ.0001085.

Mitchell, J.K., and Soga, K. 2005. Fundamentals of soil behaviour, 3rd Edition. John Wiley & Sons, New York.

NI. 2022. PID algorithms. Available from https://zone.ni.com/reference/en-XX/help/371361R-01/lvpidmain/pid_algs/ [accessed 1 August 2022].

De Nicola, A., and Randolph, M.F. 1997. The plugging behaviour of driven and jacked piles in sand. Géotechnique, 47(4): 841–856. doi:10.1680/geot.1997.47.4.841.

Nikitas, G., Arany, L., Aingaran, S., Vimalan, J., and Bhattacharya, S. 2017. Predicting long term performance of offshore wind turbines using cyclic simple shear apparatus. Soil Dynamics and Earthquake Engineering, 92: 678–683. Elsevier. doi:10.1016/j.soildyn.2016.09.010.

Oka, F., Higo, Y., and Kimoto, S. 2002. Effect of dilatancy on the strain localization of water-saturated elasto-viscoplastic soil. International Journal of Solids and Structures, 39(13–14): 3625–3647. doi:10.1016/S0020-7683(02)00171-3.

Oka, F., Kodak, T., Kimoto, S., Ishigaki, S., and Tsuji, C. 2003. Step-changed strain rate effect on the stress-strain relations of clay and a constitutive modeling. Soils and Foundations, 43(4): 189–202. doi:10.3208/sandf.43.4_189.

Page, A.M., Grimstad, G., Eiksund, G.R., and Jostad, H.P. 2018. A macro-element pile foundation model for integrated analyses of monopile-based offshore wind turbines. Ocean Engineering, 167: 23–35. Elsevier Ltd. doi:10.1016/j.oceaneng.2018.08.019.

Peng, J., Clarke, B., and Rouainia, M. 2006. A device to cyclic lateral loaded model Piles. ASTM Geotechnical Testing Journal, 29(4): 100226. doi:10.1520/GTJ100226.

PICASO AWG. 2022. PICASO project test manual (Unpublished).

Poulos, H.G., and Davis, E.H. 1980. Pile foundation analysis and design. Wiley, New York; Chichester.

Puzrin, A.M., and Houlsby, G.T. 2001. Fundamentals of kinematic hardening hyperplasticity. International Journal of Solids and Structures, 38(21): 3771–3794. doi:10.1016/S0020-7683(00)00238-9.

Qiu, Z. 2022. Personal communication.

Rad, N., and Tumay, M. 1987. Factors affecting sand specimen preparation by raining. ASTM Geotechnical Testing Journal, 10(1): 31. doi:10.1520/GTJ10136J.

Randolph, M.F., and Houlsby, G.T. 1984. The limiting pressure on a circular pile loaded laterally in cohesive soil. Géotechnique, 34(4): 613–623. doi:10.1680/geot.1984.34.4.613.

Rao, S.N., Ramakrishna, V.G.S.T., and Raju, G.B. 1996. Behavior of pile-supported dolphins in marine clay under lateral loading. Journal of Geotechnical Engineering, ASCE, 122(8): 607–612. doi:10.1061/(ASCE)0733-9410(1996)122:8(607).

Reese, L.C., Cox, W.R., and Koop, F.D. 1975. Field testing and analysis of laterally loaded piles on stiff clay. In Offshore Technology Conference. Houston, Texas. doi:10.4043/2312-MS.

Richards, I.A. 2019. Monopile foundations under complex cyclic lateral loading. DPhil Thesis. University of Oxford.

Schnaid, F. 1991. A study of the cone-pressuremeter test in sand. DPhil Thesis. University of Oxford.

Shi, Z., Muir Wood, D., Huang, M., and Hambleton, J.P. 2021. Tay creep: a multi-mechanism model for rate-dependent deformation of soils. Géotechnique. Available Online. doi:10.1680/jgeot.21.00084.

Sivaram, B., and Swamee, P.K. 1977. A computational method for consolidation-coefficient. Soils and Foundations, 17(2): 48–52. doi:10.3208/sandf1972.17.2_48.

Sorensen, K.K., Baudet, B.A., and Simpson, B. 2007. Influence of structure on the time-dependent behaviour of a stiff sedimentary clay. Géotechnique, 57(1): 113–124. Thomas Telford Ltd, London. doi:10.1680/geot.2007.57.1.113.

Staubach, P., Machaček, J., Bienen, B., and Wichtmann, T. 2022. Long-term response of piles to cyclic lateral loading following vibratory and impact driving in water-saturated sand. Journal of Geotechnical and Geoenvironmental Engineering, ASCE, 148(11): 1–17. doi:10.1061/(ASCE)GT.1943-5606.0002906.

Suescun-Florez, E., and Iskander, M. 2017. Effect of fast constant loading rates on the global behavior of sand in triaxial compression. ASTM Geotechnical Testing Journal, 40(1): 20150253. doi:10.1520/GTJ20150253.

Šuklje, L. 1969. Rheological aspects of soil mechanics. Wiley-Interscience, London; New York.

Taborda, D.M.G., Potts, D.M., and Zdravković, L. 2016. On the assessment of energy dissipated through hysteresis in finite element analysis. Computers and Geotechnics, 71: 180–194. doi:10.1016/j.compgeo.2015.09.001.

Takahashi, A., Omura, N., Kobayashi, T., Kamata, Y., and Inagaki, S. 2022. Centrifuge model tests on large-diameter monopiles in dense sand subjected to two-way lateral cyclic loading in short-term. Soils and Foundations, 62(3): 101148. doi:10.1016/j.sandf.2022.101148.

Tatsuoka, F., Di Benedetto, H., Enomoto, T., Kawabe, S., and Kongkitkul, W. 2008. Various viscosity types of geomaterials in shear and their mathematical expression. Soils and Foundations, 48(1): 41–60. doi:10.3208/sandf.48.41.

Tatsuoka, F., Iwasaki, T., and Takagi, Y. 1978. Hysteretic damping of sands under cyclic loading and its relation to shear modulus. Soils and Foundations, 18(2): 25–40. doi:10.3208/sandf1972.18.2_25.

Truong, P., Lehane, B.M., Zania, V., and Klinkvort, R.T. 2019. Empirical approach based on centrifuge testing for cyclic deformations of laterally loaded piles in sand. Géotechnique, 69(2): 133–145. doi:10.1680/jgeot.17.P.203.

Ushev, E.R., and Jardine, R.J. 2022a. The behaviour of Bolders Bank glacial till under undrained cyclic loading. Géotechnique, 72(1): 1–19. doi:10.1680/jgeot.18.P.236.

Ushev, E.R., and Jardine, R.J. 2022b. The mechanical behaviour of Bolders Bank till. Canadian Geotechnical Journal. Available Online. doi:10.1139/cgj-2021-0436.

Vaid, Y.P., and Campanella, R.G. 1977. Time-dependent behavior of undisturbed clay. Journal of the Geotechnical Engineering Division, ASCE, 103(7): 693–709. doi:10.1061/AJGEB6.0000449.

Veletsos, A.S., and Verbic, B. 1974. Basic response functions for elastic foundations. Journal of the Engineering Mechanics Division, ASCE, 100(2): 189–202. doi:10.1061/JMCEA3.0001869.

Vucetic, M., and Tabata, K. 2003. Influence of soil type on the effect of strain rate on small-strain cyclic shear modulus. Soils and Foundations, 43(5): 161–173. doi:10.3208/sandf.43.5_161.

Watanabe, K., and Kusakabe, O. 2013. Reappraisal of loading rate effects on sand behavior in view of seismic design for pile foundation. Soils and Foundations, 53(2): 215–231. doi:10.1016/j.sandf.2013.02.003.

White, J.R.F. 2020. A laboratory investigation into the behaviour of sand at low confining stresses. DPhil thesis. University of Oxford.

Wind Europe. 2021. Offshore wind in Europe—key trends and statistics 2020.

Wroth, C.P., and Houlsby, G.T. 1985. Soil mechanics - Property characterization and analysis procedures. In Proceedings of 11th International Conference on Soil Mechanics and Foundation Engineering. San Francisco. pp. 536–537.

Wu, K.-W., Byrne, B.W., and Houlsby, G.T. 2020. Investigation of rate effects for monopile foundations : laboratory-scale model tests. In 4th International Symposium on Frontiers in Offshore Geotechnics (ISFOG 2020). Austin, Texas.

Wu, K.-W., Byrne, B.W., and Houlsby, G.T. 2022a. Rate-dependent monopile response to lateral loading in glacial till: laboratory-scale model tests. In 10th International Conference on Physical Modelling in Geotechnics (ICPMG 2022). Daejeon, Korea.

Wu, T., Tong, J., Sun, H., Yuan, Z., and Guo, L. 2022b. Common characteristics between cyclic behaviours at different frequencies and monotonic behaviours of clay. Canadian Geotechnical Journal, 59(9): 1553–1567. doi:10.1139/cgj-2021-0259.

Yang, S., He, B., Andersen, K.H., and Firouzianbandpey, S. 2022. Monotonic and cyclic properties of silty sand and sandy silt for foundation design of offshore windfarms. Canadian Geotechnical Journal. Available Online. doi:10.1139/cgj-2022-0009.

Yin, J.-H., and Graham, J. 1989. Viscous–elastic–plastic modelling of one-dimensional time-dependent behaviour of clays. Canadian Geotechnical Journal, 26(2): 199–209. doi:10.1139/t89-029.

Yong, R., and Japp, R. 1969. Stress-strain behavior of clays in dynamic compression. In Vibration Effects of Earthquakes on Soils and Foundations. ASTM International. pp. 233–262. doi:10.1520/STP33643S.

Zdravković, L., Jardine, R.J., Taborda, D.M.G., Abadias, D., Burd, H.J., Byrne, B.W., Gavin, K.G., Houlsby, G.T., Igoe, D.J.P., Liu, T., Martin, C.M., McAdam, R.A., Muir Wood, A., Potts, D.M., Skov Gretlund, J., and Ushev, E. 2020a. Ground characterisation for PISA pile testing and analysis. Géotechnique, 70(11): 945–960. doi:10.1680/jgeot.18.PISA.001.

Zdravković, L., Taborda, D.M.G., Potts, D.M., Abadias, D., Burd, H.J., Byrne, B.W., Gavin, K.G., Houlsby, G.T., Jardine, R.J., Martin, C.M., McAdam, R.A., and Ushev, E.R. 2020b. Finite-element modelling of laterally loaded piles in a stiff glacial clay till at Cowden. Géotechnique, 70(11): 999–1013. doi:10.1680/jgeot.18.PISA.005.

Ziegler, H. 1963. Some extremum principles in irreversible thermodynamics, with application to continuum mechanics. Progress in Solid Mechanics, 4: 93–193.

Appendix

A.1 Kinematic hardening (Houlsby and Puzrin, 2006)

Under the hyperplasticity framework, the conceptual kinematic hardening model is described in terms of the Helmholtz free energy f and a dissipation function d below:

$$f = \frac{h_{e0}}{2}\left[u_e - \sum_{n=1}^{N} \alpha_{en}\right]^2 + \sum_{n=1}^{N} \frac{h_{en}}{2} \alpha_{en}^2 \qquad \text{Equation A-1}$$

and

$$d = \sum_{n=1}^{N} k_{en} \left| \dot{\alpha_{en}} \right| \qquad \text{Equation A-2}$$

where h_{en} and k_{en} are the spring and slider constants, respectively, and α_{en} is the internal variable.

The kinematic hardening model can be expressed using an alternative way in terms of the Gibbs energy function g and yield functions (y_1 ... y_n) below:

$$g = -\frac{H_e^2}{2h_{e0}} - H_e \sum_{n=1}^{N} \alpha_{en} + \sum_{n=1}^{N} \frac{h_{en}}{2} \alpha_{en}^2 \qquad \text{Equation A-3}$$

and

$$y_n = \frac{\chi_{en}^2}{k_{en}^2} - 1 = 0, n = 1 \dots N \qquad \text{Equation A-4}$$

in which χ_{en} is the generalised force at the loading point.

The above alternative expressions are obtained using Legendre-Fenchel transforms (see Puzrin and Houlsby (2001) and Houlsby and Puzrin (2006) for details). For the development of the model, the $g - y$ format (*i.e.* considering the Gibbs free energy and yield functions) is adopted. Following hyperplasticity theory, the following equations can be derived:

$$u_e = -\frac{\partial g}{\partial H_e} = \frac{H_e}{h_{e0}} + \sum_{n=1}^{N} \alpha_{en}\,, n = 1 \dots N$$

Equation A-5

$$\bar{\chi}_{en} = -\frac{\partial g}{\partial \alpha_{en}} = H_e - h_{en}\alpha_{en}, n = 1 \dots N$$

Equation A-6

and

$$\dot{\alpha}_{en} = \lambda_n \frac{\partial y_n}{\partial \chi_{en}} = 2\lambda_n \frac{\chi_{en}}{k_{en}^2}.$$

Equation A-7

in which λ_n is a dimensionless scaler for $\dot{\alpha}_{en}$, $y_n \cdot \lambda_n = 0$, $y_n \leq 0$ and $\lambda_n \geq 0$ under Karush-Kuhn-Tucker conditions. $\chi_{en} = \bar{\chi}_{en}$ is proven in hyperplasticity. Together these conditions are sufficient to describe the constitutive behaviour of the model.

A.2 Formulation of the general loading model (Houlsby, 2022a)

By defining $\varepsilon_t = e/L$ (normalised load eccentricity), $H = H_e$, $M' = H_e\varepsilon_t$, $\alpha_{en} = \alpha_{un} + \varepsilon_t\vartheta_n$, $\chi_{un} = \chi_{en}$ (generalised forces at the ground level and the loading point) and $\chi_{\vartheta n} = \chi_{en}\varepsilon_t$ can be derived.

α_{en}^2 and H_e^2 in Equation A-3 can be expressed as

$$\alpha_{en}^2 = (\alpha_{un} + \varepsilon_t\alpha_{\vartheta n}) \cdot \left[\alpha_{un} + \frac{\left(-f_1 f_2 \alpha_{un}\alpha_{\vartheta n} + f_1^2\alpha_{\vartheta n}^2\right)}{\alpha_{un} - f_1 f_2 \alpha_{\vartheta n}}\right]$$

$$= \frac{\left(\frac{\alpha_{un}}{\alpha_{\vartheta n}} + \varepsilon_t\right)}{\left(\frac{\alpha_{un}}{\alpha_{\vartheta n}} - f_1 f_2\right)} \cdot \left(\alpha_{un}^2 - 2f_1 f_2 \alpha_{un}\alpha_{\vartheta n} + f_1^2\alpha_{\vartheta n}^2\right)$$

Equation A-8

$$= \frac{f_1^2 + f_1 f_2\varepsilon_t + f_1 f_2\varepsilon_t + \varepsilon_t^2}{f_1^2 + f_1 f_2\varepsilon_t - f_1^2 f_2^2 - f_1 f_2 \varepsilon_t} \cdot \left(\alpha_{un}^2 - 2f_1 f_2 \alpha_{un}\alpha_{\vartheta n} + f_1^2\alpha_{\vartheta n}^2\right)$$

$$= \frac{f_1^2 + 2f_1 f_2\varepsilon_t + \varepsilon_t^2}{f_1^2(1 - f_2^2)} \cdot \left(\alpha_{un}^2 - 2f_1 f_2 \alpha_{un}\alpha_{\vartheta n} + f_1^2\alpha_{\vartheta n}^2\right)$$

and

$$H_e^2 = H_e^2 \cdot \frac{f_1^2 + 2f_1f_2\varepsilon_t + \varepsilon_t^2}{f_1^2 + 2f_1f_2\varepsilon_t + \varepsilon_t^2} = \frac{f_1^2H^2 + 2f_1f_2 \cdot H \cdot M' + M'^2}{f_1^2 + 2f_1f_2\varepsilon_t + \varepsilon_t^2}.$$

Equation A-9

By substitutions using Equation A-8 and Equation A-9, Equation A-3 is re-written as

$$g = -\frac{H_e^2}{2h_{e0}} - \sum_{n=1}^{N} H_{en} \cdot \alpha_{en} + \sum_{n=1}^{N} \frac{h_{en} \cdot \alpha_{en}^2}{2}$$

$$= -\frac{f_1^2H^2 + 2f_1f_2HM' + M'^2}{2h_{e0}(f_1^2 + 2f_1f_2\varepsilon_t + \varepsilon_t^2)} - \sum_{n=1}^{N}(H\alpha_{un} + M'\alpha_{\vartheta n})$$

Equation A-10

$$+\sum_{n=1}^{N} \frac{h_{en}(f_1^2 + 2f_1f_2\varepsilon_t + \varepsilon_t^2)}{2f_1^2(1 - f_2^2)}\left(\alpha_{un}^2 - 2f_1f_2\alpha_{un}\alpha_{\vartheta n} + f_1^2\alpha_{\vartheta n}^2\right).$$

The yield function y_n is determined using the elliptical function based on Equation 6-10:

$$y_n = \frac{\chi_{en}^2}{k_{en}^2} - 1 = \frac{1}{k_{en}^2} \cdot \frac{\chi_{en}^2(f_3^2 + 2f_3f_4\varepsilon_t + \varepsilon_t^2)}{f_3^2 + 2f_3f_4\varepsilon_t + \varepsilon_t^2} - 1$$

Equation A-11

$$= \frac{f_3^2\chi_{un}^2 + 2f_3f_4\chi_{un}\chi_{\vartheta n} + \chi_{\vartheta n}^2}{k_{en}^2(f_3^2 + 2f_3f_4\varepsilon_t + \varepsilon_t^2)} - 1.$$

It is defined that $h_n = h_{en}(f_1^2 + 2f_1f_2\varepsilon_t + \varepsilon_t^2)$ and $k_n = k_{en}(f_3^2 + 2f_3f_4\varepsilon_t + \varepsilon_t^2)$, so the above equations can be re-written as

$$g = -\frac{f_1^2H^2 + 2f_1f_2HM' + M'^2}{2h_0} - \sum_{n=1}^{N}(H\alpha_{un} + M'\alpha_{\vartheta n})$$

$$+\sum_{n=1}^{N} \frac{h_n}{2f_1^2(1 - f_2^2)}\left(\alpha_{un}^2 - 2f_1f_2\alpha_{un}\alpha_{\vartheta n} + f_1^2\alpha_{\vartheta n}^2\right)$$

Equation A-12

and

$$y_n = \frac{f_3^2\chi_{un}^2 + 2f_3f_4\chi_{un}\chi_{\vartheta n} + \chi_{\vartheta n}^2}{k_n^2} - 1$$

$$= \frac{\sqrt{f_3^2\chi_{un}^2 + 2f_3f_4\chi_{un}\chi_{\vartheta n} + \chi_{\vartheta n}^2}}{k_n} - 1.$$ Equation A-13

Following Equation A-12 and Equation A-13, the generalised physical quantities for the model and be derived, as given in Table 6-3. Along with $\chi_{un} = \bar{\chi}_{un}$ and $\chi_{\vartheta n} = \bar{\chi}_{\vartheta n}$, given in the hyperplasticity formulation, the model are fully described (see numerical implementation in Section 6.2.4.4).

A.3 Linear viscosity (Houlsby and Puzrin, 2006)

The yield stress may marginally increase with the strain rate considering soil rate effects. In Figure 6-5, the terms μ_{e1}, μ_{e2},…μ_{eN} are added to demonstrate rate dependency, so the rate-independent model becomes a multiple surface viscoplastic model. In hyperplasticity, the dissipation function d becomes “non-homogeneous” (*i.e.* dissipation is a compound process) and is the sum of the flow (w) and force (z) potentials. Their detailed mathematical derivations can be found in Houlsby and Puzrin (2006). w is expressed as

$$w = d - z.$$ Equation A-14

The dissipation function d and flow potential z for linear viscosity are expressed as

$$d = \sum_{n=1}^{N} k_{en}|\dot{\alpha}_{en}| + \sum_{n=1}^{N} \mu_{en}\dot{\alpha}_{en}^2$$ Equation A-15

and

$$z = \sum_{n=1}^{N} k_{en}|\dot{\alpha}_{en}| + \frac{1}{2}\sum_{n=1}^{N} \mu_{en}\dot{\alpha}_{en}^2.$$ Equation A-16

From the above equation, χ_{en} is derived:

$$\chi_{en} = \frac{\partial z}{\partial \dot{\alpha}_{en}} = k_{en} S(\dot{\alpha}_{en}) + \mu_{en}\dot{\alpha}_{en}$$ Equation A-17

where $S(\quad)$ is the signum function.

As $w = d - z$, w and $\dot{\alpha}_{en}$ can be expressed as

$$w = \frac{1}{2}\sum_{n=1}^{N} \mu_{en}\dot{\alpha}_{en}^{2} = \sum_{n=1}^{N} \frac{\langle |\chi_{en}| - k_{en}\rangle^{2}}{2\mu_{en}}$$ Equation A-18

and

$$\dot{\alpha}_{en} = \frac{\partial w}{\partial \chi_{en}} = \frac{\langle |\chi_{en}| - k_{en}\rangle}{\mu_{en}} \cdot S(\chi_{en}).$$ Equation A-19

in which $\langle \quad \rangle$ are Macaulay brackets.

The horizontal displacement rate at the loading point ($\dot{u}_{en}$) is given as

$$\dot{u}_{en} = \underbrace{\frac{\dot{\chi}_{en}}{E_0}}_{\text{Elastic}} + \underbrace{\sum_{n=1}^{N}\left[\frac{\langle |\chi_{en}| - k_{en}\rangle}{\mu_{en}} \cdot S(\dot{\chi}_{en})\right]}_{\text{Plastic}}.$$ Equation A-20

By incrementally calculating the pile response, the first N^{*} elements in Figure 6-5 are sliding, which means $k_{eN^{*}} \leq \chi_{en} < k_{eN^{*}+1}$. The term $\langle |\chi_{en}| - k_{en}\rangle$ in Equation A-20 becomes $|\chi_{en}| - k_{en}$ for all $n \leq N^{*}$, while $|\chi_{en}| - k_{en} = 0$ for all $n > N^{*}$.

u_{en} can be expressed as

$$u_{en} = \frac{H_{en}}{E_0} + \sum_{n=1}^{N} \alpha_{en}.$$ Equation A-21

Therefore, by re-arranging Equation A-20, the following relationship can be derived:

$$\dot{u}_{en} + \frac{h_{en}}{\mu_{en}} \cdot u_{en} + \frac{1}{\mu_{en}} \sum_{n=1}^{N^*} k_{en}\, S(\chi_{en} - h_{en}\alpha_{en})$$

Equation A-22

$$= \frac{\dot{\chi}_{en}}{E_0} + \frac{E_0 N^* + h_{en}}{E_0 \mu_{en}} \cdot H_{en}$$

It is assumed again that $\chi_{en} \geq h_{en}\alpha_{en}$ (*i.e.* $S(\chi_{en} - h_{en}\alpha_{en}) = 1$). Considering a constant rate of u_{en} under monotonic loading, denoted as $\dot{u}_{ec}$, Equation A-22 is integrated as

$$H_{en} = \left[h_{en} u_{en} + \sum_{n=1}^{N^*} k_{en} \right] \cdot a_{N^*} + \mu_{en} \dot{u}_{ec} \cdot a_{N^*}{}^2$$

Equation A-23

$$+ C_{N^*} \exp\left\{ - \frac{E_0 u_{en}}{[\mu_{en} \dot{u}_{ec} \cdot a_{N^*}]} \right\}$$

where C_{N^*} is the integration constant, and $a_{N^*} = E_0/(E_n + h_{en})$.

It is often the case that $\mu_{e1} = \cdots = \mu_{en} = \mu$ (*i.e.* strain-dependent dashpots are not considered), so here, one dashpot parameter μ is applied to the model. For some other clays, such as the Belfast clay, strain dependency may be considered (Graham *et al.*, 1983). When $\dot{u}_{en} \approx 0$ under slow loading or low viscosity, the viscous terms are omitted, with H_{en} described by purely kinematic hardening. The magnitude of μ in the model is dependent on the calibration curve; therefore, using a calibration curve at another rate will lead to a different μ value.

For numerical modelling, through defining the w function, the model is fully described with linear viscosity. The g function or f function is exactly the same as that for the kinematic hardening model. The term $|\chi_{en}| - k_{en}$ can be substituted with the yield function y_n so that the w function has variables χ_{un} and $\chi_{\vartheta n}$. Besides, $\dot{\alpha}_{un}$ and $\dot{\alpha}_{\vartheta n}$ can be obtained from $\partial w/\partial \chi_{un}$ and $\partial w/\partial \chi_{\vartheta n}$, so rate effects in both $H - u$ and $M' - \vartheta$ domains can be specified. $\dot{\alpha}_{un}$ and $\dot{\alpha}_{\vartheta n}$ in Table 6-3 are modified to include the viscous components.

A.4 Rate process theory (RPT) model (Houlsby and Puzrin, 2006)

Rate process theory describes the macro response of a rate-dependent material (*e.g.* clay) as "thermally activated processes". Mitchell and Soga (2005) discussed its applications to soil behaviour (see Section 1.2.1). In RPT, following Equation Figure 1-4, $\dot{\alpha}_{en}$ can be described as a function of the driving force χ_{en}:

$$\dot{\alpha}_{en} = T_A \cdot \sinh\left(\frac{\chi_{en}}{T_B}\right) \qquad \text{Equation A-24}$$

where T_A and T_B are the functions of temperature, as mentioned in Section 1.2.1. As temperature effects were found to be minimal in the testing, these two functions are assumed to be constants. From the above equation, χ_{en} can be expressed as

$$\chi_{en} = T_B \cdot \sinh^{-1}\left(\frac{\dot{\alpha}_{en}}{T_A}\right). \qquad \text{Equation A-25}$$

By adding the plastic dissipation term and the viscous dissipation term ($\chi_{en}\dot{\alpha}_{en}$), with T_A and T_B replaced by other constants, the dissipation function d can be expressed as

$$d = k_{en}|\dot{\alpha}_{en}| + \mu_{en}\dot{\alpha}_{ref}\dot{\alpha}_{en}\sinh^{-1}\left(\frac{\dot{\alpha}_{en}}{\dot{\alpha}_{ref}}\right) \qquad \text{Equation A-26}$$

in which $\dot{\alpha}_{ref}$ is the quasi-static reference rate when the viscosity becomes approximately logarithmic from linear, and μ_{en} can be interpreted as a linear viscosity. These definitions are also similar to the theoretical derivations by Beuckelaers (2017).

In hyperplasticity, $d = \chi\dot{\alpha}$ and $dz/d\dot{\alpha} = \chi$. Thus, z is given as

$$z = k_{en}|\dot{\alpha}_{en}| + \mu_{en}\dot{\alpha}_{ref}\left[\dot{\alpha}_{en}\sinh^{-1}\left(\frac{\dot{\alpha}_{en}}{\dot{\alpha}_{ref}}\right) + \dot{\alpha}_{ref} - \sqrt{\dot{\alpha}_{en}^2 + \dot{\alpha}_{ref}{}^2}\right]. \qquad \text{Equation A-27}$$

Meanwhile, χ_{en} can be expressed as

$$\chi_{en} = \frac{d}{\dot{\alpha}_{en}} = k_{en}S(\dot{\alpha}_{en}) + \mu_{en}\dot{\alpha}_{ref} \cdot \sinh^{-1}\left(\frac{\dot{\alpha}_{en}}{\dot{\alpha}_{ref}}\right). \qquad \text{Equation A-28}$$

As $w = d - z = \mu_{en}\dot{\alpha}_{ref} \cdot \left(\sqrt{\dot{\alpha}_{en}^2 + \dot{\alpha}_{ref}^2} - \dot{\alpha}_{ref}\right)$, $\dot{\alpha}_{en}$ can be expressed as

$$\dot{\alpha}_{en} = \dot{\alpha}_{ref}\ \sinh\left[\frac{\langle|\chi_{en}| - k_{en}\rangle}{\mu_{en}\dot{\alpha}_{ref}}\right] S(\chi_{en}). \qquad \text{Equation A-29}$$

Therefore, the following equation can be derived:

$$\dot{u}_{en} = \frac{\dot{\chi}_{en}}{h_{e0}} + \dot{\alpha}_{ref}\ \sinh\left[\frac{\langle|\chi_{en}| - k_{en}\rangle}{\mu_{en}\dot{\alpha}_{ref}}\right] S(\chi_{en}). \qquad \text{Equation A-30}$$

w can be re-written as

$$\begin{aligned} w &= \mu_{en}\dot{\alpha}_{ref}\left(\sqrt{\dot{\alpha}_{en}^2 + \dot{\alpha}_{ref}{}^2} - \dot{\alpha}_{ref}\right) \\ &= \mu_{en}\dot{\alpha}_{ref}\left\{\cosh\left[\frac{\langle|\chi_{en}| - k_{en}\rangle}{\mu_{en}\dot{\alpha}_{ref}}\right] - 1\right\}. \end{aligned} \qquad \text{Equation A-31}$$

Again, the term $|\chi_{en}| - k_{en}$ can be replaced by y_n to capture the coupled moment-horizontal load response. w, $\partial w/\partial \chi_{un}$ and $\partial w/\partial \chi_{\vartheta n}$ functions can therefore be derived and coded for numerical implementation.

In Equation A-29, if $\dot{\alpha}_{en}$ is small, $\dot{\alpha}_{en} \approx \langle|\chi_{en}| - k_{en}\rangle/\mu_{en} \cdot S(\chi_{en})$ (*i.e.* linear rate dependency). When $\dot{\alpha}_{en}$ is large, $\dot{\alpha}_{en} \approx \dot{\alpha}_{ref}/2 \cdot \exp\left(\langle|\chi_{en}| - k_{en}\rangle/\mu_{en}\dot{\alpha}_{ref}\right)$ (*i.e.* the semi-logarithmic relationship observed experimentally). For very small $\dot{\alpha}_{en}$, rate effects may be negligible (see Figure 1-22 below the upper yield).